

MSc thesis in Geomatics

Constructing a digital 3D road network for The Netherlands

Kristof Kenesei
2021



MSc thesis in Geomatics

Constructing a digital 3D road network for The Netherlands

Kristof Kenesei

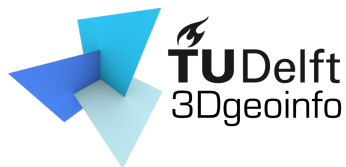
June 2021

A thesis submitted to the Delft University of Technology in partial fulfillment of the requirements for the degree of Master of Science in Geomatics

Kristof Kenesei: *Constructing a digital 3D road network for The Netherlands* (2021)

© This work is licensed under a Creative Commons Attribution 4.0 International License. To view a copy of this license, visit <http://creativecommons.org/licenses/by/4.0/>.

The work in this thesis was carried out in the:



3D Geoinformation
Department of Urbanism
Faculty of the Built Environment & Architecture
Delft University of Technology

Supervisors: Ravi Peters
Jantien Stoter
Co-reader: Stelios Vitalis

Abstract

This research concerned the design and implementation of a system to perform the 3D conversion of a national road network using airborne Lidar data and land-based road elevation measurements, preserving its topology and quantifying output elevation accuracy. While the system was designed with generality in mind, specific Dutch open data datasets were used as input which were also used in a commercial project with the same goals. In addition to designing a scientifically sound equivalent of the commercial implementation, this research also explored purely academic goals, such as selecting road surface laser reflections accurately and using them for 2.5D road surface modelling purposes. Our system was based on decomposing the 3D conversion task into individually solvable 2.5D sub-problems to enable the use of efficient terrain modelling methods, and to prove that scaling via multiprocessing would be possible. At the 10-30 points per m^2 sampling density we worked with, the road surfaces are oversampled. We found that because our elevation estimates are based on road reflections only, and because road surfaces are smooth and relatively flat, the output quality and accuracy depends only on the specific technique used to extract the elevations from the Lidar data. Using our methods, the output elevation accuracy represents a 30% increase relative to the Lidar input data, amounting to 10.6 cm at 95% certainty with our specific datasets. This is assumed to be violated only where local density drops below 3 points per m^2 , which occurs where roads are occluded by opaque objects, unless the land-based road surface measurements can provide enough additional data. Elsewhere, more than 98% of the road network conforms with the minimum point density. The 2.5D-based decomposition was found to be an effective means of simplifying the problem and terrain modelling methods were successfully used in the procedure. More than 90% of the traffic-occupied road surfaces are included in the resulting surface models, and about 75% of the total paved surfaces. We extracted the output elevations from them, using linear interpolation where they were unavailable. Our 3D conversion quality and accuracy represents an improvement relative to the commercial results, mostly due to the better prioritising of the input elevation sources, in addition to our solution's capacity to handle complex small to medium-scale occlusion better, including complex relationships between roads such as multi-level motorway junctions.

Contents

1	Introduction	1
1.1	Motivation	1
1.2	The NDW commission	2
1.3	Field and relevance	3
1.4	Research questions	4
2	Related work	7
2.1	Road identification in point clouds	7
2.1.1	Research using point clouds only	7
2.1.2	Research using input point clouds and approximate road locations	9
2.2	Lidar survey and DTM accuracy	12
2.2.1	Accuracy description of Lidar sensing	13
2.2.2	Describing the accuracy of Lidar-derived DTMs	14
2.3	Input assessment	16
2.3.1	Nationaal Wegenbestand – NWB	17
2.3.2	Actueel Hoogtebestand Nederland – AHN	19
2.3.3	Digitaal Topografisch Bestand – DTB	21
2.4	Methods of existing implementations	24
2.4.1	NDW prototype	24
2.4.2	RHDHV’s commercial implementation	25
3	Methodology and methods	29
3.1	Methodological framework	29
3.1.1	Preparation	29
3.1.2	Preliminary analysis, proposal writing	29
3.1.3	Analysis	30
3.1.4	Finalisation	30
3.2	Overview of methods	30
3.2.1	Proposed processing pipeline	32
3.2.2	Dependency of methods on specific datasets	35
3.2.3	A note on DTB’s role	36
3.2.4	Accuracy assessment of processing steps	36
3.3	Detailed methods	38
3.3.1	Splitting NWB into NBRS	39
3.3.2	Elevation estimation	41
3.3.3	Lidar segmentation	44
3.3.4	Edge approximation	47
3.3.5	Active contour optimisation	49
3.3.6	TIN construction	52
3.3.7	TIN-based interpolation and vertex snapping	57
3.4	Accuracy assessment	59
3.4.1	Detecting regions with poor sampling	59
3.4.2	Effect of interpolation on accuracy	60
3.4.3	Evaluating TIN surface completeness	61
3.5	Comparison with commercial results	61
3.6	Programming framework	62

4	Results	65
4.1	Manual pre-processing	65
4.1.1	Producing the testing datasets	65
4.1.2	Description of testing datasets	66
4.2	Results of processing steps	68
4.2.1	Splitting NWB into NBRS	69
4.2.2	Elevation estimation	71
4.2.3	Lidar segmentation	76
4.2.4	Edge approximation	80
4.2.5	Active contour optimisation	84
4.2.6	TIN construction	90
4.2.7	Interpolation in TINs and snapping	95
4.3	Accuracy assessment	99
4.3.1	Empirical accuracy assessment	100
4.3.2	Formal accuracy assessment	101
4.3.3	Ratio of accurate vertices	103
4.3.4	TIN completeness	104
4.3.5	Tabulated values	106
4.4	Comparison with commercial implementation	107
4.4.1	Representative example comparisons	107
4.4.2	Tabulated RMSE values	111
5	Conclusions	115
5.1	Usefulness and generality of datasets	115
5.1.1	General remarks about AHN3 and DTB	115
5.1.2	On the impact of input quality	116
5.2	Effectiveness of processing steps	116
5.2.1	Decomposing the 3D problem into 2.5D sub-problems	117
5.2.2	Surface modelling effectiveness	117
5.2.3	NWB 3D-conversion effectiveness	118
5.3	Accuracy-related conclusions	119
5.4	Accuracy assessment conclusions	119
5.5	Conclusions of comparison with commercial results	120
5.6	Summary conclusions	121
5.7	Future work	121
5.7.1	Eliminating active contour optimisation	121
5.7.2	Improving TIN construction effectiveness	122
5.7.3	Performance and scaling	123
5.7.4	Conditionally accepting preliminary elevations as final	124
5.7.5	Using the support dataset more intelligently	125
A	Appendix	127
A.1	Testing the updated NWB motorways	127
A.1.1	Updated NWB geometry	127
A.1.2	Impact on edge approximation	127
A.1.3	Impact on TIN construction	129
A.1.4	On improving NWB's 2D georeferencing dynamically	130
A.2	Reproducibility self-assessment	132
A.3	Self-reflection	132

List of Figures

1.1	Illustration of the 3D conversion justification	2
2.1	Illustration of the results of PCD convolution	9
2.2	Illustration of a contour optimisation procedure	10
2.3	Examples of 3D-converted multi-level road geometry	11
2.4	Illustration of the effects of terrain slope on vertical accuracy	13
2.5	Example render of NWB, colour-coded to show road ownership	17
2.6	Comparison of AHN3 with some relevant NWB centrelines	19
2.7	Render of AHN3 highlighting bridge points	20
2.8	Render of AHN3 highlighting motorway signs	21
2.9	Renders of DTB road edges overlain with NWB, illustrating various issues	22
2.10	Renders comparing AHN3 with DTB lines	24
2.11	Illustrations of the workflows of the commercial implementation	25
3.1	Illustration of my top-level methodology	31
3.2	Illustration of the top-level pipeline steps	32
3.3	Flowchart illustrating of the NBRs generation step	39
3.4	Flowchart illustrating of the elevation estimation step	42
3.5	Illustration of the elevation estimation step	43
3.6	Flowchart illustrating of the Lidar segmentation step	44
3.7	Illustration of the Lidar segmentation step	45
3.8	Flowchart illustrating of the edge approximation step	47
3.9	Illustration of the edge approximation step	49
3.10	Flowchart illustrating of the active contour optimisation step	50
3.11	Flowchart illustrating of the TIN construction step	52
3.12	Illustration of the TIN construction step	54
3.13	Flowchart illustrating the details of TIN initialisation and extension	56
3.14	Flowchart illustrating the elevation interpolation step	58
4.1	Visualisations illustrating the results of manual pre-processing	66
4.2	Renders illustrating the results of NBRs generation	70
4.3	Visualisations illustrating the preliminary elevation estimation results	72
4.4	Visualisations illustrating vertex densification	72
4.5	Visualisations comparing the preliminary 3D-NWB with AHN3	74
4.6	Visualisations illustrating the results of Lidar segmentation	76
4.7	Renders showing the disagreement between AHN3 and DTB	77
4.8	Render illustrating the handling of AHN3 gaps during Lidar segmentation	79
4.9	Renders illustrating the results of preliminary edge approximation	81
4.10	Renders illustrating challenging edge approximation scenarios	83
4.11	Renders illustrating the results of active contour optimisation	85
4.12	Visualisations comparing optimised edges to attractor maps	87
4.13	Renders illustrating the results of TIN initialisation and extension	89
4.14	Overview render of constructed TINs and renders of TIN artefacts	92
4.15	Visualisations comparing final 3D-NWB geometries with intermediate results	96
4.16	Renders comparing final 3D-NWB geometries with the underlying TIN models	98
4.17	Charts demonstrating the outcome of empirical accuracy assessment	100
4.18	Charts illustrating the formal accuracy assessment results on two LineStrings	102
4.19	Renders showing the subclouds, TINs and 3D-NWB centrelines relevant to Figure 4.18	103

List of Figures

4.20	2D comparison renders of NWB, BGT and aerial imagery	105
4.21	Charts comparing the academic and commercial results (<i>Knooppunt Deil</i>)	108
4.22	Charts comparing the academic and commercial results (<i>Gorinchem</i>)	109
4.23	Charts comparing the academic and commercial results (<i>Knooppunt Ridderkerk</i>)	110
A.1	Figure illustrating recent NWB improvements	128
A.2	Visualisation of the effects of improving NWB on preliminary edges	129
A.3	Visualisation of the effects of improving NWB on the TINs	130
A.4	Reproducibility criteria to be assessed.	132

List of Tables

4.1	Inventory of the testing datasets	68
4.2	Tabulated 3D-NWB accuracy and completeness results per testing dataset	106
4.3	Tabulated academic and commercial similarity quantification results	111

Acronyms

AHN	Actueel Hoogtebestand Nederland	11
AHN2	Actueel Hoogtebestand Nederland 2	12
AHN3	Actueel Hoogtebestand Nederland 3	7
AHN3	Actueel Hoogtebestand Nederland 3	7
ALS	airborne laser scanning	7
API	application programming interface	35
BGT	Basisregistratie Grootschalige Topografie	11
CDT	constrained Delaunay triangulation	11
DSM	digital surface model	20
DT	Delaunay triangulation	93
DTB	Digitaal Topografisch Bestand	7
DTM	digital terrain model	7
G-road	Gemeenteweg (municipal road)	17
GIS	geographical information system	3
GNSS	global navigation satellite system	1
GUI	graphical user interface	111
IDW	inverse distance weighting	14
IMU	inertial measurement unit	13
INS	inertial navigation system	12
JTE ID	<i>junctie</i> (intersection) ID number	40
MLE	maximum likelihood estimation	4
MLS	mobile laser scanning	8
NBRS	non-branching road segment(s)	32
NDW	Nationaal Dataportaal Wegverkeer	2
NWB	Nationaal Wegenbestand	2
P-road	Provincieweg (provincial road)	17
PCD	phase coded disk	8
RANSAC	random sample consensus	8
TIN	triangular irregular network	4
R-road	Rijksweg (motorway)	17
RHDHV	Royal HaskoningDHV	2
RMSE	root mean squared error	4
RWS	Rijkswaterstaat	2
W-road	Rijkswaterstaat-managed road	17

1 Introduction

1.1 Motivation

Constructing and maintaining an up-to-date graph-like road network on the national level has a range of firmly established uses. Owing to its structure, it can be used efficiently for modelling and simulation purposes, such as traffic flow simulations, passenger transport modelling, construction and upgrade impact modelling (to pinpoint optimal locations and types of investment), and traffic noise load modelling (Bell and Lida [1997]; Zhu and Li [2007]; Zhang [2011]; Durán Fernández and Santos [2014]; Peng et al. [2020]). It can also be used for navigation; a graph-like road network representation is at the heart of most road navigation services (Yue et al. [2008]). Combined with other datasets, we can mention an even wider range of use cases: complemented by ecological statistics and models, it can offer insight into the impact of the presence of roads, and planned road construction on the flora and fauna in their vicinity.

Or to mention a different type of example, a digital road network may be used as a shared working space when aggregating geospatial data relating to road infrastructure from various sources. It makes it possible for geographical road locations, topographical relationships, and arbitrary semantic information to reside in the same network-type data model, making analysis techniques more straightforward, enforcing consistency and saving effort for data providers who would otherwise all need to maintain their own road models (Ekpenyong et al. [2007]). This example is closely related to the ambitions of the provider of the Dutch digital road network that is the primary subject of this research.

One may remark that a two-dimensional representation with *approximate* geographical locations may suffice for many of the purposes I listed as examples above, topology being the main concern in network analysis. For instance, global navigation satellite system (GNSS) navigation software often use snapping methods to ensure that the navigating vehicle always traverses the road graph – ensuring that navigation remains continuous even when positioning has poor accuracy (Fouque and Bonnifait [2008]). Traffic flow simulations are primarily concerned with traffic loads, road properties, and how roads are subdivided by intersections. *Mostly*, they are not concerned with the exact geographical locations of roads – as long as the topology is relatively accurate, any geographical permutation of the network will yield largely invariant results (Thomson and Richardson [1995]).

However, some applications are concerned with the road network in the context of its surroundings, which makes the accuracy of its georeferencing important. Noise modelling is such an application, because it requires deriving the noise load affecting various objects in the vicinity of the roads. This also involves considering objects that may impact the propagation of the noise, such as noise barriers, terrain, and buildings (Ishiyama et al. [1991]; Bennett [1997]; Guarnaccia and Quartieri [2012]).

A realistic noise propagation model mainly takes into account terrain, and the 3D geometry of the surrounding objects. However, the position of roads *relative to the terrain* should also be taken into account. For instance, consider a hill with a building on one side and a road on the other, as shown in Figure 1.1. The hill (representing the terrain) in this case acts as a noise barrier affecting the noise load received by the building. Unless the assumption holds that roads are always found *exactly on* the terrain, this is not yet enough information to derive the noise load incident on the building. Roads may be elevated, sunken into the ground, or built in tunnels – meaning that the assumption does not always hold. For instance, if the road in my example was built on a bridge with a similar height as the hill, then the hill suppresses the road noise much less effectively, and “snapping” the road to the terrain by ignoring its elevation would yield incorrect noise modelling results. One way to handle such scenarios is to take into account the absolute elevation of the road surfaces, in other words to use a 3D road network.

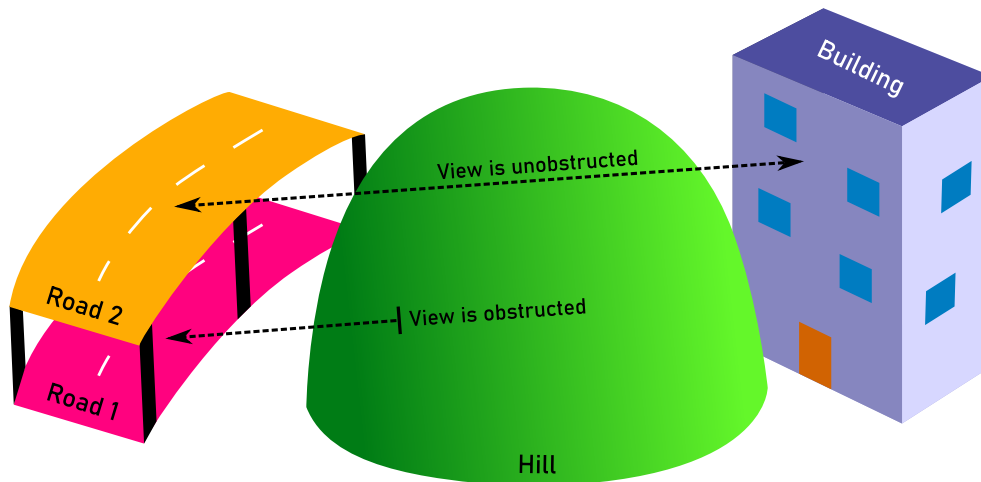


Figure 1.1: This illustration shows a justification for the 3D conversion of digital road networks. Assuming that the roads always lie on the terrain (pink road) allows one to model the propagation of noise with the surrounding terrain and 3D objects taken into account. However, roads above or below the terrain will result in faults in the model. For instance, the noise from an arbitrary elevated version of this road (yellow road) would reach the building. “Snapping” it to the terrain suggests incorrectly that the hill blocks the noise.

2D-projected digital road models with mediocre accuracy have attracted great scientific and commercial attention since the advent of digital cartography and satellite navigation (Taylor et al. [2001]; Fouque and Bonnifait [2008]; Yue et al. [2008]). However, *accurate 3D representations* are still atypical, owing to factors such as the increased cost of generation and maintenance, increased complexity of visualisation and analysis, and a lack of significant use cases (Zhu and Li [2007]; Wang et al. [2014]). As a result, 2D road models are common in terms of both public and private geospatial providers, whereas accurate 3D road models are rare in comparison.

When a use case arises and an accurate 3D model is needed, providers generally have two options: to produce a new model, or to enrich an existing 2D model with elevation data. The decision generally depends on the quality of the available 2D data set relative to the requirements for the 3D model, as well as that of the dataset(s) available as sources of elevation data, among other factors (Zhu and Li [2007, 2008]; Wang et al. [2014]). In the geospatial field data acquisition is far more expensive than re-using existing datasets, especially openly available ones. As a result, many providers first attempt to find a way to convert their datasets into 3D using existing data in such a cost-effective manner.

1.2 The NDW commission

In certain projects the accuracy requirement and restrictions on the modelling procedure may be prescribed legally. Such is the case for the client of the present research, Nationaal Dataportaal Wegverkeer (NDW) (National Road Traffic Data Portal), a division of Rijkswaterstaat (RWS) (Directorate-General for Public Works and Water Management). This Dutch government organisation is in the process of enriching their pre-existing open data 2D road model Nationaal Wegenbestand (NWB) (National Road Database) with 3D data, to attain compliance with the new version of the Dutch noise legislation or *geluidwetgeving*, coming into effect on the 1st of January 2022. The new version of the legislation prescribes, among other things, a horizontal *and vertical* accuracy of 20 centimetres for the road model underlying the noise simulations. Due to cost considerations and reasons related to NDW’s data acquisition pipeline, the pre-existing 2D version of NWB will be converted into a 3D dataset (dubbed 3D-NWB) primarily using open data geospatial datasets. They have produced a prototype implementation themselves, and subsequently contracted the consultant firm Royal HaskoningDHV (RHDHV) to create a commercial implementation based on their experience with the prototype. The development of this tool was concluded

in December 2020, with a preliminary version of 3D-NWB already publicly available on their website in addition to the original 2D version.

Thus for [NDW](#), the next year will be about assessing the quality of their new product and improving it as they see necessary. In particular, they wish to assess how it fares in terms of the requirements set by law. This dissertation research attempts to contribute to this assessment by presenting an original system design and implementation that favours scientific correctness, and in which output accuracy can be qualitatively and quantitatively described. By comparing the results of the academic system design and implementation to the commercial one, it becomes possible to indirectly evaluate the commercial results' general quality and accuracy in an indirect manner. My work also explores various related topics that are not directly intended for this purpose, which I refer to as the solely academic aims of this project.

My research was carried out in consultation with the above parties. In fact, the stages leading up to the submission of my dissertation proposal involved thorough consultation with personnel both at [NDW](#) and [RHDHV](#) while the commercial implementation was still being developed, to ensure that my research fits well with [NDW](#)'s plans and the commercial implementation.

1.3 Field and relevance

For reasons that will later become clear (see Section 2.3), I primarily focused on a Lidar point cloud and a 3D topographical line dataset as elevation sources. In both of these datasets, it is clearly evidenced that roads are occasionally in complex three-dimensional relationships with one another and with their environment. For instance, they cross above and below other roads and are also frequently occluded by other objects such as vegetation and buildings. Already in the planning phase of the project the question had arisen, how such real-world geometries should be dealt with in the conversion process – evidently they will require special treatment relative to well-exposed road surfaces. The answer to this question is closely linked with which field of the geosciences my project is positioned in.

The likely candidates in the context of digital road network modelling are geographical information system ([GIS](#)) and geomatics (also called geoinformatics). It is thus worth discussing briefly how each typically treats 3D objects. One of the reasons why 2D road models are popular is that their geometry and network properties can be analysed using a multitude of well-proven [GIS](#) methods and software kits. However, in [GIS](#) models, even if elevation measurements exist, they are generally only present as an *elevation attribute* (i.e. a semantic data field, like street names), because [GIS](#) geometrical models do not typically support true 3D operations. This is conceptually identical to projecting the geometries onto the horizontal plane. Geometric models that treat the vertical dimension explicitly are more common in geomatics; namely 2.5D and 3D models. While using 2.5D models restricts the types of physical entities that can be modelled, it also greatly simplifies certain types of analysis conceptually and computationally. This makes it ideal for working on similar scales to [GIS](#); i.e. on the national scale for instance, as in this research.

While 2.5D modelling initially appears to be a good candidate for this project, we may observe that it is by definition unsuitable for handling the 3D relationships that roads have with each other and with their environment. However, much like how the concept of divide-and-conquer works in computer science, it is possible to decompose three-dimensional, geometrical problems into smaller sub-problems until they become natively compatible with 2.5D methods which are simpler to solve individually than the 3D problem as a whole. This research is positioned in the field of geomatics because my system design is specifically intended to explore how 2.5D methods can be applied in a way that enables the *piecewise* modelling of a national road network. The divide-and-conquer concept is applied to decompose the road network into segments that can be individually, locally regarded as *terrain* (i.e. a mathematical surface) and hence be modelled in 2.5D.

Geomatics is comprised of a wide range of disciplines, several of which are relevant to the present research. As I focused on 2.5D methods to a great extent, it overlaps with the geomatics field of *digital terrain modelling* in terms of how it generates and stores the digital representations of roads, and as a

consequence, the manner in which it derives elevations from them: using *spatial interpolation*. As the overview of the methods in Section 3.2 reveals, it also strongly overlaps with the geomatics discipline of *feature extraction* (and to a lesser extent, *photogrammetry*), because of the intermediate steps used by the pipeline to derive the 2.5D road surface models from our input datasets.

This is in line with my goal to study how a combination of mainly geomatics-based tools and methods can be used to accomplish the tasks required by NDW, and to also assess their accuracy and suitability when used in this way. However, I also use GIS methods “under the hood” in all parts of the project – for instance, 2D geometry intersection tests, orientation tests and spatial queries are pervasive in the implementation, and are thus often mentioned in the detailed description of the processing steps found in Section 3.3. Furthermore, my research often touches on mathematics and statistics, for instance I use polynomial fitting and maximum likelihood estimation (MLE) throughout the implementation (as examples of the former) and metrics such as standard deviation and root mean squared error (RMSE) (as examples of the latter).

1.4 Research questions

My main research question is “*How can we achieve a 3D conversion of the NWB dataset using Dutch open geospatial data and a primarily 2.5D-based surface modelling methodology, while guaranteeing optimal and quantifiable accuracy and completeness?*”. It was distilled from the main areas of interest that we settled on during the preparatory stages of the project, while planning the project with my academic mentors, NDW, and RHDHV. The question is comprised of two halves, which I initially intended to devote equal amounts of attention to – the question of devising a system design and implementing it, and that of assessing its effectiveness and the accuracy and completeness of the output it generates (as well as comparing it with the commercial results).

I eventually settled on focusing more time and effort on the system design and integration (i.e. *performing* the elevation-enrichment of NWB), both because it required more time than initially anticipated, and because the quality and accuracy assessment of the results (and their comparison with the commercial results) was more straightforward than expected. Furthermore, I found that many of the accuracy-related questions depend strongly on the exact specifications of the system design and its implementation, meaning that not all the work necessary to answer those questions was clearly separated into a dedicated accuracy assessment process – much of it needed to be considered and evaluated during development.

The two halves of the main research question were created by collecting my sub-questions into two categories; pipeline design and implementation, and accuracy assessment. Below I present some of these sub-questions, to characterise in somewhat more detail what specifically I focused on in this research project.

1. Sub-questions related to *performing* the elevation-enrichment of NWB using Dutch open geospatial data and predominantly 2.5D geomatics methods
 - a) What are the exact methods of the commercial implementation and what do we suspect its theoretical shortcomings to be?
 - b) Does the literature suggest any methods that are suitable to this research? If so, can we make use of them in our own methods?
 - c) How can we best make use of the combined information content of the datasets used by the commercial implementation?
 - d) How should the road network be subdivided into parts that each represent a 2.5D problem? Could they be processed individually to facilitate easy parallel processing?
 - e) As we are using Lidar data, can we produce an accurate and complete triangular irregular network (TIN) surface model for each 2.5D “unit”? Can we interpolate elevations for NWB through these models?

- f) How do we “stitch” the results of the individual 2.5D procedures back together into a 3D road network with correct topology?
 - g) Can the implementation be made robust enough to handle all (or *most*) challenging road layouts correctly, such as complex motorway junctions?
 - h) How can we make the implementation perform well in areas where elevation data is scarce or missing over longer distances, such as in tunnels?
 - i) Can the computational complexity of the program be kept low enough to be suitable for processing all the relevant roads?
 - j) While solving NDW’s specific problem, can we ensure that our solution generalises well to other, similar problems?
2. Sub-questions related to the *assessment* of overall quality, completeness and accuracy of the output and its similarity to the commercial results
- a) In related work, what methods were typically used to measure empirical and theoretical output accuracy?
 - b) According to related work, what typically defines output accuracy? Do local factors also play a role, or is it reasonable to estimate it for the procedure globally?
 - c) What is the accuracy of our elevation data sources? Can we structure the pipeline in a way that their input accuracy can be propagated to the output in a straightforward manner?
 - d) To facilitate the above, can we derive our output directly from input data points, despite the large number of processing steps that are potentially necessary?
 - e) What is the effect of uncertainty in the *horizontal* position of NWB centrelines on the effectiveness of our methods, and on the output accuracy?
 - f) The road surface model TINs are also important products of the pipeline. How can we assess the overall quality and completeness of these?
 - g) Can we indicate in the output, which input elevation source each output elevation estimate was derived from, and to use this to derive the output accuracy from the appropriate input dataset’s accuracy?
 - h) How are temporal inconsistencies between the datasets manifested in the output? Can these be detected by the processing steps?
 - i) What physical features or sensing issues do drops in accuracy correspond to? If this corresponds to problems with the input, what aspects of the input datasets should be improved?
 - j) How good is the agreement between the commercial and the academic results? What could be the reason for global/local differences between them?

2 Related work

When I started the literature review, I already had a good starting point about what exactly to look for. This is because I had already known that my focus would be restricted to three specific Dutch open data datasets, and because I had already settled on a range of specifics regarding the goals and requirements of the project. The three datasets were picked early on in the planning process for reasons related to our wish to mainly use the same datasets as the commercial solution does.

As it is the most up-to-date detailed elevation source overall, my primary candidate became the national airborne laser scanning (ALS) point cloud of The Netherlands. The name of the latest release of this product is Actueel Hoogtebestand Nederland 3 (AHN3). As a result of this choice, there are two main areas that I focused on as part of my literature review: road feature reconstruction from Lidar point clouds, and the theoretical and empirical propagation of Lidar accuracy into derived models. The literature review concerning these two areas is presented below in two parts.

The other two datasets I used are NWB itself, and a 3D line dataset called Digitaal Topografisch Bestand (DTB) which has coverage in many areas where AHN3 does not. Detailed information about the choices regarding the datasets, as well as an analysis about their detailed properties, can be found in Section 2.3.

2.1 Road identification in point clouds

My main domain of interest was feature extraction from Lidar data, because tasks of this type characterised the bulk of the planned processing pipeline. Our intention was to not only query a digital terrain model (DTM) for elevations around the NWB road centrelines – an example of a simple way in which one could perform a *rudimentary* 3D conversion – but to create spatial models of road edges and surfaces, and only then proceed to extracting elevations for the centrelines. This requires one to identify, or at least approximate the geometries of these features by choosing the point cloud points that best describe them, and to apply various operations to them.

We may thus regard point cloud feature extraction as the top-level geomatics topic concerned by this research, with most other operations, such as 2.5D surface modelling and mathematical tools, to reside a level lower in the hierarchy. I use feature extraction for the purposes of identifying and modelling discrete physical features found in the point cloud (and the support dataset DTB, which will be discussed later in this chapter).

2.1.1 Research using point clouds only

Approaches based on photogrammetry

In terms of point cloud feature extraction techniques relevant to roads specifically, I studied a range of papers detailing a wide spectrum of methods. One strategy, most prominently represented by Hu [2003]; Hu et al. [2004]; Zhu and Mordohai [2009]; Zhu and Hyyppä [2014]; Lin et al. [2015], is based on the idea of transitioning to a photogrammetric analysis at some point in the process, generally quite early on. First, a set of pre-processing techniques to better characterise potential road points in the source Lidar data are applied, generally by performing some form of filtering (e.g. setting intensity thresholds applicable to Lidar returns from bitumen), or by extracting ground planes using various techniques and

2 Related work

selecting points that lie close to them. Then, images are rendered from the point cloud from various angles, often using colour-coding based on point properties, and photogrammetric methods are applied to identify roads. Sometimes, high-definition aerial or satellite imagery is incorporated in the photogrammetric workflows. The success rates of such strategies are mediocre, and they rely strongly on manual parametrisation. In particular, they are unsuitable for large study areas with inhomogeneous types and distributions of roads, as also found by the excellent literature review of this type of relevant work in Yang et al. [2013].

Approaches based on curb detection

A further popular set of strategies rely on road curb detection. Vosselman and Liang [2009], Zhang [2010], and Yang et al. [2013] are examples of such research. Vosselman and Liang [2009] presents a method in which a *DTM* is generated, points close to its surface are selected from the point cloud, and small, curb-like jumps in elevation are algorithmically detected using thresholds. The curb points are selected, and a feature extraction method (random sample consensus (*RANSAC*) in this case) is used to construct 3D lines from them. Gaps in the lines are closed procedurally, and splines are fitted to optimise the shapes of the road edges. In Zhang [2010], road cross-sections are constructed and inspected as 2D profiles, and points are classified based on whether they are likely to represent road surfaces, curbs, or off-road surfaces. To do this, they process mobile laser scanning (*MLS*) data on-the-fly (during acquisition) via a supervised classifier, and use the Hough-transform to model road surfaces. The curbs are found where the points first deviate from the model.

In Yang et al. [2013] a similar approach is presented in which cross-sections are identified by looking at *MLS* scan properties (time of acquisition, specifically), and then non-road points are filtered out in 2D profiles based on the absolute elevation of the road (known from the constant elevation of the sensor above it) and curbs of a specific type are identified in the series of ground points – all via a single moving-window operation that uses applicable thresholds.

While the results of the curb detection-based methods are more flexible, more accurate and more complete in general than the photogrammetric methods, they are not well suited for my project out-of-the box. These approaches work best with *MLS* data, where the data is either natively produced in the form of road cross-sections (the scan lines of a car-mounted front facing sensor), or can be easily extracted from the point cloud in such a form. Furthermore, in *MLS* sensing the road elevation is generally known, by considering the sensor's constant position relative to the vehicle's *GNSS* sensor – this is not the case in *ALS*, because unlike cars, aircrafts do not traverse land-based road networks. Lastly, while the above method may work well in places where curbs are well-defined, this is not a reasonable assumption to make for an *ALS* dataset with national coverage, such as our particular input.

The work Vosselman and Liang [2009] is not entirely bound by the above limitations. It demonstrates that a relatively simple approach can be used to detect curbs without the need for the point cloud to be comprised natively of cross-sections, and for accurate road elevations to already exist. However, the fact that it also uses curb detection with fixed thresholds undermines my confidence in it. Working with a national dataset and focusing on large roads (including motorways, one of our main targets for 3D conversion) means that the assumption that well-defined, uniform road curbs will exist and be reliably detectable everywhere is not a sensible assumption.

Other, purely Lidar-based approaches

There are many other papers that deal with this task without relying on external vector data. For instance, Clode et al. [2004] and Clode et al. [2007] present a set of methods in which first a *DTM* is generated, then points close to the *DTM* are selected and are further filtered based on intensity and sampling density thresholds applicable to reflections from flat bitumen surfaces. The results are converted to a raster mask which is then refined via morphological operations. It is then used to produce the output: a point cloud in which road points are marked semantically (i.e. they are classified as such). In the 2007 paper, they extended the procedure by using a phase coded disk (*PCD*), which can create a 2D map of

the predicted road parameters wherever it moves through road points. Like the morphological operations above, the PCD-convolution is in fact a photogrammetric method, because it also acts on a raster generated from the classified point cloud prior to its application. Nevertheless, the method is still more relevant to us than the rest of the photogrammetry-based research mentioned here. An example visualisation of its output is shown in Figure 2.1 – it is effectively a road centreline detector. They describe it as an alternative to using the Hough-transform for finding road centrelines, which, according to their research, is not reliable enough in this context. This spatial map can then be used to generate a vector dataset describing the geometry of the roads.

The research Gross and Thoennessen [2006] shows that point neighbourhood information can be used to generate covariance matrices of individual points, which can in turn be used directly to indicate whether the point belongs to a linear feature. They also describe how lines can be assembled from the selected points efficiently. Although their methods have very well documented mathematical foundations which could be reproduced in any programming language, their applicability in my research, especially in the context of small or even non-existent curbs, is uncertain.

Other methods relying purely on the Lidar points themselves exist, but like Zhang [2010], they are typically intended for real-time MLS applications – such as the fully convolutional neural network-based solution in Caltagirone et al. [2017]. The literature review in Yang et al. [2013] offers an excellent overview of such additional methods, but they will not be described here any further, as I found them not to be relevant to this project.

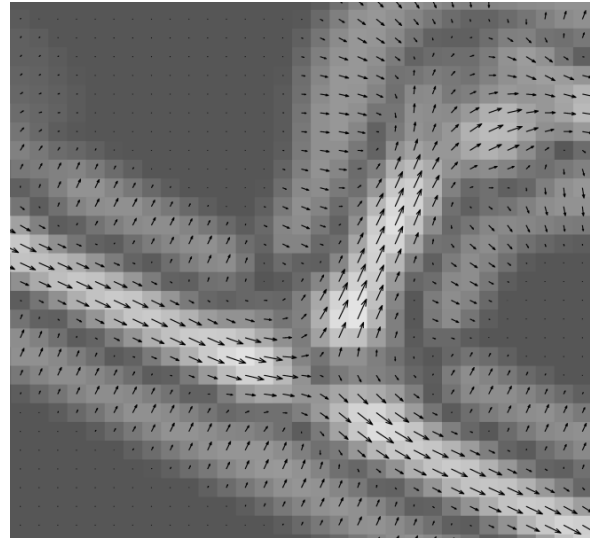


Figure 2.1: Illustration of PCD convolution from Clode et al. [2007]. The vector magnitudes quantify the support existing there for a road centreline.

2.1.2 Research using input point clouds and approximate road locations

This section contains brief descriptions of research that used similar input data to mine *in addition to* Lidar data; mainly vector datasets estimating 2D road centreline positions. These relevant papers describe work that used analogous input data to achieve similar goals to mine – as a result, they contain the methods that are the most relevant to my own research.

Relatively simple approaches

The work Hatger and Brenner [2003] presents two approaches based on region-growing. The first one is based on growing planes in the entire study area from Lidar points and correlating these with the road centrelines. Finding this to be too complex computationally, they propose another approach of treating Lidar scan lines individually, partitioning each into parametrised line segments via linear regression and then inspecting the succession of scan lines and identifying neighbouring segments that are roughly parallel. The resulting groups of roughly parallel 3D lines are then treated as cross-sections of planar regions, and an additional region growing step is performed to find any points that might have been left out in the previous steps. The results of this can then either be prepared as a full, 3D planar partition of the study area onto which road centrelines can simply be projected, or they can be further refined first by eliminating small, meaningless planes via a RANSAC-based workflow.

The work Cai and Rasdorf [2008] shows that enriching road centrelines with elevations can be achieved using even more simplistic methods. Their first method is based on finding points on opposite sides of roads (in 2D) at even distances from them, and in suitable locations to form approximate cross-sections.

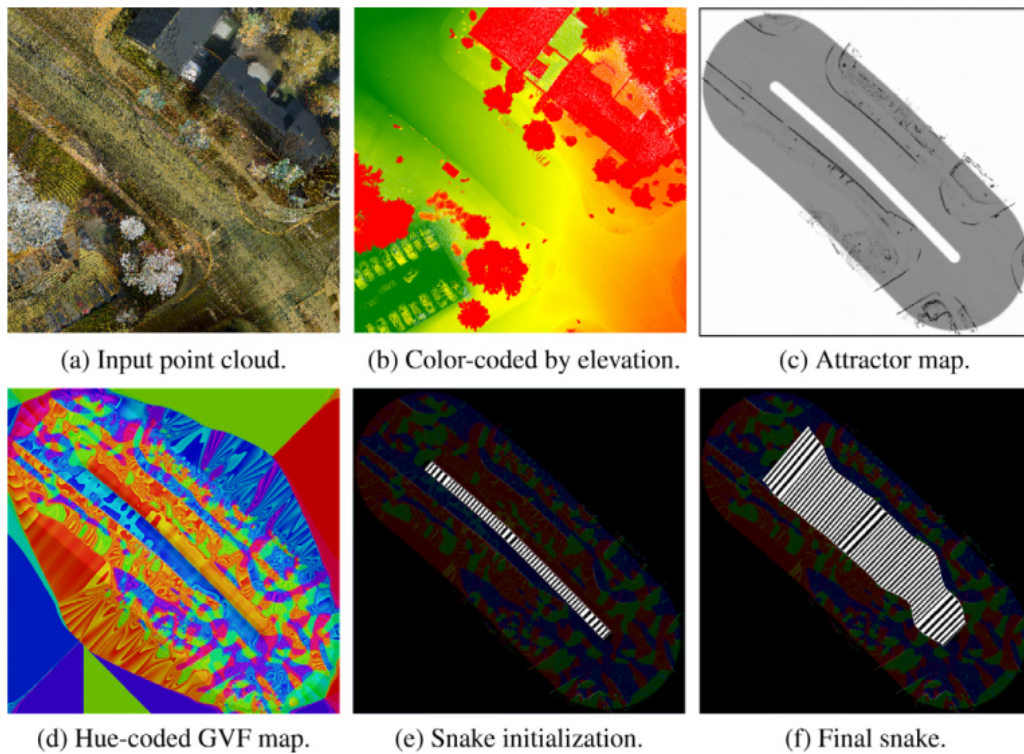


Figure 2.2: Illustration of the contour optimisation procedure used in [Boyko and Funkhouser \[2011\]](#). In the attractor map, darker colours represent stronger attraction, resulting in the active contour converging to them in the optimisation procedure. The GVF map is a vector map that contributes to favourable active contour convergence.

The centrelines are intersected with the cross-sections and are given elevations at the points of intersection. The elevations are computed by interpolating linearly inside the cross-sections, using the elevations of the two points that define each of them. Their second method is even simpler; for each road vertex (or some sampling along its length), they locate the closest Lidar point and associate its elevation with it. The simplicity of these methods is reminiscent of the [NDW](#) prototype and the commercial solution developed for [NDW](#) by [RHDHV](#) (described in Section 2.4), and highlights that a rough approximation of the road elevations can, in practice, be derived either directly from the point cloud or from a derived [DTM](#) in a straightforward manner. However, far more sophisticated methods were developed by most authors.

Complex approaches based on active contour optimisation

One landmark paper, [Boyko and Funkhouser \[2011\]](#), describes a method in which a set of 2D input geometries are used to identify and label road points in an [ALS](#) point cloud. Road centrelines are first derived from the input geometries. Then, the centrelines are associated with elevations by fitting spline curves through Lidar points close to them in 2D. Suitable Lidar points are selected by minimising an error function that includes terms related to the distance from the location of interpolation, and to elevation variance. The resulting network is guaranteed to be continuous and smooth because the densified input polylines are used as spline control points. Since the entire system of splines is connected, this is also guaranteed to minimise the effects of local issues, such as occlusion.

The point cloud is then partitioned on disk, based on fitting support planes along the 3D-converted lines and fetching points that are close to them. This solves the performance-related issues related to working with too many Lidar points at once, and minimises the effects of 2.5D violations related to overlapping features. They then construct scalar maps for each resulting segment that penalises points away from road edges (both inwards and outwards). These maps, called attractor maps, are composited from

rasters penalising locations that are outside the range in which edges are expected to be found (relative to the centrelines), and rasters produced by a curb detection metric related to the normal vectors of the point cloud points. Lastly, they apply an active contour optimisation technique (specifically, ribbon snakes) that yields the road edges in 3D, and then labels points between the two edges as road points. An illustration is shown in Figure 2.2, taken from their paper. The initial contours are based on the road centrelines.

The results of Göpfert et al. [2011] demonstrate that active contour optimisation can be used to estimate road outlines without the need for the involved pre-processing steps of Boyko and Funkhouser [2011]. They convert the input point cloud directly into a DTM, and then into attractor maps. They use the same type of active contour optimisation, and generate output centrelines and road edges with comparable quality to that of the outputs of Boyko and Funkhouser [2011]. It is worth mentioning that the type of active contour optimisation used by these two papers also optimises the road centrelines in conjunction with the road edges, which is particularly important in places where the 2D georeferencing of the original centrelines is poor.

Relevant work with Dutch data

The work Oude Elberink and Vosselman [2006] is relevant not only because of the methods it applies, but also the specific datasets. They enrich the best-known Dutch open data national topographical vector dataset (the present-day equivalent of which is Basisregistratie Grootschalige Topografie (BGT)) with elevations, and as their source of elevations, they use first-edition Actueel Hoogtebestand Nederland (AHN) data (the third edition of which I used in my own research).

They do not exclusively consider roads; all polygonal vector objects are extruded to 3D. Like in Hatger and Brenner [2003], a region growing approach is proposed as the foundation of the elevation extraction workflow. They use the Hough-transform to find seed points whose neighbourhood suggests a planar structure, fit planes and then grow them by checking the point-to-plane distances of new points, labelling them with the identifier of the planes they belong to. The vector data is then overlain on these regions and for each polygon, the plane is selected which is represented by the greatest number of labelled points in its interior. These points are re-fitted with a plane, and each such plane is used to extrude the corresponding vector geometry simply by projecting the polygon onto its surface. To improve the results of this simple extrusion, they suggest the application of algorithmic topological corrections. Furthermore, to model the interior of the extruded polygons in more detail, they recommend the construction of a constrained Delaunay triangulation (CDT) for each, first by inserting its edges as constraints, and then by inserting the Lidar points that its surface is based on. The CDT can be refined procedurally to ensure smoothness. The main limitations of their methods are that the extracted elevations (from the region growing approach) are not always accurate, and that they cannot handle overlapping objects, such as roads in motorway junctions. 3D visualisations of the results of this approach and typical artefacts are shown in 2.3. The specific artefacts shown in the figure demonstrate that in multi-level road layouts, only the topmost road is fully converted to 3D.

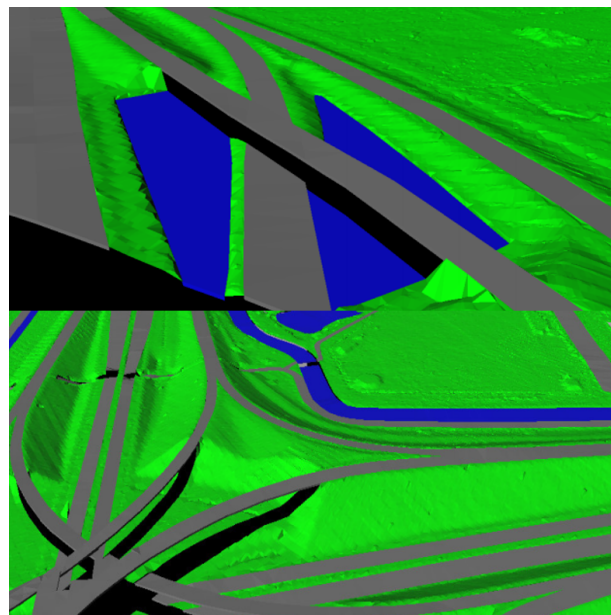


Figure 2.3: Examples of 3D-converted multi-level road geometry from Oude Elberink and Vosselman [2006]. The grey colour marks roads, green marks the terrain, and blue corresponds to water surfaces.

2 Related work

Their method was later extended in [Oude Elberink and Vosselman \[2009\]](#) to work well in complex multi-level road settings by using point cloud segmentation in a manner similar to what I already described in the context of [Boyko and Funkhouser \[2011\]](#). We may regard these procedures as ways to decompose the 3D problems into 2.5D sub-problems, which is highly relevant to my research. In his doctoral thesis [Oude Elberink \[2010\]](#) he combined this method with the overall procedure in [Oude Elberink and Vosselman \[2006\]](#) to form one integral whole. Furthermore he extended it with a road extraction quality and accuracy assessment procedure, which was later perfected and also published separately in [Oude Elberink and Vosselman \[2012\]](#).

Their quality and accuracy assessment methodology is comprised of two separate procedures and the comparison of their results: a theoretical (error propagation-based) evaluation, and an empirical one against reference data. Their error propagation-based evaluation takes into account metrics such as [GNSS](#) and inertial navigation system ([INS](#)) noise in the Lidar survey (suggesting that they had access to low-level information about the dataset), plane fit quality and observed Lidar noise. It also considers interpolation and extrapolation uncertainty, relevant in places where not enough relevant Lidar points could be located and thus gap-filling measures were used. They found that theoretical errors were generally below 20 cm, with noticeable increases only occurring where Lidar coverage was extremely sparse or non-existent, leading to the necessity of using interpolation or extrapolation.

Interestingly, their reference data was [DTB](#) for the empirical evaluation of accuracy, which I also use in my research (see [Section 2.3.3](#)). In general, their comparison with [DTB](#) showed good agreement with the road surface extraction results, except for the same places where the theoretical approach also suggested large errors, and in particular in places where this was also combined with intense vertical road curvature locally, which [DTB](#) managed to capture, but not their results. In places with good Lidar coverage, the agreement was much better, often near-perfect. Although not explicitly mentioned, it appears that they still used the earliest version of [AHN](#) (not Actueel Hoogtebestand Nederland 2 ([AHN2](#))) in this research, which may explain how it is possible that they encountered low point densities even in well-exposed road segments. [AHN2](#) and [AHN3](#) no longer have this problem, as mentioned in [2.3.2](#) and in many other subsequent parts of this report.

On using a support dataset in addition to Lidar data

In [Section 2.3](#) in this chapter, I discuss that this research is also concerned with a second source of elevations, which I often refer to as the "support dataset" in this report because [AHN3](#) is given priority to in the analysis, wherever it exists. It is a 3D line dataset, not an [ALS](#) or [MLS](#) point cloud. The one area *not* explicitly covered in any of the papers I examined is the use of such external 3D vector data as a further constraint when extracting road elevations and/or geometries from point clouds.

In relevant work, occlusion is generally accepted to represent gaps in coverage, and elevations are simply interpolated or extrapolated inside them if possible – or if not, they are not considered any further. In my research, [NDW](#) is interested in producing a 3D conversion of [NWB](#) with the highest possible *completeness*. Exploring how information from the two datasets can be combined is also interesting academically, thus my work examines how [DTB](#) can be used to patch in gaps in [AHN3](#) coverage.

2.2 Lidar survey and DTM accuracy

Relevant aspects of Lidar-related accuracy assessment can be divided into two main sub-topics: interpreting the reported global and/or local accuracy and areal sampling density of the Lidar surveys themselves, and assessing the accuracy of the terrain models ([DTMs](#)) derived from them. Although some of the relevant work I studied overlaps with both of these areas, I separated the discussion below into two sections based on them. As Lidar sensing accuracy and sampling density underlies that of the derived models, I discuss it first below.

2.2.1 Accuracy description of Lidar sensing

Global and local influences on accuracy

The notable paper [Hodgson and Bresnahan \[2004\]](#) describes the most fundamental sensing errors of Lidar measurements to be introduced by GNSS errors, INS errors, inertial measurement unit (IMU) errors, errors introduced by the waveform analysis algorithm and lastly, a general error factor that depends on the flying height. Combined, these are the primary factors that contribute to the *measurement* accuracy of the sensing system.

It is shown by various papers including [Hodgson and Bresnahan \[2004\]](#); [Su and Bork \[2006\]](#); [Kraus et al. \[2006\]](#); [Raber et al. \[2007\]](#); [Peng and Shih \[2006\]](#); [Chow and Hodgson \[2009\]](#); [Aguilar et al. \[2005, 2010\]](#); [Guo et al. \[2010\]](#) that there are local factors influencing *vertical* Lidar accuracy that are independent of the sensing equipment, and thus vary from place to place. In production datasets, whether they are considered at all or not, they are almost never *reported* locally, i.e. on the level of individual measurements. This is mainly because they are difficult to estimate without a complex analysis of the measured data and potentially, that of external data. Unless the global errors reported in the survey's specifications were derived empirically (e.g. by using ground control points), the effects of local factors may not be reflected in them at all, and they can be considered purely theoretical sensing-related values.

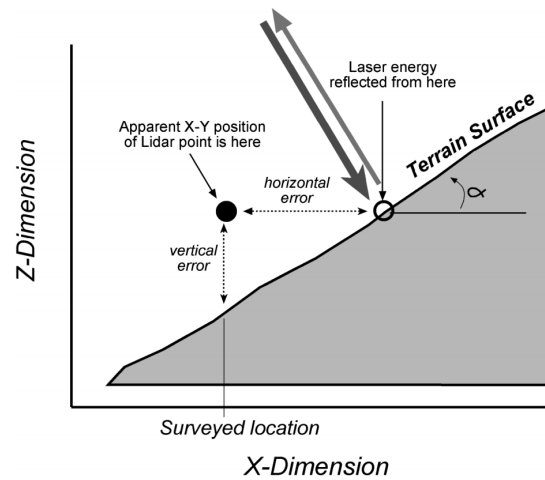


Figure 2.4: Illustration of the effects of terrain slope on vertical accuracy ([Hodgson and Bresnahan \[2004\]](#)).

What influences measurement accuracy locally?

Local accuracy depends on the inclination of the surveyed terrain at the point where the Lidar reflection occurred, as shown in [Figure 2.4](#). Any uncertainty in the lateral position of the point of reflection will be scaled by the tangent of the slope angle, denoted by α . The vertical error thus increases linearly as a function of increasing slope (commonly derived from a 2D slope map). Therefore, if the accuracy of a Lidar survey was derived empirically, this relationship will indicate higher errors than the sensing equipment's specifications would suggest in survey areas with considerable relief.

Elevation accuracy also depends on the vegetation encountered. In all cases, the presence of vegetation decreases it, with the significance of the error depending strongly on the type of vegetation. Mature trees and evergreens tend to influence accuracy to a lesser extent, whereas bushes, shrubs and undergrowth in general tend to have a decidedly larger impact. [Peng and Shih \[2006\]](#) quantified this as a function of *vegetation angle*, a qualitative metric that describes how "open" certain types of vegetation are to Lidar. They found that there is a linear correlation between elevation errors and vegetation angle, as well as canopy volume. The one exception I found is [Raber et al. \[2007\]](#) which reported specifically that in very strongly vegetated areas, no correlation could be found between vegetation classes and accuracy (or even sampling density and accuracy). Still, the majority of relevant research indicates that Lidar accuracy reflects the extent and type of vegetation coverage in addition to its dependence on the relief of the surveyed terrain.

The quantification of measurement accuracy and research tackling these topics often uses empirical methods. They generally consist of surveying ground control points accurately and either directly comparing these with nearby Lidar points, or first constructing a spatially continuous DTM and comparing the DTM-interpolated elevations with the surveyed reference elevations, with the latter approach being more relevant to the next section. The global value is usually specified as the measurement error (in

2 Related work

metres or centimetres) at one or two standard deviations, with separate values given for horizontal and vertical errors. The two errors differ in terms of the equipment influencing them, and also because the local factors I outlined above affect elevation accuracy only (as a *function of* horizontal accuracy in the case of local terrain slope). They are generally reported as one or two standard deviations, corresponding to 68% or 95% confidence, in metres or centimetres.

Sampling density as a survey property

Sampling density describes how many reflections are recorded per unit area. This is the third descriptor that is commonly found in the documentation of Lidar datasets, and like vertical and horizontal accuracy, it is generally represented by a single global value. This, too, fluctuates locally, and in this case anything between zero and the maximum nominal value of the survey is possible. The maximum possible value depends on the sensing equipment and the number of times any given area is scanned (the number of passes). Sampling density does not directly affect the accuracy of individual Lidar measurements, which is one of the reasons why it is reported separately – its effects are more relevant to the next section.

Sampling density is mostly reported as the mean number of points per square metres found in the dataset, occasionally as a range. It can be derived from the data directly, i.e. it needs no additional processing or surveying. Relevant studies report that sampling density varies mostly as a factor of terrain relief, vegetation cover, and vegetation angle, with increases in any of these factors resulting in decreases in local point density. For instance, sampling density falls off logarithmically with increasing terrain slope (Peng and Shih [2006], Chow and Hodgson [2009]).

2.2.2 Describing the accuracy of Lidar-derived DTMs

Spatial interpolation in the context of DTMs

In practice, the quality and accuracy of Lidar-derived DTMs is most commonly evaluated via sampling their surfaces to serve as the basis for comparisons. Sampling a DTM takes place via spatial interpolation. The DTM's relationship with the raw data can be established by interpolating at the horizontal locations of Lidar points, while that with the real-world terrain can be examined via surveying control points and interpolating at their 2D positions in the DTM. Intuitively, DTMs provide a link between ground control points and Lidar measurements, which in turn also provides a convenient interface for evaluating Lidar survey accuracy empirically (as I mentioned in the previous section), provided that the interpolator's effects on accuracy are known.

Raster DTMs are themselves produced via spatial interpolation. One may convert a Lidar point cloud into a TIN-based DTM without it (the TIN vertices will be Lidar points), but to create a raster DTM, one will need to use a suitable interpolator, such as inverse distance weighting (IDW). Alternatively, a TIN-based DTM can be constructed as an intermediate model and the raster can be derived from it via applying a TIN-based spatial interpolator, such as the Laplace interpolator. These observations entail that a comparison between the Lidar points and their TIN-interpolated counterparts would yield no residuals, i.e. TIN models do not lose information relative to the ground reflections found in the Lidar data.

Evaluating interpolation accuracy

Spatial interpolators do not leave accuracy unchanged, which cannot be neglected when performing the above benchmarks. For us in this research, the effect interpolators have on accuracy is particularly interesting because the final NWB elevations are produced via spatial interpolation in a Lidar-derived DTM in my pipeline. There exist various approaches to establishing the nature of the relationship between input and output accuracy, such as deriving exact error propagation formulae from the mathematical descriptions of interpolators, as well as the more popular empirical approaches based on *benchmarking*

accuracy post-interpolation via split-sample, cross-validation or jack-knife methods. Theoretically, input accuracy (survey accuracy) and any necessary metrics of local influences can then simply be plugged into the formula to obtain the local accuracy post-interpolation.

Propagating local factors through interpolation

We know from the previous section that the survey accuracy is *itself* influenced by local factors. Since only global accuracy values generally exist for Lidar surveys, the theoretical or empirical error propagation formula may need to be extended with additional terms approximating the influence of these additional factors, depending on how accurately one wishes to approximate output accuracy. The exact nature of this part of the relationship depends on the fundamental principles I outlined in the previous section, and it too, can be modelled both theoretically and empirically. Theoretical approaches are more common for simple relationships (such as that with local slope, as shown in Figure 2.4), while empirical ones are almost always employed in more complex ones (such as the relationship with vegetation). In the context of digital terrain modelling, there is an additional factor we need to consider: ground filtering accuracy. While we wish to model the terrain surface only, the raw Lidar data includes non-terrain reflections that need to be removed before constructing the DTM. This accuracy is also generally estimated, rather than derived theoretically. It is also possible to try to derive the combined effects of all these factors at once, e.g. via Monte Carlo simulations.

For instance, the research [Aguilar et al. \[2010\]](#) applies a hybrid empirical-theoretical method, in part propagating errors mathematically through the IDW interpolator to obtain part of the relationship, and for the other part relying on Monte Carlo simulations. They model accuracy to be a factor of the error-propagated value computed from global Lidar accuracy, as well as sampling density, terrain slope and ground filtering accuracy. The research [Kraus et al. \[2006\]](#) also applies mostly theoretical methods to analyse errors propagating through the moving MLE. Post-application statistical evaluation was performed by for instance in [Peng and Shih \[2006\]](#) (jack-knife, using surveyed reference points), and [Guo et al. \[2010\]](#) (ten-fold cross-validation). Notably, [Smith et al. \[2005\]](#) used all three approaches (split-sample, cross-validation, and jack-knife) for a wide range of interpolators in an urban setting.

Like [Aguilar et al. \[2010\]](#), many of the other papers also examined the influence of gridded DTM resolution on accuracy, i.e. the effects of Lidar sampling density in conjunction with the raster cell size. [Chow and Hodgson \[2009\]](#) examined via regression techniques (on IDW interpolation) how it is correlated with point density and found that the effect of increasing the cell size has a more severe negative effect on accuracy than that of gradually decreasing sampling density, and that a certain degree of correlation between them is observable. [Guo et al. \[2010\]](#) argues that for most interpolators, the overall trend is mainly linear between accuracy and grid resolution, up to the scale of the Lidar point density, from where no further increase is observable. They also found that differences in accuracy between interpolators were most prominent at the finest resolutions they examined. [Bater and Coops \[2009\]](#) found that the local influence on accuracy of slope and point density are mostly invariant relative to DTM resolution, i.e. no correlation is observable. In the case of TINs constructed from Lidar points directly, cell size and point density are in a more direct relationship, i.e. only by ignoring Lidar points can one increase the cell (triangle) sizes.

Which interpolator is the best in terms of accuracy?

In terms of the accuracy and quality ranking of interpolators, there is a clear consensus that no such ranking exists that is independent of the size and type of the study area, and the purpose of the interpolation. For instance, the accuracy of piecewise spline-based, quintic-type, kriging and ANUDEM methods were found to be lacking in the context of their insensitivity to small, sudden changes (such as natural faults in the terrain and anthropogenic modifications thereof) while they were proven to work well for large-scale terrain, as described by [Bater and Coops \[2009\]](#) and [Guo et al. \[2010\]](#) for instance. All reviewed papers agreed that the accuracy of all interpolators decreases the most in areas of *high topographical relief* (also called surface ruggedness and surface heterogeneity) and *reduced point density*,

2 Related work

with spline-based, *IDW* methods generally producing the worst results in such areas – especially for large-scale terrain.

The relative importance of interpolation-introduced errors is reportedly *low* relative to instrument-related errors and surface-related local sources of error, according to research such as [Hodgson and Bresnahan \[2004\]](#) and [Aguilar et al. \[2010\]](#). The former, which used TIN-linear interpolation, goes as far as to state that the decrease in accuracy after the application of an interpolator is insignificant, or that interpolation may even increase the overall accuracy. This is supported by the error propagation formulae derived by [Fan et al. \[2014\]](#) for the same interpolator, which shows that in areas with negligible relief, the input error may decrease by as much as 50%. TIN-based interpolation methods were recommended specifically by [Bater and Coops \[2009\]](#) for complex geometries and found it in their research to be the most conservative in terms of RMSE-analysis. Furthermore, [Peng and Shih \[2006\]](#) also used TIN-based interpolation in their research, in which they found local influences on elevation accuracy highly predictable. Unlike most papers, [Aguilar et al. \[2010\]](#) considers the accuracy of ground filtering explicitly, and states that its success is a precondition of accurate terrain interpolation wherever the terrain is occluded or shaded partially.

Oversampling the terrain

The point is made in several of these papers that because of the commonly seen logarithmic correlation between point spacing and accuracy, increasing the target point density of a survey is only justified up to a certain point. This depends strongly on the study area because point density itself is correlated with the vegetation cover and the terrain relief. It is argued by several authors, most prominently by [Guo et al. \[2010\]](#), that in vegetation-free areas of low relief, most *ALS* surveys oversample the terrain by as much as 30 to 50 percent, leading to increased processing times, reduced algorithmic stability, and no improvement in accuracy. [Bater and Coops \[2009\]](#) comes to the same conclusion, and the logarithmic trend generally observed between point density and elevation accuracy further supports this. Conversely, in rugged, vegetation-covered terrain additional cross-flight surveys can increase accuracy significantly by improving ground point density, as [Peng and Shih \[2006\]](#) noted. It appears that 1 point per m² is the approximate bare minimum, below which sampling density starts to become a significant influence on output accuracy.

The matter of oversampling the terrain is particularly important when using TIN models, because they use the Lidar points directly and may become too complex to process and visualise when they are too detailed. Considering the above correlations between point density and most other influences on accuracy, we may then assert that for flat, well-exposed surfaces the sampling density does not need to be high. This is particularly important in the context of this research, because roads represent such surfaces in most places.

2.3 Input assessment

In terms of comparing our results with the commercial ones, we were particularly interested in revealing how the effectiveness of the two sets of methods differ. To make it straightforward to isolate differences related strictly to how well the methods perform, we decided to use the same set of datasets as input as *RHDHV*. This means that in addition to using *NWB*, we made use of the same two elevation sources as they did.

In addition to helping with isolating purely processing-related differences between the results, these datasets have the additional benefit of being open data. This fits well with the mentality represented by those concerned with this research, as well as the faculty in general. For the same reason, the implementation created as part of this project is also made available in the same manner, i.e. it is open-source. Alternatives, such as Kadaster's orthoimagery-based point cloud were considered, but eventually excluded from further consideration due to not being open data, and offering inferior overall accuracy compared with *AHN3* and *DTB*.



Figure 2.5: An example render of *NWB*, colour-coded to indicate the owner. Yellow is used for type *Rijksweg* (motorway) (*R-road*), red denotes type *Provincieweg* (provincial road) (*P-road*) and magenta means *Gemeenteweg* (municipal road) (*G-road*). Type “*Rijkswaterstaat-managed road (W-road)*” is not shown in this figure. Blue roads are roads which do not fall into the above 4 categories (in this case they are managed by the TU Delft). Challenging 3D relationships are highlighted by circles.

- *NWB* - National Road Database
- *AHN3* - Current Dutch Elevation
- *DTB* - Digital Topographic Database

In the sections below, I present the results of assessing the general properties and quality of each of the three datasets listed above. As this project does not specifically concern the formal quantification of the accuracy of these datasets, it relies on the global, nominal values provided in the specifications of the datasets. Regardless of this, I still present qualitative results on this topic based examining the degree of agreement between them and attempting to explain the differences both below and in Chapter 4.

2.3.1 Nationaal Wegenbestand – *NWB*

NWB (or more specifically, *NWB-Wegen*, the *NWB* roads product) is a vector dataset comprised of a semantically enriched set of 2D *LineString* objects released in the *ESRI Shapefile* format. The *LineStrings* – dubbed *wegvakken* in the documentation – are interconnected in such a way that *NWB* can be regarded topologically as a graph representation of the Dutch road network. Although *NWB* contains all named and numbered roads in The Netherlands, we are only interested in roads that are semantically marked as state-owned or province-owned (*R-roads* and *P-roads* respectively), because the new noise regulation only concerns these types. The *NWB* product is managed by *NDW*, but it is owned by *RWS* (*NDW* being a division of *RWS*).

NWB and the road types it contains are illustrated in Figure 2.5. This render also contains examples of challenging 3D relationships. Where the provincial road *Kruithuisweg* crosses the municipal road *Schoemakerstraat* and the motorway *A13*, no intersection occurs in 2D because the roads cross over one another in 3D. These locations are indicated in the figure by red circles. Furthermore, where the bike path labelled “*Ijsmeestertunnel*” (a municipal road in *NWB*) crosses the *A13*, a series of 3 short tunnels are located in reality. This is indicated in the figure by a blue oval. Although not all these road types are relevant to this project, the 3D relationships represented by these examples still are.

2 Related work

In addition to representing the topology of the road network, the [NWB](#) lines are georeferenced with mediocre accuracy to also represent its approximate spatial layout. The quality description includes only a single figure, which is 5 m accuracy at 95% confidence, i.e. two standard deviations from the mean. It is not described in any detail, how the accuracy is evaluated for each road, for instance whether it is based on the accuracy of the vertex locations of the road, an arbitrary sampling along their length, and how exactly these are aggregated into the error figure. Furthermore, we do not know whether the reference for the accuracy assessment was empirical (surveyed control points) or whether it is purely theoretical and is based on the sources and the methods involved in creating and updating the dataset.

Adding to the uncertainty is the fact that both the topological and the geographical information content of [NWB](#) is assembled from a wide range of providers ranging from large national providers such as [RWS](#) and Kadaster, to local providers such as specific road authorities and civil engineering agencies. No clear indication is given in the documentation about the sources used for the compilation of specific [NWB](#) road types or the estimation of their accuracy, but it is mentioned that it is not consistent ([Rijkswaterstaat \[2020c\]](#)).

In interpreting the 5 m accuracy, it is important to note that the [NWB](#) lines represent road centrelines, but not of the whole paved surface. The centrelines in [NWB](#) approximate the centre of the traffic-occupied parts the roads, excluding hard shoulders and other paved surfaces connected to the roads. It is also important, that in order to reduce the total number of vertices in the dataset, [NWB](#) often does not contain vertices for more than 200 m based on my inspection (where roads are straight), and even in sharp bends for up to 20-30 m at a time. Especially in bends, this circumstance, combined with the official error figure, means that [NWB](#) often leaves the traffic occupied road surfaces, and sometimes even the paved areas. I confirmed this problem by comparing [NWB](#) with [DTB](#) and [AHN3](#).

One such comparison is shown in [Figure 2.6](#). [NWB](#) centrelines appear below [AHN3](#) points and are consequently masked out partially by them. I shifted them to match [AHN3](#)'s mean elevation locally, to make them better comparable. Comparisons such as these revealed that [NWB](#) gets close to the edges of the paved surfaces quite often, and sometimes even leaves them. In sharp bends, this is worsened by the angularity introduced by the coarse lengthwise discretisation of [NWB](#), for instance in the location annotated in the figure. In later stages of the project, I made further comparisons with [BGT](#) and with aerial orthoimagery ([Luchtfoto 2020](#) from Kadaster), discussed in [Section 4.3.3](#) and with an example shown in [4.20](#). These comparisons further confirmed the issues.

Although the above nominal accuracy and its description are certainly not good enough to ensure compliance with the new noise regulations, the 3D conversion of [NWB](#) is not concerned with improving it – in fact, it is a requirement of the project not to displace [NWB](#) horizontally. Hence, we may say that the intended outcome of the 3D conversion is to devise a method that can produce accurate elevations for [NWB](#) *assuming* that its accuracy complies with the requirements set by the new noise regulations – 20 centimetres at 95% confidence. To achieve this compliance in practice, lateral refinement is being carried out in separate projects by matching [NWB](#) roads with their counterparts in other, more accurate datasets. Specifically, [DTB](#) and [BGT](#) are being used for this. As these datasets are already theoretically compliant with the accuracy requirements, correcting [NWB](#) geometries based on them will foreseeably solve the lateral accuracy problems of [NWB](#). However, at the time of writing of this report, the [BGT](#)-based correction has only been released for municipality-owned roads ([G-roads](#), not relevant to us), while the [DTB](#)-based corrections for motorways are currently being finalised. Consequently, both the commercial and the scientific 3D-[NWB](#) project still rely on [NWB](#) data that lacks any corrections ([NDW \[2020\]](#)).

Regardless of improving [NWB](#)'s lateral accuracy not being within the scope of this project, it is important to be aware of these issues because of their implications when overlaying [NWB](#) with [AHN3](#) and [DTB](#) in the processing part of this research. The problems and the necessary workarounds are discussed in-depth in the relevant sections of the next two chapters.

The [NWB](#) product is updated every month with particular attention to always including new roads, removing outdated (demolished or permanently closed) roads and updating refurbished roads as necessary. This frequency means that [NWB](#) is always up-to-date with changes to the road network, at least to the extent where navigation (in e.g. [Google Maps](#), which uses [NWB](#)) can take place without any disruptions. However, this does not mean that [NWB](#) has a temporal resolution of one month; for that to be true, all roads would need to be re-measured every month. The monthly releases merely mean that

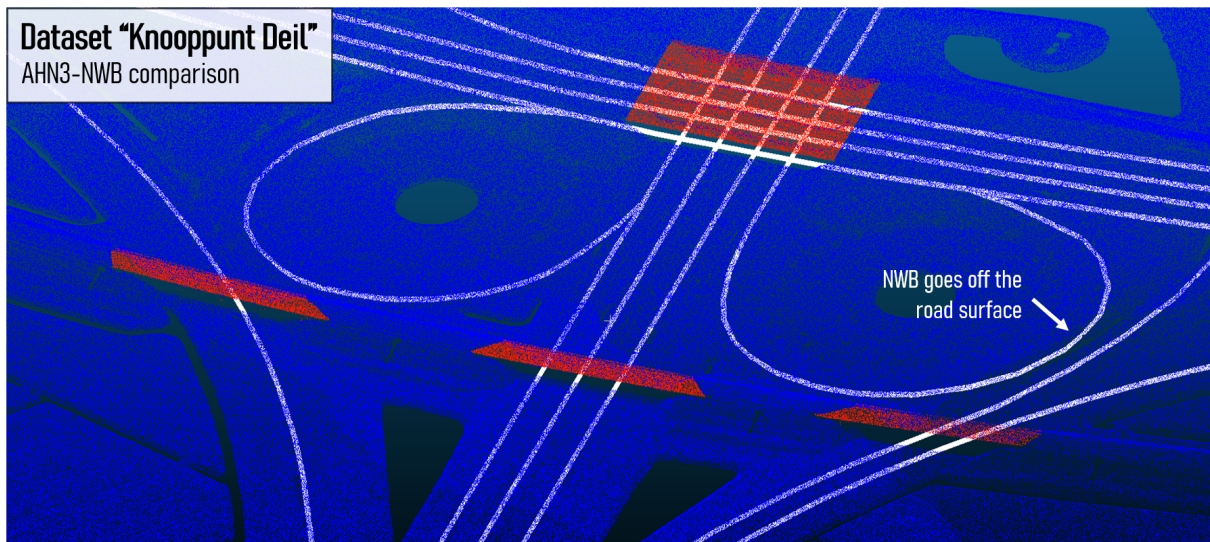


Figure 2.6: Render comparing AHN3 with the relevant 2D NWB centrelines. AHN3's ground points are coloured blue, and NWB centrelines are shown in white.

effort is concentrated into releasing known changes to the road network frequently. Since no physical phenomena exists that would move the roads laterally (without human intervention) by a significant distance, this does not cause issues in practice.

2.3.2 Actueel Hoogtebestand Nederland – AHN

AHN are ALS datasets available as open geospatial data in The Netherlands. These national surveys are commissioned every few years with AHN (the first version) to AHN3 already complete (1996 to 2019), and the first AHN4 tiles currently nearing release. At this stage of the project, we are interested only in AHN3, as it is the most recent iteration of this product. The AHN product is also owned and managed by RWS.

The dataset has a combined systematic and stochastic elevation error of 15 cm at two standard deviations (i.e. 95 % confidence), and 6 to 10 points per m² sampling density on average, corresponding to 0.32 to 0.41 m posting distance. The lateral error is 18 cm at two standard deviations (Rijkswaterstaat [2020a]). Comparing these to the descriptors of Lidar datasets used in the research examined as part of our literature review, we may assert that AHN3 can be considered accurate in comparison, and to have excellent sampling density. It is especially accurate and dense relative to the older Lidar datasets that are mentioned in these papers, including the first iteration of AHN.

The AHN3 point cloud has been classified semi-automatically also with excellent accuracy, and is released with the classification included. This means that for most purposes, the point cloud needs not be ground filtered by users, and that extracting certain features is made far easier. Of the various classes available, we are interested in class 2 the most, which corresponds to ground points, and class 26 which contains, among other things, bridge structures and the roads that are found on them.

Ground points are mainly interesting to us because they contain the points reflected from land-based roads. This includes roads that were constructed directly on the terrain, as well as roads constructed on altered terrain, such as on elevated ground or in open trenches. It also contains the points that represent the terrain in the vicinity of the roads. Elevated roads and bridges are not considered ground points and are generally represented by gaps in class 2, which can, in most cases, be filled by using data from class 26, as shown in Figure 2.7. The shapes of motorway lanes and ramps, as well as bridges are clearly defined. Roads constructed on elevated ground are reliably classified as ground, and bridges are cleanly split off by the classification. Even under thin bridges, data becomes gradually sparser at the border and becomes extinct directly below the bridge. This render also makes it clear that wherever

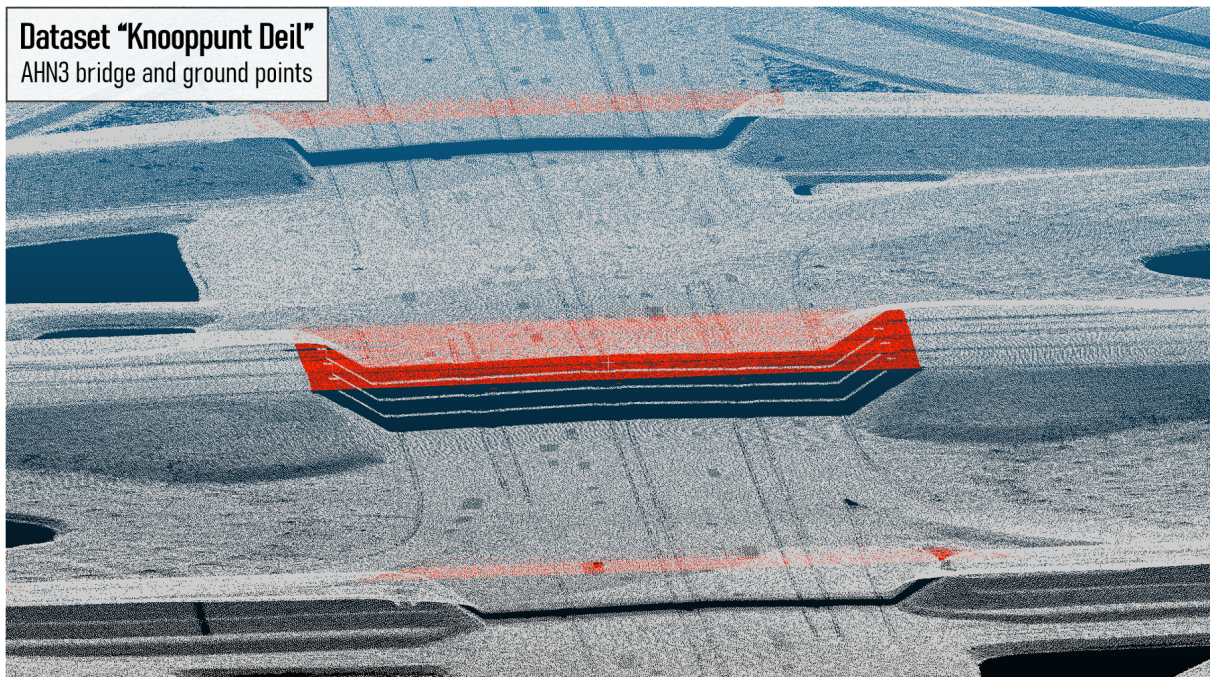


Figure 2.7: Example render of AHN3 at *Knooppunt Deil*, SW of Geldermalsen, showing ground points and bridges. The white colour marks ground points (class 2), red corresponds to bridges (class 26).

vehicles were encountered on ground-based roads, the sampling is worse locally. It does not *generally* go entirely extinct however, as most locations have been scanned multiple times, filling in the gaps left by moving vehicles. Data gaps are mostly observed where slow or stationary vehicles were encountered, and where only one scan was performed.

Class 26 also contains other types of objects, for instance large motorway signs arching over road surfaces, as well as the civil engineering structures of elevated roads and bridges (in addition to the road surfaces on them). Reflections from vehicles traversing bridges are also present in this class. Figure 2.8 shows a render from the same location as 2.6 and 2.7. The full-width motorway signs are clearly visible above the motorway lanes, coloured red because they originate from class 26. It also shows that the presence of water results in holes (the dark, linear features running parallel with the motorway in this render) in the ground-only point cloud. In this render, it is also visible that in my testing datasets, all points falling outside a 150-metre buffer zone around the NWB centrelines were removed (see more information about this in Section 4.1.2).

AHN3 is released in the form of a point cloud, as well as digital surface model (DSM) and DTM rasters. Both were produced using basic radial IDW interpolation with a fixed parametrisation. The DTM was generated by including only points from class 2 in the interpolation step. They are available at 0.5-metre and 5-metre resolutions, with the 0.5-metre resolution being relevant to this project in terms of the target accuracy. For context, this raster converts (on average) 1.5 to 2.5 points into a single raster cell based on AHN3's nominal sampling density. The commercial implementation uses these rasters instead of the point cloud tiles, as explained in Section 2.4.2.

The Lidar tiles are released in the binary LAZ format (compressed LAS, or LASzip), and are generally several gigabytes in size. As each tile only covers an approximate area of 32 km² and the LAZ compression ratio for this dataset is 0.1 on average, scaling considerations are relevant for this project if the implementation is to be capable of fully converting NWB to 3D using the point cloud tiles rather than the rasters.

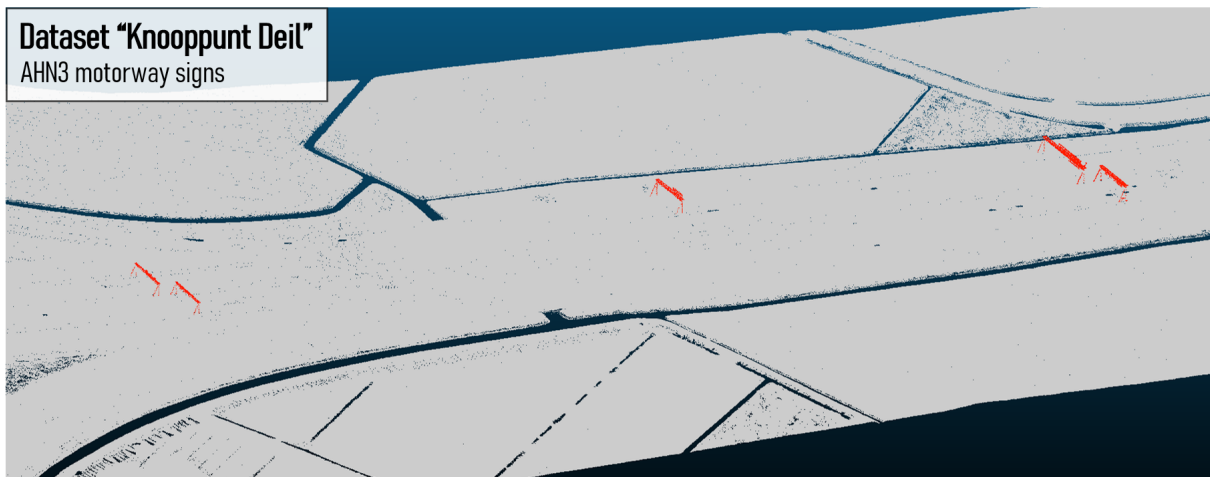


Figure 2.8: Example render of AHN3 at *Knooppunt Deil*, SW of Geldermalsen, showing ground points and motorway signs. The white colour marks ground points (class 2), red corresponds to bridges (class 26).

2.3.3 Digitaal Topografisch Bestand – DTB

Like NWB, DTB (or more specifically, DTB-Droog, the DTB product relevant to roads) is a Dutch open data geospatial dataset in the *ESRI Shapefile* format. For the purposes of this project, we only need only those DTB line features, which correspond to road surface markings. Hence we can also regard this as a dataset comprised exclusively of *LineString* objects, making it identical to NWB in its data structure apart from being a 3D dataset. DTB is also managed by RWS and it is concerned only with state-owned roads and roads on state-leased land, which translate almost exclusively to NWB R-roads, that is, motorways. DTB is, hence, not a reliable source of information about provincial road elevations (NWB P-roads), our other road type of interest.

There are various types of DTB road markings that are of interest to us, the main one being a category called *verflijnen*. These DTB lines represent the painted lines marking the outermost edges of the area open to traffic. This is a lucky correspondence with NWB, as it contains the centrelines of the areas that are open to traffic, rather than the entire paved surfaces – meaning that NWB is expected to lie between these DTB lines, wherever they exist. The other two types I found to be reliably represent road surface elevations are the categories *verfstippellijn* and *blokmarkering*, which represent lane separation lines and block marks respectively. The category *lijnverlichting* also appeared to be interesting at first, as it corresponds to road surface lighting features (not street lighting). However, I found it to not be reliably located on road surfaces in practice, hence I excluded it from further consideration.

Figure 2.9 shows a visual comparison with NWB, illustrating various types of issues. Only *verflijnen* are shown in these figures. The image in the top left shows that in practice DTB may contain several road edge markings, rather than just one on either side of NWB (pointed out by the green arrow), and that the edges may in fact include other markings, such as stop lines (shown by the red arrow). The image in the top right illustrates that NWB motorway ramps often merge with the motorway lanes at unrealistic angles, causing NWB to intersect the DTB edge markings at these locations (green arrow). The image in the bottom left shows that while in some places there are many DTB road edges, in other places they are incomplete or missing entirely (grey arrow). Furthermore, NWB centrelines may also get very close to DTB edges both inside and outside bends, as indicated by the blue and the purple arrows. The coarse discretisation is clearly visible in the bottom right image.

Like NWB (but unlike AHN3), DTB's production pipeline also concerns several organisations contributing various types of surveys, which are then semi-automatically assembled into the complete DTB product. While many DTB features are photogrammetry-derived, road surface markings are mainly derived from accurate land-based manual surveys or extracted from car-mounted MLS data (Oude Elberink and Vosselman [2012]). The documentation of DTB consists of its formal specifications (Rijkswaterstaat [2020d]) and a handbook (Rijkswaterstaat [2020b]). The former contains the accuracy-related details, reporting

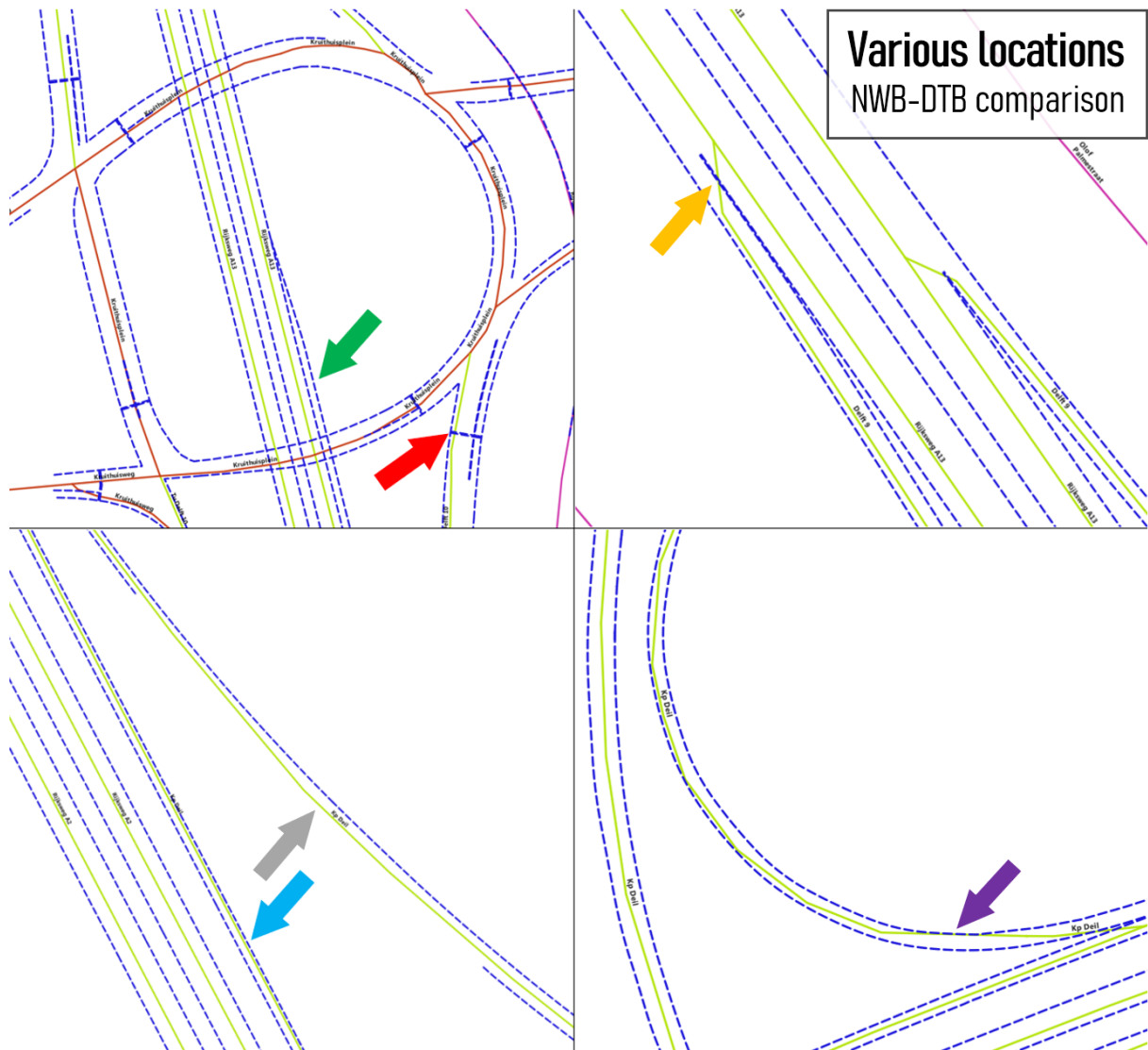


Figure 2.9: Renders of *DTB verflijnen* overlain with NWB centrelines, illustrating "compatibility issues" and individual DTB issues (pointed out by the arrows, further explained in the text). NWB symbology is identical to that which I used in 2.5, and blue dashed lines show the DTB geometries.

10 cm vertical and 5 cm horizontal standard deviations, or 20 cm and 10 cm at 95% confidence to make it comparable with the reported accuracy of *NWB* and *AHN3*.

Theoretically, *DTB* is not only accurate, it also has good temporal resolution. It is updated multiple times a year, specifically to always be up-to-date in terms of newly constructed roads and refurbished roads. This update frequency is comparable to that of *NWB*, which is part of the reason why it forms a crucial part of the commercial solution. The other part of the reason is, that it theoretically always contains data for occluded roads, even in tunnels. This means that the combined information content of *DTB* and *AHN3* theoretically amount to having complete coverage of the Dutch road network. The ease with which elevations can be extracted from *DTB* to be used in the 3D conversion of *NWB* (as well as its update frequency) prompted *NDW* to consider *DTB* as its *primary* dataset, wherever it is available.

In practice, I found evidence to support that the above decision is fundamentally flawed, already during the input assessment stage of my project. There are places where *DTB* lives up to expectations (as well as its formal specifications), but this is not the case in most of the areas I examined. Even in terms of motorways, *DTB* is often incomplete to the extent that it lacks coverage over tens of kilometers. Even where it exists, its coverage may be patchy, especially in sharp bends and on ramps. Even where it exists, it commonly contains a single line only, rather than the theoretical minimum of two (the road edges).

Furthermore, already by considering the update methodology of the dataset, one may remark that some of the elevation measurements in it must be very outdated. Indeed, a large part of the data is almost as old as the roads themselves, meaning that they were taken more than 20 years ago. This is where it becomes relevant that the update methodology of *NWB* and *DTB* does not really represent a high temporal resolution. In the absence of a physical phenomenon causing significant lateral ground motion, this does not cause problems with *NWB*, but there *is* an obvious one that may move roads up or down: subsidence. Although the surface load due the weight of the road and passing vehicles may play a role, subsidence is primarily caused by natural, geological processes. In some parts of The Netherlands, groundwater and natural gas extraction may also play a role in addition to the natural factors. Although this work does not specifically study the correlation between subsidence and problems with *DTB*, there is little else with which the noticeable differences between *AHN3* and *DTB* could be explained. The *AHN3* measurements are at least 15 years more recent than the oldest ones in *DTB*, which is where the biggest differences (often more than a metre) can be observed.

Interestingly, the opposite can also be observed, although less commonly, and in a highly localised manner. In some places, *DTB* is above the road surface measurements of *AHN3* by a significant margin, often by more than 0.5 m. While subsidence cannot be used to explain these differences, there is evidence to support that the elevations in *AHN3* are indeed correct and the ground has shifted upwards noticeably. The latest subsidence survey of The Netherlands reported positive changes in addition to the decreasing elevations that are associated with subsidence. I primarily observed *DTB* to be below *AHN3* where this map indicates negative elevation changes, and above in regions where no changes or slightly positive changes were observed in the subsidence study, verifying my hypothesis.

Figure 2.10 shows renders of *DTB* overlain on *AHN3* with all *DTB* features shown (above), and with only *verflijnen* shown (below). The top render illustrates that other features, such as roadside slopes, canals, ditches, safety rails are represented in *DTB*. Full-width motorway signs are also occasionally represented (either by lines on the road, or on the structure itself). The bottom render shows that locally, the edge markings are in good agreement with *AHN3* visually, and are only occasionally incomplete. This location has the best vertical correspondence with *AHN3*, and also the best completeness, of all the areas I examined. For illustrations of the *disagreements* between *DTB* and *AHN3*, please refer to Figure 4.7 and the associated discussion in Chapter 4.

The subsidence issue was not raised in *Oude Elberink and Vosselman [2012]*, which I attribute to the fact that they used the first release of *AHN*. This release must have been temporally consistent with the *DTB* release at that time. Furthermore, the sampling density of the first release of *AHN* was low enough to mask the effects of subsidence, which must have been much more subtle at the time due to the better temporal agreement between the two datasets.

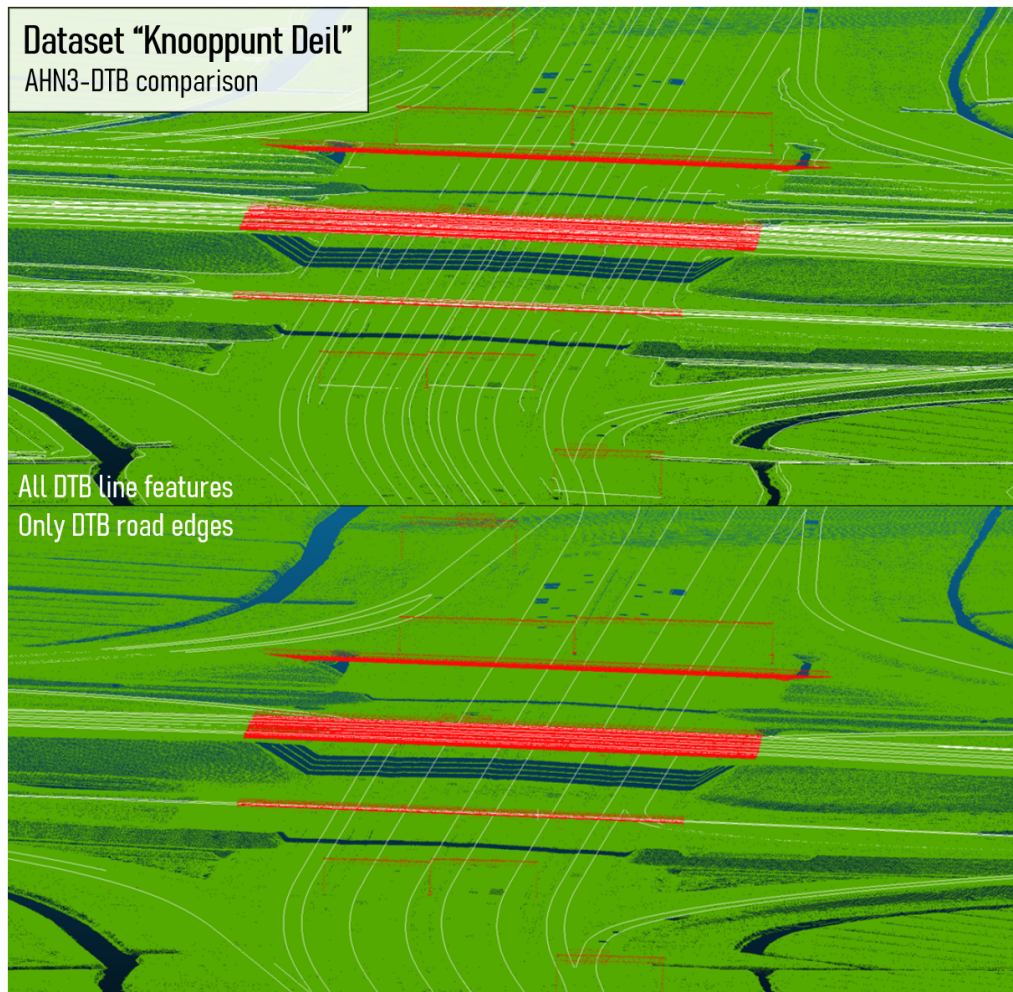


Figure 2.10: Renders showing all DTB line features (above) and *verflijnen* only (below) overlain with AHN3 in 3D. Ground points are shown in green, bridge points in red.

2.4 Methods of existing implementations

2.4.1 NDW prototype

NDW themselves produced a prototype implementation, which can achieve a 3D enrichment of NWB with only a few gaps in the produced elevation profiles. Although their workflow does not have a formal documentation, I have been given a verbal description of it, as well as the output. Based on my understanding of these, their primary technique involved snapping close-by AHN3 Lidar points to the line geometries of NWB. Notable problems with the implementation included non-road points being snapped to centrelines, causing road centrelines to be given overestimated elevations, in turn resulting in abrupt spikes in the elevation profiles.

Furthermore, no close-by points could be found for underground roads (i.e. tunnels), and strongly occluded parts of roads. For small gaps, this was resolved partially by writing an algorithm to interpolate linearly inside NWB, using the closest vertices where snapping was successful. For larger gaps, an attempt was made to resolve issues by including information from external sources semi-automatically. Neither issue could be fully resolved via these approaches, hence the results of this project were only used by NDW to gain a better understanding of the problem and the expected challenges. For the development of a reliable digital toolbox they subsequently commissioned a commercial implementation from RHDHV.

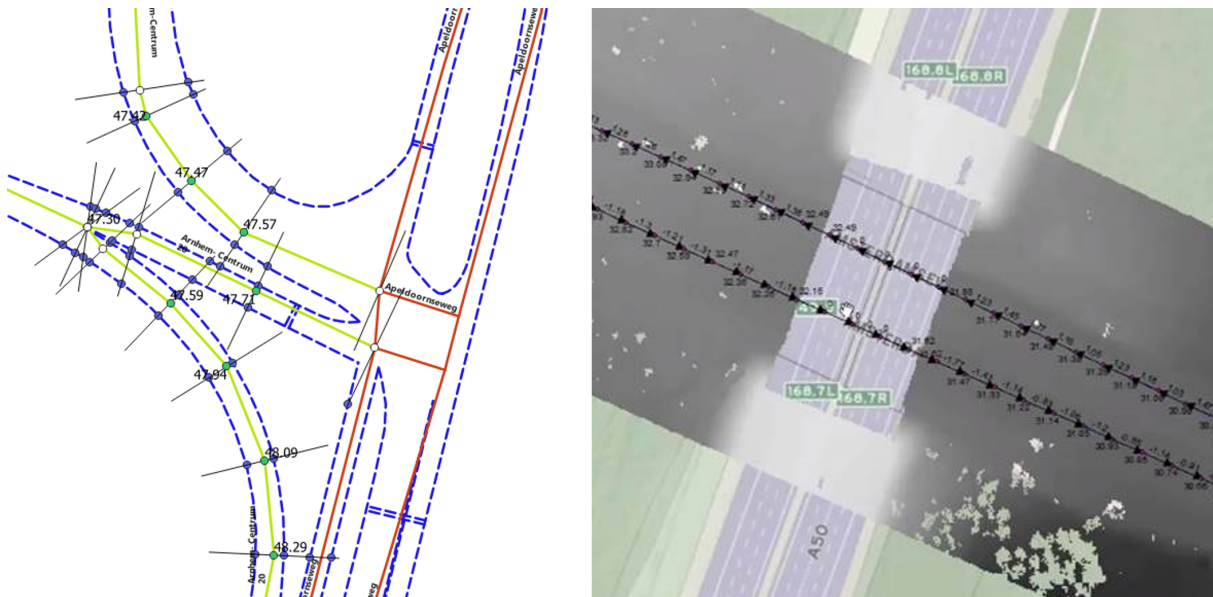


Figure 2.11: Illustrations of RHDHV's methods. Left: cross-sections are shown as black lines. Green circles denote vertices where cross-sections could be properly intersected with DTB lines (blue circles). White circles denote where the procedure failed and AHN raster-based interpolation was necessary. NWB symbology is identical to that which I used in 2.5. Right: Illustration of raster-based elevation interpolation. An AHN2 raster is shown in greyscale, overlain on a topological map and NWB lines.

2.4.2 RHDHV's commercial implementation

RHDHV developed their implementation in parallel with the planning of the present scientific research. During this time, I attended NDW-RHDHV meetings, discussed the commercial system design and implementation details directly with RHDHV personnel, and was granted access to the codebase of the project. Understanding their implementation was crucial for the planning and realisation of my research, as it was among my goals to estimate the effectiveness of the commercial implementation's methods, as well as to assess the accuracy of their final results. In addition, creating my system design while learning about the known and suspected shortcomings of their methods allowed me specifically focus on areas where a different, less pragmatic approach could yield better results.

Overview of system design

First, where NWB vertices are too sparse, vertex densification takes place; i.e. additional vertices are created inside NWB line segments until all vertices are positioned less than a certain threshold distance apart. From then onwards, *different* workflows are initiated for R-roads and P-roads.

For P-roads (where DTB data does not generally exist), the workflow is conceptually similar to the one in the prototype, with the notable difference of using AHN3 DTM rasters rather than the point cloud tiles. Because AHN3 DTM rasters are badly affected by both large holes and small groups of missing pixels (due to the fixed-parameter IDW interpolation that was used to generate them), RHDHV could only make use of them by filling in the gaps using linear interpolation in a 3D TIN created from the raster pixel centres. They then simply interpolated elevations for NWB from the rasters using bilinear interpolation. Intermediate results of this procedure are shown on the right in 2.11. It shows a raster being overlain with NWB to yield elevation values. The raster still contains the holes that; these are filled in before interpolating elevations for NWB but are shown here for demonstration purposes. Two types of holes generally occur: small-scale ones due to objects such as street furniture, vehicles and vegetation, and large ones that are typically due to large-scale occlusion due to buildings or bridges (as in this case). The test build shown here used AHN2 rasters, but their production version uses AHN3.

2 Related work

For *R-roads*, *DTB* is available, and the assumption is made that it is more accurate than *AHN3* (or at least the stock *DTM* tiles generated from *AHN3*), to the extent where it should be the primary source of elevation data. Priority is thus always given to it in the procedure, with *AHN*-based interpolation used only as a fallback mechanism in case *DTB*-based height estimation fails for any reason (anomalous elevations computed, or missing *DTB* geometry).

The goal of the underlying algorithm is to find the closest *DTB* line segments that are roughly parallel to the road at a given *NWB* vertex, and to deduce elevations from them. First, 2D road cross-sections are constructed on *NWB* vertices, with each given the mean azimuth of the two *NWB* line segments that they are part of, and then rotated 90 degrees. For vertices created during densification, this simply means the rotated azimuth of their parent line segment. *DTB* lines are then intersected with the cross-sections and for each cross-section, the closest *DTB* line that satisfies a relative angle condition is picked on both sides of *NWB*. Elevation is then first linearly interpolated inside the two chosen *DTB* segments to yield values exactly at their intersections with the cross-section. Lastly, elevation is interpolated linearly along the cross-section itself to yield the final elevation at the location of the *NWB* vertex.

The angle condition is a threshold-based evaluation concerning the angle between intersected *DTB* line segments and the cross-sections, and is used to ensure that the chosen *DTB* segment is indeed roughly parallel to *NWB* locally. This helps ensure that the algorithm does not accidentally choose a *DTB* line segment that belongs to a different (underlying or overlying) road surface. The assumption is thus made that the *DTB* line segments representing surface features of a given road are roughly parallel with the relevant *NWB* centreline, and lie close to them. Implicitly, this also assumes that even if no other *DTB* road markings are present, *NWB* centrelines will still lie between two *DTB* road *edge* markings, i.e. *verflijnen*.

In practice, backup mechanisms needed to be implemented because these assumptions do not always hold. This is mainly because in sharp bends *NWB* may not really be parallel with the relevant *DTB* lines locally, and because it is frequently not complete enough to be used for the above operations. To bridge these issues, wherever the algorithm only finds a suitable *DTB* intersection on *one* side of *NWB*, it is only that side from which the elevation value is deduced. If no suitable intersection can be found whatsoever, the *AHN3* raster-based interpolation is used instead (the same workflow that is always used for *P-roads*).

This procedure is illustrated on the left in 2.11. It is shown in this figure that in sharp bends the assumption that *NWB* and corresponding *DTB* lines are parallel does not necessarily hold, because of how coarse and inaccurate *NWB*'s georeferencing is, especially relative to *DTB* which is very accurate horizontally. The render also illustrates that *P-roads* are not processed in this way, not even if they have *DTB* lines next to them (which frequently occurs in the vicinity of motorways).

Potential limitations

The preliminary results of the commercial implementation have already been made public, as described in *NDW* [2021]. In this section I discuss the *suspected* limitations of their methods. The *observed* issues will only be discussed in the context of the comparison of the two sets of results (Section 4.4). During the project planning, system design and implementation stages, the commercial results were not yet available and as a result, the bulk of my work – almost everything apart from Section 4.4 – is based on preliminary results, verbal descriptions, and the source code.

Firstly, I suspected that using *AHN3* rasters in place of the point cloud would affect the quality of their conversion. Point cloud to raster conversion is, by definition, associated with inherent information loss (less raster cells than point cloud points), and further reduction in accuracy is introduced by the interpolation mechanism itself that created the rasters. Radial *IDW* was used to generate *AHN3* *DTM* tiles, which several of the reviewed papers found to be specifically unsuitable for interpolating large-scale areas in which zones of decreased point density or gaps exist – both of which characterise ground-filtered *AHN* data (e.g. *Guo et al.* [2010]). In addition, the procedure performs another layer of interpolation to infill gaps, which may further deteriorate accuracy. Furthermore, *RHDHV* uses bilinear interpolation inside

the raster to produce *NWB* elevations, which is suggested by Shi et al. [2005], to be less accurate than other common methods such as bicubic.

There is no explicit mechanism built into the software to deal with occlusion in the case of *P-roads*, and also *R-roads* where *DTB* is unavailable. This means that wherever *NWB* elevations are interpolated in occluded road segments from *AHN3* rasters, they may be incorrect depending on how well the gap-filling has worked. Just like in the *NDW* prototype, these values will show up as spikes in the elevation profiles, as well as longer bumps where wide features (e.g. bridges) are encountered. Since there is no outlier filtering or smoothing algorithm built into the software either, the severity of this issue is not mitigated in any way.

Based on the input assessment, it is also evident that prioritising *DTB* wherever it is available may itself be a questionable decision, in view of the fact that the output's accuracy needs to measure up to the noise regulation's expectations, at least theoretically. *DTB* is accurate horizontally, in fact it is theoretically more accurate than *AHN3*. However, even if its vertical accuracy had been accurate at the time of its acquisition, it no longer is due to subsidence, and/or due to other phenomena that I am unaware of. As elevations in *DTB* are not updated where no civil engineering changes have taken place in the road network, its road surface markings are often far too outdated to be used with any certainty, especially considering that there is no reason to do so given that *AHN3* contains equally accurate, but significantly more recent data.

Lastly, the commercial implementation lacks a formal accuracy assessment procedure. Although this is common with comparable commercial products, in this case the output dataset needs to comply with formal accuracy *requirements* set in law. Without a quantitative or at least qualitative accuracy assessment of some kind, there is not enough evidence to support the applicability of the commercial results to the noise modelling applications they are intended for.

Since the accuracy of *AHN3* rasters is known and simple bilinear interpolation is used to obtain elevations from them, deriving output accuracy would not be difficult wherever their solution uses *AHN3*. This excludes interpolating in gap-filled pixels, which would need further considerations. In the case of *DTB*, the evaluation of accuracy may be equally simple, as the underlying computations all boil down to simple linear interpolation. However, wherever *DTB* data is old, any accuracy quantification would be meaningless because *DTB* itself does not comply with its own formal accuracy locally.

3 Methodology and methods

The first section of this chapter presents a description of the methodology of the planned dissertation work. This description is limited to matters relating to planning the execution of the work, without going into specifics about the methods themselves. The second section of the chapter presents an overview of the methods themselves, including information about how these plans evolved since the release of the project proposal. This section also includes detailed accounts of the thought processes leading to the most important design choices. The rest of the chapter is devoted to a detailed account of the methods that underlie each of the processing steps in the final “proof-of-concept” software implementation, with accompanying flowcharts and vector graphics to illustrate the system design, and the details of the algorithms. A short section at the end of the chapter describes the implementation’s software architecture, with explanation about certain technical design choices regarding the implementation.

3.1 Methodological framework

This section contains a written account of the key stages into which the execution of this research can be divided. Each subsection describes one such stage, discussing the specific tasks performed during each stage as well as what has changed relative to my original plans. The methodology is also visually illustrated on a flowchart in Figure 3.1.

3.1.1 Preparation

This project concerns a client – *NDW* – with specific requirements and a pre-existing attempt at implementing a solution, in addition to aspects that are purely scientific. As a result, the first stage of the project involved *consultation with the client* and with their commercial developers – *RHDHV* – in addition to the task of *familiarising myself with the research topic and literature*. The results of these preparation tasks were *discussed internally* with my supervisors and used to *define the final list of formal research questions* on the basis of focusing primarily on academic topics while also fulfilling the requirements of the client.

I executed this stage of the project according to my initial plans, little has changed during its realisation.

3.1.2 Preliminary analysis, proposal writing

The second stage of the project involved *further consultation with the client and their developers* to determine to what extent the commercial and scientific branches of the 3D-NDW project could be linked, and to allow me to understand the exact methods used in the prototype and the commercial implementation (which was being actively developed during this period of time). In parallel with these tasks, I *performed the necessary in-depth literature review* and preliminary analysis. The preliminary analysis was comprised of a *close examination of the input datasets and their respective documentations* (input assessment), and based on this and the research questions, the *final selection of relevant concepts and methods*. I also selected a range of illustrative geographical regions during the preliminary analysis, and cropped the datasets to their extents to *create testing input files* for later development and testing. Lastly, the results of this stage were distilled to *produce the project proposal*.

I executed this stage of the project according to my initial plans, but with a few small alterations. My initial plan was to put a slightly larger emphasis on performing preliminary analysis tasks, but the

3 Methodology and methods

abundance of relevant literature and the complex task of creating a preliminary system design limited the amount of time I could spend on it. However, this meant that during the next stage, I already had a solid starting point in terms of background knowledge, and specific plans regarding what to start implementing.

3.1.3 Analysis

The third stage of the research concerned carrying out most of the analysis. The period was characterised first and foremost by the intense development effort focused on the *implementation of individual algorithms and steps of the workflow*. My original plan was to isolate this set of tasks and perform it separately from the *assembly of the pipeline* from the individual modules. However, it proved to be more effective to develop the modules and incrementally extend the pipeline with them at the same time – an approach to which I switched after implementing the first few modules. This allowed me to resolve pipeline-level issues as part of the incremental refinement of methods, in addition to problems related to specific pipeline steps only.

Carrying out the *accuracy-related analysis* was the last stage of the project that required active development on the program code. Testing the individual procedures and the pipeline was continuous during the implementation, with larger tests performed after reaching major milestones. Testing, and the assessment of performance and accuracy used the testing datasets I produced as part of the preliminary analysis. This was followed by a evaluation of the overall results of the research and a discussion of them with my supervisors, as well as a comparison of my results with those of the commercial project. A draft version of the present report was also produced in this stage.

3.1.4 Finalisation

Both *the implementation and the present report were improved and finalised* during this stage. The final version of the source code of this L^AT_EX report and the Python implementation were published in their respective GitHub repositories. Furthermore, the outcome of the research and its findings relevant to improving the commercial implementation were communicated to and discussed with NDW.

3.2 Overview of methods

This section provides a structured overview of the steps of the processing pipeline. While the detailed descriptions in Section 3.3 focus on explaining how exactly each step works, the purpose of the present section is to provide the rationale justifying their necessity and the reasons underlying certain major design choices, as well as to describe their role in the context of the system as a whole.

While the exact aims of the project materialised during the first two stages listed in Section 3.1 above, a brief description of the project already existed beforehand. The project was originally conceived as a an academic continuation to the pre-existing attempt of NDW to implement a solution to the 3D conversion of NWB, re-using NDW's prototype implementation as the basis for a completed, academically sound version. During the aforementioned two stages, it became clear that NDW's pre-existing implementation is not substantial enough to justify building the academic project on top of it. Hence, the entirety of the below pipeline was designed and implemented specifically for this academic project, no part of it represents code borrowed from the NDW prototype (or the RHDHV implementation).

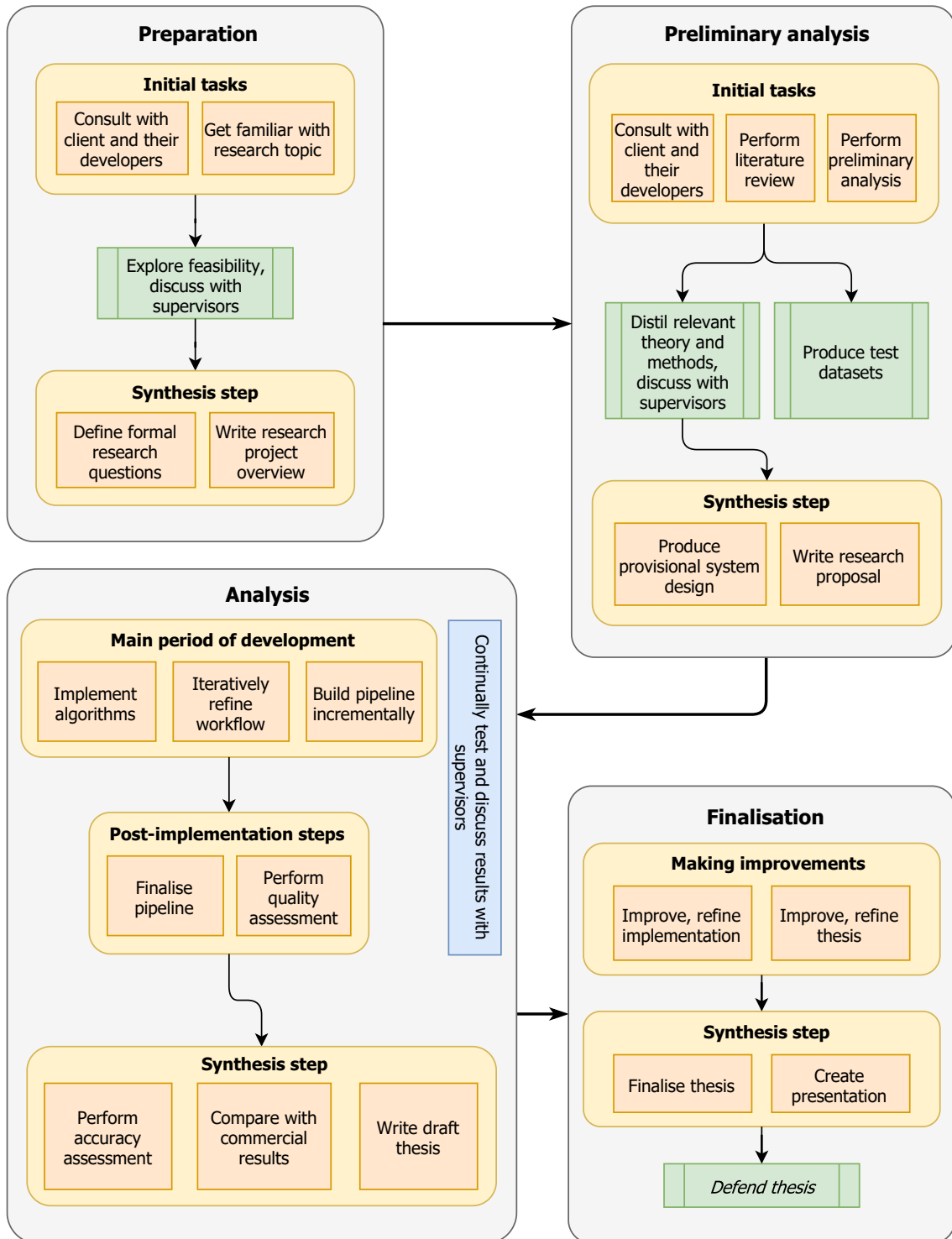


Figure 3.1: Flowchart illustration of the top-level methodology of my dissertation research.

3.2.1 Proposed processing pipeline

The design of the pipeline is the result of a combined understanding of concepts described in related work, my own knowledge and experience relating to the geomatics discipline, as well as inspiration from the methods of the commercial implementation. The proposed workflow was built with a strong focus on finding answers to the research questions. Furthermore, it is also the result of a process of iterative refinement. In most cases, this only concerns the technical details of the algorithms implementing the pipeline steps, but in some cases I also made major changes to certain aspects of the general approach. Hence, in the structured overview below, I added a list item per pipeline step specifically to describe what changes, if any, were made to the given step.

As a brief summary of the general idea, the pipeline takes **NWB**, decomposes it into roads whose surface can be modelled by 2.5D methods, and applies a set of mostly geomatics operations to produce the 2.5D road surface models that the elevations are then derived from to produce 3D-NWB. Accuracy-related considerations are not yet described in this section, these are first discussed in Section 3.2.4 below. A visual illustration of the main pipeline steps is shown in Figure 3.2.

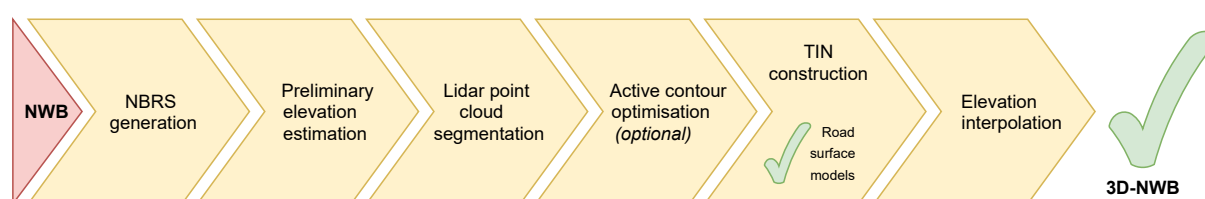


Figure 3.2: Illustration of the top-level steps and outputs of my processing pipeline.

1. Generating non-branching road segment(s) (NBRS)

- a) **Goal:** assemble optimal 2D profiles from the building blocks of **NWB**.
- b) **Approach:**
 - i. Assemble non-branching road segments, henceforth referred to as **NBRS** (in both plural and singular) from **NWB** geometry. To do so, look for series of **NWB** *wegvakken* (LineString objects) that represent the same road and “join” them.
 - ii. Perform the assembly of **NBRS** in a way that maximises their length (optimal for length-wise 2D operations such as polynomial fitting), minimising internal angles at the same time. Disallow self-intersection, so that each **NBRS** can be modelled in 2.5D.
- c) **Purpose:** this step is necessary, because in addition to working with small-scale (short wavelength) features in the road network, we wish to be able to inspect trends that take place over longer distances in the network. The building blocks of **NWB** (*wegvakken*) can sometimes be short, occasionally only a few metres long. Hence, assembling them into **NBRS** provides a better starting point for later steps.
- d) **Changes:** from the outset, I expected that simple methods based on 2D profiles (2D distances along **NBRS** + elevations for the vertices), would be useful for this project, and that a data structure serving this dual purpose would be necessary. Hence, **NBRS** have always been part of my plans and their exact specifications did not change much during development.

2. Preliminary elevation estimation

- a) **Goal:** create a rough, preliminary 3D version of **NWB**.
- b) **Approach:**
 - i. Based on the median elevation of nearby **AHN3** points, associate **NBRS** vertices with preliminary elevation approximates, thereby performing a crude 3D conversion of **NWB**.

- ii. Perform polynomial fitting on the 2D profiles that **NBRS** represent if one converts their horizontal coordinates to series of distances. Identify vertices that are outliers with respect to the models and interpolate values for them linearly.
- c) **Purpose:** this step is necessitated by the next one (point cloud segmentation). While it is possible to perform it without first performing a rough 3D conversion, I found it to be much more effective when the approximate 3D locations of **NBRS** are already known by that point.
- d) **Changes:** this step represents an addition relative to the original plans. I started suspecting its benefits during the implementation stage, and subsequently added it to the pipeline design.

3. Point cloud segmentation

- a) **Goal:** create subclouds from the Lidar data containing points relevant to the roads represented by individual **NBRS**.
- b) **Approach:**
 - i. Using their preliminary elevations, find “patches” of Lidar points in the 3D vicinity of **NBRS** vertices. Progressing along the vertices, fit planes on the Lidar patches. Where an unexpected change in the plane fits is detected, rely on points (vertices and densified vertices) extracted from **DTB** to provide support.
 - ii. Where **DTB** is also unavailable, accept the shifted (or missing) plane fits but perform a polynomial fit afterwards to identify planes that are unlikely to belong to the relevant road surface. Split the **NBRS** into parts in such places, excluding the undesired regions from further consideration until the last pipeline step.
 - iii. Based on the plane fits, decide which points in the patches are relevant to the road surface represented by a given **NBRS**, and create subclouds by merging them (one for each **NBRS** part). Include **DTB** points that were used to support this procedure.
- c) **Purpose:** like **NBRS** generation, this step also has a dual purpose. Firstly, it associates each **NBRS** with a set of relevant **AHN3** and **DTB**, thereby reducing the amount of Lidar points that will need to be processed later on. Secondly, it also excludes the majority of points which are relatively close to a given road, but which were reflected from occluding objects rather than from its surface.
- d) **Changes:** originally, I only wished to detect where plane fits become inconsistent to exclude small-scale occlusion at this point. However, I eventually realised that by tracking changes in certain metrics, I could do so even in relatively long occluded regions. I then incorporated **DTB** as a backup dataset to increase the reliability of this method, which made the solution work even where significant changes in elevation take place inside the occluded regions (such as in tunnels). I added the splitting of **NBRS** into parts as a last tweak, after implementing the rest of the pipeline. As such, this stage is a good example of iterative refinement in my research.

4. Preliminary edge approximation

- a) **Goal:** create line geometries on both sides of **NBRS** approximating the edges of the road surfaces.
- b) **Approach:**
 - i. construct cross-sections on **NBRS** vertices and convert them into 2D elevation profiles by sampling **AHN3** along their length. Perform linear regression on each, and select the outermost stable inlier points on both sides of the **NBRS**. The two points are taken to represent the road edge locally.
 - ii. Assemble approximate road edges from the discrete edge points generated by the previous step, enforcing constraints regarding the expected shape of the road edges. Relax the constraints after a certain number of successive failures, to allow the algorithm to adapt to real-life changes in the road geometry.

3 Methodology and methods

- c) **Purpose:** the sole purpose of this step was going to be to provide edge estimates for active contour optimisation. After I made the decision to make active contour optimisation optional in the pipeline (due to its ineffectiveness), preliminary edges also became needed for later steps in place of the optimised contours.
- d) **Changes:** Due to the optional use of preliminary edges in TIN construction (in case optimisation is skipped), I needed to improve their quality significantly. This entailed the implementation of significant refinements to the underlying algorithm, as well as the constraints enforcement steps that I mentioned above.

5. Active contour optimisation (*optional*)

- a) **Goal:** refine the preliminary edges based on road surface smoothness as described by Lidar.
- b) **Approach:**
 - i. Construct an attractor map from the subcloud of each NBRS part, based on a scalar metric describing the local smoothness of the points.
 - ii. Use the preliminary edges and the attractor maps to perform active contour optimisation.
- c) **Purpose:** the original purpose of this step was to optimise the preliminary edges to the extent where they can be used to classify subcloud points either as surface or non-surface points. Since this was found not to work reliably, the current purpose of the step could be described as *attempt to enhance and simplify the shapes of the preliminary edges*.
- d) **Changes:** even after improving all prior steps of the pipeline and sufficiently refining the parametrisation, the algorithm still produces mediocre results. As a result, I eventually implemented a bypass so that it can be skipped. Furthermore, I originally planned to apply morphological operations to attractor maps composited from maps generated using multiple metrics. I found this to be ineffective in practice, the final implementation simply uses the raw results of the sole best-performing metric.

6. TIN construction

- a) **Goal:** model each NBRS part by a TIN based on the subclouds and preliminary or optimised edges.
- b) **Approach:**
 - i. Seed each TIN by inserting points around the centre of the road unconditionally. Define the "centre of the road" based on the edges, not the 2D location of the underlying NWB centreline.
 - ii. Initialise each TIN by conditionally inserting points between the preliminary or optimised edges.
 - iii. Extend each TIN by conditionally inserting points further and further away from the centre of the road, beyond the edges if desired.
- c) **Purpose:** this step also serves a dual purpose. On one hand, it satisfies our academic interest in creating 2.5D surface models of the roads. On the other hand, they are used in the next step to interpolate final elevations for NWB. Furthermore, as the TIN consists of Lidar points, it allows output accuracy to be estimated in a straightforward manner.
- d) **Changes:** the original idea for this step was that the optimised road edges would be hard-coded in the TIN (a CDT was planned), and only points within these constraint geometries would be inserted. Due to the ineffectiveness of active contour optimisation, I instead needed to create a TIN construction workflow that can make the best of the edges and subclouds *without* making the assumption that the edges have near-perfect accuracy.

7. Elevation interpolation

- a) **Goal:** derive a final elevation for each NWB vertex while enforcing continuity across intersections, and augment the original dataset with the results.

b) **Approach:**

- i. Interpolate in the respective **TINs** to obtain a final elevation value for each vertex of each **NBRS** part.
 - ii. At intersections, use the first elevation that was interpolated at that approximate 3D location and connect all other **NBRS** to it that end or begin at that intersection.
 - iii. Use linear interpolation to fill in elevations in **NBRS** where **TIN**-based interpolation was not possible.
 - iv. Mark the origin of each output elevation either as **AHN3**, **DTB** or linear interpolation.
- c) **Purpose:** obtain the final **NWB** elevations and output 3D-NWB, keeping a record of which elevation comes from where.
- d) **Changes:** originally, I thought that enforcing continuity across intersections was going to be a bigger challenge. However, I found the **TIN** representations of the same intersections across different **NBRS** to be consistent reliably, hence interpolating a single elevation (based on the first **NBRS** part encountered) and grid-snapping all subsequent ones to it works without issues in almost all scenarios examined.

I was inspired by concepts and ideas from related work (see Chapter 2) while designing the original pipeline, and the final implementation retains many of these similarities. For instance, the point cloud segmentation step was inspired largely by Oude Elberink and Vosselman [2009] and Boyko and Funkhouser [2011]. The cross-section based edge detection workflow was inspired by curb detection-related work, such as Yang et al. [2013] and the methods of the commercial implementation. The use of 2.5D-based modelling methods to represent surfaces extracted from the point cloud comes from Oude Elberink and Vosselman [2006]. The active contour-based workflow was inspired by Boyko and Funkhouser [2011] and Göpfert et al. [2011]. In a way, my work can also be interpreted as a study of the effectiveness of relevant methods commonly found in the literature.

3.2.2 Dependency of methods on specific datasets

In this report I commonly refer to **DTB** as a *support dataset*. This is in part due to it being secondary to **AHN3** in my research, because its spatial coverage is vastly inferior to **AHN3** and it could not, by itself, fulfil the role **AHN3** was given in this project. For the same reason, I often call **AHN3** the *primary dataset*. **AHN3** contains enough data to make it possible to run the pipeline in the complete absence of **DTB**. **DTB** merely improves the effectiveness of the Lidar segmentation step in areas around occluding objects.

The main reason why I often refer to the two elevation sources in such a way, is that it describes their *roles* rather than their exact *identity*. For the same reason, I also often refer to **NWB** simply as the *road network*. This is in line with my goal to make my methods as independent from the exact identity and properties of the input datasets as possible. Most parts of my methods should work regardless of the exact datasets used, as long as a few assumptions are satisfied. For instance, the primary Lidar dataset needs to be accurately classified, in particular vegetation should be clearly isolated from ground reflections. The assumptions regarding the primary dataset are detailed in Section 3.4. **DTB** could also be replaced with any generic dataset that contains accurate 3D geometries representing the surfaces of the relevant roads – or better still, with **MLS** data providing coverage where the primary **ALS** one does not.

The main concerns regarding generalisation (how well the methods and the implementation work independently from the properties of the datasets) are not related to the input datasets, but to the parametrisation of certain parts of the implementation. While many such parameters are exposed as arguments and can be customised by the user, there are also some that are hard-coded to avoid creating an application programming interface (**API**) with an inconveniently long list of arguments. While the default parametrisation works in all the study areas of this project, there is no guarantee that they would always work equally well with other datasets – especially with ones containing road networks

that possess different properties than that of The Netherlands (e.g. mountainous areas). However, being an open-source, proof-of-concept software, there is nothing to prevent potential reusers of my code from adapting it to their needs, including making changes to the fixed parametrisation.

3.2.3 A note on DTB's role

In my research proposal, no specific mention was made about the role intended for DTB, but a section was dedicated to speculating about potential uses. The evolution of its role in the final implementation was entirely up to the iterative refinement of the methods. In the end, the deciding factor was that I found it to be useful for patching in gaps in AHN3 coverage, which is how the roles of primary and secondary dataset for AHN3 and DTB came about.

Among potential uses I speculated about before starting the development was the use of DTB as a means of contributing to edge estimation or optimisation, and to the lateral refinement of NWB positions. However, I found DTB road markings to be missing most commonly in the exact locations where they could have contributed to these steps, for instance in sharp bends.

Using DTB as a secondary dataset with the sole intention of characterising occluded road surfaces also generalises better, as the previous section makes clear. Consultations with NDW also suggested that they are in the position to commission the survey of additional georeferenced points or lines from Kragten (via a vehicle on which which commercial GNSS systems are mounted) or to purchase MLS data from Cyclomedia. Unlike DTB, such new data would *not* necessarily be restricted to modelling specific road markings.

These circumstances are what prompted me to treat DTB in a more generic manner, and to then extend this mindset to the way the rest of the datasets are used in my methods.

3.2.4 Accuracy assessment of processing steps

As I already emphasised, it was among the aims of this research to perform the 3D conversion of NWB in a way that output accuracy is as close to the input accuracy as possible, and that it can be evidenced and quantified either for the process as a whole, or for each output vertex individually.

As the literature review results in Chapter 2 already indicated, there are various ways to go about this problem. The first and foremost decision one needs to make is whether an empirical or a theoretical approach is better suited to the given procedure. For this research, both appeared equally suitable. I first attempted an empirical approach, but having produced uncharacteristic results using this approach, I eventually settled on a combination of simple decision-making logics (based on certain assumptions) and a theoretical, mathematical framework. I will provide the details about the procedures later in this chapter, in Section 3.4.

Below, I will outline the general approach, and the assumptions that are made when using it.

Assumptions about influences

My system interpolates the output elevations from TIN models whose vertices are the Lidar road surface measurements themselves. I opted for this approach specifically because my literature review indicated that interpolating in such a DTM appears to be the best option for large-scale terrain as well as in terms of preserving accuracy, and because – assuming perfect ground filtering – it introduces no errors relative to the original Lidar data. However, as I explained in Section 2.2, the output accuracy in such a process is a factor of not only the generated DTM and the interpolation technique used, but also of local, external factors. I made a range of assumptions regarding these influences before proceeding to the accuracy estimation step, which I will explain below.

The first factor to consider is the local *accuracy of ground filtering*. In this project, most of the Lidar data was already ground filtered, as I made use of the excellent stock classifications that are present in AHN3

(please refer to Section 2.3.2 for more information). There is one exception to this rule: roads found on bridges are classified in AHN3 as bridges themselves, including all objects on the roads such as guardrails and vehicles. Using the bridge classification also added objects over other roads elsewhere (such as motorway signs), which locally violate the assumption that the road surfaces are ground-filtered.

However, the Lidar segmentation step removes most non-road reflections automatically in the few places where they occur, and any remaining ones are eliminated by the careful conditional insertions of the TIN construction step. The number of outliers in the TINs is so small, that if we make the assumption that we only wish to interpolate elevations along the centrelines of road surfaces (i.e. that NWB is correctly georeferenced), we may regard the theoretical ground filtering effectiveness to be 100%. As a result, the influence of non-road reflections (outliers on road surfaces) need not be considered in the accuracy assessment.

The second factor to consider is the local sampling density of the Lidar points (and DTB, where it was used in place of AHN3). The assumption I made here is that as long as TINs locally conform with the theoretical minimum sampling density required to characterise a flat surface without impacting accuracy, the output accuracy will not suffer from any detrimental effects. I implemented simple logics to detect where interpolation has taken place in a location where the sampling density drops below this level. Vertices interpolated in such places do not receive an output accuracy value, and are thus flagged as having *undetermined* accuracy. The details regarding the identification of a suitable local density threshold is found in Section 3.4.1 later in this chapter.

This second assumption holds, because in well-sampled areas, literature indicates sampling density to have little to no correlation with empirically-derived error. In such areas, oversampling already occurs at point densities far lower than what is typical of AHN3 on road surfaces, apart from places where there are gaps in the data. Hence, I deemed a simple threshold-based evaluation sufficient to deal with the influence of this factor. I made this decision in view of the results of my empirical accuracy assessment results, which also indicated no correlation between sampling density and TIN model accuracy (see Section 4.3.1 for the details).

The last external influence to consider is that, which is caused by terrain slope and ruggedness. Relevant literature discussed this topic also in the context of local sampling density. because local elevation variations that the ruggedness introduces may not be captured adequately if the sampling density is also low there. Road surfaces are, however, smooth and well-sampled in AHN3. Furthermore, even inclined roads in our datasets are always characterised by smooth, gradual slope transitions – which makes sense, considering that both the motorways and the provincial roads we are working with have high speed limits. The effects of local curvature on accuracy in this case may be neglected.

This combination of factors and assumptions lead me to implement an accuracy assessment workflow that either deems the accuracy to be undetermined (where sampling density is very low) or computes its accuracy solely based on the principles of error propagation through TIN-linear interpolation. This error propagation method predicts an *increase* in the the standard error relative to that of the input for surfaces that are not very steeply inclined.

Influence of prior steps

It may appear to the reader as odd that it is almost only the last two pipeline steps that are discussed above in terms of what defines output accuracy. The reason behind this is that the TINs are constructed entirely of AHN3 (and rarely, DTB) points, thus making the standard vertical and horizontal error of each TIN node known. If the TINs were constructed from points which are themselves “secondary information” (i.e. derived information) relative to the input, then the estimation of output accuracy would be more involved. However, this is not the case in my pipeline – and therefore, wherever the above three assumptions hold, the sampling density and the interpolation technique define the output accuracy alone.

The rest of the pipeline steps only affect whether my assumptions are violated in a certain place or not. In particular, they may affect the local density of vertices in the TINs, including whether it exists at the location of interpolation or not. If we focus only on the influence of processing steps (i.e. we ignore the

3 Methodology and methods

effects of physical factors and problems with the data), this may for instance be the result of a very poor polynomial fit in the preliminary elevation estimation step causing Lidar segmentation to fail locally, or the rare cases where preliminary edge estimation fails too many times in a row. Such blunders may cause issues in the TINs, but these will be picked up by the logics and classified as unreliable accordingly.

Furthermore, we must also consider the fact that DTB is densified prior to being converted to a pseudo-point-cloud. This is important because DTB's accuracy is defined in terms of its vertices, it does not apply directly to the line segments connecting them. For simplicity, I did not specifically consider how DTB's measurement error propagates to the densified vertices because if we considered such details regarding DTB, then we would also need to consider its *temporal* inaccuracy, which affects older DTB geometry significantly. Since subsidence and potential other vertical land motions do not affect all areas uniformly, we cannot draw a simple relationship between the local age of the DTB data and its accuracy without relying on external data – such an analysis was not within the scope of this research. Furthermore, such an assessment may not apply to other support datasets.

In another words, in this proof-of-concept implementation, DTB merely *simulates* a reliable support dataset, as DTB itself does *not* represent one. It is treated like an MLS dataset, and its accuracy is also evaluated on the same basis. Users *specifically* interested in the accuracy of the output when using DTB should consider all output elevations marked as originating from DTB data to be unreliable, and to certainly not confirm with the requirements of the noise regulations – even if the threshold-based evaluation does not indicate a missing accuracy value.

Linear interpolation accuracy

In road surfaces not covered by the TINs, NWB elevations are interpolated *linearly* inside the NBRs at the end of the last pipeline step. This generally occurs under large occluding features (such as bridges), in the case of short road segments that are very poorly georeferenced in NWB, and occasionally, in places where large vehicles or dense vegetation resulted in the models not covering the entire road surface.

A typical, practical example is as follows: the Lidar segmentation workflow encounters a bridge with no AHN3 or DTB coverage underneath. It splits the NBRs into two parts, one extending to the last NWB vertex before the bridge, and the other starting at the first NWB vertex after it. TINs are constructed for the two NBRs parts, but not in the space between them, i.e. underneath the bridge. The vertices in-between the two NBRs parts (most likely 5-10 of them depending on the width of the bridge and the densification threshold used) will receive elevations that are linearly interpolated based on the closest elevations in the NBRs that were successfully interpolated in the TINs of the two NBRs parts.

The output accuracy of these points is also not estimated. The primary reason for this decision is that the local sampling density is effectively zero. Since we do not estimate the accuracy in places with low sampling densities, it is justified to also not do it where the sampling is zero. In such places, formal accuracy can be safely assumed to be worse than that which is required by NDW and the noise regulations. On the other hand, roads are not expected to change elevation significantly over short lengths of missing data, since certain maximum internal angles apply to their construction plans. I leave it up to the users of my output data to decide, what part, if any, of the linearly interpolated elevations they wish to consider usable.

To summarise, elevations marked as having been linearly interpolated always have undefined accuracy. However, undefined accuracy may also correspond to elevations that were interpolated from a TIN, but where the local TIN vertex density was too low to trust the value.

3.3 Detailed methods

Previous sections of this chapter described the methods underlying the pipeline steps in general terms. This section will go into more detail about the underlying algorithms. The level of detail will be greater than in previous sections, but not to the point where every step in the code is explained. Features of the implementation that are of a technical nature are not generally included – the reader is referred to

Geometric algorithm

This algorithm first creates a topological data structure from the input *wegvakken*. Each *wegvak* is a valid `LineString`, i.e. a connected series of line segments, which can be a few metres long or even hundreds of metres long. From here on in this section, I will consistently refer to *wegvakken* as `LineString` objects to make the description more general. The topological data structure records which `LineStrings` of the road network start and end in which intersections. As this algorithm is not allowed to use the pre-made `NWB` intersections from the attribute table, intersections are defined based on their coordinates, rounded to one decimal. The topological data structure is based on hashing, hence it has good performance despite its reliance on coordinate-based lookup. The procedure consists of examining both ends of each input `LineString` and either creating a new intersection with it (if one does not exist at that location yet), or adding a reference to it in the intersection that is already found in the topological data structure. This is shown on the left in Figure 3.3.

The next step is to iteratively nucleate `NBRS` generation until no unclassified `LineString` objects remain. The algorithm takes one `LineString`, initialises an `NBRS` with it, and then attempts to extend it with further `LineStrings` on both ends. First, recursive extension is initiated on the last vertex of the `LineString`, and once that has completed, on its first vertex. The recursion examines the vertex, uses the topological data structure to find connected `LineStrings` and to connect one of them if certain conditions are met. Then, it progresses deeper into the recursion by doing the same with the `LineString` it just connected. The recursion ends when no more suitable “extensions” can be found.

When the search for connected `LineStrings` succeeds in the above recursion, either a single one or multiple ones may be found. The latter corresponds to reaching a real-life intersection, in which case the algorithm needs to decide which one to connect based on a set of geometric conditions. First, the angles between the last line segment of the previous `LineString` and the first line segment of all the candidate `LineStrings` are examined, and the one with the angle corresponding to the straightest possible continuation of the road is selected. A composite geometry of the pre-existing `NBRS` and the new segment is then created and tested for self-intersections. If the composite geometry fails this test, the next best candidate is examined, and so on until a candidate succeeds, or the iteration runs out of candidates – in which case none of the candidates are accepted and the recursion terminates. When both recursions (starting from the first and last vertices of the `LineString` that nucleated the `NBRS`) have finished, the `NBRS` is deemed complete and the next `NBRS` is nucleated. The self-intersection test is also performed when only one connected `LineString` is found, i.e. not only when an intersection is encountered.

Semantic algorithm

The semantic algorithm is built on the same framework as the geometric one, as it is intended as a comparable alternative to the geometric one. Most steps of the procedure are slightly modified equivalents of the ones in the geometric algorithm, hence here I will focus on describing the differences.

The topological data structure of the semantic algorithm is based on the *junctie* (intersection) ID number (`JTE ID`) records found in `NWB`, which are unique identification codes belonging to each intersection of `LineStrings` in the dataset (including those of only *two* `LineStrings`, i.e. not real intersections). Each `LineString` possesses an “end `JTE ID`” and a “beginning `JTE ID`” which are used to assemble the navigation structure in place of the coordinates in the geometric algorithm. The `JTE IDs` can be used to represent the topology of the dataset entirely, without any consideration for the geometry – indeed, it often describes topology more accurately than the geometry itself.

The nucleation of `NBRS` takes place in a similar manner to the geometric approach, but here each `NBRS` is associated with a specific *wegnummer* (road number) and `BST` code (a code related to the role of each road). `LineStrings` are only joined to an `NBRS` if they have matching road numbers *and* `BST` codes, which is what the text *check attribute data* in the flowchart refers to. The candidates are still processed in the order of decreasing angle optimality, like in the geometric algorithm. However, the composite geometries need not be checked for self-intersections, as roads satisfying the semantic conditions do not self-intersect in real life. This improves performance, as the intersection and validity checks of the

resulting geometry is costly in terms of computational complexity. This shortcut is indicated by the dashed path labelled *bypass* in Figure 3.3.

Challenges encountered

I encountered three distinct issues while I was developing this part of the software. The first problem was that while *NWB* has a near-perfect topological (graph) structure in its attribute table (represented by the *JTE IDs*), the same topology is not always represented by the geometry due to small-scale georeferencing issues. This means that the topology suggested by the geometry does not necessarily map to the *JTE IDs* exactly. In particular, *LineStrings* (*wegvakken*) that are connected according to the attribute table may occasionally have disjoint or even overlapping geometries, which originally caused my software not to be able to merge them into the same *NBRS*. Fortunately, once I started using the coordinate-based topological structure, I discovered that reducing the coordinate precision to only one decimal solved the issue in most places by effectively “snapping” the *LineStrings* together. This type of snapping is often referred to as “grid-snapping” in *GIS*, because the rounding procedure effectively defines grid nodes to which the vertices of the lines are snapped. It is suitable and effective in this application because corresponding vertices in different *LineStrings* are usually displaced by distances far smaller than the 10 cm size of the grid cells that define the topological structure generated from the coordinates.

A second issue was that the geometry of *wegvakken* often *reverses* in the middle of a connected series of *LineStrings*, requiring the implementation of a workaround in the code that computes the angles. The implementation now recognises where the geometry is stored in a reversed order relative to the *JTE IDs* and adjusts the angle computation accordingly. Lastly, for reasons related to external requirements that *NWB* needs to meet, motorway ramps are connected to motorway lanes at unrealistic angles, occasionally causing the algorithm to merge ramps with motorway lanes and vice-versa. A dedicated workaround was also necessary here, to recognise this specific situation and to treat it correctly. This concerns the same issue that was shown in Figure 2.9 in the top right image.

3.3.2 Elevation estimation

The elevation estimation stage of the pipeline consists of two operations. The first operation is to associate each *NBRS* vertex with a preliminary elevation estimate based solely on nearby Lidar points, and the second is a refinement step to eliminate occlusion-related artefacts. The procedure is illustrated by the flowchart in Figure 3.4, as well as the vector graphics in Figure 3.5.

Initial elevation estimation

The process starts by importing *AHN3*, from where elevations are primarily be derived. It is assumed that the input file is sufficiently small to allow in-memory use, i.e. that it is a cropped or clipped version of the full point cloud tile. Thus, this is the point in the procedure, where a global scaling solution would be most important. All other parts of the program work on the basis of processing subdivisions of the road network independently (*NBRS* or the underlying *LineStrings* themselves), which is already a good starting point for scaling.

The imported point cloud is first converted into a 2D KD-tree, so that area-based queries can be performed efficiently on it. Then, points closer than a certain distance are fetched for each *NBRS* vertex. The median elevation of the nearby Lidar points of each *NBRS* vertex is then computed as a representative elevation estimate. Where too few points are found, the elevation is instead marked to be missing.

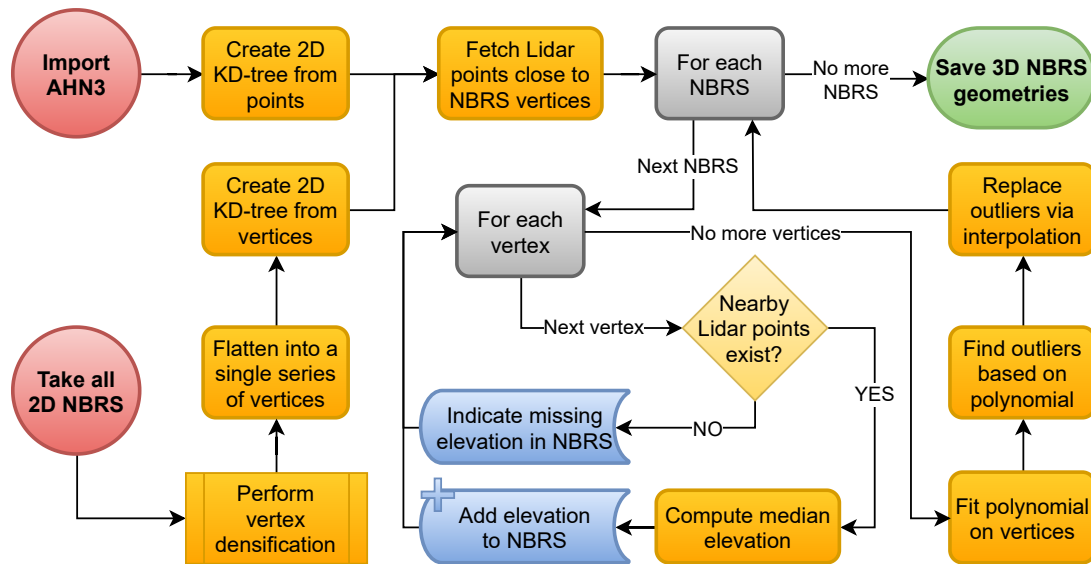


Figure 3.4: Flowchart illustration of the elevation estimation step of the pipeline.

Refining the preliminary elevations

Following this step, each of the 3D-enriched **NBRS** are fed into an outlier-filtering algorithm. The algorithm generates a distance series based on the horizontal coordinates of the **NBRS** and associates them with the preliminary elevations (thereby converting the **NBRS** into a 2D profile). It then fits a fixed-degree polynomial on the profile. Since occlusion is almost always represented by short-wavelength data gaps or positive outliers in the Lidar data, these vertices are easy to isolate. The former is explicitly marked in the elevation series, while the latter show up as local clusters of large errors relative to the polynomial model. The single outlier on the left in Figure 3.5 is an example of the former, while the bridge-related outliers represent an example of the latter type. Please note that although the polynomial fit in the illustration is shown on the road, in truth they are not georeferenced (they are just elevation profiles).

By interpolating values in such places, the quality of the preliminary elevations is improved considerably. The steps of this procedure are shown on the right in Figure 3.4. The replacement values are interpolated *linearly* based on the series of inlier vertices, i.e. they are not determined by the polynomial fits. The reason for this is, that it is not always possible to find good fits using fixed-degree polynomials, and while the polynomial model is almost always good enough to *detect* outliers, its values are not conformant enough to *replace* the original or missing elevations with. The replacement vertices and segments are shown in blue in Figure 3.5.

This polynomial-fitting approach is reused in various subsequent parts of the implementation. It is similar to the approach in [Boyko and Funkhouser \[2011\]](#), but it simplifies the global optimisation of splines into individual polynomial fits. Adapting the exact approach proposed in that research would certainly improve the effectiveness of my methods somewhat, but not drastically – I implemented subsequent steps in a way that they can deal with occasional mediocre-quality fits, and my results do not indicate that implementing a more sophisticated algorithm is justified.

Vertex densification

Although it is not strictly related to **NBRS** generation, vertex densification is not listed as a discrete pipeline step as it is a rather trivial operation. It is only presented in this report as a pre-processing operation of preliminary elevation estimation. It is shown in 3.4 as the first processing step that acts on 2D **NBRS**.

Elevation estimation

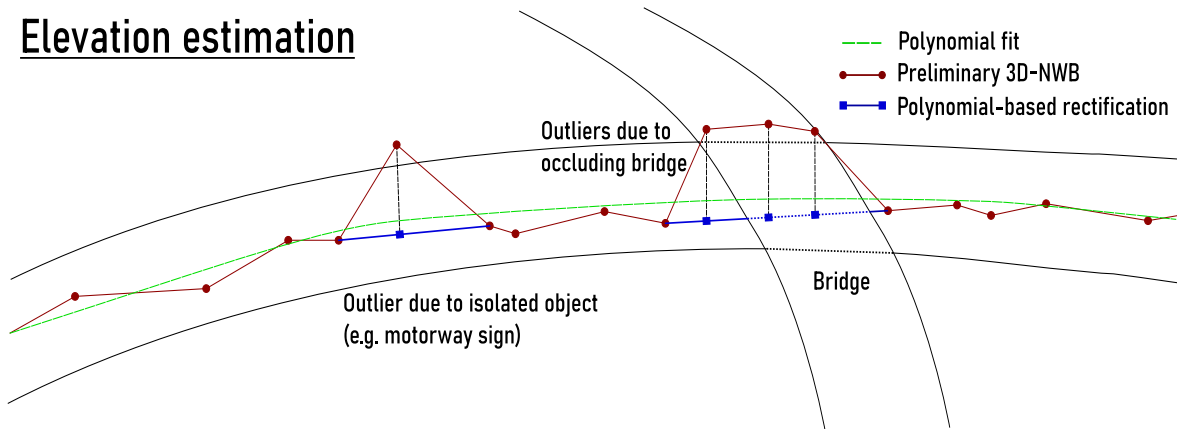


Figure 3.5: This illustration shows the main components of the elevation estimation step. The raw, Lidar-derived elevations of the vertices are shown in red, while the derived polynomial is shown in green. Non-conformant vertices are replaced in the refinement step, which is shown by the blue line segments and vertices.

Vertex densification of the **NBRS** refers to the operation of taking the **LineStrings** that make up each **NBRS**, and adding vertices to their line segments until no distance between the vertices is bigger than a certain threshold. In my implementation, this takes place as a recursion. Each **LineString** of each **NBRS** is considered, and the densification algorithm is called on each line segment. The recursion consists of breaking the line segment in two halves if it does not comply with the threshold (a vertex is added in the middle), and then proceeding deeper into the recursion by doing the same with the two resulting halves. The densified geometries are assembled when returning from the frames opened by the recursion.

Like **NBRS** generation, vertex densification is done for the benefit of subsequent operations. Many operations – such as preliminary elevation estimation – act on individual vertices, gathering information related to them from their **AHN3** and **DTB** neighbourhoods. Since the posting distance of **AHN3** is several magnitudes smaller than the length of the line segments of **NWB** **LineStrings**, increasing the density of **NWB**'s vertices has practical benefits. It not only increases the resolution at which elevation can be sampled, but it also means that large-scale trends in the data will be represented more dominantly, i.e. algorithms will be better able to tell which parts of the road represent the road surface, and which ones are outliers due to occlusion. The practical benefits of this step were observed during development, and vertex densification was made an intrinsic part of various other parts of the pipeline too.

Challenges encountered

The main challenge encountered was related to the random reversals of **LineStrings** (*wegvakken*) that I already mentioned in Section 3.3.1. At this point, I needed to implement a workaround that flips reversed *wegvakken* into the correct orientation before moving on to the polynomial fitting step. In fact, it is the polynomial fitting step that had first drawn my attention to this problem, as it was impossible to get it to work before realising that parts of the 2D profiles contained vertices in the wrong order. The rectification of the orientation of the geometries takes place relative to the first **LineString** in the **NBRS**. These are then rotated back into their original orientations after the refinement step, to avoid introducing changes to the 2D geometry of **NWB**.

A second challenge was to find a good benchmark of what to consider outliers after fitting polynomials. I needed to choose a metric that works well with all the types of typical occlusion-related artefacts that show up in the data, such as overlying bridges of various heights, civil engineering structures of such bridges next to and above roads, motorway signs, tunnels, and so on. After experimenting with various approaches, I settled on one that involves setting the threshold dynamically, as a multiple of the standard deviation of the residuals between the initial elevation estimates and the polynomial-based elevations. Where the standard deviation is smaller than a certain threshold, I artificially raise it to a preset minimum to avoid performing linear interpolation where the conformance is very good.

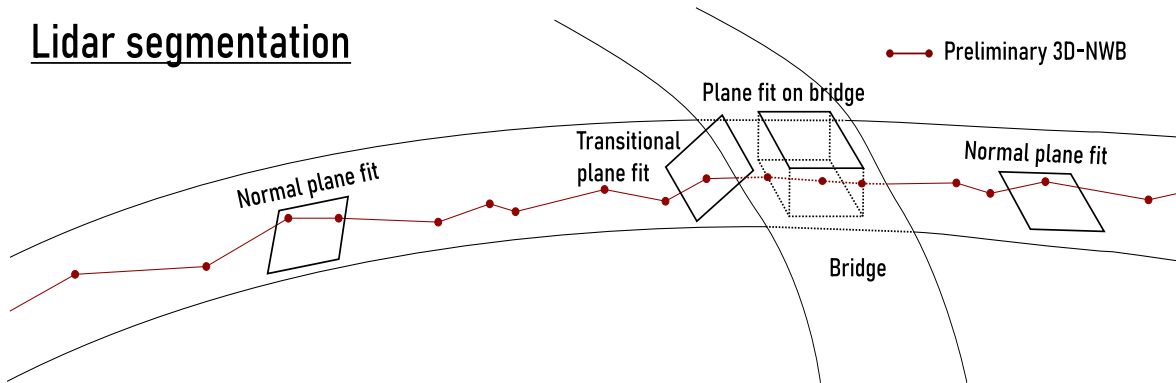


Figure 3.7: This figure illustrates the plane-fitting step of the Lidar segmentation procedure. In the case of well-exposed roads, the fitted planes lie on the respective road surfaces (“normal plane fits”). Where complete occlusion occurs, the plane will be shifted to the elevation of the occluding object, such as a bridge (“plane fit on bridge”). In the case of partial occlusion, the plane will be shifted moderately relative to the true road surface, and potentially tilted (“transitional plane fit”).

Refining plane fits and pre-selecting points

Next, the program considers the vertices of each **NBR**s one by one, in the order in which the vertices geometrically represent a valid road centreline. The program searches procedurally for places where the succession of fitted planes may indicate a break in shape of the surface. At the beginning of the iteration, the program initialises three variables describing the *previous* plane fit’s relative position to the 3D **NBR**s centreline, the median elevation of the relevant patch’s Lidar points, and the standard deviation of their distances to the fitted plane. By examining variations in these metrics, the algorithm can detect where the plane fits start to become unstable, such as where a plane is labelled “transitional plane fit” in Figure 3.7. The algorithm always compares the metrics of the current iteration to the ones from the previous iteration. Significant changes relative to the previous vertex and plane may indicate the presence of objects occluding the sensor’s view of the road’s surface. I determined the exact metrics and parameters (thresholds) to detect “plane instability” based on experimentation and iterative refinement. The current setup works well with all testing datasets examined. This step is represented in the flowchart by the conditional element labelled “*Instability detected?*”.

Originally, the algorithm was configured to automatically revert to the previous plane in case of plane instability and be allowed to use the reverted plane for a few iterations before asking help from the support dataset, in case the road emerged from underneath the occluding object after a few iterations at roughly the same elevation at which it disappeared. If the support dataset could also not help (due to e.g. a lack of coverage) after the expiration of the tolerance period, the algorithm would “give up” and move on to the next **NBR**s. This meant that long occluding objects and no **DTB** coverage could prevent the algorithm from processing certain **NBR**s, for instance ones containing tunnels.

Handling breaks in the trend and missing data

The final algorithm is only allowed to attempt to use the previous plane fit *once* before it attempts to use **DTB**. The point cloud generated from **DTB** contains road surface measurements only, so it can be relied on to provide “assistance” where **AHN3** is ambiguous. If a previous valid plane exists, then **DTB** is queried for points relatively close to it. If not, then the centre of the query becomes the current **NBR**s vertex itself.

If a reasonable number of **DTB** points are found, the process is repeated by performing a second KD-tree query on the centroid of these **DTB** points, and the plane is then re-fitted onto the returned points. The second query ensures that as many useful **DTB** points are included as possible. The program then assesses the distribution of **AHN3** Lidar points in the patch close to the re-fitted plane, and if the majority

3 Methodology and methods

are found to be conformant with it, then the plane is re-fitted a second time to make sure that in the end it is based on the Lidar points and not the support data wherever possible. The necessity of this last step is related to the temporal problems with *DTB* already mentioned in Section 2.3.3.

In the new version of the algorithm, the program does not declare failure if it is no longer allowed to revert the current plane to the previous one, and also finds support data to be unreliable or missing. Instead, it simply relaxes its conditions and continues as though it were starting to process anew (i.e. as if it were initialising a *new NBRS*). This bypass allows the program to continue the procedure even if it is aware that there was a noticeable shift in the position of the fitted planes, or a gap in *AHN3* coverage. These areas are handled separately, outside of this iteration.

Each successful iteration of this algorithm finishes by pre-selecting those *AHN3* and *DTB* points which conform well with the final plane fit, and saves them as individual patches. The median elevation of the pre-selected points is saved, as it will be used in the next step.

The above iteration is shown as the loop labelled "For each *NBRS* vertex" in Figure 3.6. In the implementation, the nesting of the iterations is different, but this description is easier to understand and is fully equivalent to the implemented version in terms of what it achieves. The same is true about the top-level iteration ("For each *NBRS*" in the flowchart), which in the implementation is broken into several parts for programming convenience.

Breaking *NBRS* into parts

After the above iteration, a post-processing procedure is executed before moving on to the next *NBRS*. Based on the median elevations of the patches saved during the iteration, the program can once again generate 2D elevation profiles which it can examine for outliers. Missing elevations in the series are indicative of a lack of coverage in both *AHN3* and *DTB*. Outlier elevations indicate that the corresponding plane fit was corrupted by occluding features that caused occlusion or partial occlusion, and that it was also not possible to rectify the plane fit based on *DTB*.

Intervals inside each *NBRS* that are affected by neither of the above two problems are detected. Through this, a further subdivision of the road network is introduced: *NBRS parts*. Each part corresponds to an interval in its parent *NBRS* with reliable combined *AHN3* and *DTB* coverage.

The patches of *AHN3* and *DTB* points are then combined into a subcloud, one for each *NBRS* part, making sure not to add duplicate points (the same point may be part of multiple patches). A quick outlier filtering step is applied to them, to eliminate points which are isolated (have no neighbours within a certain distance). This is easy and computationally efficient to execute by converting the data into KD-trees and performing nearest-neighbour queries on them.

A hashed structure is initialised at this point in the program that allows the program to remember which points in the subclouds originated from the support dataset. The use of this structure is described in Section 3.3.7.

Challenges encountered

The above description already contains mentions of how my methods relating to treating breaks in the trend and missing data evolved. Here, I will further elaborate on this topic.

The simple approach of starting on one end of the *NBRS* and examining its vertices one by one turned out to have significant limitations when I began to debug my implementation with the testing datasets. As it has no concept of global trends in the *NBRS*, it can only rely on its previous iterations to detect breaks in the trend and to make decisions based on it. Because of this, in regions with occlusion-related or missing *AHN3* data *and* missing *DTB* coverage, significant problems could arise.

The original algorithm was capable of detecting where it ran into a data gap (or occluded area), but it was not always capable of continuing on the other side. Using the last valid plane from before the problematic region did not work reliably, because even a small erratic plane tilt could become large enough

Constructing edge point candidates

First, the subcloud of each NBRS part is used to create a 2D KD-tree. 2D suffices here, because it is a reasonable assumption to make that the subclouds of NBRS parts no longer have a significant number of points that violate the 2.5D assumption (e.g. reflections from occluding objects). On each vertex of each NBRS part, a cross-section is then constructed. Cross-sections are line segments roughly orthogonal to the centreline locally. Their azimuths are based on the mean azimuths of the two line segments that contain the given vertex, except for the first and last vertices, which are simply based on the azimuth of their single parent segment. The cross-sections are vertex-densified, and their densified vertices are used in a bulk KD-tree query. Lidar points close to cross-section vertices are thus identified, and the median elevation of each group is saved as the elevation of the given cross-section vertex. This step works on a small, sub-metre scale, meaning that using the native density of AHN3 (or using a moderate amount of thinning) is particularly important from here on.

Each cross-section then represents a 2D elevation profile, with the corresponding centreline vertex in the middle. A line fit for each is computed and outlier vertices are identified based on them. The program then tries to find suitable edge points among the inlier cross-section vertices on both sides of the centreline, in each cross-section. Together, these points will form the preliminary edges. In each of the cross-sections, the program starts from the outermost cross-section vertex and progresses inwards. Once a certain consecutive number of inliers is encountered (with no outliers in-between them), the program assumes having reached the road surface and flags the current vertex as the edge vertex. This is illustrated in the inset of Figure 3.9.

The total length of the cross-sections, which is a constant parameter, represents the maximum road width the program can work with. The optimal value of this parameter depends on the possible road dimensions in the given road network. If too small a value is used, the preliminary edges may lie too far inwards from the real-life edges, thereby excluding large parts of the real-life road surfaces as a result. If it is too large however, false positive hits outside the road surfaces will corrupt the preliminary edges, especially where roads are thin and other smooth surfaces are found in their surroundings.

Enforcing constraints

Flagged vertices are only accepted as edge vertices if they also pass a range of further conditions relating to a minimum road width, as well as sudden elevation changes and road width changes. The minimum road width is enforced for each pair of edge points individually. However, much like in the first part of the Lidar segmentation step, the latter two conditions are evaluated on the basis of comparing the metrics of the current edge point candidates to a mean value from a set number of previous iterations. Only if this verification procedure succeeds, does the program extend the NBRS part's preliminary edges with the new vertices.

In areas where the above procedure fails, "gaps" are created in the preliminary edges, because the cross-sections are skipped and the preliminary edges are not extended with new vertices. These are not real gaps in the sense that the last pair of edge points before the gap, and the first pair after, are still connected in the output – it simply means that there are no edge vertices locally. Compared to the artefacts that would appear in the absence of the above threshold enforcement procedure, creating small gaps is an acceptable compromise, especially if the NBRS were sufficiently vertex-densified prior to this step. An example of this behaviour is illustrated under the bridge in Figure 3.9.

Skipping too many cross-sections may cause various problems in later pipeline steps. To avoid this, a relaxation of the conditions takes place after a set number of skips. After relaxing the conditions, the first inlier point on both sides is selected when fitting the next cross-section with a line, and the constraint regarding sudden changes in width is also ignored. Immediately after a success, the constraints are re-enabled. This temporary relaxation allows the algorithm to regain its references when a sudden real-life change in the road's dimensions is encountered. It also helps in scenarios where the location of the edge is ambiguous.

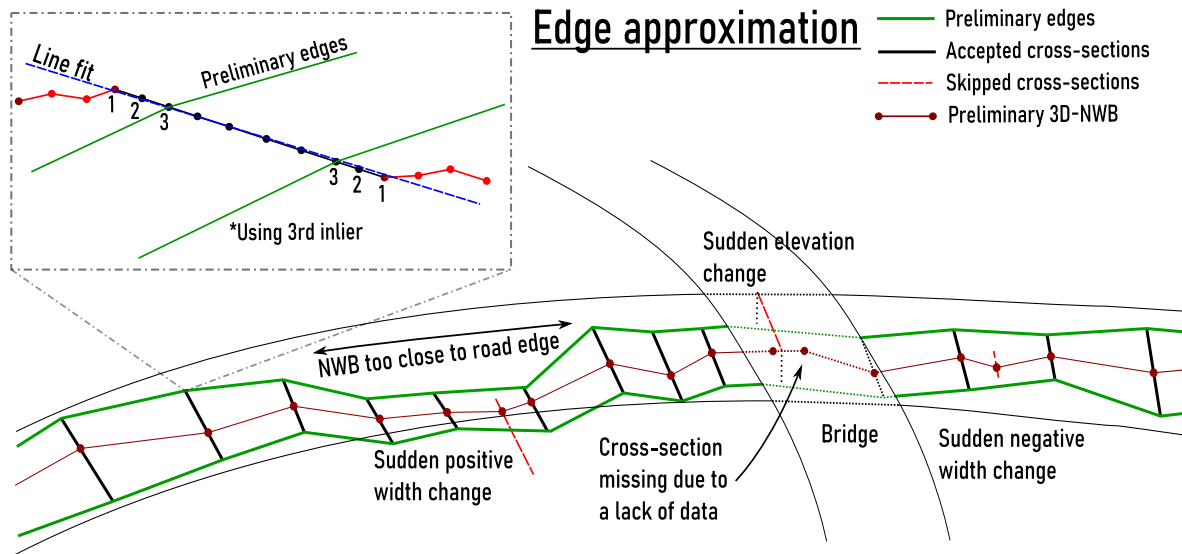


Figure 3.9: The edge approximation procedure is illustrated in this figure. The cross-sections are either accepted (black line segments) or skipped if they fail the threshold-based evaluations (red dashed line segments). They may fail to generate in the first place, if there is insufficient elevation data (under the bridge). The inset illustrates the details of the edge point identification sub-process.

Challenges encountered

Originally, this step was going to be a preparatory step for the sole purpose of providing initial edge shapes for the active contour optimisation algorithm. I first implemented it almost exactly to the specifications found in the research proposal. However, it soon became clear that better active contour optimisation results require better preliminary edge estimates, and thus I had to implement a range of tweaks and improvements in an iterative manner. It seemed that the best active contour optimisation results corresponded to where the preliminary edges were on the road surface, slightly inwards from the location of the real-life road edges. This is why the algorithm starts from the outer edges of the cross-sections, and progresses inwards until it can safely conclude that it has already been inside the road surface for at least a few vertices.

A further challenge corresponded to the point in development when I decided to make active contour optimisation optional. I needed to implement modifications to these methods to allow preliminary edges to be used for TIN construction directly, at the same time maintaining compatibility with active contour optimisation. This is what resulted in the addition of the system of constraint enforcement and constraint relaxation that takes place right before accepting a pair of edge point candidates. The main reason why this is beneficial for TIN construction is that it ensures that the edges cannot shrink too much, while also reducing the chances of road widths being overestimated due to small-scale issues.

The former ensures that road centrelines are found between the preliminary edges under normal circumstances, and with enough distance between them and the edges to ensure that Lidar points will be found there during the TIN initialisation step. Without this, it would be much more common for the TIN not to exist at the 2D positions of the NWB vertices. The latter (maximum road width) decreases the chances of including off-road points in the road surface models, both during TIN initialisation and extension. For more information about the TIN construction step, please refer to Section 3.3.6.

3.3.5 Active contour optimisation

The optimisation of preliminary edges is based on generating one attractor map for each NBRS part based on subcloud point normals, and running active contour optimisation to attract the preliminary edges to certain features in the attractor maps. The procedure is illustrated in Figure 3.10.

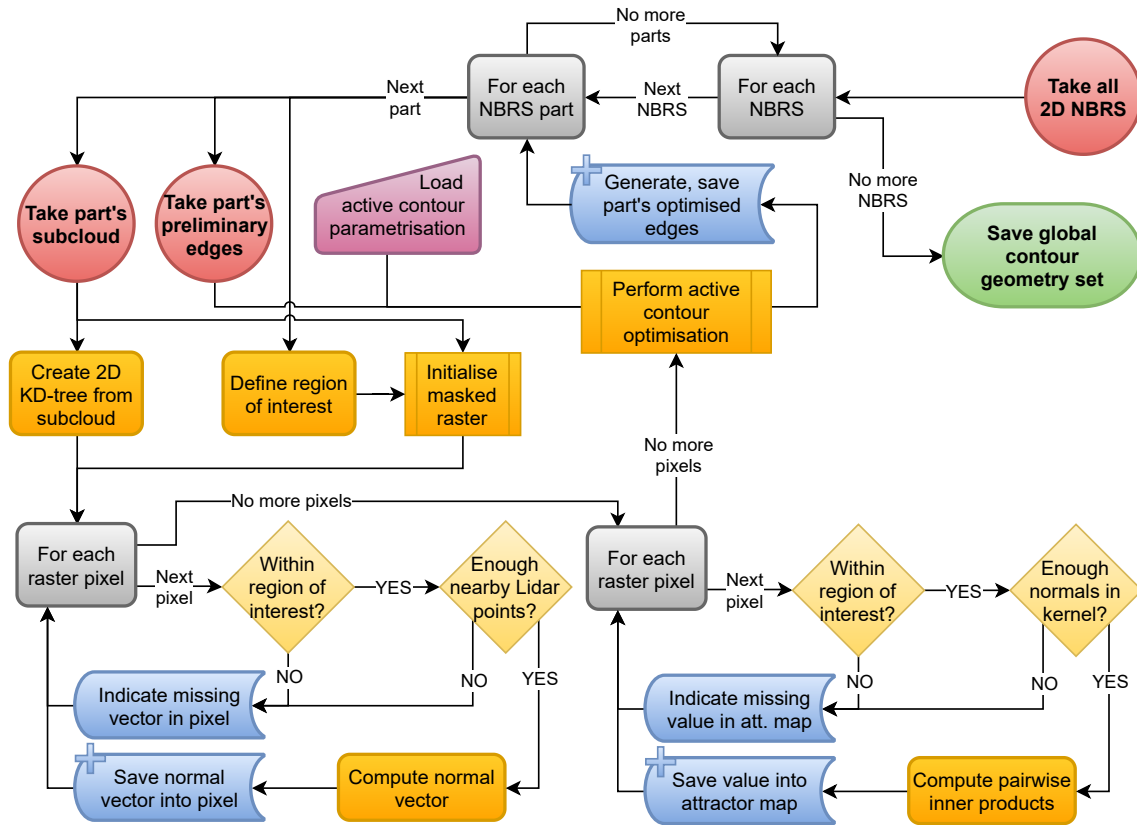


Figure 3.10: Flowchart illustration of the active contour optimisation step of the pipeline.

Attractor map generation

The procedure underlying this step is once again based on a 2D KD-tree of the subcloud of the **NBRS** part. 2D suffices because attractor maps are 2D rasters, and once again, because we are safe to assume at this point that the subclouds of **NBRS** parts mostly describe 2.5D surfaces. For each of the rasters, a region of interest is derived by buffering the appropriate centreline by a certain amount. The rectangle-shaped raster is then masked out everywhere except for pixels whose centres lie within the geographical region delineated by the buffer polygon.

The centre of each unmasked pixel is then used in a bulk KD-tree query to find a small patch of nearby Lidar points for each. Normals vectors are computer for pixels thus associated with a certain minimum number of neighbouring Lidar points. The normal vectors are based on the **MLE** plane fits of the Lidar patches.

Normal vectors can be stored in the pixels in my framework, but they cannot be used directly in active contour optimisation because it requires scalar pixel values. To derive these from the vectors, I designed a kernel-based approach. The pairwise inner products of the normal vectors falling into the moving window are computed, and the median of the value is saved. Since computing inner products is computationally expensive, not all pairwise combinations of the normal vectors in the kernel are dotted, only a representative random subset.

Running the optimisation algorithm

From here on, all operations take place in a temporary coordinate system which is defined simply in terms of the number of pixels in the X and Y dimensions from the top left corner. Before the preliminary edges can be overlain on the attractor map, they each need to be transformed into this coordinate

system via an affine transformation. Together with the attractor maps and a suitable parametrisation, the preliminary edges are now ready to be optimised. The optimisation algorithm is run separately for the edges on the two sides of the centreline, and the resulting optimised edges are then assembled into a single polygon.

The *scikit-image* implementation of active contour optimisation is based on the original paper in which this procedure was first described scientifically: Kass et al. [1988]. In addition to taking the attractor maps and the preliminary contours as input, it also takes a set of parameters that can be tweaked to manipulate aspects of the optimisation. The most important ones for us in this project are the parameters controlling contour smoothness, attraction to brightness or darkness, attraction to edges and the total number of allowed iterations. In Section 4.2.5 I describe the final configuration of values for these parameters.

Challenges encountered

In terms of the first version of my implementation, the main challenge here was the trial-and-error nature of getting active contour optimisation to perform acceptably for the wide variety of road geometries and attractor map features that are possible in our datasets. I needed to refine the parametrisation to work well with the input data, but since I was also producing the input data myself, I was also in the position to fine-tune that in turn. As a result, the task was a joint refinement procedure involving all prior steps in the pipeline leading up to this point.

Of all the aspects of the input data that I tried to optimise, I invested the greatest amount of effort in trying to pre-process the attractor maps to enhance their compatibility with contour optimisation. I tried various moving-window techniques such as many types of edge detection, edge enhancement, blurring, as well as morphological operations such as dilation, erosion, opening, closing, and many combinations thereof. I also tried compositing the resulting rasters. I eventually concluded that none of these operations can achieve a noticeable improvement in the results, with the original kernel-based normal vector attractor maps and the native edge detection of active contour optimisation still producing the best results.

Furthermore, I found active contour optimisation to work only at high raster resolutions, with a pixel size around 0.5 metre typically producing the best results overall. Unfortunately, computational complexity grows non-linearly with decreasing pixel size, making debugging and fine-tuning very difficult, as well as putting the usefulness of such an algorithm into question considering the scale of the input data.

A further problem I found is that there are occasional small-scale features in the input data that tend to confuse active contour optimisation. Even for relatively short iteration lengths, such small artefacts may unpredictably corrupt entire NBRS part contours. For instance, small Lidar gaps due to stationary vehicles frequently overlap with the region where the road edges are suspected to be found. Active contour optimisation has no concept of no-data pixels, and reacts unpredictably to these holes regardless of what one uses as filling values. Another similar issue is that road edges are often characterised by sudden slopes beyond their edges, but with further flat regions beyond them. This often creates a second contrast in brightness that active contour optimisation may confuse with the real road edge. Features such as these frequently draw the contours further from the roads than what would be acceptable to accurately classify Lidar points within the contours as road reflections.

Lastly, the effectiveness of the method is also far too reliant on the accuracy of the preliminary edges. The algorithm is sensitive to even the smallest of blunders in preliminary edge detection, and is also prone to fail in no-data regions due to large, occluding objects. After I implemented the code to split NBRS internally into parts where longer regions suffer from the absence of data, part of this issue was solved, but another remained: where DTB is available but not AHN3, preliminary edges tend to shrink significantly, which often corrupts the optimised edges.

While the method works and produces usable results, the poor quality of the output and its unreliability in general prompted me to make it possible to bypass its use in the software. This required modifications to various previous steps of the pipeline, as well as all subsequent ones – a significant challenge. This

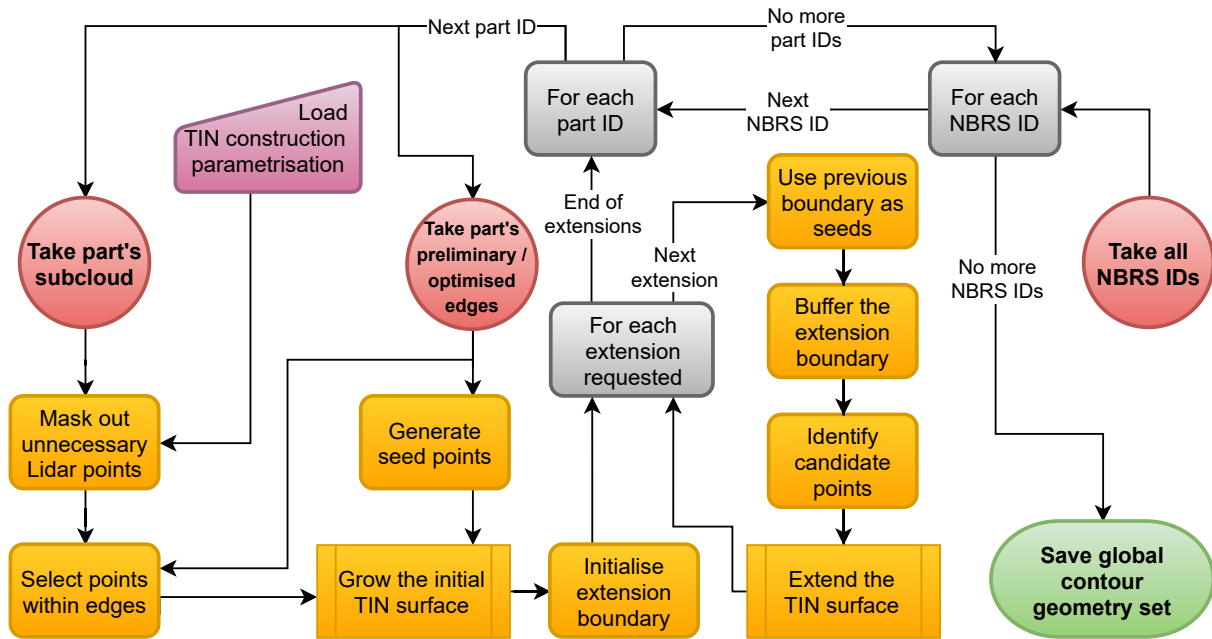


Figure 3.11: Flowchart overview of the TIN construction step of the pipeline.

bypass in turn puts into question the relevance of some of the pipeline structure, especially the parts that were intended to lay the groundwork for active contour optimisation, and to make use of its output. I elaborate on this topic further in Section 5.7.1.

3.3.6 TIN construction

As I noted in the previous section, various aspects of active contour optimisation were found to be lacking. The severity of the issues with this step prompted me to develop TIN construction in a way that enables it to function without active contour optimisation. Bypassing the active contour optimisation step altered the requirements that the TIN construction algorithm needs to satisfy.

In my planned pipeline, I made the assumption that points falling within the area of contours could be safely considered road points, and that conditional insertions would primarily be used to filter out any remaining *vertical* outliers. Working with preliminary edges (as well as *inaccurate* optimised edges) necessitates a less straightforward, but more robust implementation that is capable of telling apart road surface reflections and non-road reflections. The result is an algorithm that borrows ideas mainly from region growing and ground filtering algorithms.

The outermost iteration of the algorithm loops over NBRIS, and NBRIS parts are iterated one level below. In Figure 3.11 this is explicitly indicated as an iteration over NBRIS IDs and NBRIS part IDs respectively. In contrast with previous steps of the pipeline, the centrelines themselves are no longer used, hence the change of notation. The procedure is further illustrated by the vector graphics in Figure 3.12.

Preparation for TIN initialisation

Based on the parametrisation, the outermost boundary within which points will be considered for insertion (including TIN extension) is constructed as a polygon, and points falling outside of its interior are excluded from further consideration. Then, either the preliminary edges or the optimised edges are fetched for the given NBRIS part. Since they are almost identical structurally, they can be treated the same way.

They are used for two tasks: firstly, to construct a line halfway between the two edges to form the basis of seeding the TIN (the *seed line*), and secondly, to select points that fall between the edges as insertion candidates for the TIN initialisation step. This step is labelled “*Grow the initial TIN surface*” in Figure 3.11, marked as a pre-defined procedure because the underlying procedure is fairly complex. To keep the complexity of the flowchart manageable, both the TIN initialisation and the TIN extension workflows of this step are illustrated in a separate diagram, which shown in Figure 3.13.

TIN initialisation

TIN initialisation refers to the process of constructing an initial, conservative approximation of the road surface. As I noted above, it considers those Lidar points only, which fall between the preliminary or optimised edges. It first looks up those Lidar points, which are very close to the seed line that was derived from the preliminary or optimised edges. As these points are all but guaranteed to fall on the real-life road surface, they are unconditionally inserted into the TIN and are then pushed on a stack that I will refer to as the “buffer”. At this point in the algorithm, as Figure 3.13 shows, we leave the “*TIN initialisation*” group of operations and enter the “*Conditional insertions*” group (which is shared with “*TIN extension*”). The boundary vertices are also inserted into the TIN at this time (at an elevation of zero), which guarantees that conditional insertions always take place within the convex hull of an existing triangulation.

At this time, the TIN contains a high density of small triangles in the immediate vicinity of the seed line. It also contains larger triangles connecting this area with the insertion boundary (the preliminary or optimised edges). Lastly, it contains large triangles and sliver triangles on the convex sides of any bends in the given road, which are not necessarily connected to the insertion boundary, but which are also artefacts in the sense that they do not describe the road surface – they are simply a byproduct of using Delaunay triangulation.

The buffer at this point consists of all the seed points that were inserted unconditionally. It is used to query all the points between the edges in a bulk KD-tree query, and is then emptied. All points returned by the query are pushed on a stack, and this stack forms the basis for the conditional insertions. One by one, the candidate points are popped, and are conditionally inserted into the TIN. Figure 3.13 does not describe the conditions themselves, but I will go into detail about them here.

First, the triangle containing the popped point is located. Since the boundary is at an elevation of zero in the TIN, the program can easily identify when it is *growing* the Lidar-defined surface rather than just *refining* it, because one or more of the located triangle’s vertices may be found at an elevation of zero. If no such vertices are found, an additional test is performed to see if the triangle is large or has a long circumference, to further verify that the triangle describes the surface of the road, rather than being a meaningless “filler” triangle of the Delaunay triangulation. The seed points and refining/growing insertions are illustrated by circles of various colours in Figure 3.12.

In case of normal (refining) insertions, the elevation of the point according to the triangle is interpolated. A threshold applies to the difference between the real and the interpolated elevations of the point. If the threshold is not violated, then the angles between the triangle’s plane and the line segments connecting the point to the three vertices are computed. If any of the three angles violate the applicable threshold, the point is not inserted.

In case of a growing-type insertion, elevation difference is computed in a different way. Growing the TIN needs to be done with some caution, as introducing erratic points around the edges would entail that future insertions would have an incorrect basis for the conditional insertions and as a result, the surface would occasionally be allowed to grow in undesired directions. To minimise the chances of this, growing the surface takes into account multiple pre-existing TIN triangles in the neighbourhood, not just the one containing the point that is being considered. Specifically, all triangles containing the non-boundary vertices of the located triangle are fetched. Then, this is repeated with all the vertices of the resulting set of triangles. The vertices of this collection of nearby triangles are then fitted with a plane (re-using, once again, the MLE-based workflow), and the distance of the tested point to the plane is used for the threshold-based evaluation. The angle-based test is then administered the same way as

TIN Construction

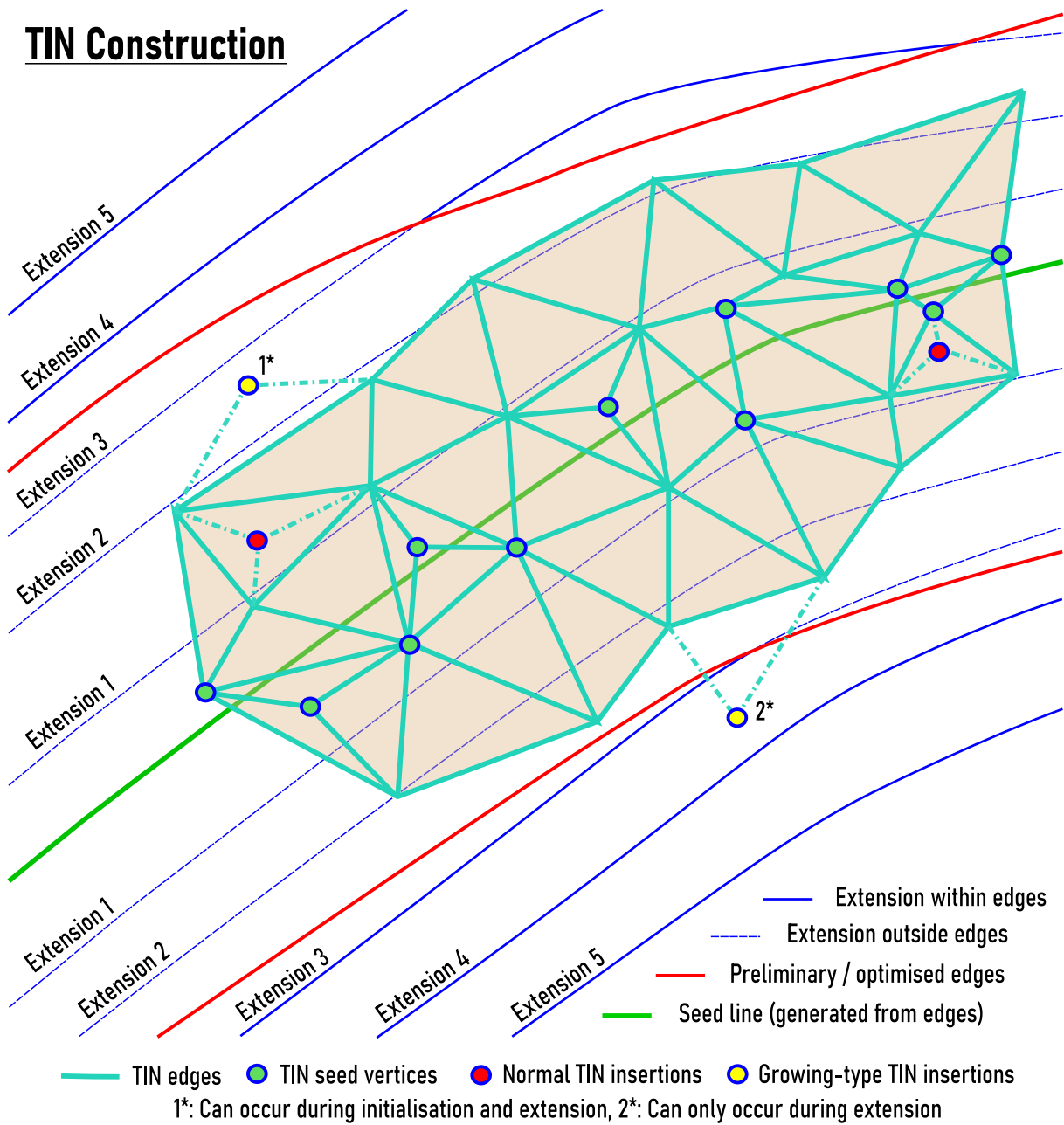


Figure 3.12: This figure illustrates the TIN construction step visually. In the initialisation step, the green seed line is constructed from the road edges, and it is used to insert the green seed points into the TIN. Further points are then inserted conditionally, and they may either refine (red points) or grow (yellow points) the triangulation. In the extension step, the algorithm progresses away from the seed line to further consider points for insertion. For instance, in the 3rd extension, the points between the lines labelled "extension 3" and "extension 4" on both sides on the seed line would be considered.

for regular insertions, except that the angles relative to any boundary vertices (which are at an elevation of zero) are ignored.

Each popped point that ends up being inserted into the TIN is also pushed onto the buffer, which was previously emptied after it had been used for the KD-tree query to fill the stack. Once the stack becomes empty, the procedure restarts by performing another KD-tree query using the buffer, and refilling the stack with new points to try to insert. Only those points from the spatial query results are considered, which are not part of the TIN yet. In other words, as long as points are being inserted, and these points have *uninserted* neighbours in the subcloud, the procedure will repeat. The buffer and the stack are kept separate so that KD-tree queries can be performed periodically as bulk operations, rather than individually – this is more efficient computationally.

Once there are no more uninserted neighbours to re-fill the buffer with, the iteration ends and returns all points inserted into the TIN, in the order they were inserted. The TIN itself is not kept, instead it is reconstructed later on – this is due to the fact that point deletions in the triangulation package *startin* do not appear to work reliably in this workflow, but we do not wish to keep the boundary points in the TIN either. The straightforward way to achieve this without point removal is by reconstructing the TIN with the subcloud points only.

While the final implementation of this step is not too complex, it is in fact the result of an experimental development process in which several previous versions of the design were implemented and discarded after I found them lacking in effectiveness. The final version of the TIN initialisation procedure is effective, and not too complex computationally owing to the buffering-based implementation of the spatial queries. Other than improving its performance via adding the buffer-based approach, I also needed to improve its reliability. Originally, I implemented TIN point removals to remove the insertion boundaries. In fact, in the first version of the implementation, I inserted points and then conditionally *removed* them depending on the geometry of the three triangles created upon insertion. However, as I mentioned above, I found that using point removals in practice made *startin* unstable, causing it to crash at random points in the process. However, from previous experience with this package, I knew that it is extremely efficient in building TINs and interpolating in them, owing to its Rust-based implementation. Ultimately, I made the choice to keep using *startin*, but to implement the workflow in a way that the conditional insertions are based on the pre-existing TIN layout, rather than that which results from inserting a candidate point. This is what necessitated inserting the preliminary or optimised edges in the TINs and carefully detecting when the TINs are being grown, and when they are being refined.

A further important performance consideration was to efficiently find Lidar points falling within the insertion boundaries prior to starting the insertions. I found that testing the points one-by-one using *shapely* takes an unacceptable toll on performance, hence I modified this procedure to work as a bulk task via the *path* module of *matplotlib*, which is capable of finding points within a polygon formed of a single ring of coordinates with much lower computational complexity.

TIN extension

The extension of the TIN takes place in an iterative manner. The implementation accepts arguments that set the amount by which the boundary should be buffered in each iteration, as well as the number of extension iterations (steps). The starting boundary is *not* the same as the one used during the initialisation of the TIN. There, the preliminary or optimised edges were used, but here the first iteration's boundary is buffered from the seed line by a small distance. This allows the algorithm to take another look at the points between the edges in case it missed any good candidates during initialisation.

Depending on the parametrisation, the boundary may be buffered to examine areas *beyond* the preliminary or optimised edges. This allows the program to try to grow the surface into road surface areas which were not between the edges because of issues with the edges themselves. It is specifically intended to counteract the problem where road surfaces might get very thin where edge detection or optimisation significantly underestimated their width. Extension boundaries that result in this behaviour are illustrated by the blue dashed lines in Figure 3.12.

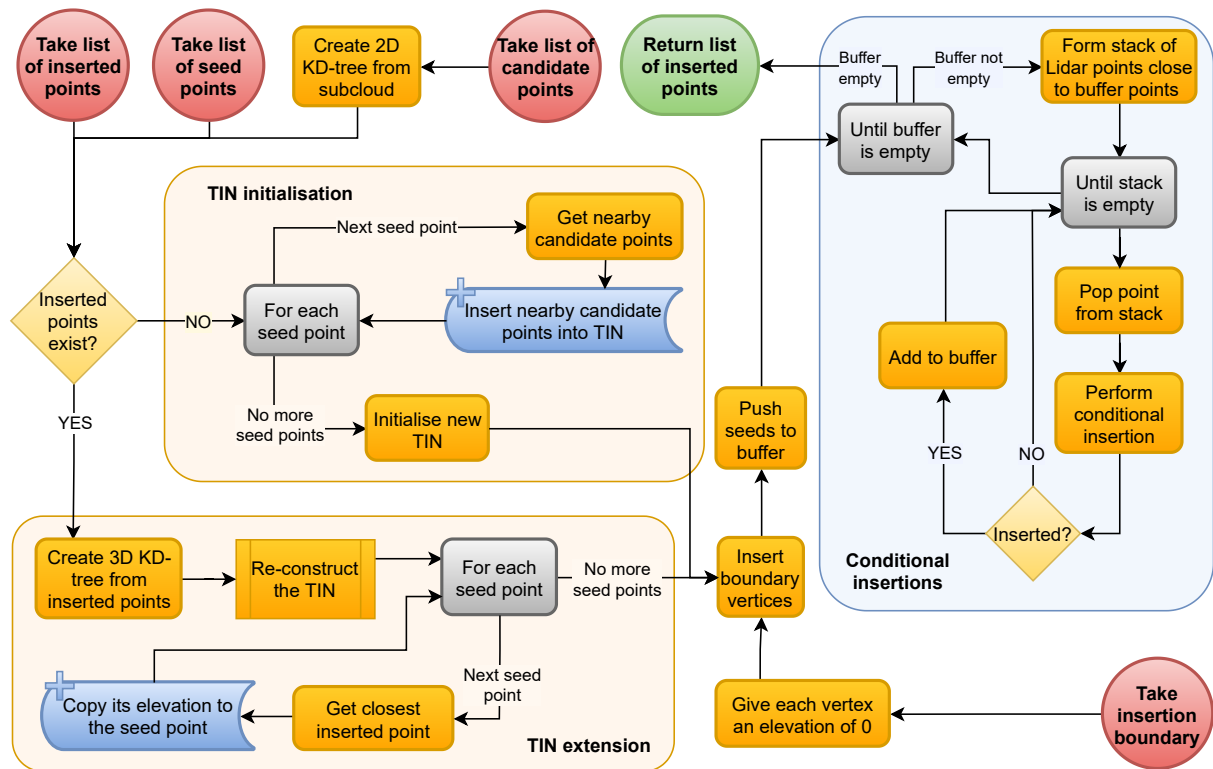


Figure 3.13: Flowchart illustration of the details of TIN initialisation and extension.

The seeding of extension iterations is different than that of the initialisation step. The seed points are always derived from the boundary used in the previous extension iteration (except for the first iteration). Furthermore, in TIN initialisation the candidate points included all points between the road edges, whereas in the extension steps only the points located between the previous and the current boundary (in 2D), are considered. Otherwise, the workflow is largely identical to TIN initialisation.

Each iteration first reconstructs the TIN yielded by the previous iteration, and inserts its new, buffered boundary into it. Since boundaries are always at an elevation of zero, when the previous iteration's boundary is reused to seed the current iteration, it first needs to be *transposed to 3D*, otherwise spatial queries based on it would not work. This is done by creating a KD-tree from all pre-existing TIN vertices and associating the closest one's elevation with each vertex of the 2D boundary geometry. It is then ready to seed the new iteration, by itself being the basis for KD-tree queries on the new candidate points. Naturally, the 3D points yielded by these seed-queries are not inserted into the TINs unconditionally like they were in TIN initialisation – they are simply pushed to the buffer to start the main iteration involving the conditional insertions.

Once TIN extension has finished, the final TIN is reconstructed and is saved. Thus, one TIN object per NBR part is saved, and these are not merged or joined together into a single TIN in any way.

Challenges encountered

As implementing such a complex algorithm in this pipeline step was not originally intended, the biggest challenge here was to come up with a good solution within the available timeframe. In terms of the methods themselves, I spent the most amount of effort on developing a solution that allows road surfaces to grow into regions not covered by the preliminary or optimised edges. While in all cases, the surfaces generated by TIN initialisation are adequate for the generation 3D-NWB, my desire was to not only model the central, traffic-occupied parts of the roads, but to grow the surfaces as close to the real-life edges of the paved surfaces as possible.

I initially wished to build TINs as a single growing operation, but this proved to be prone to spreading into off-road regions. Depending on what order certain groups of points are examined in, even relatively sharp breaks in the underlying surface may appear smooth. This is the reason why I eventually implemented the final version of the method as a combination of first initialising a conservative TIN in a large-scale growing operation, and then extending it carefully by examining thin “layers” of additional points progressing outwards from the centre of the road.

Creating the growing-type insertion algorithm has been most challenging. Simply interpolating in triangles is not a possibility here, but the importance of assessing the compliance of the tested points with their TIN neighbourhood is ever so important – in fact, it largely depends on these insertions, whether a TIN might accidentally spread into an off-road area, or not. The careful treatment of these insertions via detecting where they occur, and using additional triangles for the insertion tests, turned out to be a key step towards achieving my desired results.

3.3.7 TIN-based interpolation and vertex snapping

Interpolation and origin tracking

This is the last step in the pipeline, and its main purpose is to use the TINs generated in the previous step to compute the final elevation values for the road network. As Figure 3.14 shows, the first step in this procedure involves iterating through all NBRS parts, and performing the interpolation step on each of their vertices.

An additional step takes place during this iteration. To make it possible to keep track of which elevations come from where exactly, the algorithm recognises triangles that have vertices that originate from DTB. Before performing the interpolation, the triangle in which the interpolation will take place is fetched, and the origin of its vertices is examined. If any of them are from DTB, then the origin of the triangle is deemed to be DTB overall. For simplicity, mixtures of AHN3 and DTB vertices are not treated differently. The resulting labels are used in the accuracy estimation step, primarily to advise the user which output elevations were affected by DTB, and should therefore be treated with caution. Please refer to Sections 2.3.3 and 4.4 for more information about this topic.

The implementation uses linear interpolation in the TINs (also called TIN-linear interpolation). This is one of the simplest interpolation techniques available for TINs, and it is also the one most widely studied among them in the literature I reviewed (see Section 2.2). It is particularly suitable to this research, because its error propagation formulae are readily available in the literature, and because an implementation of it already forms part of *startin*. This interpolator uses the barycentric position of the point where interpolation is desired. The closer it is to one of the vertices of located triangle, the bigger the vertex’s influence becomes on the interpolated elevation. If it is closer to the centre of the triangle, the influence of the vertices is more evenly distributed. The technique is governed by the formula

$$z_p = \begin{bmatrix} x_{pt} \\ y_{pt} \\ 1 \end{bmatrix} = \begin{bmatrix} a_0 & a_1 & a_2 \\ b_0 & b_1 & b_2 \\ c_0 & c_1 & c_2 \end{bmatrix} \begin{bmatrix} z_0 \\ z_1 \\ z_2 \end{bmatrix}$$

where x_{pt} and y_{pt} denote the X and Y coordinates of the location of interpolation (inside the triangle), the matrix in terms of a_0 to c_2 contains terms dependent on the 2D geometry of the triangle, and where the last vector corresponds to the three elevations of the three vertices of the triangle. Lastly, z_p is the interpolated elevation. Please refer to Fan et al. [2014] for the expressions for a_0 to c_2 .

Vertex snapping and gap filling

The next step is to perform vertex snapping at intersections. TIN surfaces close to intersections are expected to be comprised of roughly the same vertices, hence the assumption is made that snapping intersection vertices together will not introduce abrupt elevation discontinuities. The procedure, performed for each NBRS, consists of taking each vertex one by one, and constructing a hashed data structure

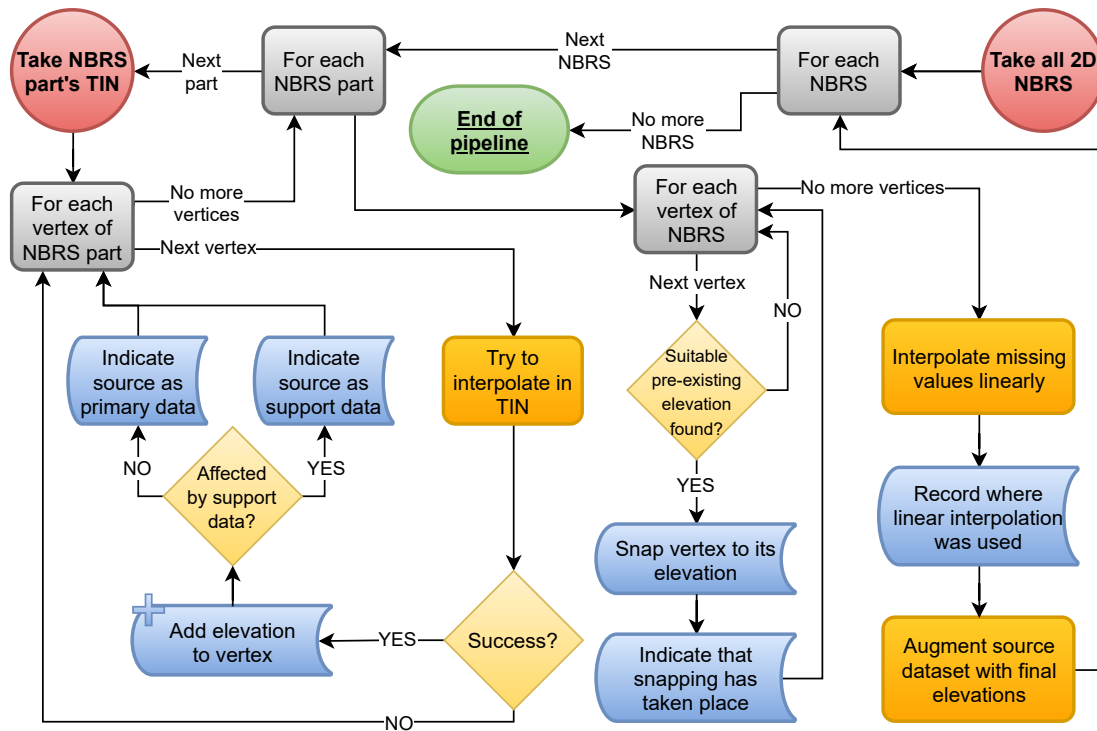


Figure 3.14: Flowchart illustration of the elevation interpolation step of the pipeline.

mapping their approximate 2D positions (coordinates to one decimal) to their exact elevations. In the underlying iteration, if the approximate 2D position of a point is already found to exist in the hashed storage, its elevation is replaced with the one already mapped to that 2D location (i.e. it is snapped to it). Since self-intersections of **NBRBS** are not possible, such a match necessarily represents a location where one or more other **NBRBS** end or begin – in other words, a real-life intersection.

Due to **NWB**'s coarse georeferencing (often only one decimal or no decimals), checking 2D matches of coordinates is not enough. Each time a match is found, vertical distance is also examined prior to snapping, to avoid merging vertices that are at (nearly) perfectly matching 2D coordinates, but which in fact belong to roads that are in a non-intersecting 3D relationship (i.e. one passes above the other). The procedure is conceptually identical to the grid-snapping workflow used in the **NBRBS** generation step (see Section 3.3.1), but in this case the underlying grid is in 3D.

The last step of the procedure is to infill gaps in the elevation profiles left by failed interpolation. Missing elevations are most commonly the result of there not being **AHN3** and **DTB** coverage in a certain place. Vertices in such locations are not part of an **NBRBS** part, meaning that their elevations cannot be extracted from an underlying **TIN**. Missing elevations inside **NBRBS** parts are also possible, since **TIN**s may occasionally shrink locally. This was discussed in Section 3.3.4.

These gaps are infilled using linear interpolation, and instead of indicating their origin as **AHN3** or **DTB**, it is recorded to be the result of this step.

Outputting 3D-NWB

The last step of the pipeline converts the internal road centreline data structure of the program (**NBRBS** parts and **NBRBS**) back into the data structure used by the input data (the **LineStrings** or *wegvakken* of **NWB**). In effect, the 2D geometry of each input **LineString** is overwritten with the new 3D geometry created using the original 2D coordinates, and the newly generated elevations.

Unlike at the end of preliminary elevation estimation (see Section 3.3.2), the original orientations of the *wegvakken* are automatically respected irrespective of some of them having been internally reversed

earlier in the pipeline. This is because the elevations are taken from the hashed data structures, not from the internal representations of these geometries (which are often reversed relative to the input).

Challenges encountered

As the tasks carried out in this pipeline step are relatively trivial, all challenges encountered were equally simple to solve. The only part that proved to be less straightforward was the tracking of the origin of vertices through the TIN-based interpolation – this required some minor modifications to previous steps. The implemented approach is also based on hashing: all DTB points that make it into the subcloud of an NBRs part are stored in a hashed data structure, making it quick to identify whether one of the triangle’s vertices are among them, that is being used for the elevation-interpolation of an NWB vertex.

3.4 Accuracy assessment

As I explained in Section 3.2.4, the estimation of output accuracy assumes no other influences than that which can be propagated through the interpolation technique relative to the input accuracy, in zones that are properly sampled. Identifying such regions and computing output accuracy represent the two main parts of this step, the details of which are explained in this section.

3.4.1 Detecting regions with poor sampling

Details of sampling-related assumption

The circumstance that local sampling density *below a threshold value* does not affect interpolation accuracy is proven by previous work in this field, as mentioned in my literature review results. Of particular importance for us is Guo et al. [2010], which provides the most amount of detail on this topic. Neither this work, nor any other work to my knowledge derives an explicit mathematical formula that expresses a relationship between local sampling density and output accuracy below the threshold level, but this is not strictly necessary for my research, for a specific reason which I outline below.

AHN3 has a nominal mean point posting distance of around 30 to 40 centimetres (6 to 10 points per m²). Considering that the dataset has a high vertical and horizontal accuracy (around 15 to 20 centimetres at two standard deviations), we may start to suspect that TINs generated directly from AHN3 will heavily oversample the road surfaces. Any unevenness seen in the models will be due to stochastic Lidar noise, rather than systematic errors due to local variations in sampling density or real-life road features.

In practice, the sampling density on road surfaces is often far higher than the nominal value I quoted above (see Section 4.3). At the exceptionally high baseline sampling rates seen in the data, typical small-scale variations in local sampling density are of no consequence regarding the overall output accuracy. This is simply because these random, stochastic variations will never decrease the local point density to anywhere near the threshold below which output accuracy would become affected.

Picking an appropriate threshold

The thresholds I used are based on the results of Guo et al. [2010]. They concluded that in the case of general terrain (not roads specifically) modelled by a raster DTM at a 0.5 m resolution, RMSE with respect to control points does not significantly decrease below 0.2 points per grid cell. Cross-validation-based RMSE values around this density were still consistently below 20 cm. In other words, 0.2 points per 0.25 m² appears to be sufficient, or equivalently, 0.8 points per 1 m². This is much lower than AHN3’s mean density of 6 to 10 points per 1 m², especially considering that this is even higher locally on road surfaces

3 Methodology and methods

owing to their flatness. Furthermore, the Lidar data used in Guo et al. [2010] has inferior accuracy relative to AHN3.

The additional points may be useful for detecting small-scale features (such as e.g. small slumps in the roads surface), as well as better characterising the edges of roads. However, if we look at the problem strictly from the point of view of the 3D conversion of NWB and the modelling of the surface's overall shape, then we are only interested in monitoring where the point density goes below the threshold above which the RMSE with respect to surveyed control points remains relatively constant. If we assume that about 1 point per 1 m² is sufficient to characterise a rugged surface using Lidar, then we could consider drops of up to 90% in AHN3's point density to be acceptable, based on the nominal values.

To make sure I use a conservative value, I opted to stay somewhat above this estimate. At each NWB vertex, I examine the number of TIN vertices that fall within 3 metres of it, and if it is less than 9 points, then I flag the output accuracy at that point to be unreliable. This corresponds to a threshold of approximately 3 points per 1 m².

As we lack a mathematical formulation describing the exact nature of the influence below the threshold sampling rate, the best we can do is mark the accuracy of vertices falling into such areas as *unknown* in the output.

Types of areas violating the assumption

Places where linear interpolation was used, the threshold-based evaluation is automatically assumed to be violated. They generally correspond to areas where there is no AHN3 and DTB coverage, meaning that the local sampling density is zero, or nearly zero. Even in areas where linear interpolation had to be used due to the poor georeferencing of NWB, the values were not based on the samples in the local TINs, hence sampling density can be considered to be zero there, too.

The threshold may also be violated due to an insufficient amount of detail in the TINs, but this is atypical in practice. Sampling density can only reach such low values in the TINs due to *significant* amounts of occlusion due to objects opaque to Lidar (so not vegetation). Notably, the threshold of 3 points per m² deems it reasonable to regard most elevations reliable which were interpolated inside medium-sized gaps resulting from vehicles or other stationary objects on the roads, as well as some that are found in regions where only DTB coverage is available – although the latter should be treated with some skepticism, as I noted in Section 3.2.4 earlier in this chapter.

3.4.2 Effect of interpolation on accuracy

Theoretical proof suggests that the interpolation step generally *improves* output accuracy. This can intuitively be thought of as the result of basing each output elevation on the combined information stored in the three vertices of the triangle in which the interpolation takes place.

This is contrary to what one might assume based on thinking about the pipeline as a whole, but both in practice and in theory, it is the *other* influences on accuracy that generally have the opposite effect. For instance, problems with ground filtering and a sparse local sampling may have negative effects on accuracy (locally). However, the interpolation itself has no such effect on the output under normal circumstances. We can thus assert that the formal accuracy of the output will *mostly* increase relative to the input in well-sampled regions. I present the relevant error propagation results from Fan et al. [2014] below.

Let $\sigma_{z_{vx}}^2$ denote the elevation variance of the vertices of the triangle, and $\sigma_{xy_{vx}}^2$ denote the horizontal variance. We may then express the relationship between the elevation accuracy at the point of interpolation $\sigma_{z_{pt}}^2$ as

$$\sigma_{z_{pt}}^2 = M \left(\sigma_{z_{vx}}^2 + \sigma_{z_{node}}^2 \left(\tan(\alpha_x)^2 + \tan(\alpha_y)^2 \right) \right)$$

where $\tan(\alpha_x)^2$ and $\tan(\alpha_y)^2$ correspond to the angle between the triangle's plane and the X and Y axes of the coordinate system. The expression takes into account the steepness of the plane to be able to propagate the horizontal error, hence the necessity of computing these angles. The variable M is a parameter that needs to be pre-computed for each triangle, as it depends on their 3D geometry. The underlying formula will not be listed here as it is not relevant to this discussion. Please refer to [Fan et al. \[2014\]](#) for more details.

Since [AHN3](#) and [DTB](#) points and vertices have no individual accuracy measurements, the above formula takes a single accuracy value per triangle, rather than a separate value for each vertex. Like in the origin-labelling step I described in Section 3.3.7, I make the assumption that [DTB](#)'s accuracy should only be used in this formula, if all three triangle vertices are based on [DTB](#) data.

The expression is, in essence, a sum of the input variances scaled by geometric variables. Most importantly M has a range between about 1/3 and 1, taking its lowest value around the centroid of the triangle, and increasing to 1 at the triangle's vertices. Intuitively, the closer we are interpolating to one of the vertices, the smaller the other two vertices' influence is going to be due to the nature of TIN-linear interpolation. We are thereby gradually taking into account less and less information, decreasing to the minimum at the vertices, where only one input elevation measurement is considered. Assuming that the [NWB](#) vertices are randomly distributed relative to triangle vertices, the expected value of M is 0.5.

Substituting values into the above formula with $M = 0.5$ reveals that applying TIN-linear interpolation to surfaces with sufficiently low inclinations decreases the elevation error relative to the input. For instance, a triangle with a 2-degree inclination and vertices with 10 cm vertical and horizontal standard deviations (similar to [AHN3](#)) yields an output elevation standard deviation of 7 cm, a 30% decrease. Increasing the inclination to 45 degrees decreases the vertical accuracy of the output to 12 cm, which is now worse than that of the input.

Such steep roads are practically absent in The Netherlands. For Dutch roads, the accuracy is thus expected to increase. However, oversampling the surfaces too heavily with a non-zero stochastic scatter in the elevations can yield small artefact triangles that are inclined anomalously. These inclinations are meaningless, as they do not represent the geometry of the underlying road surfaces, and care should thus be exercised when interpreting the accuracy assessment values of results that were generated using most of the original Lidar points. More information on this topic is found in Section 4.3.

3.4.3 Evaluating TIN surface completeness

To evaluate how complete the generated [TIN](#) road surfaces are relative to the true road surfaces, I relied on a visual comparison of the [TINs](#) with the subclouds, as well as on a comparison with [BGT](#) ([Kadaster \[2021\]](#)). Like [AHN3](#) and [DTB](#), it is a Dutch open data geospatial dataset. It is maintained by Kadaster, the national cadastral agency. It is a topographical map of the country which contains a wide range of classified areal features – such as city, building, and *road* extents.

Like [NWB](#), [BGT](#) is also primarily intended to offer good topological accuracy, thus its 2D georeferencing is also relatively crude. However, upon a comparison with the Luchtfoto 2020 orthoimagery (also from Kadaster, see [PDOK \[2021\]](#)), I deemed its road polygons reliable and accurate enough to serve as a reference with which my results can be compared. To make the comparison, I plotted some of the output [TINs](#) against the relevant [BGT](#) road outlines in 2D and assessed the agreement between them visually. An example of the results of this step, as well as a comparison of [BGT](#) and [NWB](#) with the aerial imagery are shown in Figure 4.20.

3.5 Comparison with commercial results

A simple method to evaluate the relative quality and accuracy of the commercial results is to examine variations in the agreement between the elevations predicted by the academic and commercial results

3 Methodology and methods

visually, and quantitatively by computing residuals and [RMSE](#) values. Furthermore, where output accuracy is quantified in the academic results, it can be used as a reference to advise us about the absolute accuracy of the commercial results.

In places where the academic results have unknown accuracy, the commercial elevations are also necessarily uncertain because the same datasets were used in their production. This excludes places where the unknown accuracy of the academic results is due to limitations of the system design, or small-scale blunders. As a result, it is best to rely on a combination of qualitative, visual analysis and quantitative comparison.

To aid the interpretation, I computed and plotted the residuals between the two sets of results in a number of LineStrings (*wegvakken*) that I picked for comparison. Correlating these with comparison plots of the elevation series, as well as 3D plots of the data and underlying [AHN3](#) and [DTB](#) points provided further input to this process. I also employed the generation of [RMSE](#) values on the level of *wegvakken*, as well as for entire testing datasets. The [RMSE](#) is given by

$$RMSE = \sqrt{\frac{\sum_{t=1}^T (z_{a,t} - z_{c,t})^2}{T}}$$

where the elevation samples in a profile are numbered from $t = 1$ to T . $z_{c,t}$ denotes the elevation estimated by my method. $z_{a,t}$ and denotes the commercial result at the same location.

When performing the above comparison on a LineString, the distances from its first vertex along the profile from $t = 1$ to T are computed, this is what the elevation series and residuals are plotted against. The residuals are the values taken by $z_{a,t_{nwb}} - z_{c,t_{nwb}}$ where t_{nwb} corresponds to *original NWB vertices*. Both the academic and the commercial pipelines use vertex densification, but the resulting vertices are not located in the same place. Thus, the residuals and the [RMSE](#) values describe only how well the two methods agree at the location of the *original NWB* vertices.

3.6 Programming framework

The implementation part of this project is intended to investigate how well each step of the pipeline works in practice, how well they work together as a pipeline, and how accurate their output is. In turn, these serve the purpose of answering the research questions detailed in [Section 1.4](#). In addition, implementation-related tasks were also important in iteratively revising the methods based on the practical experience gained in the process, making them better adapted to real-life scenarios (and as result, more relevant to reusers).

Notes on performance

As the implementation is primarily intended for demonstration and reference purposes, it is by no means ready for all types of academic and commercial use out of the box. One limiting factor in this sense is the lack of a scaling mechanism in the implementation, because this was not part of this research. Furthermore, I developed all parts of the pipeline in Python 3.8, which means that the code is more concise than a binary implementation would be, but its runtimes are higher. To improve performance, I relied on binary libraries such as *numpy*, and parts of *scipy*. In addition, I used hashing-based data structures (in Python these are called dictionaries and sets) extensively, which are also known to benefit performance greatly. Many of these uses of hashing are mentioned previous sections explicitly, and wherever I mention using KD-trees, I refer to building code on top of the binary implementation in *scipy*. Uses of *numpy* are so pervasive in the code, that I opted not to mention them explicitly in the text.

While geometries (and geometric operations) are sometimes handled in *shapely*, I avoided its use in all cases where geometries are bulk-processed via long iterations. I found that implementing the geometric operations from first principles in *numpy* in such cases resulted in a noticeable gain in performance.

Unfortunately, the implementation of active contour optimisation in *scikit-image* is mostly based on native Python iterations, not on binary packages. This circumstance, in conjunction with the large number of vector inner products that the attractor map generation requires, means that the computational complexity of the active contour-related part of my software is a magnitude slower than all other parts.

GitHub release and code structure

I released the source code of the implementation in the following GitHub repository: <https://github.com/kriskenesei/geo2020-modules>. Most functionality resides in the class `nbrs_manager` inside the file `nbrs_generation.py`. I factored out some functionality into `lib_shared.py` to somewhat simplify the code in `nbrs_generation.py`. Both files contain an extensive set of docstrings and inline guidance on what each part of the code does. The intended audience of this information includes those simply interested in knowing more about the practical aspects of processing that underlies this research, as well as potential reusers.

The class `nbrs_manager` is intended to be instantiated with the cropped road network, followed by the invocation of class methods corresponding to each pipeline step. In addition, vertex densification is also implemented as its own class method, and a range of methods are provided for basic operations such as setting individual *wegvak* geometry, as well as writing the intermediate results of each pipeline step to disk separately. Furthermore, the class holds certain intermediate results in its class variables which cannot be written to disk natively, but which may be interesting to reusers.

The structure of the next chapter (Section 4.2) is modelled on the steps one would take to run my software, to create a stronger link between the explanations and the implementation. The method invocations that I used to generate the results shown in the chapter are explicitly listed at the end of the sections describing the relevant pipeline steps. A condensed explanation of how the implementation is meant to be used can also be found in the docstring of `nbrs_manager`, and a set of example calls are also provided at the end of the file `nbrs_generation.py`.

4 Results

In the previous chapter, I described the theoretical structure of my processing pipeline, giving a detailed account of the algorithms and procedures relevant to each pipeline step. Being the result of a process of iterative refinement and revision, these were partly based, in fact, on my practical experience at implementing them and testing how effective they are at fulfilling their roles. As a result, the final methods and results of this research are interlinked and were thus difficult to separate into two chapters.

In this section, I will not dedicate much attention to the changes introduced during development, as I already addressed this topic in the previous chapter. Instead, I will restrict the discussion to the relationship between the final version of the code and the outputs it produces. In this chapter, I will only mention the challenges that lead to changes in the system design, where figures are shown that illustrate them well.

In the following sections (4.1 and 4.2), I will show the intermediate results of each step of the pipeline visually in figures, as well as describe them in the text. This showcase and description of the results will focus primarily on the effectiveness of the final implementation of system design, and the quality of the results it produces.

The last sections of the chapter (4.3 and 4.4) discuss the results of quantifying the quality and accuracy of the output, and the results of comparing the commercial results and the present academic results, respectively.

4.1 Manual pre-processing

4.1.1 Producing the testing datasets

Implementing a scaling solution was not part of this project, although all parts of the implementation were designed in a way that a scaling framework could be added to it with a relatively small amount of effort. Among other things, scaling in this project concerns the need to subdivide the input data in a way that the software never runs out of memory while processing it. These subdivisions could be generated, in the simplest case, based on tiling, i.e. overlaying a 2D raster on the extents of the input datasets and cropping them to the extents of individual cells.

As scaling was not part of this project, the task of creating manageable subsets of the input data was carried out manually. The procedure consisted of cropping the input vector datasets (NWB, DTB) into tiles showing interesting and representative road layouts, and for each of them, creating an AHN3 file with those points, which are a set maximum distance from any relevant roads (R-roads and P-roads) in their respective NWB tiles. For vector data processing, I used QGIS, and for Lidar processing I used LASTools.

I derived the area of interest in which to keep Lidar points by buffering the relevant centrelines in the NWB tiles by 150 metres, and passing these geometries on to LASTools to use to *clip* the relevant AHN3 tiles. AHN3 itself comes tiled in the official release (on a much larger scale), and I derived each testing dataset from a single AHN3 tile to keep the manual procedure simple. I also discarded AHN3 points not classed as ground or bridge points at this stage (2 and 26 respectively), as they are not relevant to our methods.

The relevant visualisations are shown in Figure 4.1. The clipping polygon was manually edited to have sharp, linear boundaries and NWB *wegvakken* intersecting its interior were included in the testing dataset. The resulting occasional overshoots of NWB centrelines (relative to AHN3) allowed me to test how well

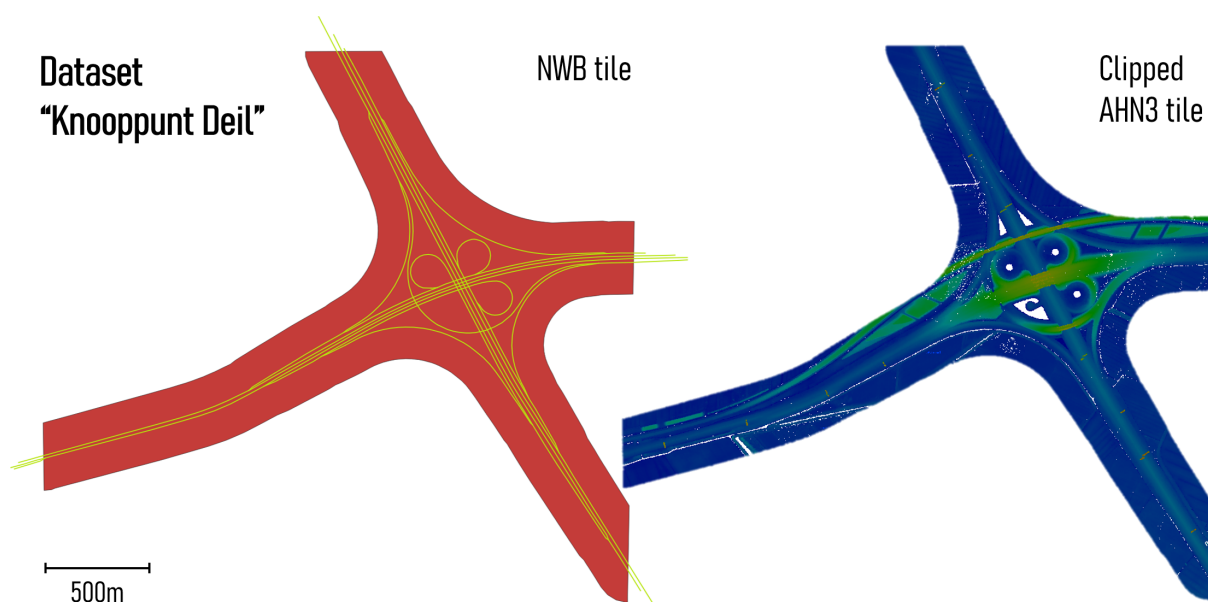


Figure 4.1: Visualisations illustrating the results of manual pre-processing. An NWB tile (yellow lines) and the corresponding Lidar clipping polygon (in red) are shown alongside the clipped point cloud tile (on the right). Darker areas represent lower elevations, the total elevation range shown is about 10 m.

the procedure performs in areas where AHN3 is completely unavailable for a short distance, but where DTB coverage is present. At the end of the research, they also turned out to cause unforeseen issues with accuracy assessment, which I discuss in Section 4.3.5. On the right, the point cloud is shown in its original density, not a derived DTM.

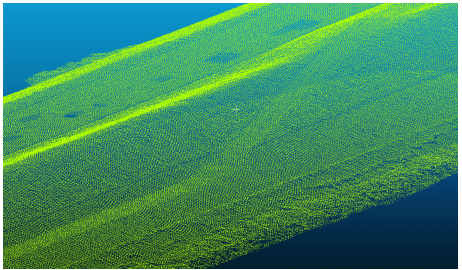

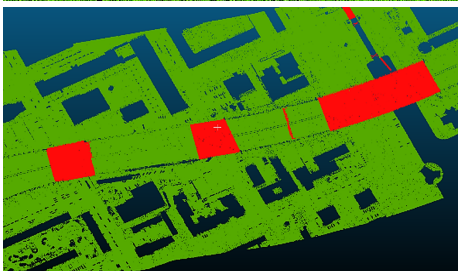
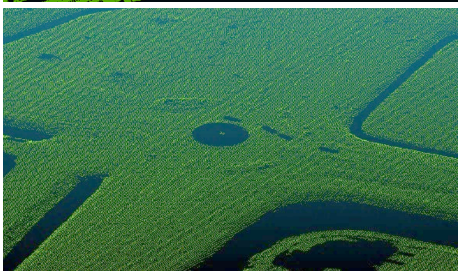
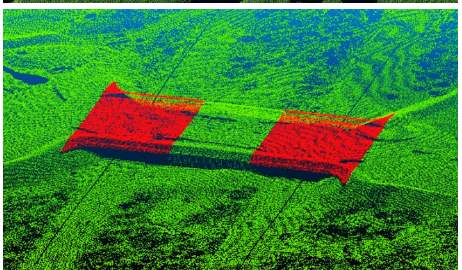

I created 11 testing datasets in total, each with its own cropped or clipped NWB, DTB and AHN3 files, which are described in the next section. The dataset shown in this figure is *Knooppunt Deil* (from AHN3 tile 39CZ1).

I picked 150 metres as a buffer distance for point cloud clipping not because I expected road surfaces to be so wide, but because I found that it reduced the volume of points to manageable levels in my testing tiles, while retaining plenty of neighbourhood information which I found to be useful for debugging purposes, and for the assessment of how well my algorithms perform in various environments next to roads – in other words, they provided context for the interpretation of intermediate results, and for the algorithms themselves. Using a smaller buffer distance would lead to slightly reduced runtimes.



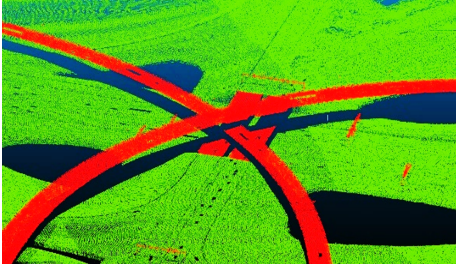
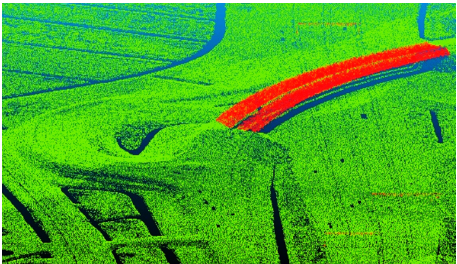

4.1.2 Description of testing datasets

The set of chosen areas needed to be representative of the whole country to provide an insight into the effectiveness and performance of the algorithm in as many scenarios as possible. Furthermore, I also deliberately included areas which I thought would prove especially challenging, such as roads with many stationary vehicles, roads in multi-level 3D relationships (in motorway junctions), as well as tunnels.

Table 4.1 provides an inventory of these datasets. The tile identifier in the first column refers to those used in PDOK [2020]; each dataset is found within a single AHN3 tile as I mentioned in the last section. The resulting datasets fit into memory easily even on a mediocre computer, and are also small enough to allow intermediate results to be visualised and interpreted quickly.

Title, tile	Features	Render
Markerwaarddijk, 20BN1	provincial road on a dike in the Markermeer. Very limited amount of terrain around the road. Road consistently built on ground, there are no bridge structures.	
Amsterdam Hemhavens, 25BZ2	Ringweg-West motorway as it crosses the IJ through the Coentunnel in a densely built-up environment. It is built on artificially elevated ground and on bridges in this area. Part of Westradweg also included, built entirely on a long bridge.	
Amsterdam Zuid, 25DN2	R-roads with many closely spaced bridges, small tunnels, dense grouping of holes around roads due to presence of water and buildings	
Bunschoten, 32BN1	P-roads with three big roundabouts, and one road that ends in a small roundabout. Amersfoortseweg has its two lanes on separate road surfaces (like motorways), but with frequent connecting segments.	
Veluwe, 32FZ2	Straight R-roads surrounded by dense forest and crossed by wide wildlife overpasses.	
Apeldoornseweg, 32HZ2	P-roads in dense forest with canopy frequently occluding the road surface, decreasing point density and occasionally creating gaps. The road has small parallel branches running very close to it, which may make it difficult for the algorithm to distinguish between them. It also has roundabouts.	

4 Results

Hoenderloo, 33CN2	<i>P-roads</i> in extremely dense, continuous forest with canopy frequently occluding the road surface, decreasing point density and occasionally creating gaps. Both lanes are on the same road surface	
Rotterdam Ketheltunnel, 37EZ1	This segment of the A4 heading North from Rotterdam has been recently reconstructed in an underground tunnel. In addition, a significant portion of this motorway now runs in a trench towards Delft. <i>AHN3</i> was imaged during the reconstruction, and hence contains anomalous data about the road surface.	
Knooppunt Rid- derkerk, 37HN2	The Ridderkerk junction is one of the largest of its kind in The Netherlands, in one place containing 4 overlapping <i>R-roads</i> . Furthermore, it contains a high density of <i>R-roads</i> in a small area, many of them very tightly packed. Many of them have very sharp bends.	
Gorinchem, 38GZ1	Complex junction between <i>P-roads</i> and <i>R-roads</i> with small ramps, roundabouts and overlapping geometries.	
Knooppunt Deil, 39CZ1	Less complex, but analogous junction to the Knooppunt Ridderkerk.	

Please refer to Figures 2.7, 2.8, 2.6 and 2.10.

Table 4.1: Inventory of testing datasets. In the renders, ground points are shown in green and bridge points in red.

One instance of my software can process a single testing dataset at a time. However, running multiple Python instances in parallel allows one to easily parallel-process multiple tiles depending on the CPU installed in the computer. Each dataset consists of a cropped *NWB* and *DTB* file, and the clipped *AHN3* point cloud.

All datasets mentioned in Table 4.1 are part of the GitHub release of the results. A compressed archive with the input testing files (as well as all intermediate results and the final results) can be downloaded via a link found in the repository's readme file.

4.2 Results of processing steps

The results below are presented in the same section structure as the detailed methods were in Section 3.3 of the previous chapter. This is intended to make it easy for readers to correlate the results with the theory underlying the relevant processing mechanisms. In each section, I describe – with the help of 3D visualisations – how well each processing step performs, and how effective and useful they are in the

context of the entire pipeline as a whole. I also devote attention to describing typical scenarios in which algorithms are useful and perform well, as well as ones where the opposite is true and they may produce sub-optimal results. Since the section structure also corresponds to the overall implemented pipeline structure, in each of the pipeline steps I describe how exactly the underlying software implementation is meant to be used, with notes on the recommended arguments.

4.2.1 Splitting NWB into NBRs

Each colour in Figure 4.2 corresponds to a specific NBRs ID, meaning that LineStrings (*wegvakken*) belonging to the same NBRs are coloured the same. The figure demonstrates that as a result of the NBRs generation step, the cropped road network becomes semantically enriched with identifiers linking certain LineStrings together, based on semantic or geometric conditions depending on which algorithm was used.

The colours are generally inconsistent between the results of the two algorithms (top and bottom parts of the figure). The same colour scheme was used to generate the two figures, but the two algorithms distribute NBRs IDs differently.

Issues with geometric algorithm

Figure 4.2 also serves to illustrate the fundamental differences that exist between the results of the two algorithms. The geometric algorithm makes the assumption that the 2D georeferencing of NWB is fully representative of the real-life geometry of road centrelines. However, I found this to be violated in various places as already mentioned in Section 2.3.1. In short, where R-roads intersect (this includes ramps, motorways and all combinations thereof), they often do so at abrupt angles, which can be observed in various places in Figure 4.2, and especially in the insets. These angles are not representative of the real-life road geometry, they were drawn manually by data handlers to ensure that NWB complies with certain external requirements. Consequently, they may prevent correct decisions from being made based on the intersection angles.

In places where this problem exists, choosing the straightest continuation across an intersection when building an NBRs does not necessarily represent the optimal choice, because the angles are artificial. This can be observed in the inset of the top chart in Figure 4.2, where I numbered some of the NBRs on the geometric results. While the geometric algorithm obviously made the right choice *based on the angles* between the individual road segments concerned, *attribute table data* told the semantic algorithm that the role and road number of certain parts of NBRs 0 and 2 are the same as that of NBRs 1, which resulted in these parts of NBRs 0 and 2 connecting via NBRs 1. The “discarded” ends of NBRs 0 and 2 then became two unique NBRs by themselves. In the large-scale context of the road network, the semantic algorithm evidently made the correct choice, even though this introduced some small, abrupt internal angles into the NBRs.

Issues with semantic algorithm

The green dotted circle in the semantic NBRs generation results points out a place where the role and road number of a ramp changes suddenly, outside of a real-life intersection, which results in the algorithm abruptly starting a new NBRs there. This is indicated by a change of colour from dark to light purple. The break happens in an unfortunate location, in the middle of a multi-level junction where the continuation of NBRs is crucial so that large-scale trends across the complicated zone may be recognised effectively in later steps. This demonstrates that while the geometric algorithm is sensitive to problems with the georeferencing of the data, the semantic algorithm is sensitive to issues with the attribute table data. Within the testing tiles I examined, the two algorithms offered a comparable amount of benefits and drawbacks.

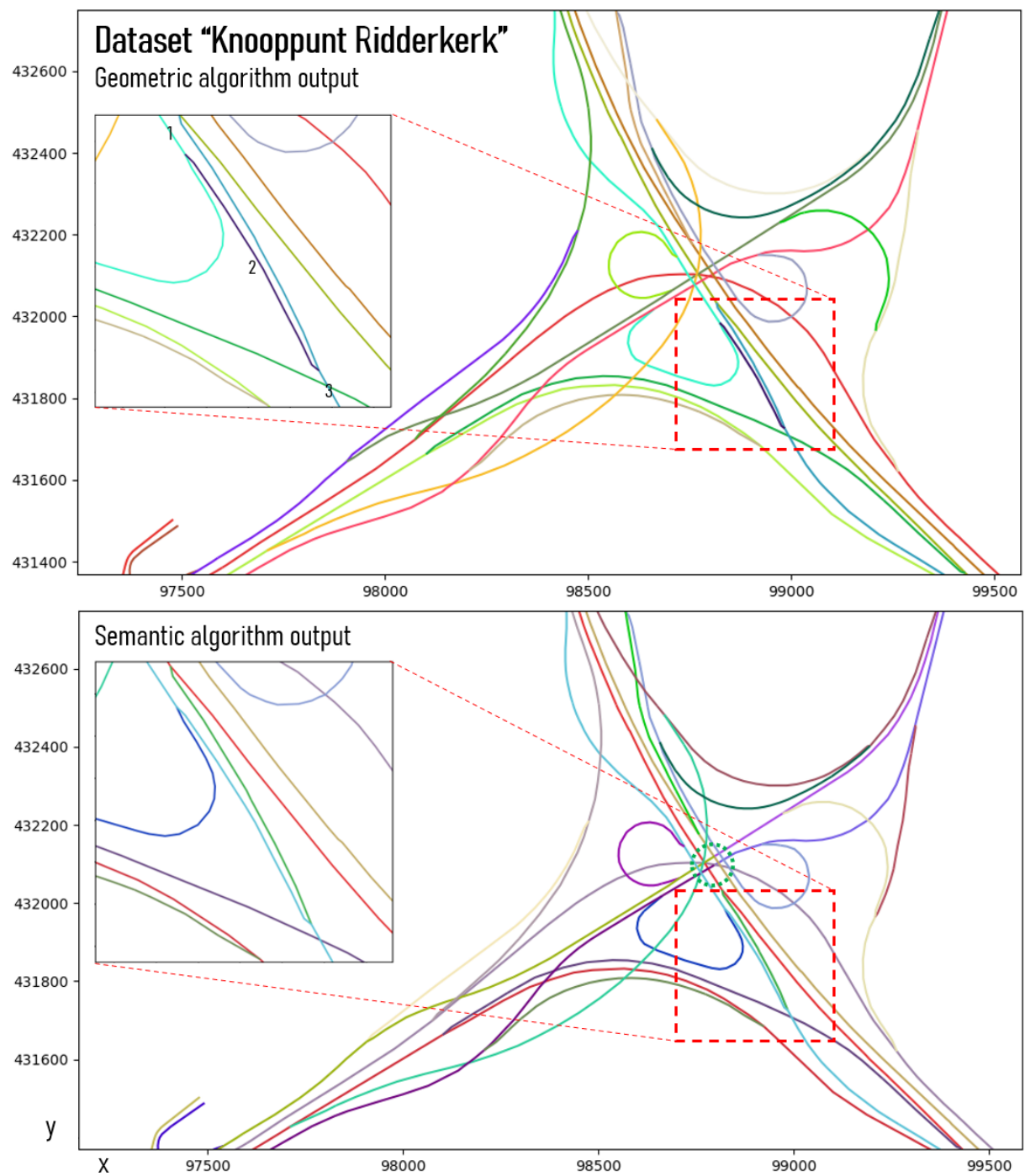


Figure 4.2: Visualisations illustrating the results of *NBR*S generation. The colour-coding was randomly generated based on the generated ID numbers of the *NBR*S. The insets and annotations highlight differences between the results of the two algorithms, which are further explained in the text.

Evaluation and choice of algorithm

Both algorithms produce usable results overall. In general, the resulting chains of LineStrings satisfy all the original requirements I set for the outputs of this step (minimise internal angles, maximise length, disallow self-intersections and branching). Based on some further testing after implementing the rest of the pipeline, I also verified that the choice of algorithm does not significantly influence the output of subsequent steps.

Since the geometric algorithm generalises to arbitrary road networks better than the semantic algorithm (i.e. does not rely on specific properties of NWB), I used it to generate the rest of the results shown and discussed in this report.

Using the implementation

In the software, before NBRs generation can be executed, the `nbrs_manager` class needs to be initialised with the file path to the cropped NWB file of the desired dataset. Example calls to perform geometric NBRs generation are provided below.

```
roads = nbrs_manager(fpath = nwb_fpath)
roads.generate_nbrs(algorithm = 'geometric')
```

In the code snippet above, `nwb_fpath` refers to a variable containing the file path to the cropped NWB file of the desired testing dataset. For instance, the file path could end in `.../C_39CZ1_nwb.shp`, using the naming convention of the released testing files, the dataset called *Knooppunt Deil* is desired. Switching to `algorithm = 'semantic'` triggers the use of the semantic algorithm.

The invocation `roads.plot_all()` may be executed to plot the results on a 2D diagram using random colours to distinguish between NBRs. At this point, NBRs generation results are saved in class variables only (see `roads.nbrs_wvkn`), hence running `roads.write_all()` at this point is **not** going to write the NBRs IDs into the attribute table. The imported road network is stored in `roads.nwb` in a GeoDataFrame which also contains the generated NBRs IDs.

4.2.2 Elevation estimation

Figure 4.3 shows the results of this step in two 3D visualisations. The NWB centrelines are now shown at their estimated elevations. The figure contains two visualisations that allow the reader to examine the same results from multiple viewing angles.

The vertical dimension in this visualisation and all other 3D visualisations in this chapter are exaggerated 5-fold, so that changes in elevation are made better visible.

Vertex densification

The vertices were densified before running preliminary elevation estimation; I used a threshold of 5 metres for all my final results. This means that no individual line segment in the 3D road network is longer than 5 metres. I found this threshold value to offer a compromise between longer processing times (in later steps) and more refined results.

We may say that while the horizontal dimensions were merely oversampled, the vertical sampling benefited from the vertex densification in the sense that it is far more detailed than it would be without it (as also mentioned in Section 3.3.2). An example visualisation of what happens to a specific NBRs during vertex densification is shown in Figure 4.4.

4 Results

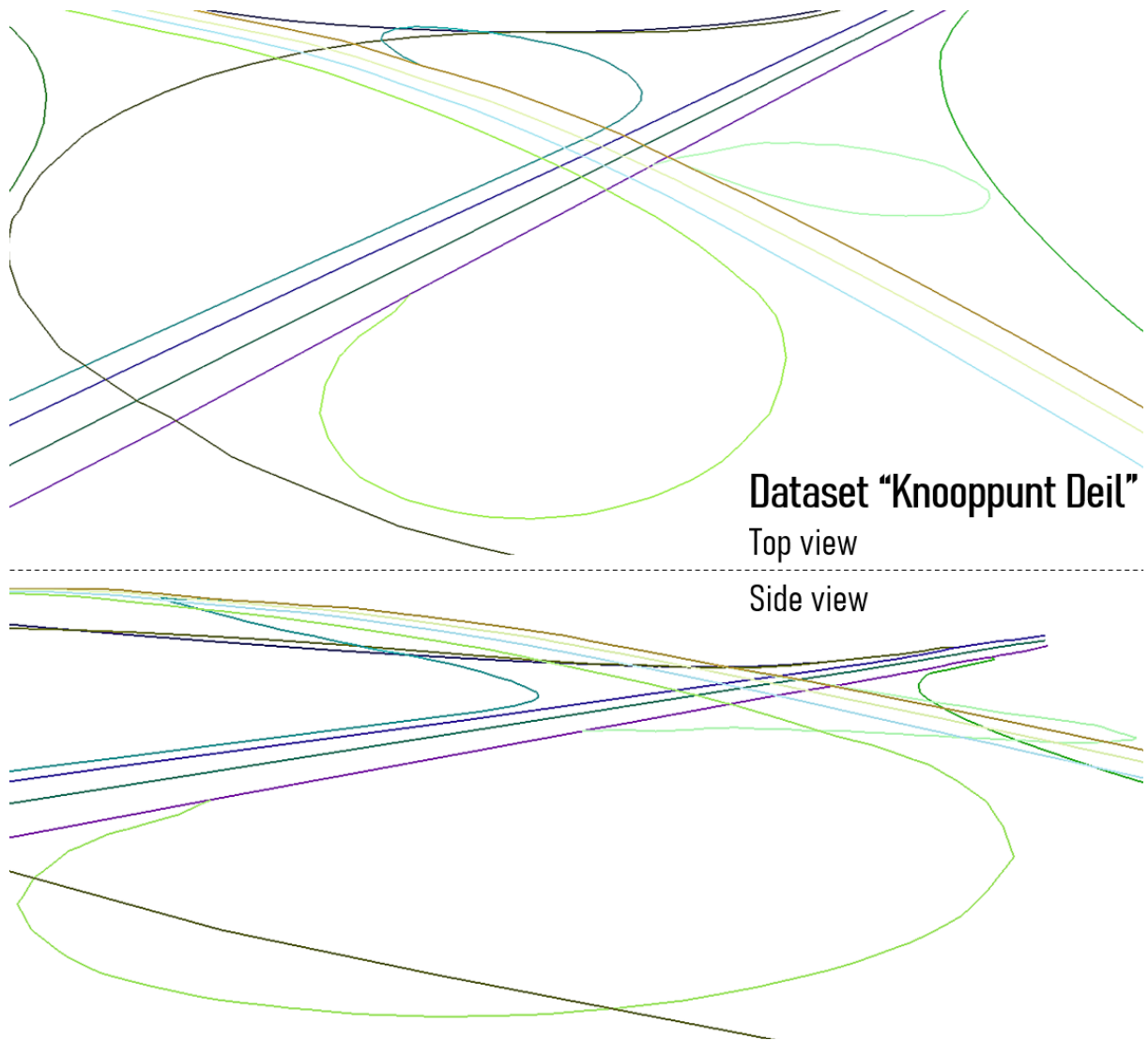


Figure 4.3: Visualisations illustrating the preliminary elevation estimation results. The colour-coding of the 3D NBR lines was randomly generated based on their NBR IDs.

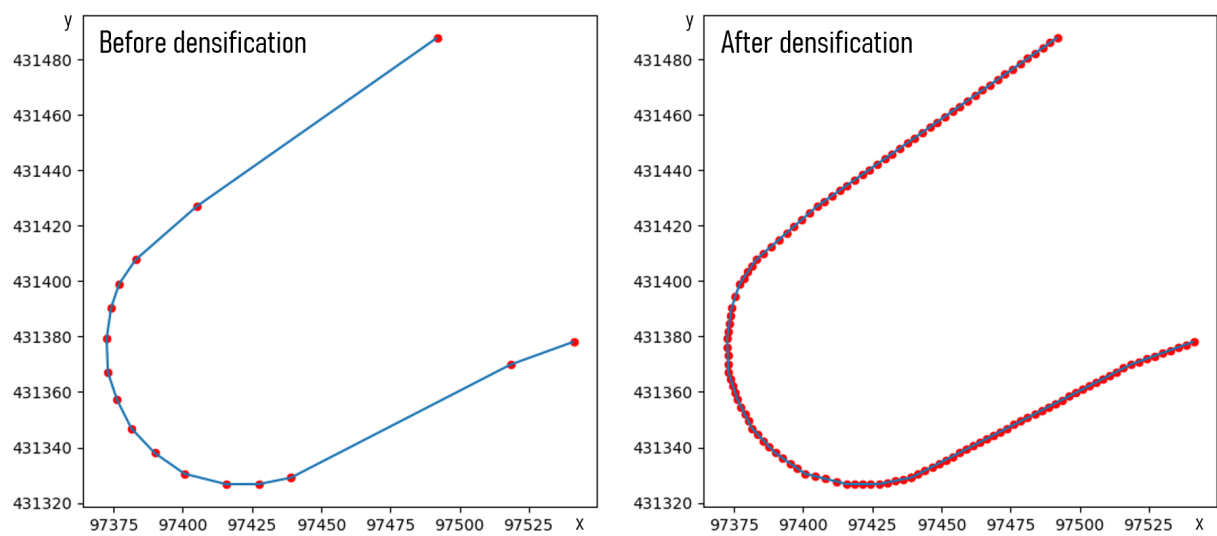


Figure 4.4: Plots illustrating vertex densification. Vertices are marked as red circles on the blue NBR.

Types of challenging scenarios

Instead of focusing on details, I will only comment on the general quality of the results, since accuracy is not yet important at this step – this 3D conversion is merely a stepping stone towards the goal of performing Lidar segmentation. It only needs to help find candidate points for the subclouds, rather than to be a perfect representation of 3D road geometry. In fact, in practice it just needs to be closer to the relevant road surface, than to other roads (or other occluding objects) above or below it.

There are two main aspects of the output that require our attention: how well the 3D centrelines conform with the real-life road surfaces (effectiveness of the 3D conversion), and how successfully outliers are being eliminated (effectiveness of the refinement step). The former can be assessed via a visual comparison with the underlying [AHN3](#) point clouds, while the latter can be examined by looking for artefacts at locations where occlusion happens. Figure 4.5 shows two further 3D visualisations that contain examples of the features that are relevant for this assessment.

Effectiveness of 3D conversion

The top visualisation in Figure 4.5 illustrates that in the case of flat lengths of roads, centrelines are generally positioned very close to the Lidar-defined road surfaces (within a few centimetres in general). Outliers are atypical in well-exposed areas, corresponding to the lack of outliers in [AHN3](#) itself (and its ground classification). The procedure is fast, runtimes for the testing datasets are generally in the range of 1 to 5 seconds on a mediocre computer.

Thinning the input point cloud aggressively can marginally improve the performance of this step, but it also drastically reduces its effectiveness in areas that are poorly sampled. This in turn may result in artefacts on a scale that may also confuse the refinement step. I found that working with no thinning applied, or a maximum thinning factor of 3 (33% of points kept) at most, works best. My final configuration uses a thinning factor of 2 when it imports the [AHN3](#) data, which is carried over to all subsequent steps that work with it.

There is a range of factors that may result in the computation of anomalous preliminary elevations due to occlusion. Firstly, if an [NWB](#) centreline is positioned far from the actual road centreline (or next to the road), then the 3D elevations will be derived from a patch of Lidar points that may include a significant number of off-road points. This may result in both positive and negative outlier elevations being computed relative to where [NWB](#)'s georeferencing is correct. Furthermore, bridges in [AHN3](#) include reflections from civil engineering structures, which are often attached to roads close to their edges. If the centreline of an [NBRS](#) falls too close to the edge of the road where such objects are present, its elevations may be corrupted by Lidar points reflected from them, rather than from the road surface.

Furthermore, slow or stationary vehicles and motorway signs (due to their presence in classification 26), and larger occluding objects (e.g. bridges built *over* a given road) tend to generate a sequence of outlier vertices, depending on the size of the object. Gaps in [AHN3](#) coverage (e.g. where a road passes underneath water in a tunnel) can also give rise to missing elevations in the output of this step. Both the outlier elevations and the missing elevations resulting from these artefacts are mostly eliminated by the refinement step.

The query radius used in the KD-tree queries in my final configuration is 1 m. At the typical local posting distances found in [AHN3](#), this represents a compromise between fetching enough samples to minimise the effects of small-scale outliers and minimising the chances of including off road points where [NWB](#) deviates from its optimal position. This query radius corresponds to a query area of $\pi \text{ m}^2$, which typically corresponds to selecting about 30 to 120 [AHN3](#) points in practice, depending on the local sampling density (assuming a thinning factor of 2 was used).

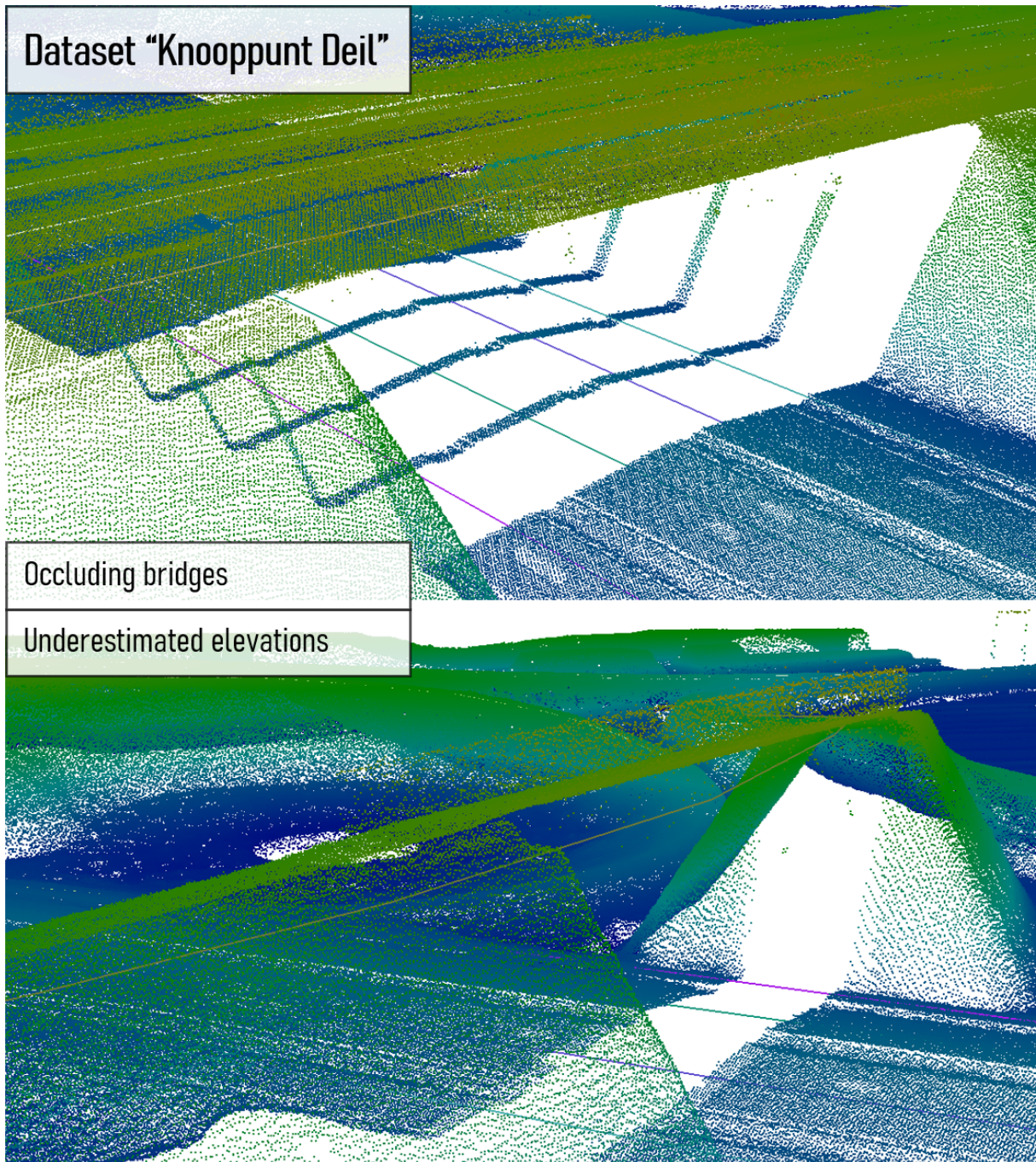


Figure 4.5: Visualisations comparing preliminary 3D conversion results with the [AHN3](#) point cloud. The colour-coding of the 3D [NBRS](#) lines was randomly generated based on their ID numbers. Darker areas represent lower elevations, the total elevation range shown is about ten metres.

Effectiveness of refinement step

The effects of the refinement step can be observed in the shape of the *lower* set of 3D centrelines shown in the top visualisation in Figure 4.5. The series of bridges causes occlusion, meaning that Lidar coverage is intermittent for the lower set of roads, for a distance of about 70 metres. Initially (before the refinement step), the centrelines of the lower set of motorway lanes thus became snapped to the elevation of overlying roads. The resulting outliers were easily identified using the polynomial model that was fitted on the NBRS, and new values were interpolated linearly.

For my final results, I used a degree of 8 for the fixed-degree polynomials, and set the outlier filtering threshold to 0.2 times the standard deviation of the data-model errors in the given polynomial fit. I found that in general these parameters work best with the testing datasets. Standard deviations below 0.4 metres are artificially increased to 0.4 metres to avoid modifying elevations in roads whose conformance with the model was already found to be near-perfect.

This approach proved to be an effective solution in terms of eliminating occlusion-related artefacts. It is ineffective only in places where the occluding geometry is very close to the road surface. For instance, stationary vehicles occasionally introduce outliers that are not far enough from the model to be detected in the refinement step, thereby giving rise to small spikes in the output. This does not happen frequently, and does not represent a problem in the context of the pipeline as a whole. This step also replaces outliers caused by motorway signs.

The optimal lower limit for the outlier filtering threshold is determined, in practice, by the accuracy of the polynomial fits themselves. If the value is set too low, elevations that were in fact already correct may be replaced with values from poor polynomial fits. This issue arises where the vertical curvature of the modelled roads is unusually complex, such as in the overpass shown in the bottom visualisation in Figure 4.5. Complex curvature is difficult to approximate using fixed-degree polynomials, which becomes especially relevant when processing very long NBRS.

Even when using a sufficiently high outlier filtering threshold, the algorithm may occasionally identify lengths of such roads as outliers and reposition them to the incorrect elevation level suggested by the polynomial model. I successfully bridged this relatively uncommon issue by taking it into account while implementing the Lidar segmentation workflow. Therefore, these inaccurate elevations do not represent a problem on the scale of the pipeline as a whole, because the next pipeline step is not sensitive to them. Shorter NBRS lengths could help deal with this problem in a more explicit manner, but this would also mean that certain longer trends would become impossible to model later on.

Using general curve fitting or an interconnected set of splines (in place of fixed-degree polynomials) could help solve this issue in a more direct manner, but the toll this would take on computational complexity and the complexity of the code is not justified by the issues that arise.

Using the implementation

The below code snippet shows the code that I used to generate my final results.

```
roads.densify(thres = 5)
roads.estimate_elevations(fpath = ahn_fpath, r = 1, thin = 2)
roads.write_all(fpath = simpleZ_fpath)
```

The first line performs vertex densification with a threshold of 5 metres. The second line performs the preliminary elevation estimation (and refinement) step, the variable `ahn_fpath` is assumed to contain a file path to the clipped AHN3 file belonging to the desired testing dataset. For instance, it could be `.../C_39CZ1_2_26_clipped.las` using the naming convention of the input files I released on GitHub. The tags `_2_26_clipped` in these file names refer to having kept only points in classes 2 and 26 (ground and bridge points respectively), and having clipped it to the extents of buffered centrelines. The variables `r` and `thin` control the query radius and thinning factor respectively, their default values are shown.

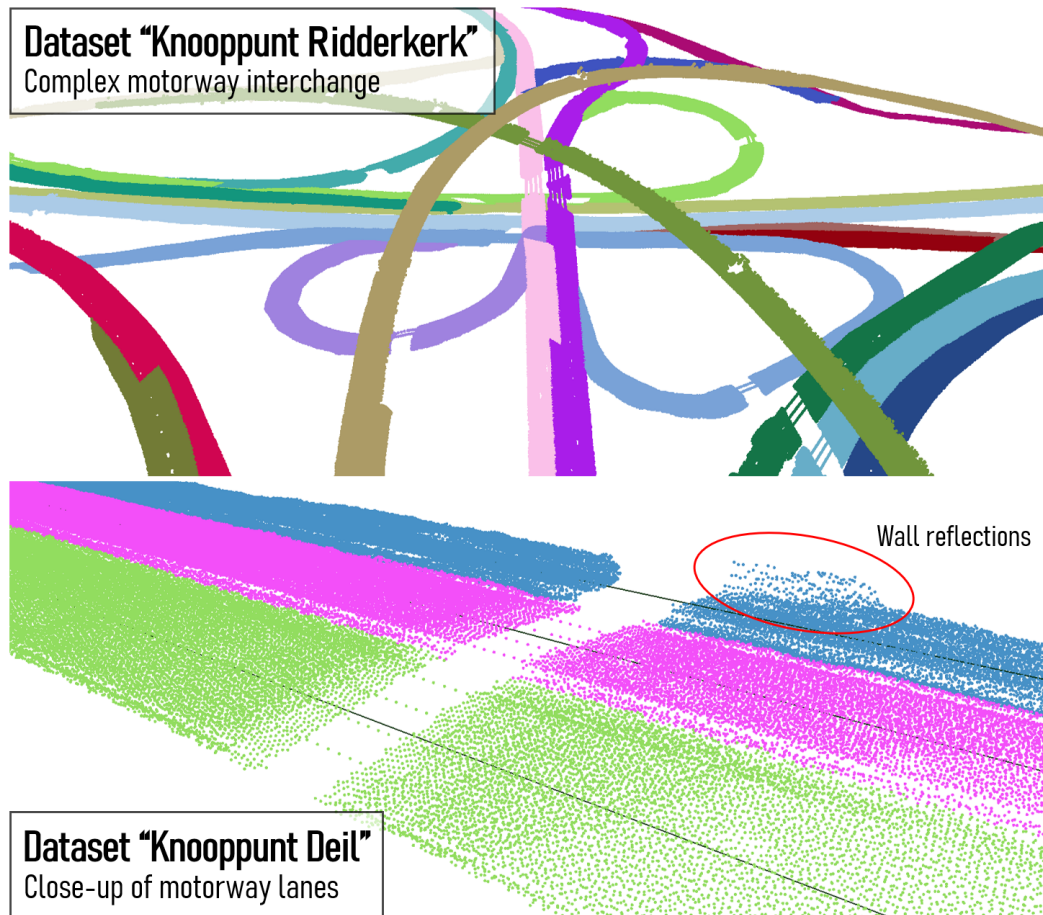


Figure 4.6: Visualisations illustrating the results of Lidar segmentation. The colour-coding of the subclouds was randomly generated based on their NBRs IDs. In the bottom image, the centrelines are shown in black.

The last line of code writes the resulting 3D geometry to disk, “mimicking” the structure of the input file. The variable is named in such a way to distinguish it from the variable containing the file path where the final 3D-NWB results will be written, called `accurateZ_fpath`. This step is optional, it is intended for debugging and demonstration purposes only.

The results of this step are not stored in a separate variable, but are added to the `GeoDataFrame` representation of the input NWB Shapefile, found in the `.nwb` variable of the `nbrs_manager` class.

4.2.3 Lidar segmentation

Figure 4.6 shows some visualisations of the results of Lidar segmentation. For subclouds which are positioned far from each other, a clear separation is observable. Ones that are close to one another often overlap, such as in various places in the top visualisation. This is the result of there not being much space between the roads themselves. The overlapping parts of such subclouds may contain duplicate points (in other words, points may be part of multiple subclouds). Out of these “duplicate” points, the visualisation only shows the ones that were loaded last, hence some subclouds may appear thinner than they are.

General description of results

The properties which we are looking for in the resulting subclouds is that they contain as many of the road surface points, and as few of the surrounding unrelated points, as possible – especially with

regards to points reflected from occluding objects. Figure 4.6 illustrates quite vividly that indeed, each NBRs' subcloud is clearly related to the underlying real-life road surface and that very few unrelated points are included.

Since this is not yet the stage where conservative thresholds are enforced, it is possible that a small number of unrelated points will be retained. This mostly happens just before and after regions of occlusion, where the underlying plane fits have already been affected by the occlusion but not enough to be excluded (i.e. due to a "transitional plane fit" illustrated in Figure 3.7). An example of such a group of points (the bottom part of a wall) is found in the blue subcloud in the bottom part of Figure 4.6. Reflections from tall vehicles, as well as from roadside guardrails and small signs may also be retained in this step sometimes, which explains the fuzzy appearance of the bridges on the left in the same figure.

This circumstance arises because the Lidar patches inevitably include off-road points, causing the fitted planes not to lie perfectly on the road surfaces. This in turn means that using very strict point-to-plane thresholds is not advisable, in turn making it possible for non-surface points to make it into the subclouds. While iteratively refining the plane fits could reduce the impact of this issue, it would also introduce unnecessary computational complexity. This step of the pipeline does not *need* to produce perfect results yet, the small number of unrelated points can be handled by later pipeline steps.

The top visualisation in Figure 4.6 shows the *Knooppunt Ridderkerk* motorway junction in which many motorway lanes and ramps are present in complex 3D relationships, in one place including an area with 4 overlapping roads. The correctness of the resulting subclouds demonstrates that although some of my approach is procedural and relies on a fixed parametrisation, it is still robust enough to work in the simplest, as well as the most challenging environments.

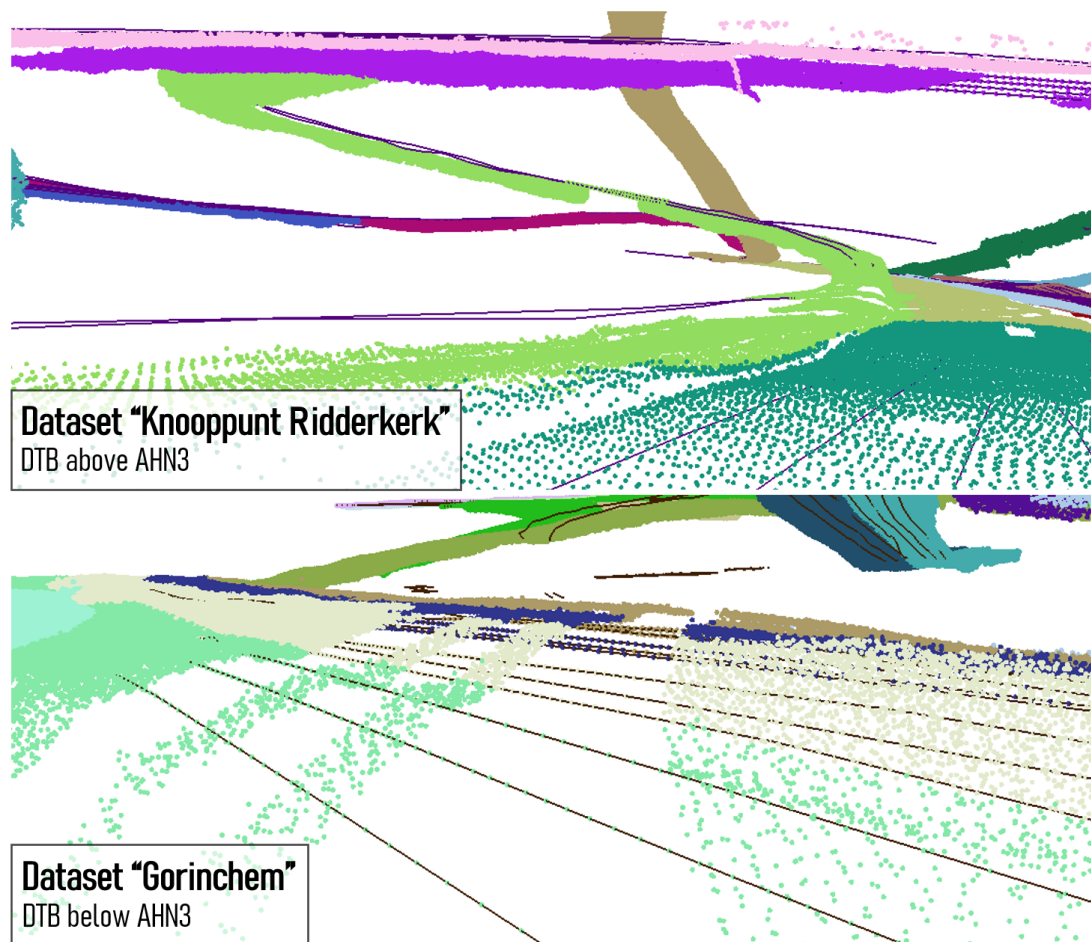


Figure 4.7: Renders showing the disagreement between AHN3 and DTB. Same symbology as in Figure 4.6.

DTB's usefulness

As discussed in-depth in Section 3.3.3, the final version of my code works well even in the presence of long occluded regions, even without DTB coverage. However, DTB is still used wherever available and useful. One clear benefit is that DTB can help rectify plane fits, thereby segmenting AHN3 more accurately in the vicinity of the gaps. Often, this automatically fixes the outlier-related issue I mentioned above in the context of slightly corrupted plane fits just before and after data gaps.

Furthermore, even in the knowledge that DTB is severely outdated in many places (see Section 2.3.3), it is still the only information source we have about roads where AHN3 coverage is missing. Where the break in AHN3 coverage is short and DTB is outdated (or missing), linear interpolation prevails. However, where longer gaps are present and the road's elevation may change inside of them, DTB is important even if its data is outdated.

Unlike in most locations, DTB has good coverage in the particular motorway junctions depicted in Figures 4.6 and 4.7, especially in the *Knooppunt Ridderkerk* junction. Each of the visualisations in these figures contain examples of how DTB-based "assistance" manifests itself in the output. Where subclouds contain Lidar-gaps filled with points in a linear arrangement, one can be certain that DTB was used to re-fit planes and to supply points to the subcloud. In the upper part of Figure 4.6, these linear sets of points appear in the lower motorway lanes and ramps wherever the overlying roads cast "shadows" on them, creating occluded zones of various shapes. Each level of the stack of roads has such features, except for the one on the top, which is not occluded by any objects.

While this demonstrates that DTB – or any support dataset with road surface elevation measurements – can be helpful in complementing this procedure (which is otherwise based entirely on AHN3), it also highlights one of DTB's weaknesses. While the areas shown in these figures have good DTB coverage, the DTB lines in the *Knooppunt Ridderkerk* dataset are in some cases approximately two decades older than AHN3 (they are up-to-date in *Knooppunt Deil*). Figure 4.7 demonstrates that there are noticeable systematic differences between the road elevations as depicted by AHN3 and DTB.

In *Knooppunt Ridderkerk*, DTB is above AHN3 consistently, but the *Gorinchem* dataset and several others show DTB below AHN3. Moreover, as the top visualisation in Figure 4.7 shows, perfectly and poorly matching DTB and AHN3 data can often be found side-by-side. While in Section 2.3.3 I primarily attributed these problems to the effects of subsidence, a further investigation of the problem is justified based on these results. The reasons for the differences may be more complex than simply being the result of subsidence.

This issue draws our attention to the general issue of temporal discrepancies between all our datasets – NWB, AHN3, and DTB. This is further discussed in Sections 4.2.6 and 4.2.7 in the context of how it affects our results. Overall, the results suggest that even if we solely attribute the vertical land motion to subsidence, a 20 cm vertical accuracy can only be guaranteed by periodically re-measuring the input elevations in both the primary and the support datasets.

Splitting NBRS into parts

On the right in Figure 4.8, a road with neither AHN3 nor DTB coverage under some bridges is shown. The relevant NBRS was split into two parts. The matching colour of the points (purple) shows that they still belong to the same NBRS. However, the program stores a separate subclouds for each NBRS part, meaning that they are loaded as a separate MultiPoint object in the 3D viewer I used to generate these figures. NBRS splitting also performs as expected in my final implementation.

Parametrisation

The parametrisation of this pipeline step is extensive, because many parts of the algorithm are of a procedural nature. Hence, I will dedicate some attention here to describing the final configuration I used

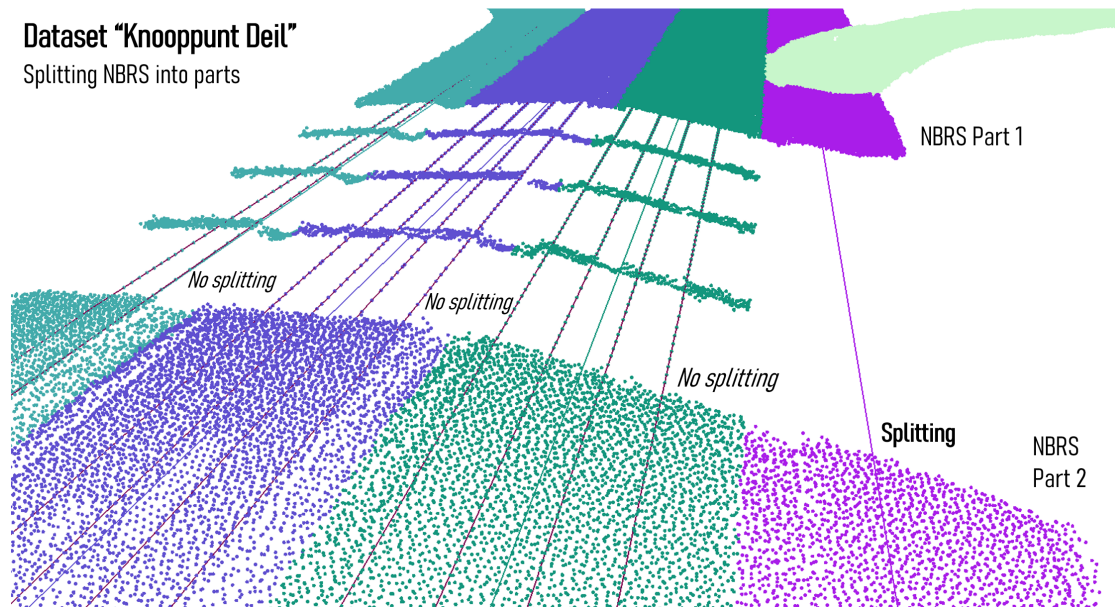


Figure 4.8: Visualisation illustrating the handling of gaps in AHN3 coverage during Lidar segmentation. The colour-coding of the 3D NBRS lines and the subclouds was randomly generated based on their NBRS IDs. The relevant DTB lines are shown in dark red, where available.

to produce my final results. Here I will not go into detail about the exact way in which these parameters are used, as I have already described this in Section 3.3.3 without specifying numerical values.

All parameters were derived from a process of experimentation and fine-tuning, although a good understanding of the problem, the procedures, and the properties of the input data were also essential in being able to define the parameters as well as to find suitable values for them.

Firstly, a query radius for the generation of the Lidar patches needs to be specified. I used a query radius of 10 metres, which is sufficiently long to allow most of road surface reflections to be included between centreline vertices. Using a smaller radius could, in some cases, improve the plane fitting results, but it would also cause the exclusion of useful Lidar points from the patches simply due to the spherical geometry of the query regions. While the radial queries are not perfectly suitable for this step, I did not implement a custom query mechanism because the performance of the radial KD-tree queries is needed for this step. Performance is also heavily influenced by the vertex densification threshold and Lidar thinning factor used previously; denser NBRS vertices and a denser input point cloud means that the processing time will increase considerably.

When the program examines the Lidar patches corresponding to each NBRS vertex, it either fits a plane and passes on the patch, only passes on the Lidar patch, or does neither. The program stops fitting planes below 2 points per square metre, and stops passing on points below 1. In this step, "points per square metre" is interpreted rather loosely, since the patches are actually based on points falling into spheres of a given radius rather than circles. However, since Lidar points are assumed to have been reflected from a *nearly* 2.5D surface locally, this assumption is not unreasonable.

The next set of parameters control the detection of "plane instability" while examining the succession of plane fits and underlying Lidar patches. DTB-based assistance is attempted if any of the following conditions are met: the standard deviation of the Lidar patch's elevations exceeds 10 cm, the distance between the plane and the corresponding NBRS vertex increased by more than 50% relative to the previous iteration, or the median of the Lidar patch's elevations increased by more than 50% since the last iteration. The latter two conditions are only considered if the absolute value of the underlying metric (distance from NBRS, median elevation) exceeds 20 cm.

The way the metric related to the centreline-subcloud elevation differences is enforced represents the workaround that ensures that the occasional poor polynomial fits of the preliminary elevation estima-

4 Results

tion step do not cause problems. These incorrect fits cause the preliminary elevations to underestimate or overestimate elevations locally. Making this metric detect *abrupt changes* rather than simply evaluating a distance threshold adds enough flexibility to bridge the problem.

When DTB-based assistance is attempted, the initial query radius when looking for DTB points is 40 cm. If enough points were found to re-fit the plane (more than 2), then the second repositioning query is performed with the same radius as the one used in the generation of the Lidar patches (10 m in my final parametrisation), because at this point it is assumed that the query position has been moved close to the true elevation of the road surface. When deciding whether to do a final re-fit on the nearby part of the Lidar patch, the program once again uses the condition that the density of these points should at least be 2 points per m². Lidar points are deemed to be close if they are less than 1 m away from the plane.

When pre-selecting the final set of conformant points from the patches, the program uses a threshold distance of 5% of the query radius used in the initial Lidar patch queries, corresponding to 50 cm in my final configuration. In other words, points less than 50 cm away from the final (potentially adjusted) plane fits are marked as road surface points.

While the post-processing operations of this pipeline step (breaking into NBRS parts and filtering outliers) also have a few parameters, these are insignificant and are thus omitted from this discussion.

Using the implementation

The below code snippet shows the code I used to generate my final results.

```
roads.segment_lidar(fpath = dtb_fpath, r = 10)
roads.write_subclouds(fpath = subclouds_fpath)
```

The first line performs the point cloud segmentation itself, with a radius of 10 m for the KD-tree queries that generate the Lidar patches. The variable `dtb_fpath` is assumed to contain the file path to the cropped DTB file belonging to the desired testing dataset. The second line writes the resulting subclouds to disk, the argument variable is assumed to contain the file path to the desired output file.

The intermediate results that the second line writes to disk “mimic” the structure of the input LAS file. However, each point is given three new properties. The property `ORIGIN` determines whether the given point originates from AHN3 (denoted by the value 0) or DTB (denoted by the value 1). The properties `NBRS_ID` and `PART_ID` determine which NBRS, and which part of that NBRS a given point belongs to. NBRS that were not split into parts are still represented by the same data structure, but all their points are found in a single part with `PART_ID = 0`.

In the class itself, the resulting subclouds can be accessed via `.nbrs_subclouds[nbrs_id][part_id]`, where `nbrs_id` and `part_id` are variables which should contain the ID of a specific NBRS, and the ID of one of its parts respectively. Furthermore, one can find the vertex indices corresponding to intervals with AHN3 or DTB coverage in `.nbrs_parts[nbrs_id]`, which is used to define the NBRS parts in the software.

4.2.4 Edge approximation

Visualisations showing the results of the edge approximation step are shown in Figure 4.9. The black lines correspond to NWB centrelines, while the closely spaced, orthogonal lines are the cross-sections that the program attempts to create on each centreline vertex. The lines connecting the ends of the cross-sections on each side of the centrelines are the preliminary edges that represent the main product of this processing step. As in all 3D visualisations in this chapter, the vertical dimension is once again exaggerated five times to make vertical changes better visible.

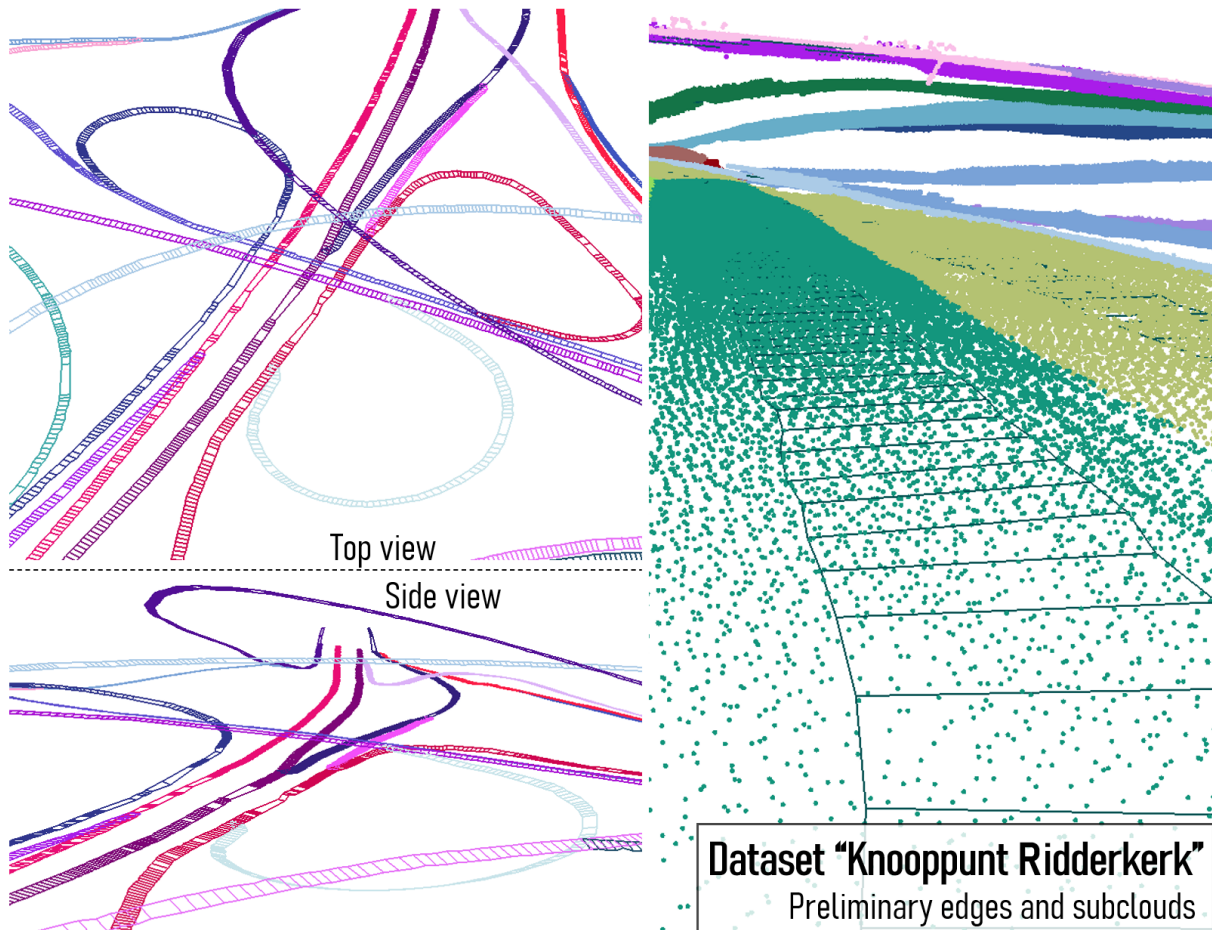


Figure 4.9: Renders illustrating the results of preliminary edge approximation. Left: visualisations showing the generated preliminary edges and cross-sections. Right: visualisation comparing the edges and cross-sections to the subclouds. All geometries are coloured randomly based on their NBRS IDs.

General description of results

The output of this step is mostly satisfactory, no road layouts apart from tunnels are known to me which would cause the algorithm to fail, or produce unusable results with the final parametrisation. Furthermore, owing to the verification step that takes place before accepting a cross-section (and extending the preliminary edge with its end vertices), the general shape of the edges is also quite well-behaved, and their elevation reflects what one would expect based on the underlying subclouds. In my final configuration, cross-sections have vertices every 10 cm (created via densification), and their elevation is derived from points no further than 25 cm away. This dense quantisation allows the algorithm to reconstruct road edges on a fine scale.

In the two visualisations on left in Figure 4.9, I show the preliminary edges only. The top image looks down on *Knooppunt Ridderkerk* from above, while the one below presents a sideways view of the same location. On the right in the figure, I show a visualisation in which a pair of preliminary edges and the underlying cross-sections can be compared with the subcloud that was used to generate them. In most cases, cross-sections and preliminary edges lie flat on the road surfaces, and even where noticeable blunders are observed, they correspond to underestimating or overestimating the road surface extents by about 2 m maximum.

While the overall quality is good and the results are certainly usable in terms of the requirements of the next two pipeline steps, there are a few properties and limitations of these results that are worth discussing.

On road width bounds

As I already mentioned in Section 3.3.4, the algorithm works with a fixed minimum and maximum road width. The maximum is enforced by using it as the length of the constructed cross-sections, while the minimum is enforced as part of the verification step.

The enforcement of the minimum width is less of a limitation; it merely prevents the edges from shrinking too much. However, the way in which the maximum width is enforced can be considered a limitation because road surfaces that are unusually wide will not be covered by the edges in their entirety. Using longer cross-sections (increasing the maximum width) increases the chances of returning false hits due to off-road points that conform well with the elevation of the road. With shorter cross-sections, the chances of this happening are reduced drastically. My final parametrisation uses minimum and maximum road widths of 3.5 and 7 m respectively.

There is a further reason why a fixed maximum width is useful. Motorway lanes are represented by discrete centrelines in *NWB*, which means they will be treated as separate *NBR*s in my system. However, such lanes are often constructed on a single paved surface, meaning that my method cannot be used to derive edges at least for one side of them. This is another reason why the maximum width is important; one such scenario is shown on the left in Figure 4.10.

NWB's crude georeferencing necessitates the use of a lower-than-optimal value for the maximum road width. If *NWB* itself is shifted towards the edge of a road locally, generated cross-sections will be corrupted there by off-road elevations. Using larger values for the maximum width will only make this problem worse. In the absence of this problem, the value could be increased by a few metres based on my experience with the data. I implemented a workaround that mitigates the effects of this issue. The line fits that are generated for every cross-section are actually only fitted on the central 40% of the densified cross-section vertices, which is then extrapolated to the outer vertices. This helps minimise the effects of the off-road elevation measurements that may affect the outer cross-section vertices.

Failed edge detection

While in well-exposed, straight roads this does not generally happen, there are lengths of roads where finding edge points will fail repeatedly. In such places, the algorithm does not save the cross-sections, and also does not add edge points to the preliminary edge *LineStrings*. One the left in Figure 4.9, this can be clearly observed, most commonly in occluded areas. It is also illustrated in Figure 3.9 under the bridge.

Cross-sections and corresponding edge vertices may be missing from the output for 3 main reasons. The first potential reason is the lack of sufficient elevation data in the neighbourhood of the cross-section. This happens in data gaps where both *AHN3* and *DTB* are missing, but *also* in most gaps where *DTB* is available. The latter is due to the fact that *DTB* samples linear features *along* the length of each road, and has a poor resolution in the direction that the cross-sections are attempting to sample. *DTB* would require special treatment to be more useful in such cases.

Such data gaps may exist under bridges for instance, but also in places where vehicles occluded a significant portion of the road. In the latter case, artefacts may be generated if the cross-sections are accepted because there is enough data *not* to trigger a skip while the conditions are relaxed due to repeated previous failures. This is shown on the right in Figure 4.10.

The second potential reason is the generation of poor line fits. If the elevation estimates of the cross-section vertices are scattered, the errors in the fit will be large. Elevations further than one standard deviation of the data-model error are not considered any further. If too many points are filtered out in such a way, the cross-section will be skipped. This happens most commonly due to *NWB*'s poor georeferencing, i.e. in the rare cases when not even only using the central 40% of the cross-section vertices could avoid including a large number of off-road elevation measurements.

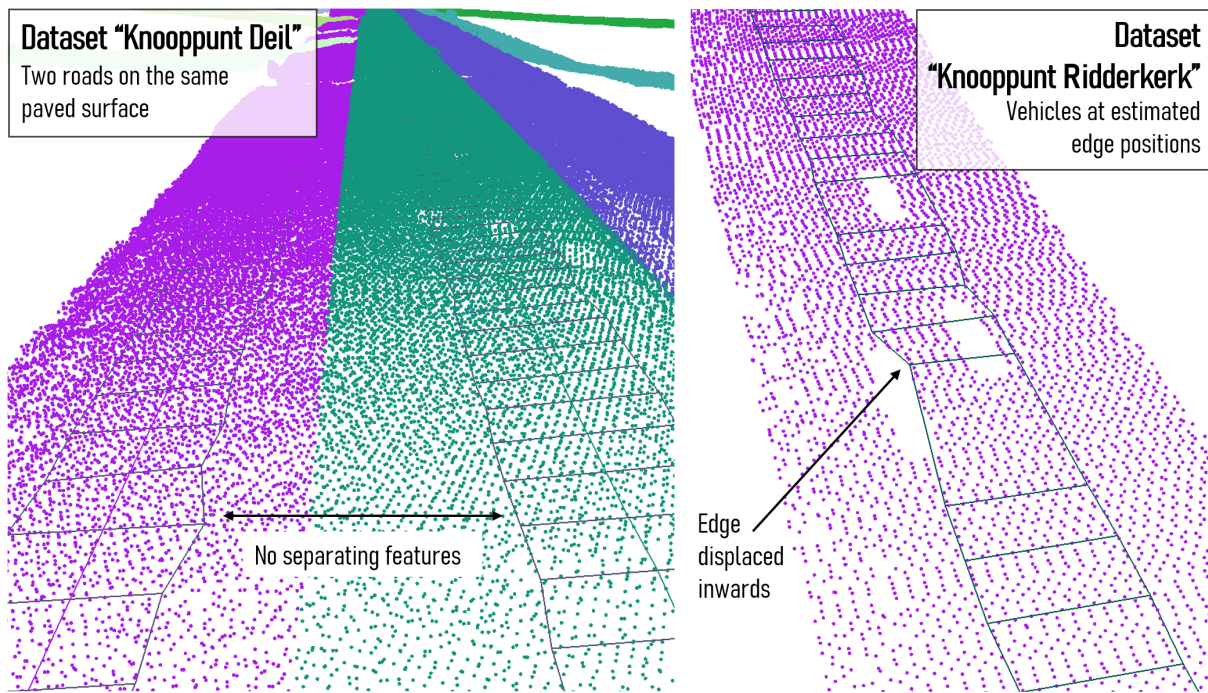


Figure 4.10: Visualisations illustrating challenging edge approximation scenarios. The preliminary edges and cross-sections are shown as dark lines, and the subclouds are coloured randomly based on their *NBR*S IDs. On the left, the relevant preliminary 3D-NWB centrelines are also shown in the same colour.

The third reason is the violation of one or more of the trio of threshold-based evaluations (minimum width, width change, elevation change). This is comparatively rare, but some of the missing cross-sections in the images on the left in Figure 4.9 are the result of this.

Edge generation in data gaps

In the absence of sufficient elevation data, cross-sections will be skipped frequently as I mentioned above. However, quite frequently, a small number of cross-sections will be accepted in such regions too, if *AHN3* coverage reappears temporarily, for instance due to a small gap between two bridges. Due to the repeated skipping of vertices, the conditions will almost certainly be relaxed there, hence sudden width or elevation changes will be allowed. This combination of factors may result in the generation of strange edge geometries in occluded zones.

Where roads are straight and the gaps are short, this does not represent a major issue. Even if the shape of the preliminary edges will be sub-optimal as a result, it will still respect the minimum road width condition, meaning that most *DTB* and *AHN3* points that may appear in the gap will still fall between the edges, which is useful for *TIN* construction.

Serious problems only arise when the gap appears at the end or the beginning of an *NBR*S part. In such cases, especially if there is no intermittent *AHN3* coverage in the gap, no cross-sections will be accepted at all, and therefore the program will be unable to extend the edges to the end of the *NBR*S part. The beginning or the end of the centreline will simply not be covered. Later in the *TIN* construction step, this means that the local *DTB* points will not be inserted into the *TIN* (because they are not between the generated edges), and the *TIN* surface will, as a result, also not extend all the way to the end of the *NBR*S part. This introduces many linearly interpolated elevations to the final 3D-NWB output, which may be incorrect.

A similar problem arises when a road is occluded in a bend. Depending on the sharpness of the bend and the extent of the occlusion, the preliminary edges may end up directly connecting the last cross-section before the occlusion and the first one after. Taking such a "shortcut" means that *DTB* points

4 Results

in the data gap will mostly be ignored during TIN generation because they will not fall between the preliminary edges.

I have not observed the above limitations to cause issues with most roads. However, they do mean that my system design is not compatible with *longer* tunnels out-of-the-box. Unless the tunnel is mostly straight and the relevant NBRs part continues across its full length, the DTB points in the tunnel may be ignored during TIN construction, and therefore the TIN models and the 3D conversion of NWB will be incorrect locally. I tested and verified this issue with the *Amsterdam Hemhavens* and *Amsterdam Zuid* testing datasets, which both contain tunnels.

As I noted in Section 2.3.3, I treat DTB as a *placeholder* for a better supporting dataset (optimally, MLS data). As a result, its vector properties are not used – it is assumed to consist of generic point data. However, treating it properly as a 3D line dataset inside AHN3 data gaps would fix the above issues, i.e. it would become possible to generate edge estimates from DTB much like in the commercial implementation. Such an additional feature did not fit into the schedule of my project, hence it is only further discussed in the Future work section in the Conclusions chapter (see Section 5.7).

Using the implementation

In my example code on GitHub, I use the following two lines to generate and export the preliminary edges:

```
roads.estimate_edges(min_width = 3.5, max_width = 7, thres = 1, perc_to_fit = 0.4)
roads.write_edges(fpath_edges = edges_fpath, fpath_crosses = crosses_fpath)
```

The first line generates the preliminary edges. The arguments (all compulsory) set the minimum and maximum road width, the outlier filtering threshold, and the ratio of how much of the cross-sections should be fitted with lines. The first two arguments should be specified in metres. The second argument specifies the number of standard deviations of data-model errors, within which points should be considered inliers, so the current value means one standard deviation. The last argument accepts values between 0 and 1, the current value means that the central 40% of cross-sections will be used as the basis for the line fits.

The second line writes the results to disk. Both the edges and the cross-sections are written, `edges_fpath` and `crosses_fpath` are assumed to contain file paths where these should be written (as Shapefiles). In the class itself, the results are found in `.nbrs_edges` and `.nbrs_crosses` as GeoDataFrame objects.

4.2.5 Active contour optimisation

As Figures 4.11 and 4.12 show, all planned parts of this pipeline step output the expected results, albeit with occasional artefacts and mediocre overall quality. The contours are smooth, they generally reflect the shape of the roads accurately, and only occasionally suffer from major blunders. However, even small deviations beyond the road edges would cause off-road Lidar reflections to be classified as road points, and thus be inserted in the TIN models in the next step. Unfortunately, such deviations of various sizes occur frequently, as the close-up images in Figure 4.12 demonstrate. This section will focus on explaining why exactly it is difficult to guarantee that this workflow functions reliably, as this was the reason for a major revision of the design of the preliminary edge detection and TIN construction steps, which I already mentioned in Section 3.3.4.

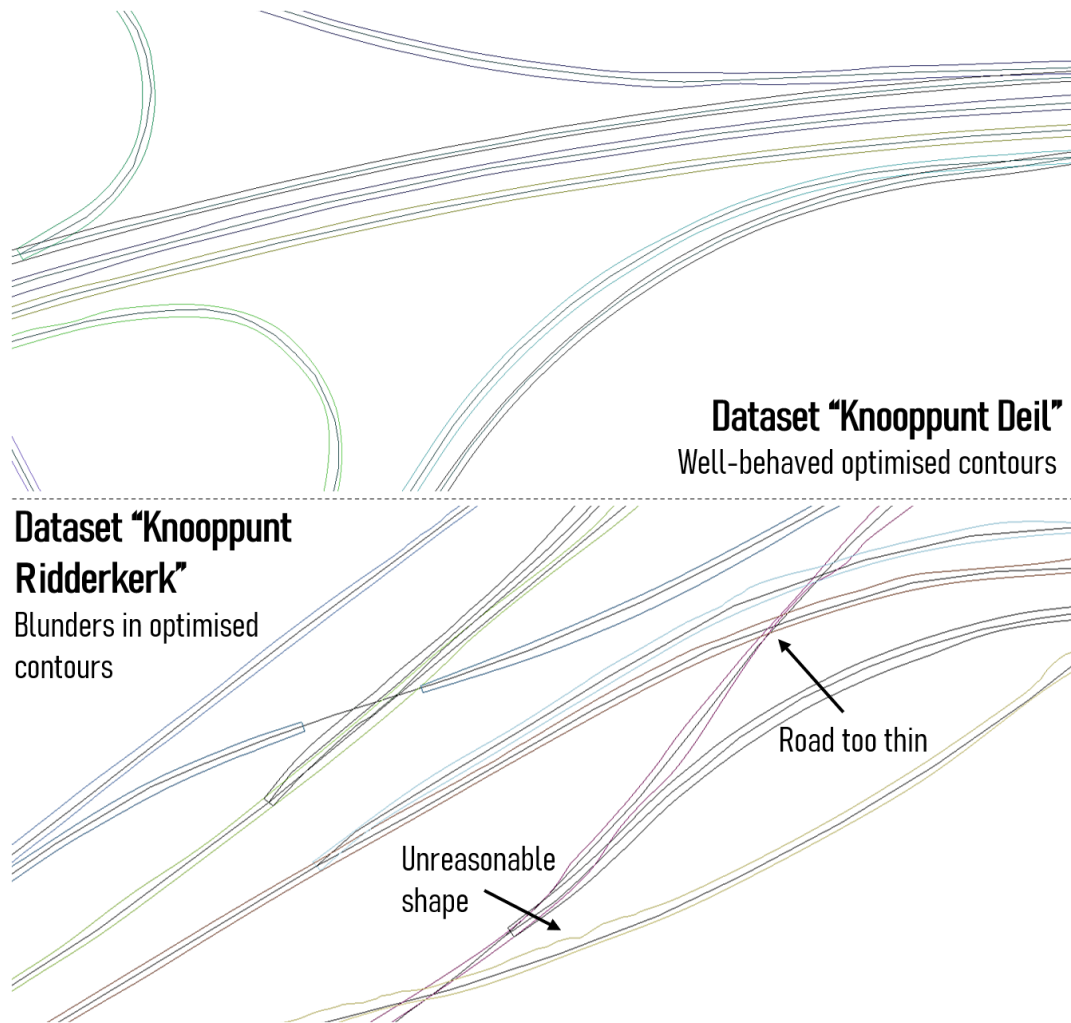


Figure 4.11: 2D visualisations illustrating various degrees of active contour optimisation success. NWB is shown as dark grey lines, whereas the optimised edges are coloured randomly based on their NBRS IDs.

Attractor maps

Some attractor maps can be seen in Figure 4.12. Each NBRS part has its own attractor map, and since subclouds may overlap, so can the attractor maps. In the figure, attractor maps that are separated from others by a fair amount of distance can be examined in their full width, while only the one the was drawn last by the visualisation software can be examined completely where overlapping occurs.

The bright parts of the attractor maps correspond to regions where the normal vectors of the Lidar points are oriented uniformly, while the darker regions indicate divergent normal vectors. The linear boundary between such regions thus marks the edge of the smooth road surface in most places, as it corresponds to an abrupt increase in normal vector divergence. I used a pixel size of 0.5 m (in both dimensions) to generate these attractor maps, and the attractor map values are based on using a 5-by-5 kernel, sampling the neighbourhood via approximately 30 inner products for each pixel.

The optimised contours are shown overlain on the attractor maps in Figure 4.12. While the *general* appearance of the contours (shown in Figure 4.11) is acceptable in many places, comparing them with the attractor maps reveals that they are not reliably positioned on the breaks in smoothness. As the annotations in the figure show, perturbation due to vehicles (or gaps left by vehicles), and optimised edges lying consistently outside the road surfaces represent a significant problem. Together with the issues seen in Figure 4.11, we may conclude that the results contain large and small scale issues in equal measures, and that these are disruptive enough to justify considering alternatives.

Patterns of failure

One important pattern is that the contours are sensitive to small-scale disruptions in the preliminary edges, and it tends to exaggerate them. A few outlier edge points for instance (a short, abrupt expansion of the preliminary edges) can introduce large bulges into the optimised edges. Similarly, where the preliminary edges shrink (for instance due to the influence of stationary vehicles), the optimised contours will tend to do so too, but on a much larger scale. The severity of the generated artefacts also depends on the local properties of the attractor maps.

Another pattern which I already mentioned in 3.3.5 is that where preliminary edges fall outside the bright parts of attractor maps, the the optimisation procedure will often fail to move them back to the primary break in smoothness. The off-road areas may contain other high-contrast features due to the unevenness of the underlying real-life surfaces, and the edges will often be drawn to these instead of the edge of the road. This is in part due to the large weight the optimisation algorithm gives to the *proximity* of the edges.

For the same reason, deliberately underestimating the road width (which was done in [Boyko and Funkhouser \[2011\]](#)) does not represent a solution here. If the preliminary edges are too far inwards from the break in smoothness, they will simply stay unchanged during optimisation. This behaviour cannot be changed simply via the parametrisation – I already give nearly full weight to edge detection in my final configuration. I also experimented with underestimating the preliminary road widths and giving more weight to attraction to darkness. Unfortunately, the results of this approach are even more unpredictable because the algorithm will frequently move the contours into the dark areas rather than stop at the edges.

Lastly, the contours may also become corrupted if the break in smoothness is itself missing from the attractor maps. The two most common reasons that tend to cause this are unusually wide paved surfaces (wider than the maximum width of the underlying subcloud), and occluded zones where only *DTB* is available. The former is manifested in the attractor maps by the bright zone extending all the way to the edge of the map. In such regions, active contour optimisation will leave the preliminary edges mostly unchanged, but large-scale artefacts can also happen because of it. The latter (missing *AHN3* coverage) mostly causes unpredictable artefacts because the edge needs to step into the no-data region and then back into the road surface on the other side, transgressing two “edges” that are orthogonal to its general direction. Using a no-data value that is almost the same as typical road surface pixel values helped, but it could not solve the issue completely. Only by splitting *NBR3* into parts here too, could this issue be eliminated.

Finding a suitable value for no-data pixels required some experimentation. I found it most effective to set all no-data pixels to a value close to the values seen in bright road surface areas. So, in addition to the occluded areas, all other parts of the rectangular rasters are set to this value (specifically, a value of 1). While this creates artificial high-contrast edges in the attractor maps at the boundaries of the underlying subclouds, the preliminary edges do not get drawn to them because they are generally much closer to the edge introduced by the edge of the road.

Active contour optimisation parameters

The α parameter controls lengthwise shrinking. I set it to a value of zero to indicate that this behaviour is undesired. In theory, the optimisation procedure introduces length changes into the contours naturally, by adjusting their shape. α should therefore be set to a small, but nonzero value to allow this behaviour. In practice, I found that this affects the results negatively, and a value of zero works better.

The parameter β controls the smoothness of the resulting contours, which can also be intuitively thought of as controlling the tension of the underlying splines that active contour optimisation repeatedly fits. I set this value to 0.01, which in my experience corresponds to medium tension. Based on the testing I have done, smoothing the preliminary edges is one task in which active contour optimisation excels; it can eliminate small-scale protrusions that are generally meaningless, and can thus be considered noise.

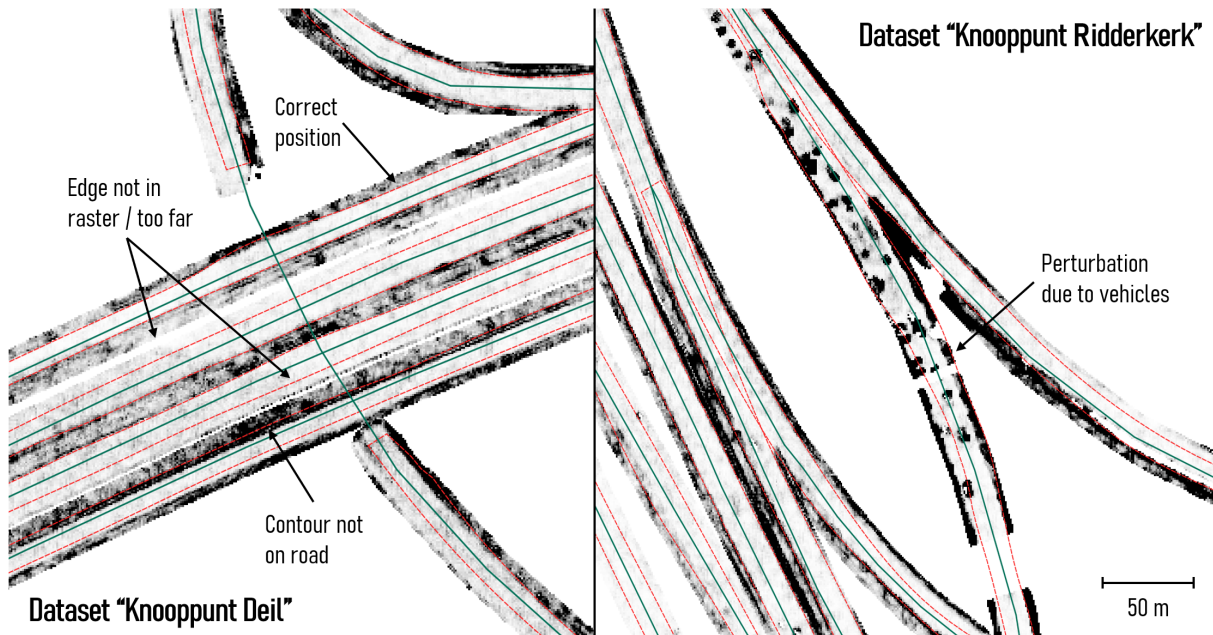


Figure 4.12: 2D visualisations comparing optimised edges to the underlying attractor maps. The attractor maps contain a single band with scalar values, hence they are shown visually as greyscale rasters. The NWB centrelines are shown in dark green, and the optimised contours as dashed red lines.

This in turn helps minimise the impact of the types of small-scale issues with preliminary edges by keeping contours relatively tense across them.

The parameter w_{line} controls attraction to dark or bright pixel values. The attractor maps that I described above have a sharp contrast between the brightness of off-road pixels (which are dark), and road pixels (which are bright). However, this contrast is localised to the edges of the roads, and any amount of attraction to either dark or bright areas would draw the contour deeper into that region rather than keep it on the boundary, both in theory and in practice. In my final implementation, it is set to 0.05 to introduce a very small amount of attraction to bright areas, so that the contours are more likely to stay on the inner side of the road edges rather than go past them.

Thus, attraction in my recommended parametrisation is controlled almost entirely by edge detection (parameter w_{edge}). I set it to 1, meaning that the iterative refinement of the contours will be governed primarily by attraction to edges, for reasons I already discussed above.

I decided to work solely with a maximum number of iterations (parameter $max_iterations$) rather than to use condition-based termination. Setting a boundary condition would terminate the optimisation process when the contours no longer move significantly, i.e. it checks when a minimum displacement threshold first becomes violated. Where the attractor maps are perfectly suitable for active contour optimisation, this approach works well. However, letting the contours evolve in such a way where the attractor maps are sub-optimal results in the drastic enlargement of the generated artefacts, as well as an unacceptable increase in computational complexity. This happens, for instance, where edges are not defined well enough, and where Lidar gaps are present. I found iteration limits between 1000 and 5000 to be the most effective.

The time step parameter γ and the number of pixels the contours are allowed to shift in a single iteration (parameter max_px_move) can be used to further fine-tune how quickly the optimisation lets the contours evolve. I set these two values to 0.005 and 1 respectively, which corresponds to a relatively slow iteration, appropriate to the relatively small-scale changes we desire.

The above configuration of values is the result of a process of iterative combined revision of the values themselves, and the attractor map generation technique, as I mentioned in Section 3.3.5. While I experimented with a wide range of parametrisations, the possibility remains that a better one exists. The

4 Results

parameters themselves offer many permutations, and the fact that the preliminary edge and attractor map generation also affects the results further increases the range of possibilities.

However, despite having tried most types of parameter configurations and many different adjustments to the preliminary edges and attractor maps, I was unable to find a configuration that produces satisfactory results within the development time reserved for this step. The quality of the optimised edges is simply not good enough to be used to classify Lidar points reliably based on them. The situation was worsened by the fact that the combined computational complexity of generating high-resolution attractor maps and of using the optimisation algorithm made the refinement procedure a rather difficult and time-consuming task. This is what eventually led to my decision to instead focus on improving the quality of the preliminary edges and use them directly in the TIN construction step.

Choice of algorithm

Contributing to the above uncertainty regarding the effectiveness of active contour optimisation is the fact that in relevant literature (e.g. [Boyko and Funkhouser \[2011\]](#)), mentions of its ineffectiveness relative to more sophisticated algorithms is made. My hypothesis was that with a sufficiently good pre-selection of Lidar points and pre-processing of attractor maps, conventional active contour optimisation could still work well, but this appears not to be the case in practice.

Lesser known, but more sophisticated offshoots of active contour optimisation exist, but have no open-source Python implementations. One such example is the “ribbon snakes” method. Considering the volume of further tasks in this project, I opted not to attempt to implement it based on first principles, especially considering that their superiority is not clearly demonstrated in relevant literature. They, too, are prone to producing artefacts of various types, even if they perform slightly better than conventional active contour optimisation.

Using the implementation

The following lines of code may be used to run active contour optimisation and export the attractor maps and resulting optimised edges:

```
roads.optimise_edges(size = 0.5,
                    a = 0, b = 0.01, g = 0.005,
                    w_l = 0.05, w_e = 1,
                    max_iter = 1000)
roads.write_maps(fpath = maps_fpath)
roads.write_contours(fpath = conts_fpath)
```

The first argument `size` in the active contour optimisation method corresponds to the desired pixel size. The rest of the parameters expose some of the active contour optimisation parameters that I found to be useful for making smaller changes to the algorithm’s behaviour. The arguments `a`, `b` and `g` correspond to α , β and γ respectively, while `w_l` and `w_e` correspond to the two parameters controlling attraction to brightness and edges (`w_line` `w_edge` respectively). The last parameter sets the maximum number of iterations.

The `.write_maps(maps_fpath)` method writes all attractor maps generated (one per NBRS part) as GeoTIFF rasters, tagging the file name with the relevant NBRS ID and part ID. Hence, the argument file name is expected to correspond to the first part of the file name only, e.g. `.../C_39CZ1_map` would work. Reserving a separate folder for these is recommended. The contours are written as a single Shapefile.

In the class, the maps can be found in the variable `.nbrs_maps[nbrs_id][part_id]`, while `.nbrs_contours` contains the contours in the form of a GeoDataFrame.

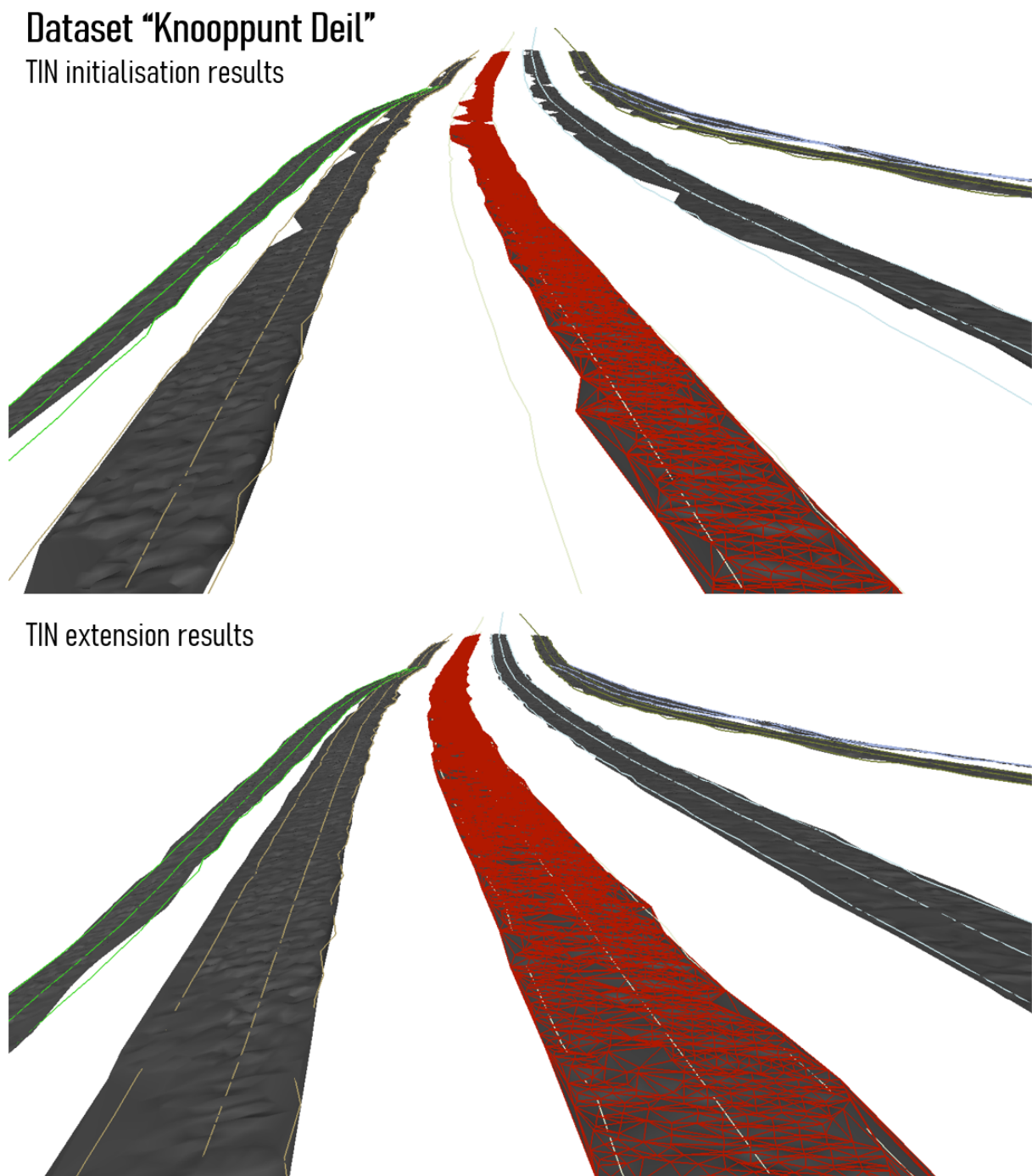


Figure 4.13: Visualisations illustrating the results of TIN initialisation and extension. The TIN surfaces are shaded in gray, and the preliminary 3D-NWB and edge geometries are coloured randomly, based on their NBRS IDs. The triangulation of one of the TINs is shown as a red wireframe.

4.2.6 TIN construction

By adjusting my methods to the circumstance of not being able to produce accurate enough optimised edges, I created a different implementation than originally planned, but one which is still robust and accurate. Figures 4.13 and 4.14 show examples of the resulting models compared with the preliminary edges and preliminary elevations. The images in Figure 4.13 show an initial TIN surface, and the same TIN after the extension stage. In these figures, the preliminary edges are shown because the initial TIN surface is seeded halfway between them, and because the TIN is only allowed to grow between them in the initialisation stage. The upper, large-scale image in Figure 4.14 shows an overview of all TIN surfaces in the *Knooppunt Deil* dataset, and the bottom two images show small-scale examples of typical extension artefacts. The TIN structure is highlighted in one of the TINs in Figure 4.13.

TIN initialisation

A comparison of the initialisation step's insertion boundary is shown in Figure 4.13 both with initial TINs and extended ones. The pre-selection step takes place in 2D, but for viewing convenience I used preliminary edges in this example visualisation, which are originally 3D geometries (in contrast with the optimised edges, which are 2D geometries).

While in most cases this does not represent a practical issue, my results suggest that there is a theoretical limitation to my methods. Since they were inspired by ground filtering algorithms, they are not particularly sensitive to gradual changes in the road surfaces, and especially insensitive to smooth transitions. The approach appears to excel at eliminating outlier points that were left undetected during previous steps, and detecting the edges of the roads where they are clearly defined by a significant vertical shift in the Lidar points, for instance a high curb or a wall. However, the conditional insertion tests often have difficulty in reliably recognising points close to, but not quite on the road surface where the edges are not well defined. Avoiding the insertion of such transitional points is key, because they may then act as bridges between road points and off-road points in subsequent iterations, thereby allowing the surface to grow in undesired directions.

The image on the bottom left in Figure 4.14 shows an area that exhibits the above type of challenging scenario and causes a small region of sloping terrain points to be added to the initial TIN. The bottom right image in the same figure shows a similar type of artefact which occurs due to NWB getting as close as within 5-20 centimetres from the outer edges of the bending road, resulting in the insertion of many off-road points. In the latter case, it is possible that the "bridge" points were already inserted in the seeding step, because the outer preliminary edge was constructed far beyond the road's real edge.

Had my original intention of producing more accurate (optimised) road edges succeeded, this would not have been a problem because the pre-selected Lidar points would have nearly all part of the road surface. Although I adapted my approach to the less optimal quality of the input edges, I was unable to completely overcome this limitation without a complete redesign, which was not possible within the available timeframe. Fortunately, in practice the initial TIN models are almost always well-behaved around the centrelines, and suffer from very few artefacts of this kind where NWB is *correctly positioned*. The careful conditional insertions when growing the TINs (where not only one, but multiple surrounding triangles are used to model the planar trend in the surroundings) helped mitigate this issue significantly.

For the TIN initialisation step, I used an elevation discrepancy threshold of 10 cm, and an angle threshold of 0.12 radians (about 7 degrees) in my final configuration. For the radial point queries that occur at the locations of successful insertions (to fill the buffer for the next iteration), I used a radius of 1 m.

In all study areas, and especially where NWB lies correctly on the road surface in 2D, my approach produces smooth 3D surfaces in which, as Figure 4.13 shows, most of the variation is solely due to stochastic noise in the Lidar data. Off-road points are only inserted in significant numbers, where the above conditions are satisfied; i.e. a very smooth transition characterises the edge of the road or the underlying preliminary or optimised road edges were also significantly shifted outside of the road surface (due to problems with NWB, or for any other reason).

TIN extension

Figure 4.13 shows the visual appearance of one particular NBRS part before and after applying TIN extension, in a location where it works nearly perfectly. The effectiveness of this step relative to its planned purpose is not uniform across all areas. Most road geometries allow it to perform well, but in certain places it may only serve to further exaggerate pre-existing artefacts.

TIN extension considers additional layers of points progressing away from the road's centre and moving towards the edges – even beyond them, if desired. For the final results I used 5 steps, each extending the boundary by 0.5 m via buffering and subtracting it from the polygon formed by the previous boundary to obtain the ring-shaped region of interest. Only those points are considered for insertion, which fall into the given region of interest in each iteration. The first iteration starts at a boundary half a metre from the seed geometry, hence 5 steps of 0.5 m each expand the maximum distance from the centre to 3 m, meaning that the largest boundary will be 6 m away from the centre of the road. One may notice that this is still smaller than the maximum road width I allowed in the preliminary edge approximation step (7 m). There are two reasons for this; firstly, in my final results I primarily used TIN extension to refine the TIN surfaces *within* the width of the preliminary edges. Secondly, wherever the width of the preliminary edges goes below the maximum (which happens quite often), this still represents an extension beyond those boundaries.

For instance, consider the example shown in Figure 4.13. In the highlighted initial TIN, the width of the model is only about 3 to 5 m on average, even though the preliminary edges are 6 to 7 m apart (close to the allowed maximum). Not all relevant points between them were inserted into the TIN in the "first pass" provided by TIN initialisation. TIN extension can solve this issue, effectively by executing additional passes over the same candidate points.

In the same visualisations, the road on the left of the highlighted one has a slightly thinner preliminary edge representation. These edges are already mostly filled by the TIN during the initialisation stage. For this particular road, extending beyond the preliminary edges is more important than reconsidering data within the preliminary edges. In this specific case, it is the hard shoulder that gets added to the TIN during extension. This illustrates the dual purpose of this part of the workflow.

Since the extension procedure considers points beyond the preliminary or optimised edges, it needs to exercise additional caution against including off-road points. In places where the edges underestimated the road width, further surface points may be discovered and added to the model – which is the main purpose of this step. However, where the edges are correct, it is important that the algorithm does not add further points. The same goes for areas affected by the artefacts described in connection with the bottom two visualisations in Figure 4.14; i.e. TIN extension should try not to worsen them.

Therefore, the algorithm uses stricter thresholds for the conditional insertions than the TIN initialisation step. In my final configuration, the values are 3 cm for the elevation discrepancy threshold (elevation above underlying triangle), and 0.04 radians (about 2 degrees) for the angle threshold. The radius of the buffer-filling queries was also reduced to 0.8 m.

While such a conservative parametrisation certainly avoids the addition of clearly defined outliers, I found it to offer only a partial solution to the above issues. After some careful inspection, I concluded that in almost all cases, pre-existing "bridge points" from the TIN initialisation step appear to be the culprits. They eliminate the gradients that would otherwise stop the extension from growing in a particular direction. Furthermore, it appears that the transition from road to off-road surfaces may occasionally take place on such a fine scale that not even these thresholds can prevent the surface growing towards them, even where TIN initialisation did not introduce such bridges.

On using small thresholds

An obvious solution to the issues related to inserting off-road points would be to use preliminary edges that are closer to the centrelines, and to make the parametrisations of both TIN initialisation and TIN extension stricter. However, there is a specific reason why this approach is guaranteed to fail. Both parametrisations already cause the conditional evaluations to be carried out on a scale comparable with

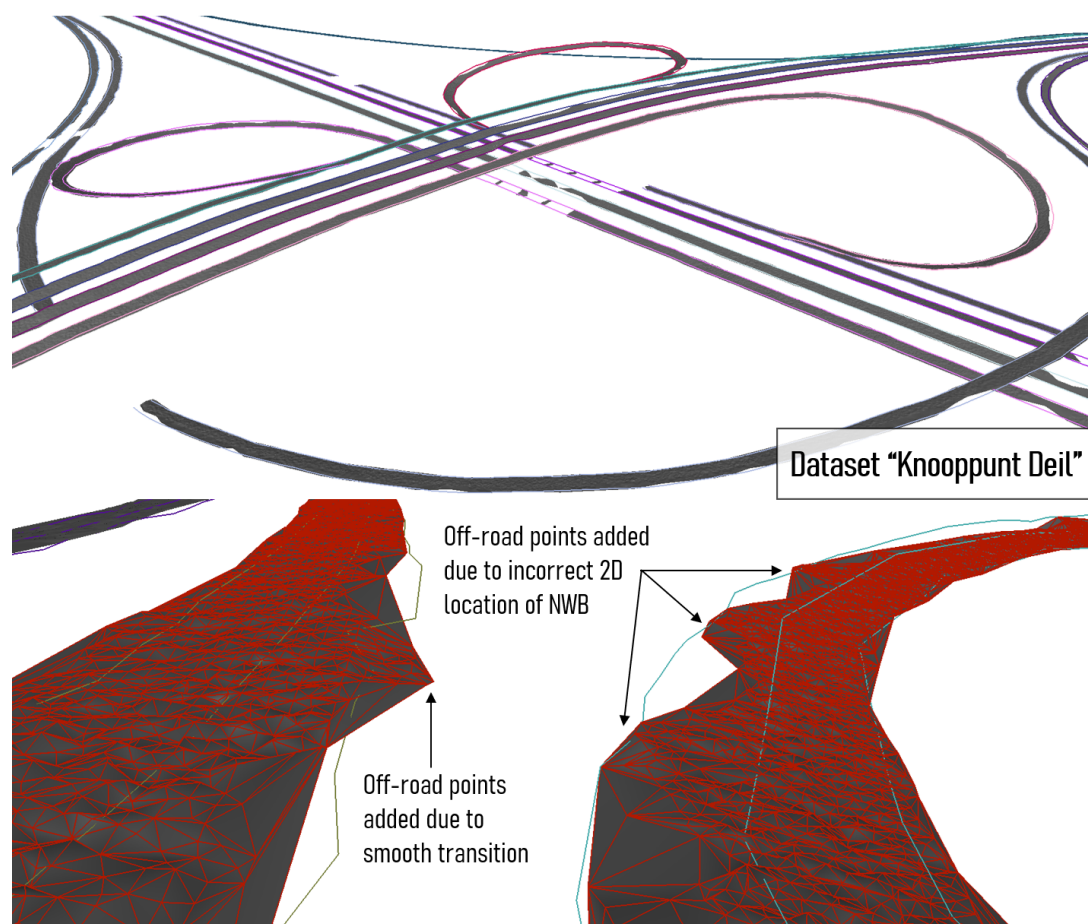


Figure 4.14: Visualisations providing an overview of constructed TINs (above) and illustrating TIN artefacts (below). The surfaces are shaded in gray, and the preliminary edge geometries are coloured randomly based on their NBRS IDs. The triangulation of some of the surfaces is shown as a red wireframe.

AHN3’s vertical accuracy. As 2.3.2 mentions, AHN3 has an elevation uncertainty of 15 cm at 95% uncertainty. This means that many insertions will actually fail due to the noise, not because of meaningful features.

The parametrisation of TIN initialisation (10 cm for the distance tests, 7 degrees for the angles) is already on a scale that falls within the territory of random noise. However, since the radial buffer-filling queries fetch many points rather than just a single neighbour, this generally does not affect the effectiveness of the method; the algorithm will inspect enough neighbours to still find a subset that are conformant, despite the noise. Even where this fails to an extent, the TIN extension algorithm will provide the additional passes that are necessary to overcome the issue; this is precisely what happened with the highlighted road in Figure 4.13.

As a result of this phenomenon, reducing the thresholds any further without increasing the query radius will inevitably block the surface from spreading into certain areas. Increasing the query radius is, in turn, not desired because it will create too large buffers (increasing computational complexity drastically), and also cause large triangles to be constructed in the TIN, which can in turn act as blocking factors in their own right if they do not represent the trend of the points in their interior accurately. Using large query radii also increases the chances of spreading TINs off the road surfaces, as it results in more off-road points being added to the buffers.

In TIN extension, I could use smaller thresholds than during initialisation because of the differences in the underlying workflows. Since extension considers “layers” of points progressing away from the centres of the road, it considers candidate points in a more “orderly” fashion. In TIN initialisation, the TIN

only grows towards a certain area if insertions lead the algorithm there, whereas the repeated seeding mechanism in the extension stage represents a more *targeted* growing approach. In practice, this means that the candidates are simply examined in a better order, leading to more efficient decision-making. This counteracts the increased impact the Lidar noise has on the scale of the thresholds that are being used.

A side-effect of this is that growing may be restarted during extension after a relatively large hiatus in certain places, leading to large triangles appearing in the TINs. The gaps – or more precisely, the small number of successful insertions in them – are mostly caused by the larger, slightly inaccurate triangles which I already mentioned in the previous paragraph. This can be seen in the TIN structure in the top image in Figure 4.13 – while the right half of the suspected area of the road has points spaced uniformly, the left side has large, slightly inaccurate triangles that prevented Lidar points from being inserted within their areas and growing the TIN further in that direction. As the bottom image in the same figure shows, the “second pass” over the data via the TIN extension solved this issue for the most part, although some of the large triangles remained.

Inspecting a larger area around the point that is being considered for insertion (instead of just the one triangle containing it) could reduce the impact of this issue, but it is costly in terms of computational complexity. This is part of the reason why I only use that approach when performing growing-type insertions. The illustration in Figure 3.12 may help the reader distinguish between the concepts of refining and growing-type insertions.

Note on figures

Both figures in this section (4.13 and 4.14) show TIN road surfaces that appear to be constrained by “invisible” external line geometries, as one would expect large triangles to fill the rest of the convex hull of the vertices in a Delaunay triangulation (DT). Originally, I planned to use a CDT to achieve this appearance, but in my final implementation I merely improved the appearance of the models before visualising them, by removing meaningless triangles based on area and circumference thresholds. This proved to be effective in eliminating the large triangles and sliver triangles that appear in the DT to fill the convex hull of the inserted points.

While these redundant triangles represent no issue in terms of interpolating elevations for NWB, they make the visual interpretation of the results difficult. Exporting the TINs after generating them automatically applies this filtering step in the final release of my code.

AHN3 data gaps that are patched in with DTB data tend to be covered by triangles in the TINs if the preliminary edges extend through them. The reason why in the top image in Figure 4.14 this appears not to be the case, is that some of these triangles were large enough to be filtered out to improve visual appearance. In the underlying data structure, the triangles are still there. The thresholds can be adjusted in my code to alter this behaviour.

TIN point density

While using 50% of the AHN3 point density (via a thinning factor of 2) offered practical benefits for all pipeline steps up to this point (especially the Lidar segmentation and edge approximation steps), the *quality* of the generated TINs does not significantly increase because of it.

Before running the TIN construction procedure, the program is equipped with subclouds, each with Lidar points relevant to a specific NBRS part. Since all prior steps are configured to keep as many of the surface points as possible, it is generally the case that their point density on the road surface is comparable to the thinned point density of the imported AHN3 data. Inserting such a large volume of points into the TINs may not always be practical. For instance, visualising the generated surfaces becomes slow even with modern software, and the stochastic Lidar noise becomes clearly visible (the ripples can be seen very clearly in Figures 4.13 4.14 due to the 5-fold vertical exaggeration). This much detail may also be impractical for applications that deal with modelling processes using the surfaces, and has implications for the accuracy assessment step too (see Section 4.3).

4 Results

The performance of this step thus depends on the input Lidar thinning. In practice, a thinning factor of 2 means that we are still working with around 10-30 point insertions per m^2 on the road surfaces, which results in mediocre performance. While my implementation did take performance considerations into account initially (for instance the buffer-filling approach is the result of this), later modifications, such as working with multiple triangles and plane fitting when growing the road surface resulted in the performance of the final implementation decreasing gradually. In particular, not running `TIN` extension can improve runtimes drastically, which may be useful for users who are only interested in interpolating `NWB` elevations.

As I will further explain in Section 4.3), the system design guarantees that `NWB` will generally lie on the `TIN` models in 2D, making it possible to interpolate elevations in it for its vertices. Exceptions to this rule occur in places where preliminary edge estimates or optimised edges disagree with `NWB` badly. Where this occurs, `TIN` initialisation will not be able to insert points into the `TINs` at the 2D location of `NWB`. With preliminary edges, this may only occur where cross-sections were skipped too many times in a row where the road is not straight, which may happen under various circumstances that I have already described in Section 4.2.4. With active contour optimisation, this may occur more frequently, depending on the local density of generated artefacts.

Two different kinds of quality

While the above discussion focuses on describing issues with the quality of the generated `TINs`, many of these issues are constrained to the academic goals of the project only. The academic goal related to the `TINs` is to make them complete and accurate representations of the real-life road surfaces. This is the quality on which I primarily focused in this section, while the next section will see more mentions of quality in terms of their suitability for interpolating elevations for `NWB`.

These two qualities need to be distinguished not only because of the conceptual differences, but because there are much less issues with the less academic goal of converting `NWB` to 3D than with producing ideal road surface models. The reason is, that for the 3D conversion to be accurate, one only needs complete and accurate `TIN` surfaces close to where the centrelines are found in 2D. Fortunately, these locations generally correspond to areas which are less difficult to reconstruct, than for instance the immediate vicinity of road edges.

Using the implementation

The following two commands may be used to run `TIN` construction and to export the resulting 3D surface models:

```
roads.build_tin(max_dh_int = 0.1, max_angle_int = 0.12, r_int = 1,
               max_dh_ext = 0.03, max_angle_ext = 0.04, r_ext = 0.8,
               ext_steps = 5, ext_dist = 0.5,
               type_edges = 'preliminary')
roads.write_tins(fpath = tin_fpath)
```

The first method invocation performs the `TIN` construction itself. The first line of arguments corresponds to the elevation and angle thresholds, and the buffer-filling query radius used in `TIN` initialisation, respectively. The role of the second line of arguments is identical, with the exception that they are used for `TIN` extension. The next two arguments (`ext_steps` and `ext_dist`) specify the number of extension steps to be performed, and the distance by which the query region should be expanded in each step. The first insertion boundary for extension is always a polygon created by buffering the seed `LineString` by 1 m; the extension starts from this base boundary. If no extension is desired, `ext_steps` should be set to 0. The last parameter, `type_edges` can be set either to `preliminary` or `optimised`; it controls which type of road edges the user desires to use.

The second method invocation writes the TINs to disk, one OBJ file for each NBRS part. As mentioned above, it also filters out large triangles and sliver triangles in the process. The supplied file path should only include the first part of the file name, as the NBRS ID, part ID and file extension will be added automatically (for instance `.../C_39CZ1_tin` would work). The use of a dedicated folder is recommended.

4.2.7 Interpolation in TINs and snapping

Figures 4.15 and 4.16 show examples of the results of interpolating elevations for NWB in the TINs generated in the previous step (including the use of the snapping feature that enforces continuity). Visual inspection of the results reveals that the methods used to generate them are robust and effective under almost all circumstances, including where complex 3D relationships and the extensive presence of other types of occlusion are encountered. The example visualisations shown here contain comparisons between the final elevation profiles and various intermediate results, namely the preliminary elevations, subclouds and preliminary edges in Figure 4.15, and the TIN models in Figure 4.16).

Generally, the results are in line with my expectations both in terms of overall completeness and quality. I do not attempt to characterise the accuracy of the results in this section – for a quantitative analysis, please refer to 4.3.

Comparison with preliminary elevations

Comparing the final 3D-NWB results with the preliminary elevations sheds some light on the nature of the improvements that are the result of the complex processing steps that occur in the later stages of the pipeline. The preliminary elevations (shown in a brown colour in the top visualisation Figure 4.15) represent the 3D conversion that can be achieved using only a few simple steps of processing: NBRS generation, elevation estimation, and the polynomial-based refinement step. The final results are coloured randomly based on their NBRS IDs.

The first difference that stands out is that those NBRS that I described as having complex vertical curvature and being difficult to model by polynomials in Section 4.2.2 are modelled much more realistically in the final output. One only needs to take a look at the comparison in the top image in Figure 4.15) to tell that it must be the final results that are correct, not the preliminary ones. The change represents a fundamental difference between these two stages in the pipeline. Preliminary elevation estimation relies on a workflow to detect elevation estimates corrupted by occluding geometry and to supply replacement values for them, while the final elevations come from TIN models that are guaranteed to only contain vertices that represent measurements of the relevant road's elevation.

While the biggest differences can be observed where the polynomial fits were poor in the preliminary elevation estimation stage, there are many other scenarios where smaller improvements can be seen. For instance, the preliminary elevations may contain outliers that were not detected as outliers in the refinement step. On bridges, AHN3 may contain reflections from vehicles. These are often not far enough from the road surface to be replaced by polynomial values, introducing small spikes into the elevation series. In the final results, such outlier points are guaranteed not to be inserted into the TIN models, and cannot affect the 3D conversion as a result. The inset in the figure also illustrates that while preliminary 3D conversion is not continuous across intersections, the snapping workflow ensures that the final 3D conversion is.

Another scenario in which clear benefits can be observed (not shown on these figures) is the presence of many occluded regions concentrated into a small area, or equivalently, one long occluded zone. In preliminary elevation estimation, such occluding features may attract the polynomial towards themselves, thus corrupting the fit and potentially introducing incorrect elevations into the profiles. This may happen, for instance, where many bridges are constructed across a motorway in a row, and the NBRS is not long enough to include enough non-occluded elevation measurements. Later pipeline steps almost always recognise these mistakes for what they are (data gaps), and either use DTB if available, or break the NBRS into parts locally.

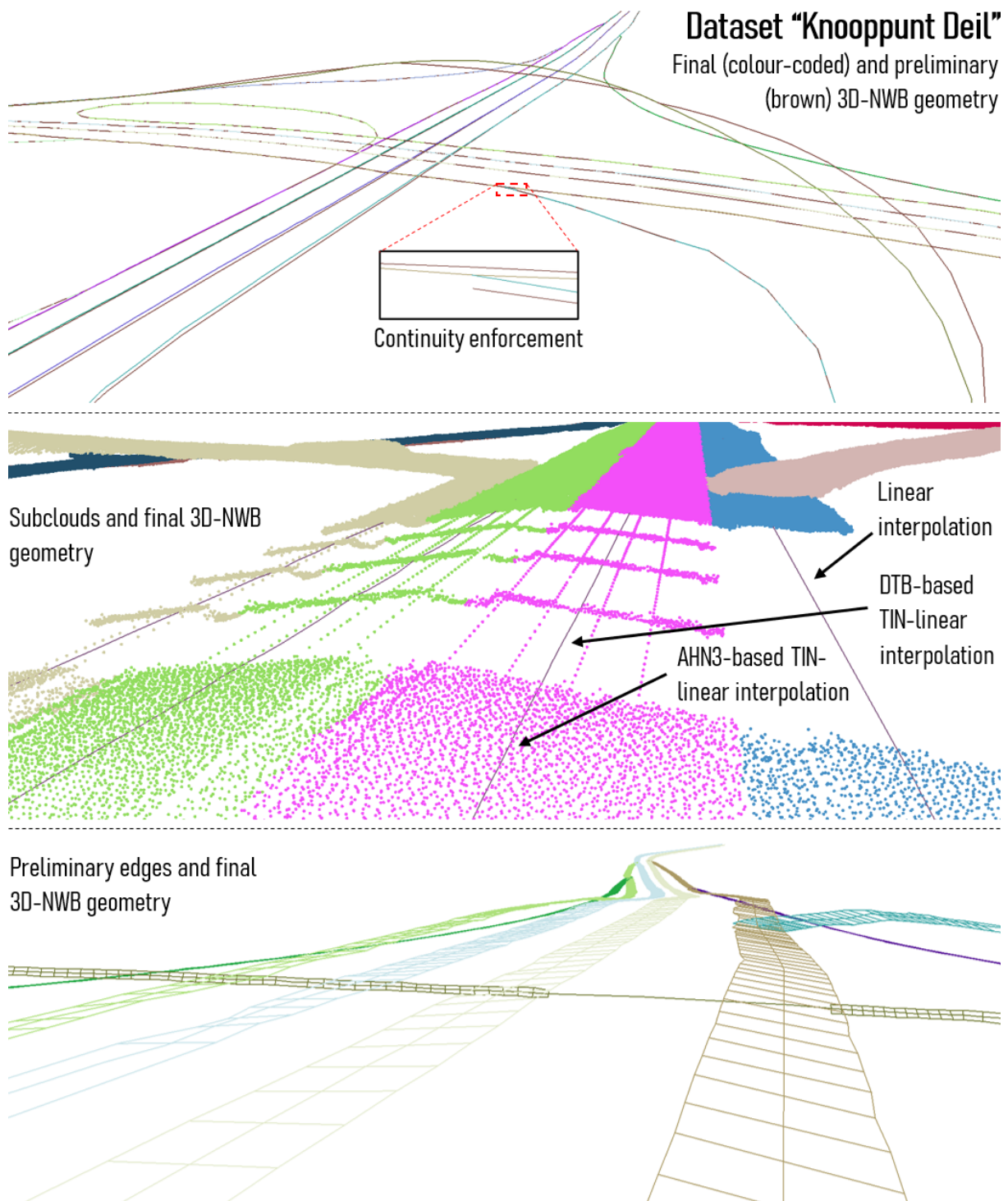


Figure 4.15: Visualisations comparing final 3D conversion results to preliminary conversion (above), subclouds (in the middle), and preliminary edges (below). In the upper visualisation, the final 3D-NWB geometries are shown coloured randomly based on their NBRS IDs, and the preliminary 3D conversion in brown. In the subcloud comparison, the subclouds are also coloured based on their NBRS IDs, and here the final 3D conversion of NWB is shown in a constant colour to help distinguish it from the points. In the bottom visualisation, the final 3D-NWB geometry, as well as the preliminary edges and cross-sections are coloured randomly, based on their NBRS IDs.

There are features in the final output that may appear to the untrained eye as a deterioration in quality with respect to the preliminary elevations. Small jumps in elevation may be observed where **AHN3** gives way to **DTB** points in the underlying **TIN**s. The new baseline elevation continues across the region where **DTB** was used, and reverts to the **AHN3**-based baseline elevation once the road emerges from the zone not covered by **AHN3**. This is simply a manifestation of the temporal discrepancy between **DTB** and **AHN3**; using better support data would eliminate such shifts from the output. This is only visible in the middle image in Figure 4.15, and the reader is referred to Figure 4.7 and Sections 4.3 and 4.4 for further details.

Lastly, one may observe that the amount of small-scale noise in the final 3D-NWB output is noticeably larger than that in the preliminary profiles. This also has a simple explanation: the preliminary elevations are based on taking the median of the elevations of a small patch of Lidar points, whereas the final elevations are all based on 3 samples each, due to having used **TIN**-linear interpolation. The amount of noise is no greater than the stochastic scatter in **AHN3**; it is only visible in the visualisation due to the vertical exaggeration.

Comparison with subclouds

This comparison is demonstrated in the middle image in Figure 4.15. The most important aspect here is that the final 3D road centrelines all lie flat on those parts of the Lidar subclouds that one intuitively recognises as road surfaces. This is always the case as long as **NWB** is correctly positioned, such as in this location.

The figure shows that this also holds for regions affected by occlusion. In places where **DTB** was added to the subcloud in the Lidar segmentation step, the centrelines are shifted vertically to conform with the surfaces defined by **DTB**. Where **AHN3** coverage reappears, they immediately shift back to its elevation, creating a geometry akin to suspension bridges in this example visualisation. Regardless of which dataset is used, the main point here is that the 3D conversion continues across the gaps without snapping to the bridges above that are causing the periodic occlusion.

The visualisation also illustrates that linear interpolation through regions with no measurements represents a good solution for small gaps of coverage where roads are straight. The road with the blue-coloured subcloud (on the right) has no **DTB** coverage, hence the small patches of **AHN3** points between the bridges could also not be detected. In spite of this, the elevations are actually more optimal here than elsewhere, because they are not affected by the small sifts introduced by **DTB**.

Comparison with preliminary edges

This comparison reveals that interestingly, the final 3D conversion of the centrelines and the preliminary edges are in near-perfect agreement with each other where coverage is good. As the bottom image in Figure 4.15 shows, even a five-fold vertical exaggeration cannot reveal significant differences between them. This is intriguing, as there are various pipeline steps in-between the generation of these results; most importantly, **TIN** generation. Small differences are only found between the elevations of the preliminary edges and 3D-NWB, where the preliminary edges were generated off the road surface, in which case the final results are better.

While the two outputs are not directly comparable, the exceptionally good match between them indicates that a 3D conversion with similar quality could potentially be achieved via a procedure that involves the subclouds and 2D centrelines only, perhaps using a workflow based to some extent on that which currently I used to generate the preliminary edges.

It is also important to note here that while the preliminary edges may be missing vertices in some places (indicated by the cross-sections also being absent), this is not the case in any of my final 3D-NWB results. As long as the centreline is found between the edges, a **TIN** will be constructed locally and **TIN**-based elevations will be computed. As I already described previously, this is only violated in places where many cross-sections are skipped in a row, which is rare in my results.

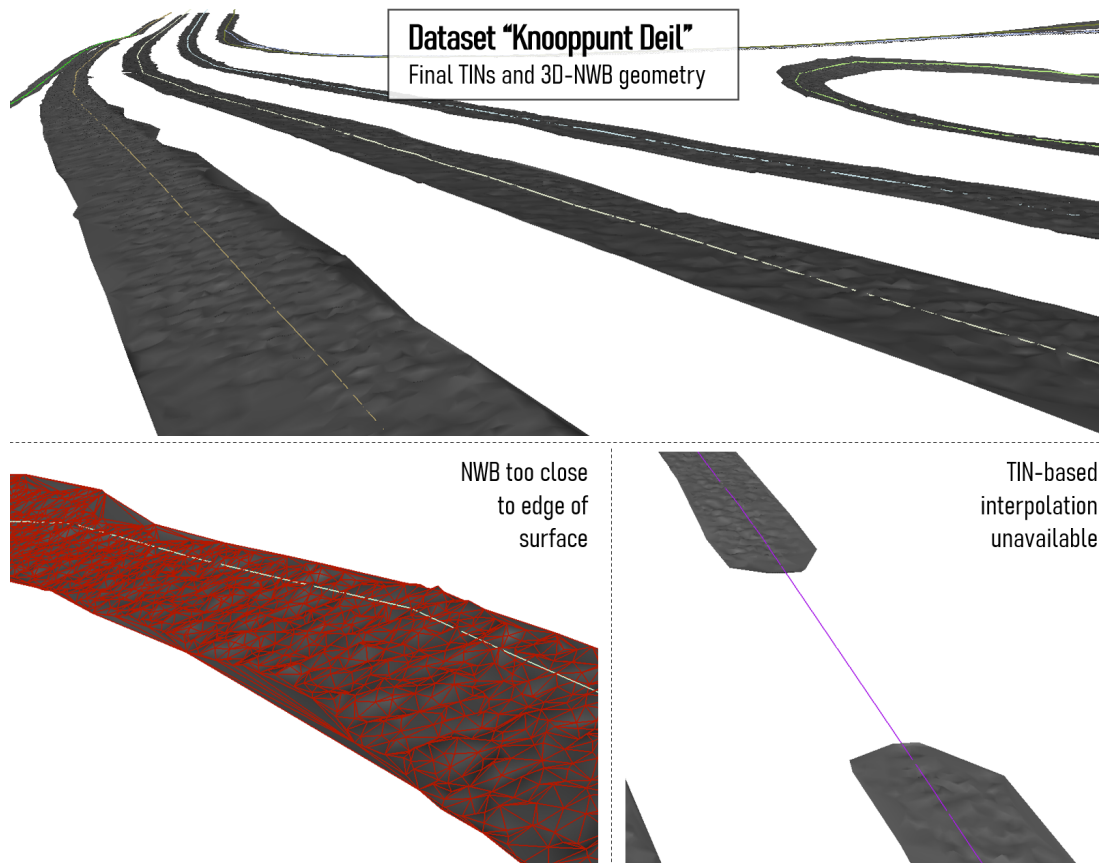


Figure 4.16: Visualisations comparing final 3D conversion results to the underlying TIN models. The surfaces are shaded in gray, and the final 3D-NWB geometries are coloured randomly based on their NBRS IDs. The triangulation of one of the surfaces is shown as a red wireframe.

Comparison with TIN models

Example comparisons between the final output and the TINs are shown in Figure 4.16. An interesting aspect of this comparison is that the final 3D-converted centrelines are often found slightly above or below the models (less than a centimetre, typically). This is best evidenced in the output by the intermittent disappearance of the 3D centrelines beneath the TIN triangles. This is the result of the georeferencing of NWB being coarse *relative to the TINs* even after applying vertex densification. NBRS parts only have vertices approximately every 5 metres, whereas AHN3 has up to 10 to 30 points per m^2 after thinning using a factor of 2.

This disparity simply indicates that if we wanted to, we could sample the TIN at smaller intervals to increase the output's vertical resolution. This would allow steep road segments to be better characterised in the output. In the case of flat road surfaces, no improvement would be noticeable. NDW officially requires elevations to only be estimated at the *original NWB* vertices, which can be many times further apart than my densified vertices. In other words, these TINs offer far more detail than that which would be minimally required for the conversion, as expected from such a high-resolution surface model. However, using only the original vertices loses so much vertical detail that I recommend retaining the densified vertices, even if this means that a stark contrast will be present between the horizontal and vertical "resolution" of the output.

An example where NWB gets close to the edge of a TIN is shown in the bottom left image. This is representative of the typical severity of the NWB georeferencing issue in sharp bends. While it was difficult to overcome numerous processing difficulties related to this problem with NWB, it bears almost no influence on the *effectiveness* of the TIN interpolation process as long as the TIN exists locally. Where NWB lines are close to road edges, the underlying TIN models will still always describe the surface of

the road according to our expectations. They will potentially include off-road points, but from the point of view of the 3D conversion of *NWB*, this does not matter. Even if *NWB* is not on the road surface, the *TIN* will likely be constructed locally and off-road elevations will be interpolated for it – although this means that the resulting elevation series will be corrupted. The elevation of the surrounding terrain will be reflected in it instead of that of the road.

The interpolated elevations will always correspond to the exact horizontal position of *NWB*, meaning that as long as its georeferencing is not corrected, the interpolated elevations will also not always correspond to the road’s real centreline. As I noted above, this could cause problems if *NWB* is not on the road surface. However, even if it *is* on the road surface, a small overestimation or underestimation relative to the elevation of the centre of the road is possible, if the road’s surface has a significant sideways tilt. Rectifying *NWB*’s georeferencing would automatically solve these issues and would also improve the effectiveness of many previous steps. No modifications to the algorithms would be needed to achieve this. A demonstration of this is found in the Appendix (Section A.1).

Where no *AHN3* or *DTB* coverage is available, the *TIN* will not exist and values will be interpolated linearly. A location with this property is shown on the bottom right in Figure 4.16. Such gaps correspond to zones *between* *NBRS* parts, hence the two *TIN*s shown in this image belong to two different *NBRS* parts.

Using the implementation

The following two commands may be used to run the final elevation interpolation code, and export the resulting 3D-converted version of *NWB* as a Shapefile:

```
roads.interpolate_elevations()
roads.write_all(fpath = accurateZ_fpath,
               to_drop = ['geometry_simpleZ'])
roads.write_origins(fpath = origins_fpath)
```

The algorithm does not have a parametrisation, hence the method invocation does not require any arguments. The `.write_all()` invocation requires a list of GeoDataFrame columns to drop, as the Shapefile can only have one set of geometries in it. The column name in `['geometry_simpleZ']` corresponds to the preliminary elevation estimates. The original 2D *NWB* geometries are always dropped automatically, so that column does not need to be manually specified.

In the *nbrs_manager* class, the final results are added to the class’s `.nwb` variable, as the `geometry_simpleZ` geometry column of the GeoDataFrame. Since Shapefiles also cannot accept arrays into their attribute tables, the vertex origin indicators (*AHN3*, *DTB*, or linear interpolation) are also not written into the output file. These can be found in `.wvk_z_origins[wvk_id]`, a dictionary that needs to be indexed with the *wegvak*’s ID whose vertex origins are desired. They can be written separately to disk as a CSV file using the last line in the code snippet above, where `origins_fpath` represents the file path where the CSV file should be deposited.

4.3 Accuracy assessment

In this section, I will present the accuracy assessment results focusing on a particular dataset: *Knooppunt Deil*. This dataset exhibits most of the unique features that are relevant for this part of the analysis, and it is my hope that such a “case study” approach makes understanding the assessment’s results more straightforward. Following the case study, I will present and discuss an overview of the relevant accuracy metrics for all testing datasets, in a tabulated format.

I will first focus on the results of computing local sampling densities and formal output accuracy values (error propagation results). Then, I will discuss how often the accuracy needs to be deemed unknown and for what reasons. Lastly, the completeness of the output *TIN*s relative to the *BGT* reference polygons

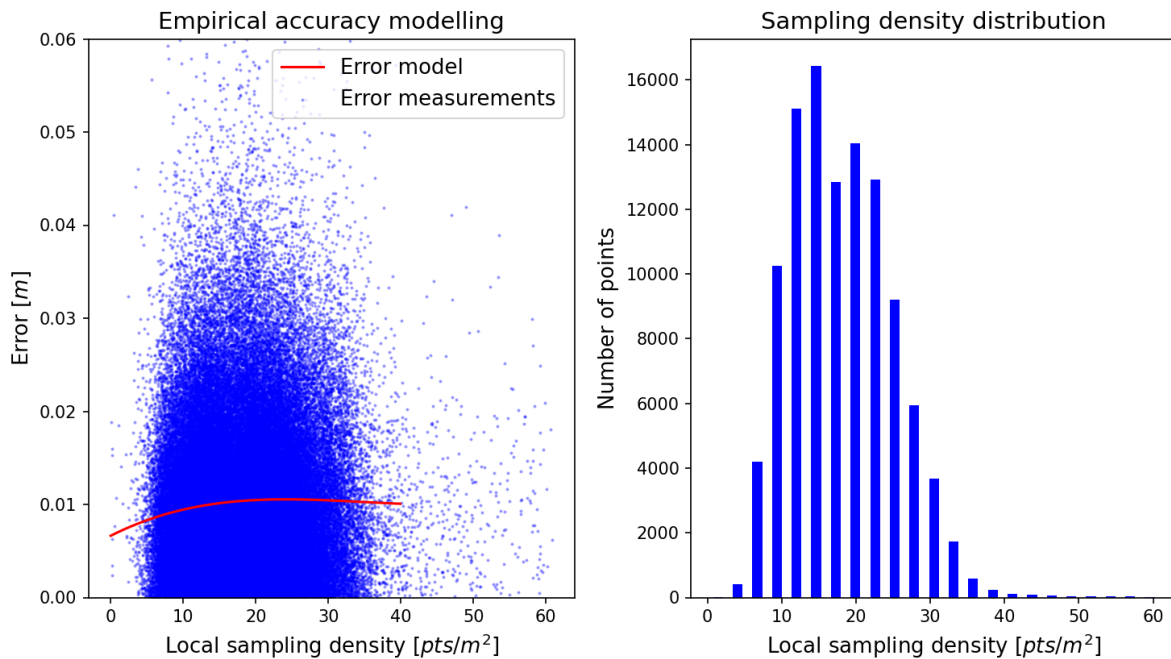


Figure 4.17: Charts demonstrating the outcome of the empirical accuracy assessment process.

will be examined. Please refer to the relevant sections in Chapter 3 (3.2.4 and 3.4) for the background theory and the detailed description regarding the assumptions I made.

4.3.1 Empirical accuracy assessment

As I briefly mentioned in Section 3.2.4, I first attempted to assess accuracy based on an empirical approach. Before performing the necessary steps, I was yet unaware of how the combination of factors that define output accuracy interact in our particular case. Most importantly, I was yet to discover that a range of assumptions regarding ground filtering accuracy, influence of surface ruggedness and sampling density can be made. In fact, it was this failed attempt that directed my attention to the fact that in our particular case, there are very few external factors that influence accuracy.

My initial hypothesis was that the primary influence on accuracy has to be sampling density and interpolation error, because ground filtering errors and surface ruggedness already appeared to me as irrelevant based on my experience with the data and the results. To be able to verify the hypothesis and compute empirical errors based on it, I constructed an error model and derived errors for each output vertex from it. I constructed the model by removing samples (vertices) from the output TINs, interpolating their values via the TIN-linear method, and computing the differences between the removed Lidar samples, and the interpolated elevations (in essence, a jackknife approach). I fit a cubic polynomial on the part of the scatter where we have enough data, and derived NWB accuracy values from it.

While I was doing this, I noticed that all my output errors were extremely small, and all roughly the same. This made me start suspecting the irrelevance of sampling density in our particular scenario, so I plotted the data and the model to verify this new hypothesis. Figure 4.17 shows an example visualisation created from the empirical accuracy assessment of testing dataset *Knooppunt Deil*. The chart on the left shows local sampling density plotted against the jackknife errors, computed for about 10^5 TIN vertices (10% of the total number of TIN vertices of all TIN models generated from this testing dataset).

While at a first glance one might think that the inverse parabola shape in the scatter plot represents a meaningful trend, it does not, in fact, possess the correct shape for the relationship. We know from literature that when a correlation exists between errors and sampling densities, it tends to be logarithmic, and the trend in my chart does not appear to have that property. The fitted model does appear

to have a weak logarithmic component, but it shows errors to increase in the wrong direction (towards larger sampling density), and the predicted error magnitudes are far too small to be meaningful. The histogram on the right reveals that the shape of the scatter plot does not correspond to a statistical trend that concerns a relationship between sampling density and jackknife error – it can be fully explained by the distribution of the sampling densities in the dataset.

What is also interesting in these plots, is that jackknife errors remain negligible even at the lowest values encountered. Overall, about 96% of the jackknife samples showed an error less than 3 cm, which is well below the nominal vertical and horizontal accuracies of *AHN3* and *DTB*. In other words, we may safely conclude that the variation in jackknife accuracy, on the scale observed in this experiment can be explained simply by the noise in the input datasets. The random distribution of the variations, evidenced by the bell-shaped trend, further confirms this theory.

Although this analysis suggests that any errors in the output will be small and that they will be mostly independent of external factors, the qualitative and quantitative estimation of output accuracy is among the main original goals of this project. Hence, I decided to find further evidence. This is why, even after performing the above analysis, I proceeded to propagate errors through the interpolation technique, and to also examine this in comparison with sampling density data.

As I discussed in Section 3.4, the above results are explained by some of the related work I examined. The accuracy of the produced *DTM* is not expected to be affected by sampling density because the terrain is not rugged, the slopes are very small, and ground filtering is near-perfect. Even in much less ideal areas, literature indicates that accuracy is not significantly affected above sampling densities in the range of 1 m². The range depicted in Figure 4.17 is much higher than this, and the modelled surfaces are ideal for terrain modelling, explains the lack of any correlation.

4.3.2 Formal accuracy assessment

The charts in Figure 4.18 show interpolation error profiles from 2 *wegvakken* from our chosen testing dataset. From the lack of a trend in the errors, and their small magnitudes overall, we may deduce that the output accuracy is sufficiently high with respect to the 20 cm requirement of the noise regulations. Any differences due to the TIN-linear interpolation represent an *increase* in accuracy relative to the 15 cm elevation accuracy of *AHN3*. The two *wegvakken* shown in the figure exhibit theoretical interpolation elevation errors in a range of about 4 to 7 cm, with mean errors of 5 cm for both. The variation is always randomly distributed, because the positions of *NWB* vertices relative to the containing triangles' vertices also lack correlation (which is what controls the value of *M*, which determines how much the accuracy has improved). In theory, the only factor that could introduce correlation into these profiles would be roads with very steeply sloping surfaces, but no roads in this dataset (or any of my datasets) reach a slope steep enough to affect the errors significantly, and to introduce correlation.

The top part of Figure 4.19 shows the 3D geometry of the subclouds and centrelines of the same two *wegvakken*. *Wegvak* #288259033 has a shape which is representative of the steepest slopes and sharpest bends one can expect from the Dutch road network; it connects a ground-level motorway lane with another one running orthogonal to it directly above, on a bridge. *Wegvak* #600127973 is the ground-based motorway lane that it connects. It lies entirely flat on the ground, with little to no variation in its elevation. I picked it because its shape is the opposite of that of #288259033, and because it had been split into two parts due to a 15-20 m long data gap which is visible in the figure. The gap also lacks *DTB* coverage. The bottom image in Figure 4.19 shows the corresponding *TINs*, and it is visible in this figure that *NWB* veers to the outer edge of the steep, curved *wegvak*, almost reaching it. The relatively thin width of the *TIN* and its rugged outer edge is a result of this; the preliminary edges were constructed partially off-road due to *NWB*'s poor georeferencing.

I added sampling density plots on the right in Figure 4.18. The first important observation to make about these charts is that the data gap in sampling density between 100 and 200 m along the profile in #600127973 is due to the data gap I mentioned above; here the density is 3 points per m² or less – which is the threshold below which the cut-out happens, i.e. accuracy is not computed – visible in the chart on the left in the same figure. The sharp drops in density around the gap illustrate that the neighbourhood

4 Results

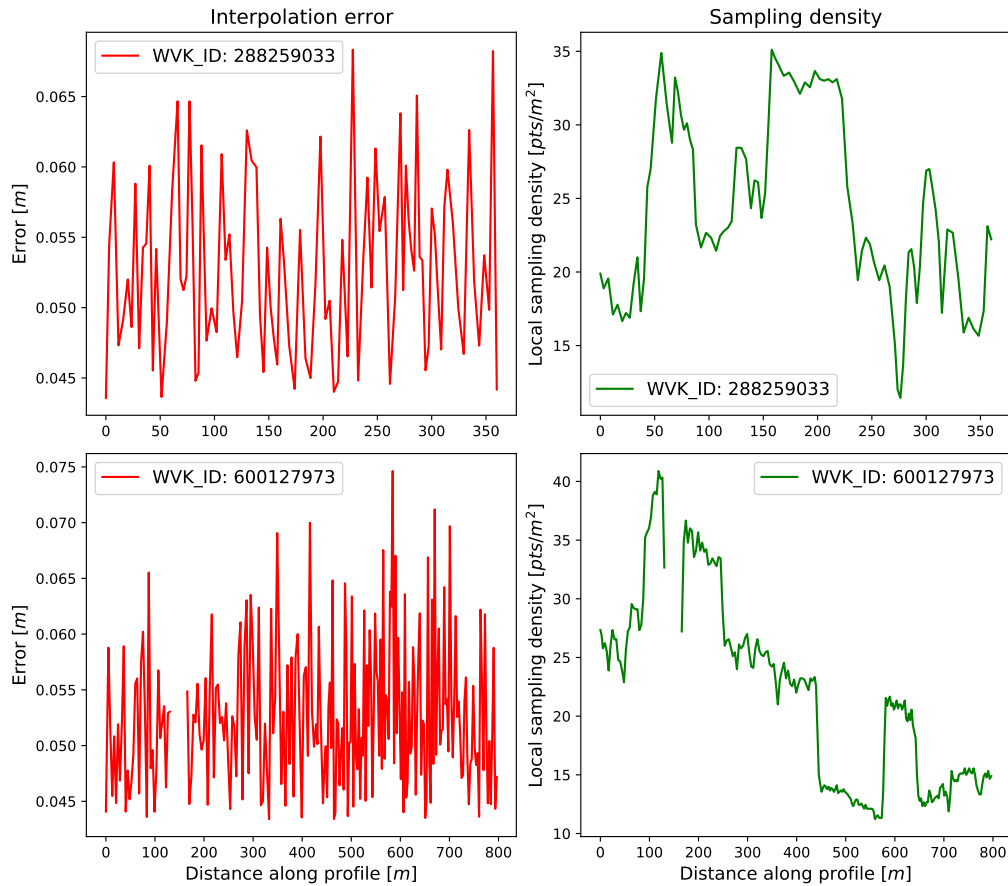


Figure 4.18: Charts illustrating the formal accuracy assessment results on two *wegvakken*.

queries already indicate the presence of the gap right before and after reaching the centreline vertices that fall into it. The two *wegvakken* #288259033 and #600127973 have mean sampling densities of 24 and 21 points per m^2 respectively – well above the nominal accuracy of the dataset, primarily owing to the flatness of the road surfaces.

The second important observation is that while local sampling density fluctuates by as much as 80-90%, it never reaches the minimum threshold in places other than no-data zones and where only *DTB* data is available (the latter is not separately illustrated here). The fluctuation is due to the inhomogeneous sampling rate of *AHN3*. It is already present in the raw point cloud, and is simply a factor of how many times a given area was scanned by the aircraft's laser sensors. The figure was generated from my final results, which all use a thinning factor of 2 – meaning that the values seen in the charts are half of the maximum available. The results shown in these two charts are representative of all testing tiles; significant deviations from what I described above and what is shown in the figure were not observed elsewhere either.

The third, and last important observation is that neither the recorded sampling rates, nor the theoretical accuracy values are indicative of locations where *NWB*'s 2D georeferencing is poor. While *NWB*'s location is far from the road's real centre in #288259033, it is not off the road, and as a result the interpolated elevations will still be correct, or at least they will definitely correspond to some part of the road surface. As far as theory is concerned, the elevation is the *correct elevation* at the *incorrect NWB location*. This also holds for places where *NWB* is not on the road surface, but here both the sampling density and the accuracy may drop, the former because the *TIN* construction algorithm is not meant to be used in uneven areas, and the latter because of (and only in the case of) introducing sloping triangles into the *TINs*.

The mean error and sampling density of the entire testing dataset are 5 cm and 19 points per m^2 .

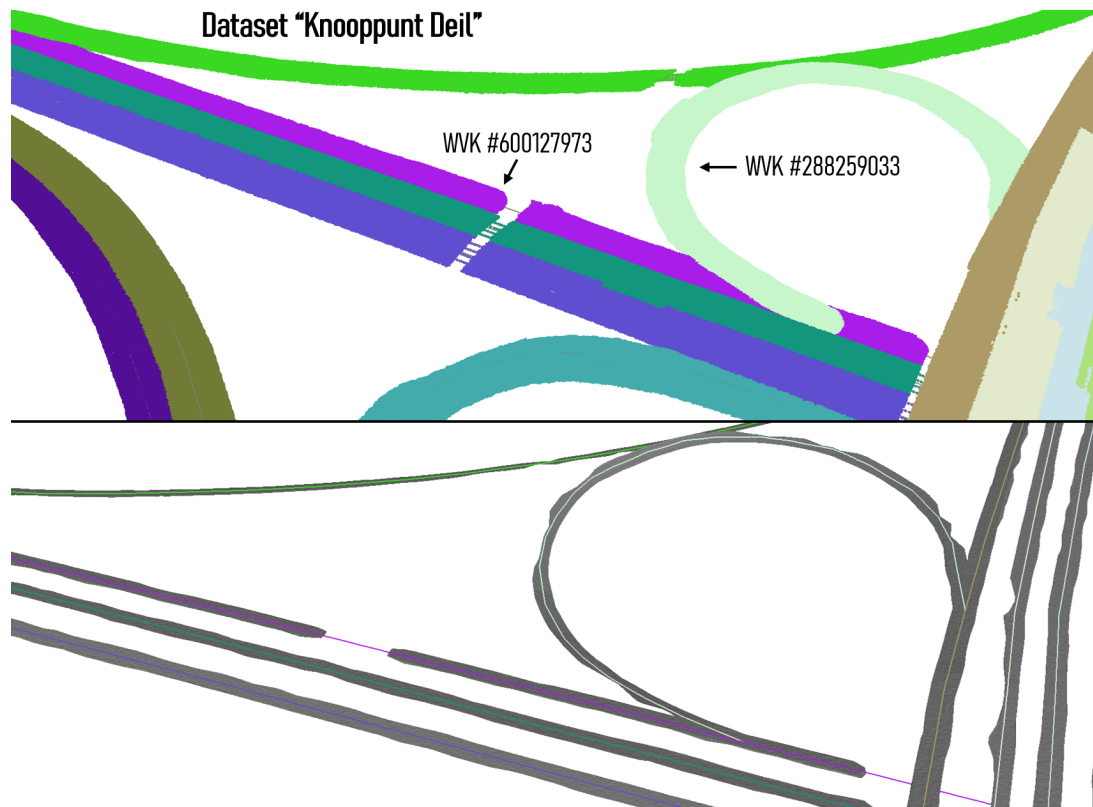


Figure 4.19: Visualisations showing the subclouds, TINs and 3D-NWB centrelines in the area concerned by Figure 4.18. In the top visualisation, the subclouds and final 3D-NWB geometries are shown coloured randomly based on their NBRS IDs. In the bottom visualisation, the TIN surfaces are shaded in gray, and the final 3D-NWB geometries are coloured randomly based on their NBRS IDs.

Using the accuracy assessment implementation

The following two commands may be used to run the formal accuracy assessment code, and to write the results to disk:

```
roads.generate_theoreticalerrors(ahn_zse = 0.075, ahn_hse = 0.09,
                                dtb_zse = 0.1, dtb_hse = 0.05,
                                r = 3, thres = 3)
roads.write_errors(errors_fpath)
```

The first line of arguments in the first method call correspond to the vertical and horizontal accuracy of **AHN3**, and the second line to the same metrics of **DTB**. The last two arguments represent the radius of the spatial queries that will be used to gather neighbouring TIN vertices to assess sampling density, and the minimum sampling density. The configuration shown here is the same as the one introduced in previous sections, i.e. a radius of 3 m is used for the queries, and a threshold of 3 m² is applied.

The second line of the code snippet writes the accuracy assessment results to disk as a CSV file – errors_fpath represents the file path where the CSV file should be deposited. This is necessary, as this information cannot be written into the exported 3D-NWB dataset.

4.3.3 Ratio of accurate vertices

The frequency at which the algorithm has to deem output accuracy unknown fluctuates significantly both inside and between testing datasets. How often this happens depends on the number of linearly

interpolated values, and how often the sampling density drops below the 3 points per m² threshold. The percentage ratio of accurate vertices varies, under normal circumstances, between 85 and 95%. Special circumstances (such as tunnels) may further decrease this, which will be discussed in Section 4.3.5.

Where no special circumstances are encountered, variations can be traced back to two main controlling factors: how much of the road network is occluded, how accurate the preliminary elevations are, and how complete DTB is in the given testing dataset. The relevance of the amount of occlusion is straightforward to understand: the more occlusion we have, the bigger the chances are of encountering an AHN3 data gap where linear interpolation may need to be used.

The completeness of DTB is a factor here because it prevents linear interpolation from being used. However, for the program to consider interpolation accurate locally, DTB *also* needs to have good enough coverage. Therefore, only a subset of the DTB-covered data gaps will be deemed accurate. DTB rarely exists for provincial roads (P-roads), hence Lidar data gaps in such roads will *almost always* result in linear interpolation. In turn, this means that data sets comprised primarily of P-roads will have lower accurate vertex ratios. Preliminary elevation accuracy and lateral NWB accuracy are also important, because they control DTB coverage to an extent. If either is inaccurate, then even if DTB exists locally, it may potentially not be found.

As I mentioned in Section 3.2.4, DTB is effectively a placeholder for a more accurate dataset in terms of this accuracy assessment workflow. Records of which vertices were affected by DTB data are generated by my implementation, and reusers are advised to consider all of these vertices inaccurate due to the temporal issues. For the purposes of this accuracy assessment demonstration, DTB-based interpolation with high enough local sampling density was considered accurate and included in the percentage values. However, because DTB-based sampling density also reflects the line densification threshold used when converting it to a point cloud (in addition to the number of DTB lines available locally), I must emphasise here that DTB-based sampling density values are partly artificial.

Linear interpolation is rare outside of AHN3 data gaps (including those due to occlusion), and especially rare where NWB's georeferencing is correct – in my datasets, 98-100% of non-occluded vertices are interpolated in the underlying TINs. The majority of these are due to the rare cases where too many cross-sections are skipped during preliminary edge estimation, preventing proper TINs from being constructed locally.

4.3.4 TIN completeness

I evaluated the completeness of the TIN road surface models via a comparison with BGT polygons. Figure 4.20 shows the results of one such comparison, which I deemed representative of the relationship overall. The top part of the figure shows some of the TINs overlain on the outlines of BGT geometries, which allows one to see how well the TINs agree with these reference geometries. The bottom half of the figure compares the BGT geometries to aerial imagery – to verify how well BGT itself agrees with what we can consider an accurate representation of the visual appearance of these roads. The orthoimagery is from the 2020 edition of Kadaster's Luchtfoto dataset, available as open data like all other datasets used in this research.

The NWB centrelines are also shown here to demonstrate the extent of the georeferencing issues relative to BGT and to the orthoimagery. The poor agreement is the result of two factors combined: NWB approximates the centrelines of the traffic-occupied road surfaces rather than the paved surfaces, and its georeferencing is inaccurate in general. The definition of traffic-occupied road surfaces excludes hard shoulders. If the traffic-occupied surface is close to the edge of the paved surface (which is generally the case), NWB's poor georeferencing is more likely to cause it to be close to or beyond the edges of the relevant paved surface.

BGT, on the other hand, appears to be an accurate 2D representation of the paved road surfaces. Its extents do not, however, correspond to that which I can *typically* model reliably using the pipeline I developed. Ideally, the surface model should cover the entire paved area, but as I described in Section 3.3.4, I found using a maximum road width to be the only viable means to ensure that my approach works in most cases. The TIN extensions that are part of the TIN construction step (Section 3.3.6) mitigate

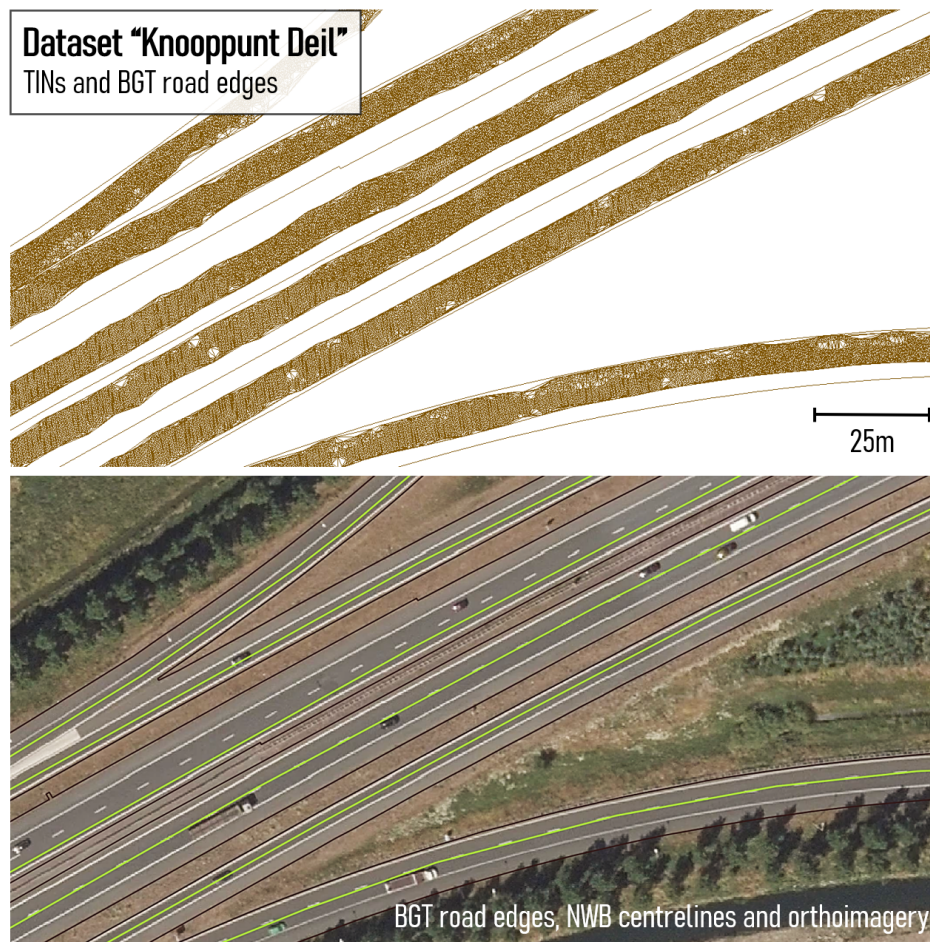


Figure 4.20: Above: 2D visualisation comparing BGT road edges with the TINs (beige lines and wireframes). Below: comparison of BGT road edges (dark brown) with NWB centrelines (green) and Luchtfoto 2020 aerial imagery.

this issue to a certain extent, but they do not eliminate it entirely. Allowing the TIN extension to go too far beyond the preliminary / optimised edges increases the chances of extending the surface models into unwanted areas, and also increases runtimes significantly.

Motorways with hard shoulders, which are shown in the centre of Figure 4.20, are particularly difficult to handle because the hard shoulders and potential extra lanes extend their width far beyond that, which could be reasonably expected from motorway ramps, municipal roads and even dual carriageways – which are the road types that my implementation prioritises. A solution to this issue could be to automatically select pre-set configurations of the parametrisation appropriate to each road type, but this is not an area that my research explored.

The TIN models in the top part of the figure show that the TINs are in good agreement with the BGT geometries. The same issues which I described in Section 4.2.6 are also manifested here, for instance the on-ramp model in the top of the image contains some off-road points where both NWB and BGT appear to veer too far from their ideal positions. In general, based on examining all my results, I estimated that the TIN surfaces cover approximately 95% of the traffic-occupied surfaces found in my testing datasets, and about 75% of the total paved surfaces as shown by BGT. The only major issue appears to be the one I mentioned above, that the full extent of the paved surfaces cannot be modelled without dynamically adjusting the parametrisation of the pipeline's algorithms.

Figure 4.20 is also illustrative in terms of showing just how detailed these TIN models are, even with an input thinning factor of 2 for AHN3. On the scale shown in this image, and in comparison with the orthoimagery, it becomes visually perceptible that the road surfaces are being oversampled vastly by inserting too many points into the TINs.

4.3.5 Tabulated values

In the sections above, I focused on assessing the accuracy and completeness of specific LineStrings (*wegvakken*) in one testing dataset. In Table 4.2, I present mean error, sampling density and accurate output vertex ratio values for *all* my testing datasets.

	20BN1	25BZ2	25DN2	32BN1	32FZ2	32HZ2	33CN2	37EZ1	37HN2	38GZ1	39CZ1
A	5.26	5.26	5.30	5.26	5.28	5.29	5.28	5.34	5.30	5.29	5.29
B	26.82	19.81	20.04	14.89	16.72	14.95	16.20	13.52	13.77	15.47	19.28
C	93.03	76.14	95.08	91.74	95.51	94.18	90.52	56.19	85.18	89.00	91.68

A = Mean error [cm], B = Mean sampling density [pts/m²], C = Accurate ratio as % of all vertices

Table 4.2: Tabulated 3D-NWB accuracy and completeness results per testing dataset. Results based on original and densified NWB vertices.

Almost no variation is observed in the mean **formal output vertical error** across the datasets. As explained in the sections above, this is due to the fact that propagating errors through the interpolation technique only exhibits large (positive) fluctuations in the output error when steep triangles are encountered. The first row of tabulated values thereby represent evidence that triangles steep enough to affect accuracy are decidedly rare in our TINs, and the output accuracy is, in effect, roughly constant and almost entirely determined by the input accuracy.

The **sampling density** values show that the density of points is reliably high, consistently staying well above the threshold below which accuracy is deemed undetermined. However, large variations are still observable between the testing datasets, with values ranging from about 14 to 27 points per m². The variation has several reasons based on my analysis, each with non-negligible influence. The first reason is that the stock sampling density of AHN3 appears to vary on a large scale, in various parts of the country, and also locally, which I have already shown in Figure 4.18. The second reason is that accuracy is computed based on radial queries around NWB vertices, and will therefore show lower values for very thin roads where NWB is close to the edge of the road.

Lastly – but most importantly for us – it gives an indication of the pervasiveness of occlusion. Partial occlusion (due to vegetation) and complete occlusion (due to bridges and other opaque structures) decrease the TIN vertex density significantly. For instance, the low value seen in 33CN2 (dataset *Hoenderloo*) is primarily due to the road being situated in a dense, old-growth forest, and the one in 37HN2 (dataset *Knooppunt Ridderkerk*) is mainly due to occlusion resulting from the roads passing above and below one another in the motorway junction.

However, the medium value seen in 25BZ2 (Amsterdam Hemhavens) does *not* reflect the fact that there is a sizeable tunnel in the dataset. Since the tunnel has no DTB line coverage, the TINs of the relevant NBRs parts do not extend into the tunnel. As I explained in the sections above, these densities are computed from the TINs, and therefore road sections without AHN3 and DTB coverage are not allowed to affect the sampling density measurements. I made this design choice because in these areas, my implementation simply interpolates linearly. Therefore, these areas do not, strictly speaking, constitute areas in which we can predict elevation with any certainty, especially not where they are long, such as the tunnel in this particular testing tile. Although I am providing linearly interpolated output values in these regions, I essentially consider them to be excluded from my analysis, and thus I also exclude them from the accuracy and density computations.

The presence of the tunnel can still be recognised in the **accurate vertex ratio** row in Table 4.3.5. The lower value seen for 25BZ2 is simply due to the tunnel – almost all other parts of the roads in this dataset have detailed TINs associated with them. In this row, there is another value that stands out. The rest of the ratios show that between about 85% and 95% of the output vertices have reliable, estimated accuracy, whereas this ratio is only 56% in the case of dataset 37EZ1 (*Rotterdam Ketheltunnel*). This is the combined result of two factors: as the name implies, this dataset also contains a tunnel. But, as Table 4.1 mentions, the AHN3 data pre-dates the completion of the tunnel and the surrounding parts of the motorway, and as a result, part of the output is corrupted. Already during preliminary elevation estimation, the standard

deviations are a magnitude larger than those encountered in other locations, because the construction works represent rugged surfaces. In the Lidar segmentation step, the roads are split into many small **NBR**s parts, with much of the road thereby becoming flagged for linear interpolation. As a result, many of the **NWB** vertices' accuracy will be deemed unknown. This issue could be resolved in this case, if the large standard deviation in the preliminary elevation estimation triggered an alternative workflow in which only the support dataset is used in the region in which the primary data is unreliable. Developing and implementing such a workflow was not part of this research, hence it is further discussed in Section 5.7 in the context of recommended future work.

The values in the bottom row of the table are sometimes slightly lower than I was expecting. For instance 85% for the 37HN2 (*Knooppunt Ridderkerk*) dataset seemed to me to be too low, because almost all gaps have good **DTB** coverage, and **NWB** almost never misses the **TIN**s. The reason why this value is lower than expected is because there are many **AHN3** data gaps, and the point density in the **DTB**-defined parts of the **TIN**s appears to consistently miss the minimum above which the vertices would be deemed accurate. The process also appears to sometimes filter out vertices that were interpolated in locations where although **DTB** was "sparse", it still managed to characterise the road surface quite well. This further suggests that it would be better if the decisions regarding where to trust **DTB** were not based on the same type of evaluation as **AHN3**, and were instead based on the geometric layout of the **DTB** lines. While this would indeed improve the accuracy assessment results, it would also mean that the procedure would become specialised to **DTB**, and would not work with other types of support datasets. This is elaborated on in further detail in Section 5.7.

Some of the **NWB** centrelines overshoot the Lidar testing tile extents by up to 20-50 metres. These were left in some of the testing tiles deliberately, to test certain aspects of the the behaviour of the algorithms (as also mentioned in Section 4.1). These can further decrease the accurate vertex ratios by about 2-4% artificially. The overshoots are visible in Figure 4.1.

4.4 Comparison with commercial implementation

Like in the accuracy assessment above, I picked some specific *wegvakken* that are representative of the overall results of this comparison. However, here I did not restrict the selection to be from the *Knooppunt Deil* dataset, because the results are very different across my set of testing datasets. Where the agreement is good, the two sets of results can be similar to a degree where it is difficult to tell them apart in a 3D visualisation. Examining the correspondence on 2D charts (see Figures 4.21, 4.22 and 4.23) works far better in terms of characterising the nature of both the small-scale and large-scale differences that are typically observed when comparing the two datasets. For this reason, I opted to show only 2D visualisations in this section. I also present tabulated mean **RMSE** values for all testing datasets in Section 4.4.2.

4.4.1 Representative example comparisons

Knooppunt Deil

The top chart in Figure 4.21 shows a **LineString** (*wegvak*) in which the **RMSE** between the two datasets is only 3 cm. The *Knooppunt Deil* dataset, from where these **LineStrings** in this figure were taken, shows exceptionally good agreement between the results and a 3 to 5 cm **RMSE** can be regarded as typical everywhere in it. Such a small disagreement could be deemed unimportant, unless systematic – however, in this case there appears to be a small systematic component to it. Notably my results seem to consistently estimate higher elevations for the roads than the commercial ones here. The reason for the systematic nature of these differences is that this **LineString** represents a motorway, and the commercial implementation always takes motorway elevations from **DTB** wherever it has coverage. My implementation does the opposite; it prioritises **AHN3**. As a result, the systematic differences between **DTB** and **AHN3** are manifested in these 2D profiles. This is further illustrated by the residuals dropping to almost zero in one place at around 220 m along the profile, and then for about 50 m starting at 800 m along the profile.

4 Results

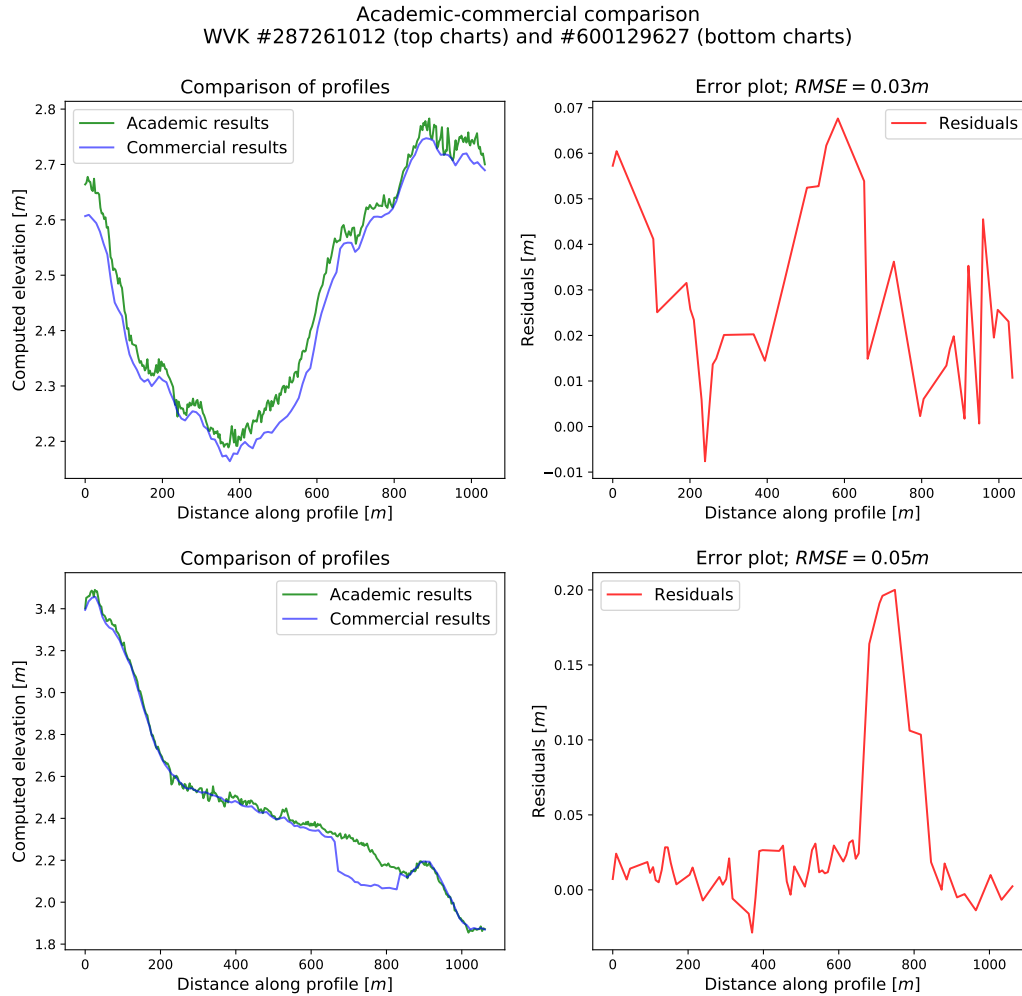


Figure 4.21: Charts comparing the academic and commercial results using two *wegvakken* from *Knooppunt Deil*.

Here, the chosen *wegvak* passes underneath bridges, hence my implementation also used *DTB* locally – thereby triggering near-perfect agreement with the commercial results. Since the absolute value of these systematic differences is minuscule in this location, it can be regarded as unimportant.

In this particular dataset, the agreement between the two datasets is almost always this good – the one exception I found is shown in the bottom charts in Figure 4.21. The difference represents a roughly 20 cm erratic drop in elevation in the commercial results. I could not explain this blunder by looking at the input data, hence it must have been introduced by the commercial processing pipeline. The error is large enough to break compliance with the 20 cm accuracy requirement of *NDW*, but it is an isolated issue – I have not found other examples of it in this dataset.

Gorinchem

Both *wegvakken* in Figure 4.22 were taken from *provincial roads* in the *Gorinchem* dataset. The top two charts were generated from a *LineString* that is situated in a well-exposed area, free of occlusions. While the *RMSE* is extremely low – as in the previous figure – we may notice that here a systematic deviation can also *not* be observed at all. This is because the commercial implementation uses *AHN3 rasters* to interpolate elevations. Although this does not affect the *RMSE*, it is evident from this chart that the commercial results are less detailed than the academic ones. This is simply the result of the academic results using

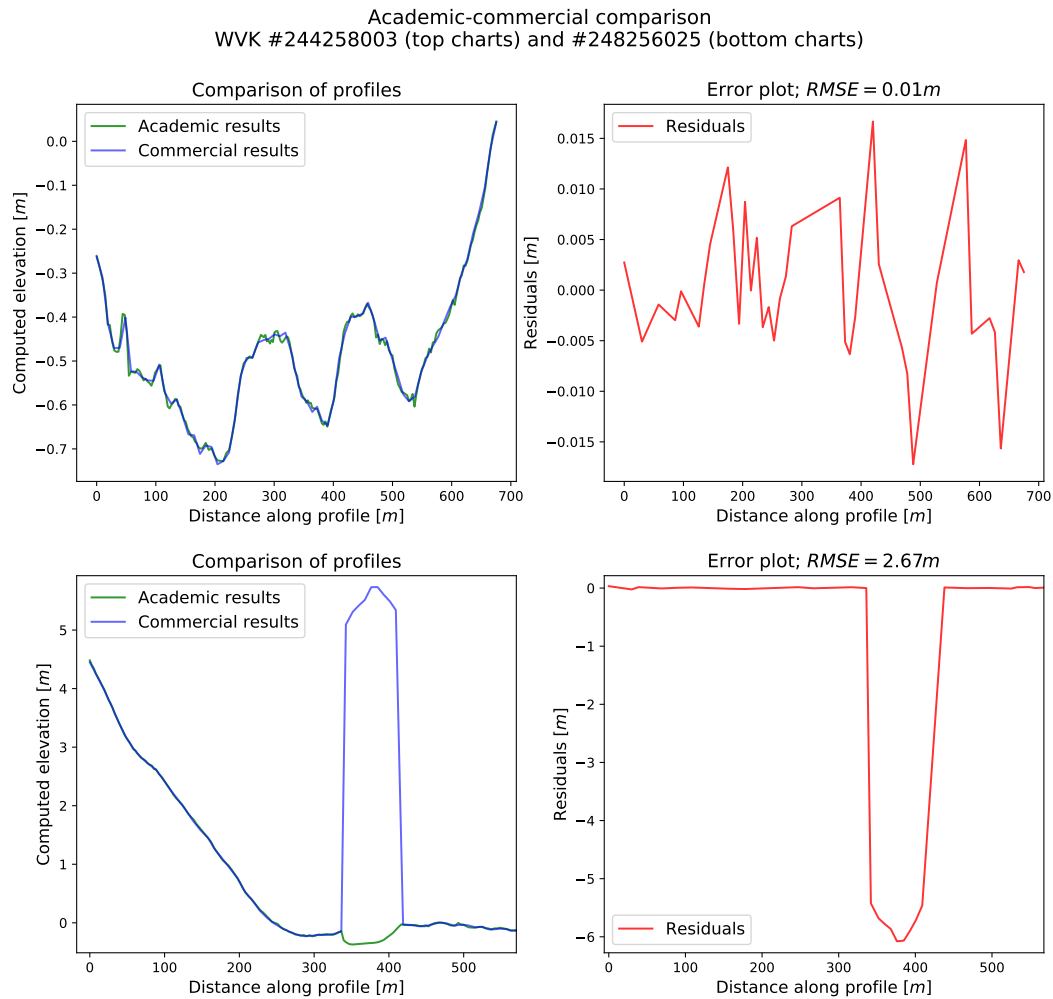


Figure 4.22: Charts comparing the academic and commercial results using two *wegvakken* from dataset *Gorinchem*.

10-metre vertex densification, whereas my final results were generated using 5-metre vertex densification. Both result in much denser elevation profiles than the original *NWB* vertices would allow, which is apparent relative to the residual plots because they only contain values for original *NWB* vertices.

While it might first appear to the reader that the agreement for provincial roads is even better than that for motorways, this is in fact not the case. The commercial solution has no feature implemented to intelligently switch between *AHN3* and *DTB*, and also lacks a set of features that could enable it to handle occlusion correctly in the absence of *DTB*. I illustrate both of these limitations in the bottom two charts in Figure 4.22. Between about 330 and 420 m along the profile, the commercial results show a sudden elevation increase, while the academic ones show a (much smaller) abrupt change in the opposite direction. Everywhere else in the *wegvak*, the agreement is at least as good as in the top chart.

This artefact was created by the combination of the above missing features in the commercial software. At this location, the provincial road from which the *wegvak* is taken passes underneath a series of bridges. Here the *AHN3* DTM rasters contain holes, which the commercial methods infill using simple methods. It appears that the hole-filling step is not particularly effective, because the artefact represents an approximately 5 m systematic overestimation of elevations over a 100 m section along this road. My results, on the other hand, *underestimate* the elevations in this zone by about 30 to 40 cm. This is not an issue with the academic methods or implementation, it is due to *DTB* being outdated locally. For this particular set of provincial roads, *DTB* exists because of their proximity to motorways – in general,

4 Results

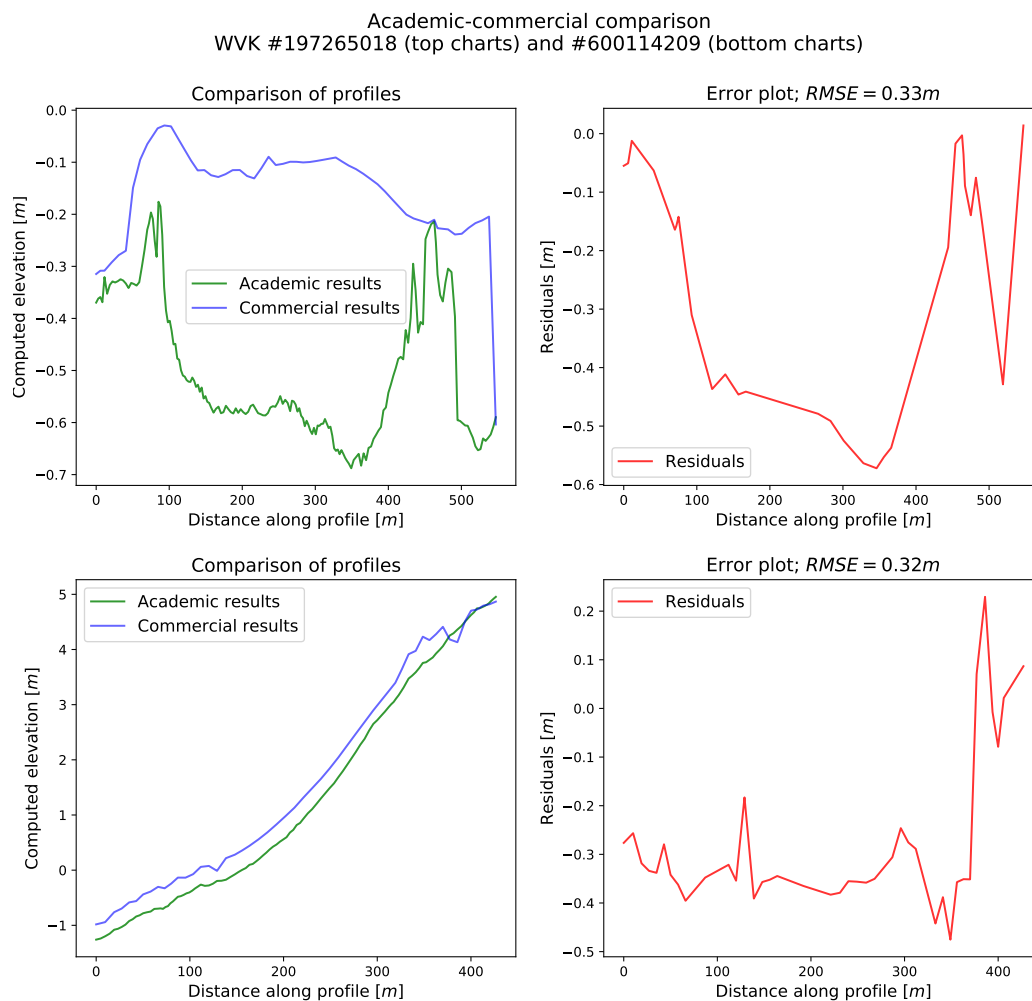


Figure 4.23: Charts comparing the academic and commercial results using two *wegvakken* from dataset *Knooppunt Ridderkerk*.

provincial roads do not have *DTB* coverage. My implementation recognised the presence of *DTB* lines, and made use of them.

The *DTB* data was close enough to the predicted elevation of the road for my implementation to deem it reliable. However, inspecting them on this 2D elevation profile reveals that *DTB* is, locally, itself underestimating the elevation of the road. This can be explained by the temporal difference between *AHN3* and *DTB* locally. Had there been accurate support data available, my implementation would have produced correct results – and even in the absence of support data, it would have interpolated linearly across the region.

Knooppunt Ridderkerk

Figure 4.23 shows motorway *wegvakken* taken from the *Knooppunt Ridderkerk* dataset. The reader might recall that I used this dataset as an example of where the temporal differences between *DTB* and *AHN3* give rise to significant disagreements between the road elevations they contain. This last comparison figure serves to illustrate that this is directly reflected in the differences between the commercial and academic results.

The outdated elevations in *DTB* are the only ones considered by the commercial implementation, which results in elevations being consistently overestimated by up to half a metre relative to *AHN3*, and therefore also my results. Good agreement between the two sets of results only emerges where my implementation also resorted to using *DTB*, because *AHN3* was missing locally. This is the same phenomenon that caused the small, systematic deviations in Figure 4.21, the only difference is that *DTB* is particularly affected by the temporal issues here.

This demonstrates the flaws in *NDW*'s unconditional assumption that *DTB* is more accurate spatially and temporally than *AHN3*, especially from a temporal perspective. They specifically opted to prioritise its use as it is updated far more frequently than *AHN3*. However, this assumption likely did not consider the fact that the updates only concern roads that underwent refurbishment, upgrades or other modifications, and roads that were newly built. Otherwise, the position of *DTB*'s line features is *not* re-measured regularly, as I also mentioned in Section 2.3.3. These outdated elevations represent a further disparity between the noise regulations' requirements and the commercial results, and they affect the results in the *Knooppunt Ridderkerk* area significantly.

Summary of detailed comparison

It appears that relative to the commercial implementation, there is a clear set of areas where the academic solution performs better. Notably, these are the smarter use of the available input data, and the better handling of occlusion. We may also add to this a better evaluation and quantification of output accuracy, as proof of such an analysis (or at least the assumptions made that justified omitting such an analysis) is missing from their results.

There is an area, however, in which the relationship is reversed: the commercial implementation can be run on the whole country, using a user-friendly graphical user interface (*GUI*), and with a far lower computational complexity than that of the academic implementation. In fact, I needed to extract the *LineStrings* for this comparison from the preliminary country-wide 3D-NWB release that was generated using the commercial implementation.

This is a manifestation of the main difference between the two solutions' paradigms of an ideal implementation: the commercial project focused on developing a straightforward solution that works reliably out-of-the-box, even if corners need to be cut to achieve this and the results sometimes do not comply with the official requirements. In contrast, the academic project focused on exploring how various scientific approaches can be put to use in such a practical problem, and on scientific correctness and accuracy.

4.4.2 Tabulated RMSE values

In the section above, I discussed detailed comparisons between my results and the commercial results, on the level of specific *LineStrings*. In addition to this, in the present section I present and discuss tabulated, aggregated comparison values to provide an overview of the similarity between the two sets of results on the level of testing datasets.

Table 4.3 shows the results of quantifying the similarity between the academic and commercial *NWB* 3D-conversions. It contains *RMSE* values for each testing dataset, computed based on the residuals between the elevations estimated by the two methods for the same original *NWB* vertices.

	20BN1	25BZ2	25DN2	32BN1	32FZ2	32HZ2	33CN2	37EZ1	37HN2	38GZ1	39CZ1
AHN3	0.0081	1.5501	0.0384	0.0153	0.0787	0.0171	0.0087	1.7271	0.3417	0.7593	0.0692
DTB	-	-	0.0491	-	0.0383	-	-	2.0478	0.6391	4.3053	0.0166
L.I.	0.0108	7.1152	3.3000	0.0692	0.2636	1.1244	0.3528	2.7504	0.7174	0.3036	0.1634

L.I. stands for linear interpolation.

Table 4.3: Tabulated academic and commercial *RMSE*-based similarity quantification results.

4 Results

My accuracy assessment code looks up the commercial counterpart of each elevation I computed for original (non-densified) *NWB* vertices, and subtracted it from my results to obtain the residuals. Before computing the *RMSE* values, I separated the residuals into three groups based on which of the three possible origins is associated with the given vertex in the academic results: *AHN3*, *DTB* and linear interpolation. The relevant classification rules are elaborated in 3.3.7. I expected the comparison to yield vastly different results for the three groups, because of the known conceptual differences between the two implementations, and also because the detailed comparison above (in Section 4.4.1) already indicated this.

Unlike in Table 4.2, clear trends cannot be observed in the data. There appears to be some scatter in all rows and columns. This is connected to the observation mentioned in the detailed comparison, that similarity is a factor of both the particular location in question, and the source of the data (*AHN3*, *DTB* or simple linear interpolation). I will present examples based on the table above, to illustrate this.

Dataset 39CZ1 (*Knooppunt Deil*) generally shows good agreement between the two sets of results, with the *RMSE* metric not exceeding 20 cm in either of the three “classes”. As I mentioned above, this is because at this particular location, *NWB* is comprised of *R-roads* only, the completeness of *DTB* is good, and *DTB* and *AHN3* are in good agreement. The extremely low *RMSE* in the case of the *DTB*-sourced academic elevations (only 1,5 cm) can be explained by both implementations relying on the exact same road surface elevation measurements locally.

In the case of 38GZ1 (*Gorinchem*), the middle value (*DTB*-based similarity) is equally simple to explain – the commercial methods were not aware of the presence of *DTB* data for provincial roads, and thus grossly overestimated road elevations in regions of occlusion. The *AHN3*-based *RMSE* of 0.75 m is because the dataset also contains *R-roads* where the *DTB* data is outdated (most of it is from 2004), and is consistently at lower elevations than *AHN3*. In both cases, it is the academic results that show elevations that are closer to reality, considering that they are much more recent.

The dataset 25BZ2 (*Amsterdam Hemhavens*) contains the largest tunnel among my datasets, and one which has no *DTB* coverage. As a result, the academic implementation interpolates linearly across the gap, resulting in the output containing an elevation profile close to the ground and water level above the tunnel. This is what gives rise to the 7 m *RMSE* in the table. The commercial results contain the correct, V-shaped elevation profile of the subterranean road – the explanation of this difference is simple: they consider a certain type of *DTB* line feature (*lijnverlichting* – road surface illumination) as reliable road surface measurements. My implementation filters these out, as I found examples of this line feature not lying flat on the road surfaces in other locations. In any case, including them in my results is a matter of adding this keyword to a variable in my code. The large *AHN3* *RMSE* in this dataset is also due to the tunnel; my implementation erratically identifies Lidar points describing the tunnel service structure as a continuation of the road, and uses it in the elevation interpolation step.

In 25DN2 (*Amsterdam Zuid*), The agreement between the datasets is generally very good (as the *AHN3* and *DTB* values indicate), but the linear interpolation agreement is anomalously poor. This is the result of a single *wegvak*, which contains a medium-length tunnel. This tunnel contains good *DTB* coverage which my implementation correctly identifies and uses during the Lidar segmentation step, but which it then fails to make use of when constructing the preliminary edges, breaking off the edge geometry at the tunnel entrance. As I mentioned in Section 3.3.4, this is because preliminary edge detection will mostly fail to construct cross-sections where only *DTB* is available, which will result in no *TINs* being constructed locally, if there is a bend in the road in the occluded area, or if the given *LineString* ends there. The particular *LineString* in question falls into both categories, as it contains a bending road in a tunnel that ends roughly in the same place where the *LineString* itself ends. Fixing this issue falls into the category of future work, as it did not fit into the timeframe reserved for this research.

The results in 32HZ2 (*Apeldoornseweg*) are interesting because the dataset contains tightly packed, thin, parallel provincial roads (no *DTB* coverage) in an old-growth forest that often completely covers the sky above the roads. This decreases the mean *TIN* vertex density to 14 points per m², often dropping below 10 in the most densely vegetated areas. In this case, my attention was piqued not by a disagreement between the datasets, but near-perfect agreement. Of course, both sets of results rely on *AHN3* here, but the commercial ones used *AHN3* *DTM* rasters, rather than Lidar points. The similarity is likely to indicate that the raster-based *AHN3* terrain model is very accurate in this area, despite the forest. The only (minor)

artefacts – affecting both the academic and commercial results – are due to [NWB](#) sometimes missing the real centrelines by a significant margin, veering off into ditches and other sharp terrain features. The 1 m [RMSE](#) seen for linear interpolation in this dataset are due to the [NWB](#) centrelines often extending beyond the corresponding clipped point clouds, which I had already discussed in terms of the accurate vertex ratios, i.e. it is artificial and meaningless in the context of this comparison.

Lastly, all three [RMSE](#) values computed for 37EZ1 (*Rotterdam Ketheltunnel*) are anomalously high due to the tunnel construction works. The large [RMSE](#) values for [AHN3](#)-based and linear interpolation are easy to explain: both the small [TINs](#) that are constructed inside the construction areas, as well as the linear interpolation between them (where no [TINs](#) exist) are expected to be inaccurate, and certainly different from the commercial results which rely on [DTB](#) here. [DTB](#) has already been updated with line geometries that correspond to the re-built motorway. Hence the commercial implementation's single-minded goal to reflect [DTB](#) in its output prevails in this case. However, it is unexpected that even where my implementation also uses [DTB](#), noticeable disagreement is still observed: an [RMSE](#) of 2 m. The reason for this is, based on a visual inspection of the results, that the confusing elevations shown by [AHN3](#) often result in the preliminary elevations matching the elevation of *unrelated* [DTB](#) lines, causing them to thus be added to subclouds in the Lidar segmentation step. The occasional use of wrong [DTB](#) lines corrupts the overall [RMSE](#), which is what we see in the table.

In the context of the above paragraph, it is important to note that while [DTB](#) certainly is superior to [AHN3](#) in this particular location, its quality and completeness are still far from perfect. For instance, the *lijnverlichting* features (and various others) are still from the *old* version of the road, the one that used to run on the surface rather than in a tunnel. Furthermore, [DTB](#) is incomplete in this location, which prompted the commercial implementation to use [AHN3](#) rasters in certain places, especially on the ramps. Due to this, it still produced some artefacts much like the ones generated by the academic implementation.

5 Conclusions

In this chapter, I present an evaluation of my results in the context of the original aims of this research, and specifically, the research questions. Rather than to follow the report structure that I used in the previous two chapters (3, 4), here I will present overviews independent of the pipeline steps. The following sections are based on an integrated understanding of the problem and relevant literature, of the results of my solution, and the accuracy and quality assessment thereof.

Our original summary research question was *"How can we achieve a 3D conversion of the NWB dataset using Dutch open geospatial data and a primarily 2.5D-based surface modelling methodology, while guaranteeing optimal and quantifiable accuracy and completeness?"*. I explored one possible way of performing such a conversion, which intuitively followed from the methods of relevant work, knowledge acquired during my geomatics education, and the main type of elevation measurements we used – ALS. The exploration of these topics necessitated designing a processing pipeline and implementing it. The pipeline produces accurate 2.5D road surface models, and uses these to perform the 3D conversion of NWB. The evolution of the data through this pipeline is comprehensively documented in the previous chapters of the present report, as well as the results of accuracy and quality assessment procedures.

Based on these, we may conclude that the process and the results of this research represent a fulfillment of its original aims as recorded by the research questions. All planned topics were examined in detail, the system design and implementation were completed and the accuracy and quality assessment verified our results.

At the same time, it is important to note that this is only one possible avenue of producing a 3D version of NWB, as illustrated by, for instance, the commercial system which uses a different set of methods to generate comparable output data. While I managed to develop a working solution to the problem, it is by no means the *only* possible solution. It is merely the solution I found to be most fitting to our research questions, the available tools and datasets, as well as the designated project timeframe.

In the sections below, I will present conclusive remarks regarding various aspects of the research. Some of these are based on specific research questions, which I indicated in their first paragraphs. These sections tackle the conclusive evaluation of both the processing pipeline and the results produced by it. At the end of the chapter, two final sections are found, providing summary conclusions (Section 5.6) and recommendations in terms of potential future work (Section 5.7).

5.1 Usefulness and generality of datasets

This section provides conclusions regarding the research questions *"How can we best make use of the combined information content of the datasets used by the commercial implementation?"*, *"What is the accuracy of our elevation data sources? Can we structure the pipeline in a way that their input accuracy can be propagated to the output in a straightforward manner?"* and *"While solving NDW's specific problem, can we ensure that our solution generalises well to other, similar problems?"*. In addition, it contains further conclusive remarks related directly to the input data used in this research but not specifically related to these questions.

5.1.1 General remarks about AHN3 and DTB

We set out to use Dutch geospatial open data in this project, and succeeded in doing so. I made use of no data that is not available to the general public, facilitating the easy reproducibility and reusability of my results – which was part of the reason why I restricted my attention to such datasets in the first place.

5 Conclusions

This also ensured that we build on exactly the same input data that the commercial implementation does, apart from the minor difference of using point cloud data directly rather than via derived *DTM* rasters – although this appeared to make little difference in practice, judging by the comparison of our results with theirs.

Using *AHN3* and *DTB* is also favourable in the sense that we may generalise their identities into a “primary dataset” and a “support dataset” respectively, the former with a nearly complete *ALS* coverage of the road surfaces, and the latter with accurate surface elevation measurements with coverage in the few places where there are gaps in the primary data. We may conclude that in terms of the necessary input data, my solution is quite versatile and general. Any large-scale datasets with a point cloud structure (be it Lidar data or dense image matching data for instance) could serve as the primary dataset, and any type of surface measurement data with areal coverage of road surfaces could serve as the support data (for instance, multiple *GNSS*-vehicle tracks for each road).

5.1.2 On the impact of input quality

In terms of the second research question above, my conclusion is that the accuracy of both input datasets is documented in their user manuals, which I successfully propagated through the interpolator to compute the formal output accuracy. However, it is worth noting that both datasets contain very basic accuracy information, i.e. a single vertical and horizontal accuracy value. While this is sufficiently detailed for most purposes typically concerned with using these datasets, point-level information could be beneficial for this application. The accuracy assessment steps could easily take the additional detail into account.

This brings us to the wider topic of local accuracy quantification. While some descriptors can be measured (such as the local sampling density), others, such as local ground filtering effectiveness or general classification accuracy cannot be easily determined by users of the data. The concept of temporal accuracy is also relevant to these datasets and not explored by their providers; for instance the specifications of *DTB* suggest that the underlying linear road features have a vertical standard deviations of 5 cm, while I observed up to 1 m deviations from present-day elevations.

Where the datasets indeed comply with their specifications, they make for a very good basis for my analysis, but not elsewhere. I found that on road surfaces, *AHN3* almost always complies perfectly (even exceeds) the accuracy and sampling density suggested by its specifications, whereas *DTB* does not generally appear reliable in this sense. A large amount of the elevations contained by it are questionable due to their age, and its coverage is also far from optimal. This leads me to conclude that for my procedures to work with a better efficiency, a better support dataset is needed, preferably *MLS* data of the roads specifically where *AHN3* is suspected to have little or no coverage. Both my results and the commercial results suffer from the issues introduced by *DTB*.

With this being said, both datasets were found to be useful for the pipeline, and especially for the analysis itself. Without *DTB*, I could not have created the dual primary-support input model and the associated pipeline workflows. Furthermore, even at the relatively poor quality that *DTB* represents now, it helps the procedure greatly where it *has* coverage. For instance, the processing of complex motorway junctions (such as *Knooppunt Ridderkerk*) would not have been possible with such good effectiveness without relying on *DTB* to navigate across the gaps of coverage resulting from bridge-related occlusion, even if the elevations it contains are not entirely correct locally.

5.2 Effectiveness of processing steps

This section is based in part on the research questions *“How should the road network be subdivided into parts that each represent a 2.5D problem?”*, *“As we are using Lidar data, can we produce an accurate and complete TIN surface model for each 2.5D “unit”?* *Can we interpolate elevations for NWB through these models?”*, *“Can the implementation be made robust enough to handle most challenging road layouts correctly, such as complex motorway junctions?”* and *“How can we make the implementation perform well in areas where elevation data*

is scarce or missing over longer distances, such as in tunnels?”. It also presents conclusions that are more general, regarding the overall effectiveness of my processing pipeline.

5.2.1 Decomposing the 3D problem into 2.5D sub-problems

My implementation followed, for the most part, the original plans I set out in the research proposal. Significant modifications were required only due to the unsatisfactory results of active contour optimisation.

The pipeline and its implementation adhered to our primary aim of decomposing the Dutch road network into segments which can be modelled via 2.5D methods. The **NBRS** (and **NBRS parts** on a lower level) represent the results of this “segmentation” – they are guaranteed never to violate the 2.5D assumption to a significant degree. As a result, all intermediate results of the pipeline – be it preliminary elevations or edges – will be concerned with modelling 2D elevation series and 2.5D surfaces of road surfaces that we can reasonably assume to be *mathematical surfaces*. This underpins the success of the **TIN** generation step, as without succeeding in this regard, it would have been impossible to generate **TINs** that behave correctly where occlusion occurs. This in turn also defines the effectiveness of the 3D conversion of **NWB**, as it relies on these **TINs**.

We may thus conclude that the divide-and-conquer approach to reduce the 3D problem into 2.5D sub-problems succeeded, and based on the quality and accuracy assessment, any remaining small-scale issues could be resolved by adjusting the parametrisation and making small revisions to the methods and the implementation. I encountered no problems that would have put into question the plausibility of employing this approach, in fact I found it intuitive to work with. Furthermore, based on the experience I gained during the development, this approach allows the computational complexity of the software to be reduced, and the generation of *independent* problems in the process also means that theoretically, it would be straightforward to adjust the implementation to use parallel processing. From the creation of each **NBRS** up to the point where snapping takes place in the last interpolation step, they are processed independently. This can be regarded as the foundations on which a low-level scaling implementation could be built on (rather than a top-level one, e.g. one simply tiling the input data). Hence, we may conclude that we have also found at least a partial answer to the research question “*Could [the NBRS] be processed individually to facilitate easy parallel processing?*”.

Owing to the general success of this approach, stitching the independent results into a single 3D-NWB output was also far less challenging than originally suspected. Wherever the program managed to identify the correct approximate shape of roads early on and to carry this all the way into the **TIN** construction step, the **TINs** themselves became almost identical in intersections, meaning that snapping typically concerned moving end-vertices only by a few centimetres. This is in sharp contrast with my original suspicion that this would be a complex task. Hence a conclusive answer and practical solution was also found for the research question “*How do we “stitch” the results of the individual 2.5D procedures back together into a 3D road network with correct topology?*”.

5.2.2 Surface modelling effectiveness

My work demonstrated that the **TIN** initialisation-extension procedure is capable of constructing accurate surfaces under most circumstances. We may conclusively remark that almost all the resulting **TIN** models lack outliers on road surfaces, save for the relatively rare occasion of **NWB** getting very close to road edges or leaving the road surfaces altogether. This issue is not related to our methods or implementation, and **NDW** is already working on fixing it. Section [A.1](#) presents a demonstration of how the results further improve when **NWB** itself improves.

The fitted road surfaces are smooth on the scale of the roads themselves. They are also almost as detailed as the underlying Lidar subclouds, meaning that most input information is piped directly into the models. In the accuracy assessment step, I discovered that the small-scale noise in the models is indicative of a significant degree of oversampling. The road surfaces are simple geometrically in the

5 Conclusions

context of terrain in general, hence the high inserted point densities (between 10 and 30 points per m² even after thinning by a factor of 2) are not truly necessary and can be reduced by reusers as needed.

The completeness of the generated surfaces is generally good. However, due to the combined limitations of my preliminary edge detection and TIN construction methods, the TINs may not fully cover the paved surfaces, and in rare cases (motorways with 2+ lanes) also not the entire *traffic-occupied* road surface. For the ultimate aim of using these models to convert NWB into a 3D dataset, this is irrelevant because under normal circumstances, it will still be possible to interpolate at NWB vertices in the TINs. Our original, academic aim of exploring the possibility of producing 3D road models in addition to 3D-NWB output was conclusively satisfied regardless, and it is my suspicion that by refining my methods, the average completeness of my road models could be improved from the current 75% relative to BGT road polygons.

This part of my research proved that it is possible to not only produce 2D elevation profiles for the underlying roads, but to increase the dimensionality to a surface-modelling level without having to rely on additional data relative to the commercial implementation. The most important question I found is that one either constructs edges that can be definitively assumed to contain most of the road surface reflections, or one needs to algorithmically grow the surfaces beyond the initial estimates of the edge locations. Having been unable to attain an edge quality where such growing is unnecessary, my implementation relies on the latter approach.

The downside of this method is that the generated TINs will often have rugged edges, depending mainly on the physical characteristics of the edges and their surroundings. In other words, the models may occasionally overestimate or underestimate the road extents. An ability to produce better edge estimates (with or without active contour optimisation) would have allowed the TIN construction step to have a better indication of where it should expect to find the road edges (or to omit a growing-type algorithm altogether), whereas in my current implementation needs to look *beyond* the edge estimates.

In terms of complex road layouts, we can assert that the TINs are generally accurate enough, considering the properties of the input data. In places where only DTB is available, the TINs shrink in width and become sparsely sampled, but this is expected given the nature of DTB. The continuation of the TINs across these regions ensures that 3D-NWB elevations can be interpolated there the same way as elsewhere. Where DTB is also missing, the TINs become split into parts, each belonging to a segment of the NBRS with continuous AHN3 coverage, and with properties identical to that which I described above. In tunnels, the existence of the TINs depends on the existence of DTB and the shape of the road. Depending on these factors, the program may or may not succeed in extending the preliminary edges into the tunnels, which in turn decides whether the TINs will exist there or not. More information on this topic is found in the next section.

We may conclude that this research proved that even in the lack of accurate edge estimates, TINs with reasonably good quality can be constructed. Proposed further improvements to the relevant pipeline steps may be found in Section 5.7 below.

5.2.3 NWB 3D-conversion effectiveness

There are many parts of my processing pipeline that are specifically aimed at characterising the shapes of the road surfaces and their boundaries well in the 2.5D models, and this is primarily where some issues were encountered. The 3D conversion of NWB was not affected by them.

The output elevation series lie flat on the TIN surfaces, and their overall visual quality is exceptionally good. In particular, spikes and other types of sudden outliers are absent from the output where they were extracted from the surface models. The results have a 100% completion ratio in the sense that linear interpolation is used to fill in all gaps. The snapping procedure almost never fails either, NBRS are all properly connected geometrically in the vertical dimension. Since the workflow does not modify the horizontal georeferencing of NWB, its own connectedness issues are retained in the output.

The conversion effectiveness remains unchanged in the presence of both partial and complete occlusion where they occur over short distances. Weak occlusion (e.g. due to vegetation) does not decrease AHN3's

sampling density below the level from where noticeable problems in any part of the implementation would arise, up to an input thinning factor of about 4. In the case of occlusion due to opaque objects (such as where roads pass above and below one another in large junctions), the results are also not significantly affected as long as DTB exists locally. The exception to this rule is where DTB exists and is outdated, because this introduces noticeable jumps or drops in elevation. Even in the absence of DTB, small data gaps generally do not represent a problem because linear interpolation is suitable to approximate elevations across them (affecting only the output accuracy), and because the NBRs splitting workflow ensures that they do not cause problems with any of the modelling steps.

The effectiveness of the conversion mechanism is only low where AHN3 coverage is missing for longer distances, such as in long tunnels. If no DTB coverage is encountered, then the NBRs will be split into parts, and the distance in-between will be interpolated linearly. Such estimates may be far from reality, but this behaviour is expected – the program cannot “predict” elevations where it has no data available for very long distances. Due to certain limitations of treating DTB as a point cloud, even in long tunnels where it has coverage, the preliminary edge detection algorithm will not always succeed in generating them, which results in the same issue.

We may conclude that the overall effectiveness of the 3D conversion of NWB is exceptionally good, apart from the tunnel-related issue. To solve it, the preliminary edge estimation step of the pipeline would either need to be modified to work better with the specific vector geometry of DTB, or DTB would need to be replaced with better support data (preferably, MLS data) with which the current methods would work also in tunnels, automatically.

5.3 Accuracy-related conclusions

5.4 Accuracy assessment conclusions

I set out to satisfy the practical aims of this project in a way that allows output accuracy to be quantified in a straightforward manner. This is reflected by the main research question, as well as sub-questions such as *What is the effect of uncertainty in the horizontal position of NWB centrelines on the effectiveness of our methods, and on the output accuracy?* and *[...] can we derive our output directly from input data points, despite the large number of processing steps that are potentially necessary?* and *How good is the agreement between the commercial and the academic results? What could be the reason for global/local differences between them?*, as well as all the rest of the questions in the second half of the list in Section 1.4.

As the work presented in the literature review (Section 2.2) and accuracy assessment-related sections (3.4 and 4.3, respectively) demonstrates, I examined this topic in-depth throughout the research. Below, I will present concluding remarks distilled from Section 4.3 in the previous chapter.

In terms of a preliminary indication of confidence in my results (prior to the accuracy assessment step), I classified the origin of all output elevations based on which input dataset was used to generate them. This classification is based on the TIN triangle in which they were interpolated. When the triangle was comprised of vertices sourced from a mixture of AHN3 and DTB data, treated it as originating from DTB for simplicity, and because DTB is less reliable than AHN3. Elevations not acquired via TIN-linear interpolation but through simple linear interpolation represent the third category, in addition to AHN3 and DTB. It is only the vertices marked as originating from AHN3 that can be fully trusted. I recommend treating elevations derived from DTB and via linear interpolation as unreliable, due to the problems with the underlying data and the method’s uncertainty, respectively. Only if visual inspection confirms their correctness locally, can they be trusted.

Through an attempt at estimating output accuracy empirically, I found that with the particular datasets, surface types and geographical locations concerned by this research, ground filtering imperfection, surface ruggedness and sampling density can be assumed to have no influence on output accuracy. This also assumes that local sampling density is higher than the minimum density below which it would start to have an impact on output accuracy, which I estimated as 3 points per m³ in this research. This part of the assessment yielded typical sampling density values in the TINs between 10 to 30 points in

places that are not occluded by objects that are entirely opaque to Lidar. Sampling density does not drop below the above threshold in well-exposed areas using an input Lidar thinning factor of two.

Thus, my analysis considered the formal output accuracy to be a function of only error propagation through the interpolation technique above the sampling threshold mentioned above, and found that in such places vertical output error was almost always about 5.3 cm, so 10.6 cm at 95% certainty. The smallness of this value is explained by the fact that accuracy is expected to increase due to using 3 samples for each interpolation rather than just one, in triangles which are not significantly inclined – which is always the case with our TIN triangles.

In places where sampling density dropped below the threshold and where linear interpolation was used (zero sampling density assumed), I classified the output accuracy as “undetermined” to indicate that these values have little to no evidence to support their correctness. In testing datasets without large-scale problems (due to tunnels or construction works), this affected about 5 to 15% of the output elevations. These values are likely to be slightly exaggerated by DTB’s sampling “density” often not being high enough to be included in the accuracy assessment, which is not meaningful because it depends on the vertex densification used to convert its lines to a pseudo-point-cloud. Elsewhere, my results can safely be considered conformant with the vertical accuracy-related requirements of the new Dutch road noise regulations.

5.5 Conclusions of comparison with commercial results

The comparisons with the commercial results often indicated a surprising degree of similarity, considering that I prioritised the use of the AHN3 point cloud, whereas RHDHV prioritised DTB and only relied on AHN3 rasters in its absence, and when processing P-roads. In places where the agreement between DTB and AHN3 was good, the RMSE between the two sets of results was less than 10 cm, and often as low as 2-3 cm. Generally, this corresponds to regions where DTB contains up-to-date data with good coverage. In such locations, my results still tend to be more accurate, because the DTB results are generally still older even where the agreement is relatively good between the two datasets. In places where agreement was poor between AHN3 and DTB the RMSE was defined primarily by the mean magnitude of the elevation difference between them. RMSE values up to 0.75 m were observed in such places, with individual residuals sometimes exceeding 1 m in places where DTB data is more than 15 years old.

In *well-exposed* regions where both implementations relied on AHN3, the RMSE was typically between 1 and 5 cm. In these zones, both sets of results are equally accurate and reliable; using a raster DTM does not appear to have significant drawbacks. However, in places where the commercial results are based on the AHN3 rasters and *any amount of occlusion* is encountered, RMSE values up to several metres were encountered. This includes regions where my software interpolated linearly through small gaps and also ones where DTB was used by it, but was missed by the commercial software. Wherever the occlusion does not represent a long tunnel, it is always the academic results that are closer to reality, regardless of whether their formal output accuracy exists locally, or not.

Where the commercial implementation certainly fares better than the academic one is where only DTB data is available for long distances, especially in tunnels and on bending roads (or a combination thereof). The commercial method simply intersects nearby DTB lines with cross-sections extending from the NWB centrelines, and will produce elevations reliably wherever at least one DTB line exists. In contrast, the preliminary edge estimation in my pipeline may fail in such places. In the rare places where AHN3 is outdated relative to DTB, the same is true because this is likely to indicate that the given road does not yet exist in AHN3 in its present form (e.g. it missing, or is under construction in it).

To conclude, I have established that outside of the above two examples to the contrary, the academic results generally appear to be superior to the commercial results, but that the reason for this is not strictly related to the fact that the commercial implementation takes its output elevations from AHN3 rasters rather than the point cloud. Instead, we can conclusively say that the reason is the combination of their unconditional prioritising of DTB, and pragmatic methods that do not attempt to deal with occlusion-related issues explicitly. The commercial results also lack an accuracy assessment analysis comparable with the one found in my work.

5.6 Summary conclusions

The above sections show that all planned stages of this research were conducted successfully, including a functioning proof-of-concept implementation and an associated accuracy analysis. The solution proposed in this research is capable of performing the 3D conversion of *NWB* with accuracy estimated on the level of individual elevation estimates. Error propagation yields output errors around 10.6 cm at 95% certainty, lower than that of our main dataset, *AHN3*. This applies to more than 90% of the output elevations on average, not including locations with large scale issues such as tunnels and large-scale construction works captured by *AHN3*. The implementation records where the minimum sampling density was not reached to advise users of locations where the output has undetermined accuracy. Similarly, the program also records which input dataset was used to interpolate the elevation of each 3D-*NWB* vertex and where linear interpolation was used, explicitly.

My output shows good agreement with the commercial results, with the best agreement seen in well-exposed provincial roads where both solutions rely on *AHN3* data, with some datasets exhibiting an *RMSE* as low as 1 cm or less. The worst disagreements are seen in places where the commercial implementation uses outdated *DTB* data, and where it neglects to handle occlusion correctly and snaps the road centreline to overlying features, the prior corresponding to up to 0.75 m *RMSE* values, the latter to residuals of several metres locally.

My work proves that the approach of decomposing the conversion problem into 2.5D sub-problems works well in this scenario, and offers not only a more straightforward implementation and more effective means with which the elevations can be estimated, but also an interface for adapting the solution in a potential scaling-enabled implementation. While the proof-of-concept implementation proves that my system design can perform the conversion of *NWB* to a 3D dataset, it also successfully explored the academic aims of this project – mainly, whether the 2.5D approach is also a suitable framework for the production of accurate surface models of the roads, from which the output elevations can be derived.

While issues were encountered with the active contour optimisation part of the planned system, a small set of revisions to the system design allowed me to still generate the 2.5D models – albeit at the price of increasing the complexity of the design of certain pipeline steps and resulting in somewhat worse overall *TIN* quality than originally hoped. The *TIN* models cover about 75% of the cumulative paved road surface areas in the areas examined, which means that they may not be directly usable in some potential applications, such as the interpolation of elevations reliably in places other than the road centrelines. They generally do, however, cover most of the traffic-occupied parts of the roads.

Fortunately, the system design guarantees that under normal circumstances, the *TINs* will still be complete where they need to be to enable the interpolation of elevations for *NWB*, even in places where otherwise their quality may be sub-optimal. Hence, the quality issues with *TIN* generation did not affect the models' suitability for use in the 3D conversion of *NWB*, and the exploration of an alternative approach was not necessary. Recommended improvements to the *TIN*-related part of the pipeline are mentioned in the next section.

5.7 Future work

I have identified several directions in which work could continue. Below, I present ideas for both small-scale extensions and improvements, as well as large-scale design changes. I developed these suggestions with particular focus on the most likely reusers of my methods, namely *NDW* and academics.

5.7.1 Eliminating active contour optimisation

As I discussed in the previous chapters, I found active contour optimisation to be ineffective in this application, regardless of its parametrisation. While attempting to improve its performance in a wide variety of manners, I discovered that the primary control on its effectiveness is preliminary edge and

attractor map quality. Not only are these the most important controls on its performance – it is particularly sensitive to small imperfections in them. A few small protrusions in the preliminary edges or a series of small vehicle-related *AHN3* holes in the attractor maps can, for instance, corrupt the output to the point where it will almost certainly not provide accurate road/non-road point classifications. In fact, the current *TIN* construction algorithm produces better results using the preliminary edges rather than the optimised ones.

As I outlined in previous sections, bypassing active contour optimisation and using the growing-type *TIN* construction approach does not affect the 3D-NWB conversion efficiency. However, it does make the output *TIN*s less appealing visually and in terms of completeness and quality around the road surface edges. Depending on the application, reusers may wish to improve this. While other image-processing-type algorithms exist that can achieve similar, perhaps somewhat better results (ribbon snakes, Chan-Vese algorithm, etc.), my recommendation is not to invest time and effort in trying to replace the active contour optimisation algorithm with one of these.

The original system design was based on pre-processing the data in preparation for active contour optimisation, and relying on its output to determine which Lidar points are found on road surfaces, and which are not. While I managed to bypass active contour optimisation in the end by adapting the preliminary edge generation and *TIN* construction algorithms, the final (implemented) system design is still relatively conformant with this planned structure – to the point that active contour optimisation can be run, optionally, and produces usable results.

A larger-scale redesign of my system should eliminate active contour optimisation altogether. Doing this makes another pipeline step redundant at least partially: preliminary edge estimation. The original purpose of this step was to provide initial edge estimates for the active contour optimisation algorithm. In the final implementation this has changed; they are only used to provide better centreline locations than *NWB* for the seeding of the initial *TIN*s, and to delineate the approximate location of the road surface for the *TIN* *initialisation* step.

However, neither of these uses may be absolutely essential, nor is their effectiveness fully satisfactory in their current state. *NDW* is already hard at work improving *NWB*'s 2D georeferencing quality, and I can think of no reasons why the *TIN* initialisation algorithm could not be slightly modified to work without the preliminary edges. It is even possible that simply buffering *accurate* road centrelines to yield theoretical edges corresponding to the minimum expected road width would work in place of these in the *TIN*-initialisation step. Alternatively, road edges could also be derived from *BGT*.

In short, eliminating active contour optimisation from the software would make preliminary edge estimation partially redundant. A few modifications to the *TIN* construction workflow (in addition to the assumption that *NWB* is accurate enough) could theoretically make it redundant entirely, in which case preliminary edge estimation could also be eliminated. This would reduce runtimes somewhat, and would make future work on the system simpler, by taking out two relatively complex steps from the pipeline.

5.7.2 Improving *TIN* construction effectiveness

In addition to the smaller modifications I recommended above, the *TIN* construction step could also use a few modifications. Based on my experience in working with the implemented system design, the approach works well, but there is one further component that could improve the results of the procedure.

Conditional point insertions into pre-existing *TIN* triangles are based on distance and angle thresholds that examine the conformance of the candidate points with a single *TIN* triangle only. Insertions *outside* of these triangles (growing-type insertions) are based on examining the candidate's conformance with a plane fitted on some nearby *TIN* vertices. Although the latter represents a better sampling of the overall local trend where the point is being considered for insertion, it still ignores the global trend that exists on, at least, the scale of the local width of the road at the time of the test. In other words, as long as the transition from road to off-road points is sufficiently smooth, it is not impossible that the surface will be allowed to grow beyond the true road edge.

This serves to highlight that most roads are flat on a scale larger than that which concerns the insertions. Making the conditional insertions perform tests on this scale could potentially improve the effectiveness of filtering out points that do not fit the overall shape of the road. This property already represents the foundation of the Lidar segmentation pipeline step, which fits planes on the same scale that could also potentially be appropriate here. Performing such larger-scale checks could eliminate insertions that cannot be detected as erratic on the local scale.

Another approach that could achieve a similar result would be to use point normals to detect breaks in smoothness that could indicate the approximate edges of the surface. The advantage of this approach over the simple plane-fitting one is that based on my experience, it can detect small changes more reliably. One only needs to look at the generated attractor maps in active contour optimisation to see that a scalar field derived by the interaction between the point normals can characterise road surfaces very accurately. It is even possible that the attractor maps could be directly employed in the TIN surface growing algorithm.

Neither of the above recommendations addresses the matter of maximum road widths. While a refined implementation using the above ideas could offer a better success rate in terms of accidentally overgrowing the road surface, it would still not be able to identify places where no physical evidence exists that the road's surface should end, i.e. no sudden or even gradual change in elevation can be observed. In such places, I recommend exploring two possible approaches.

Either one can implement a workflow that monitors the evolution on the width of the road along its length on-the-fly as the TIN is being grown, like the enforcement of the conditions in my preliminary edge estimation workflow. Alternatively, one can simply enforce a maximum road width appropriate for the the specific road *type* in question, or perhaps sample BGT to obtain a local estimate. The advantage of the former is that it has good generality, i.e. one does not need additional road attributes to make it work. By keeping track of the evolution of the road width, one can effectively monitor, and perhaps model these edges and ensure that the growing algorithm does not introduce any sudden bulges into them. For this to work, growing would need to take place with a roughly identical "speed" along the length of each NBR part, for which my TIN extension workflow is better suited than the initialisation algorithm.

5.7.3 Performance and scaling

While the comparison with the commercial implementation primarily discovered areas in which the academic implementation performed better than the commercial one, it is important to point out that the commercial software has a crucial property which the academic one does not: not only does it work for the whole country (with a total runtime of a few days on a computer optimised for GIS processing), it works *without* having to rely on a scaling implementation even though it is also partially based in Python. This is not to say that its runtime could not be reduced by introducing a scaling solution into it – I merely wish to point out that their solution is far more lightweight than mine. Without performance improvements (and potentially, a binary implementation of my system design), the academic solution would not be able to process the whole country's dataset in a few days, it would possibly take significantly longer. Based on my benchmarks, a week would be a rough estimate, assuming that active contour optimisation is not used, only TIN initialisation is enabled and not TIN extension, and also that a rudimentary scaling solution exists to at least automate the production of the input "tiles" of data and the stitching of the output back into a national road network.

In part, this inferior performance is to be expected – the academic implementation carries out computationally complex operations, such as plane fitting and vector inner products *in bulk*. Furthermore, it does so in a programming language not particularly good at processing long iterations containing such operations. The solution is therefore not practical for processing the whole of NWB (and the necessary AHN3 and DTB data) all at once, it is more of a technology demonstrator than a production software package.

However, the system design and its open-source nature leaves the door open to anyone to develop production software based on it, with an associated scaling solution potentially on the level of parallel-processing individual [NBRS](#). Reusers considering such a project must bear in mind however, that small-scale optimisations may be necessary. For instance, the analysis, and in particular the accuracy assessment, indicated that the constructed [TINs](#) oversample the road surfaces to a significant degree – in fact, to the point where the small-scale noise introduced is likely to have a negative effect, for instance it can give rise to small triangles at surprisingly high angles in places where samples are tightly packed into small clusters. Optimising and equalising the quantity of the inserted points would yield not only a significant improvement in terms of computational complexity, but it would also solve potential processing issues and make the models better suited to practical applications.

I suspect that introducing the enforcement of such a maximum sampling density earlier on, perhaps during the Lidar segmentation step, could increase the performance even more, because it would affect more processing steps – one would simply need to find the minimum sampling density, at which all parts of the pipeline still work reliably.

5.7.4 Conditionally accepting preliminary elevations as final

Part of the high computational complexity of my implementation may not be justified for all roads, assuming that one only wishes to convert [NWB](#) to a 3D dataset. As I mentioned in various places in this report, [TIN](#) extension is not necessary if one only needs the 3D conversion of [NWB](#); it can be safely disabled. However, there is an additional way in which bypasses could be implemented to make the overall process more efficient.

Assuming that the 2.5D surface models are not needed by the reusers for anything else other than to interpolate elevations for [NWB](#), then it may be a good idea to modify the preliminary elevation estimation algorithm in a way that it can intelligently recognise where its output is already accurate enough, and to skip all subsequent pipeline steps in such cases.

This is an idea that occurred to me while I was comparing the preliminary and final 3D-[NWB](#) geometries. For well-exposed roads, the [RMSE](#) between them can be as low as 0.5 to 2 cm and even where there are small gaps in coverage, the refinement step usually approximates elevations in the gaps quite well. The deciding factor in terms of telling whether these results can be deemed “final” appears to be related to how much of the full length of a given [NBRS](#) is occluded, and how much vertical curvature it possesses. If either or both are high, then the polynomial fit will only be accurate enough to provide support for subsequent steps of the pipeline.

For roads where this is not the case, one may regard the preliminary elevation estimates to be almost on par in terms of quality with the final output. In fact, it may even be theoretically more accurate in certain cases, because each elevation value that does not come from the refinement step is sourced from more Lidar points than the constant number of 3 samples used by [TIN](#)-linear interpolation in the last pipeline step. Therefore, it may be an interesting area to explore in future work to identify such roads based on certain metrics (for instance, the standard deviation with respect to the polynomial model and the total number of outliers detected) and to skip all subsequent steps for such [NBRS](#).

Furthermore, an alternative avenue of research may be to attempt to base most output elevations on the type of simple computations performed during preliminary elevation estimation in my pipeline. For this to be possible, the polynomial fitting workflow would need to be changed to work on the scale of the entire dataset as a whole, so that the models better fit the data. Specifically, this would presumably require the global optimisation of a network of polynomials, which is not something I had time to explore in my particular research. Successfully implementing such an alternative workflow may allow one to bypass most other pipeline steps in many places. This can be interpreted as adapting the spline-fitting pre-processing steps from [Boyko and Funkhouser \[2011\]](#).

Both of these approaches would reduce computational complexity drastically, since they would bypass the costly operations (e.g. [TIN](#) construction) in most cases.

5.7.5 Using the support dataset more intelligently

Our support dataset, *DTB*, is currently used in a way that effectively ignores its topology. By converting it into a point cloud as soon as it is imported, my implementation treats it as an extension of *AHN3*, partly because I wished to make this step to have good generality (i.e. to make no assumptions about the topology of the support dataset), and because my solution would perform best if the support dataset were itself an *MLS* dataset. *DTB* is useful, but it offers too little coverage of the road surfaces to be used to construct good *TINs*, especially considering that even where *DTB* is available, it may only have a single line feature available for a given road. The *TINs* generally have poor quality where only *DTB* data was available.

The targeted acquisition and use of *MLS* data in these regions could drastically improve my results. At the very least, elevation data should be used that delineates the entire road surface, for instance surveying *dense*, accurate elevations for *BGT* polygon outlines would presumably do the trick.

However, if this is not an option, then reusers may wish to examine the simple alternative: to treat *DTB* properly as a line dataset, and to thereby use its topology to somewhat improve the completeness of the output (to reduce the amount of elevations that are computed via linear interpolation). Specifically, the cross-section-based workflow that my preliminary edge estimation workflow uses could be adjusted to intersect *DTB* lines directly, where *AHN3* data is missing, or has a poor sampling density. This would somewhat improve the overall quality of the preliminary edges, and in turn, that of the *TINs*. However, it would not make them cover the full extent of the paved areas, or be able to provide *NWB* elevation estimates with the desired accuracy. In fact, the relevance of such a procedure (which is not unlike the way the commercial implementation uses *DTB*) is drawn into question by my findings regarding the temporal and completeness issues that *DTB* has. The main advantage of such an approach would be, as the academic-commercial comparison also suggested, that *DTB* could be used more reliably to help extend the *TINs* through long tunnels and other types of occlusion – or to derive elevations for 3D-*NWB* in such places directly from *DTB*.

A Appendix

A.1 Testing the updated NWB motorways

In an effort to resolve some of the problems regarding NWB's georeferencing issues, NDW commissioned several commercial projects. One of these projects performed a BGT-based refinement of municipal road (G-road) centrelines, and these improvements already form part of the regular NWB release. A more recent project performed a similar refinement of motorway (R-road) centrelines. Like the commercial counterpart of the present research, this project also relied entirely on DTB. I was given access to preliminary results of these updated geometries, and present the results of testing them in this additional section.

A.1.1 Updated NWB geometry

My project was affected noticeably by the coarse georeferencing of NWB. While it is theoretically possible to derive elevations for the road network that comply with the 20 cm elevation accuracy requirement, the elevations will not necessarily reflect elevation at the desired 2D locations where NWB's georeferencing is particularly inaccurate. Furthermore, the fact that it is impossible to predict where the centreline lies on a given road surface (and in some places, *whether* it even lies on it) caused practical issues with my algorithms.

Figure A.1 shows the differences between some original NWB geometries and the updated ones in the *Knooppunt Deil* area. The displacements are typically on the 0-1 m scale, but I observed up to 5 m deviations in certain locations, as also suggested by the nominal accuracy of the dataset. In the region shown by the figure, the displacement is 1-2.5 m in the locations labelled as "large shifts in NWB's location". As noted in various places in this report, problems are most common in sharp bends. Accordingly, the updated geometry shows the largest displacement relative to the original in such places. The second most common location is where no NWB vertices are present for hundreds of metres due to the local straightness of certain motorways. This type of simplification results in several metres of displacement that may be present for most of the simplified length of the given road.

As the centrelines were "re-centred" using DTB lines, the refinements were only carried out for motorways, and only where sufficient DTB data is present, i.e. at least the two road edge lines. In the testing dataset shown by Figure A.1, this means about 75% of the total length of the roads.

A.1.2 Impact on edge approximation

The procedures from my processing pipeline that suffer the most from the NWB-related issues are the edge approximation (and optimisation) and TIN construction workflows. In this section, I will discuss how edge approximation is affected by the improvements.

The main reason why edge approximation is sensitive to NWB's 2D location is that it assumes that the centrelines are always located on the road surfaces, and because the fixed-length cross-sections may extend into confusing areas if NWB is close to either of the edges of a given road. For instance, if a centreline veers to the right and there is a flat region with a similar elevation beyond the edge of the road, the cross-section's elevations may not be classed as outliers there, in turn attracting the generated edges off the road. The workarounds I implemented to bypass the issue do not have a 100% effectiveness, meaning that improvements to the 2D georeferencing accuracy of NWB are expected to result in noticeable improvements in the effectiveness of this pipeline step.

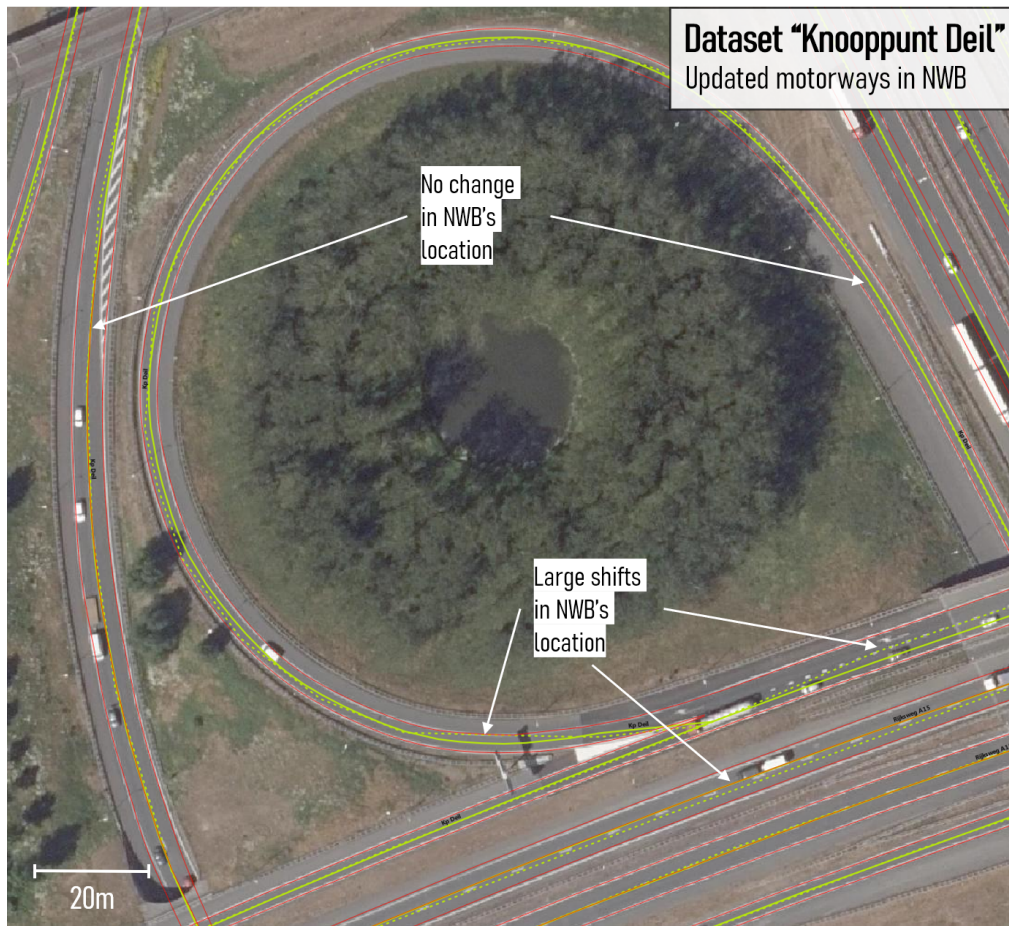


Figure A.1: This 2D visualisation compares the original version of *NWB* (on which the present research was based) to the newest release, in which *R-road* centrelines were improved using *DTB*. Solid green lines show the new position of the centrelines, while the dashed ones show the original ones. The thin red lines show the relevant *DTB* features.

Figure A.2 compares the generated edges prior to the refinement of the centrelines, and after. The main type of improvement noticeable in the new edges and cross-sections is that in bends, less cross-sections are skipped, and the new edges better define the extents of the road surfaces. The edges no longer contain short-wavelength extensions into off-road areas and are thus at a relatively constant distance from each other, even where the bends are quite sharp. This improvement is also noticeable where the same issue exists for the opposite reason (i.e. where *NWB* is vastly oversimplified due to it being straight for a long distance).

The second, less intuitive improvement is due to the fact that already during the Lidar segmentation step, points relevant to the given road surface are selected more efficiently. Less off-road points being included in the queries results in the plane fits being more accurate. This bump in efficiency means that the algorithm now performs well in areas where it had failed before. In the upper visualisation in Figure A.2, one of the *NBRs* has been split in two due to the Lidar segmentation algorithm's inability to work properly around the entrances of the small tunnel that exists there. This also resulted in the *DTB* points inside the tunnel not being found, which is why the *NBRs* was split into two parts there.

With the new *NWB* geometry, this is no longer an issue. Due to the improved georeferencing, the Lidar segmentation algorithm's plane fits are mostly defined by road surface points around the tunnel entrances, improving its performance drastically. The *DTB* elevation measurements are found and used to navigate through the tunnel. Ultimately, the *NBRs* needs not be split into two parts and several additional, meaningful cross-sections appear around the tunnel entrances, increasing the area properly covered by the generated road edges.

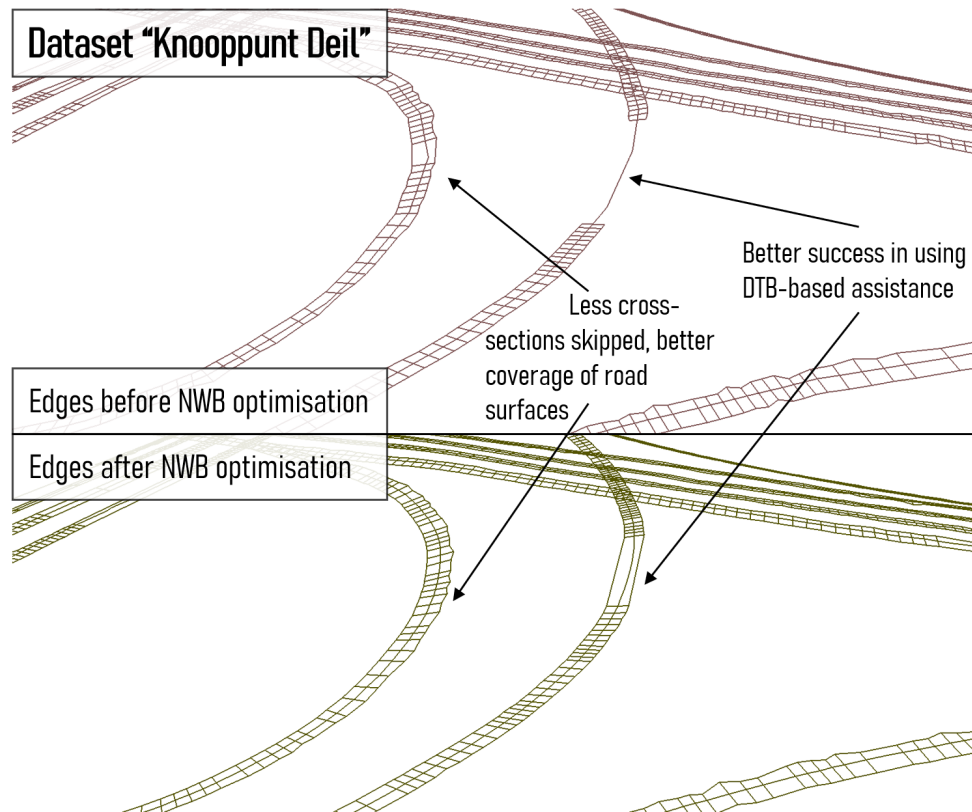


Figure A.2: This visualisation compares the cross-sections and preliminary edges generated using the original *NWB* centrelines (above, in dark red) with the ones derived from the refined centrelines (below, in beige).

The improved edges also positively affect the performance of active contour optimisation, although not to an extent where re-introducing it into the recommended pipeline configuration would be justified.

A.1.3 Impact on TIN construction

The *TIN* construction effectiveness also improves as a result of using corrected *NWB* geometry. Figure ?? compares some of the *TIN*s before and after the refinement of *NWB* in the same area as the one shown in Figures A.1 and A.2. There are less off-road points between the updated edges (relative to the originals), and they better define the true road edges in general. This means that the seed line derived from them will also be more accurate.

As a result, the *TIN* initialisation step will be more reliable both in the seeding stage and during the conditional insertions that follow. Less off-road Lidar points will be tested with the (less strict) initialisation thresholds than before, since most of them will no longer fall between the road edges. Instead, they will be examined with the stricter insertion thresholds of the *TIN* extension stage. At the same time, many road surface points that were previously missing will now correctly lie between the road edges. This is likely to occur on the opposite side of the road relative to the side where off-road points were moved outside the edges. In simpler terms, moving the centreline in a certain direction often moves the preliminary edges in the same direction, which results in these two changes taking place simultaneously. It may also happen that one of the edges is left virtually unchanged while the other moves into its proper position, although this is somewhat rarer.

The fact that the edges extend closer towards areas with partial or full occlusion (such as the tunnel in this area) also means that the *TIN*s now also provide far better coverage in such regions. In fact, the *TIN* in this case extends all through the tunnel although this is not shown in the visualisation since the large tunnel-based triangles were removed when the *TIN*s were exported.

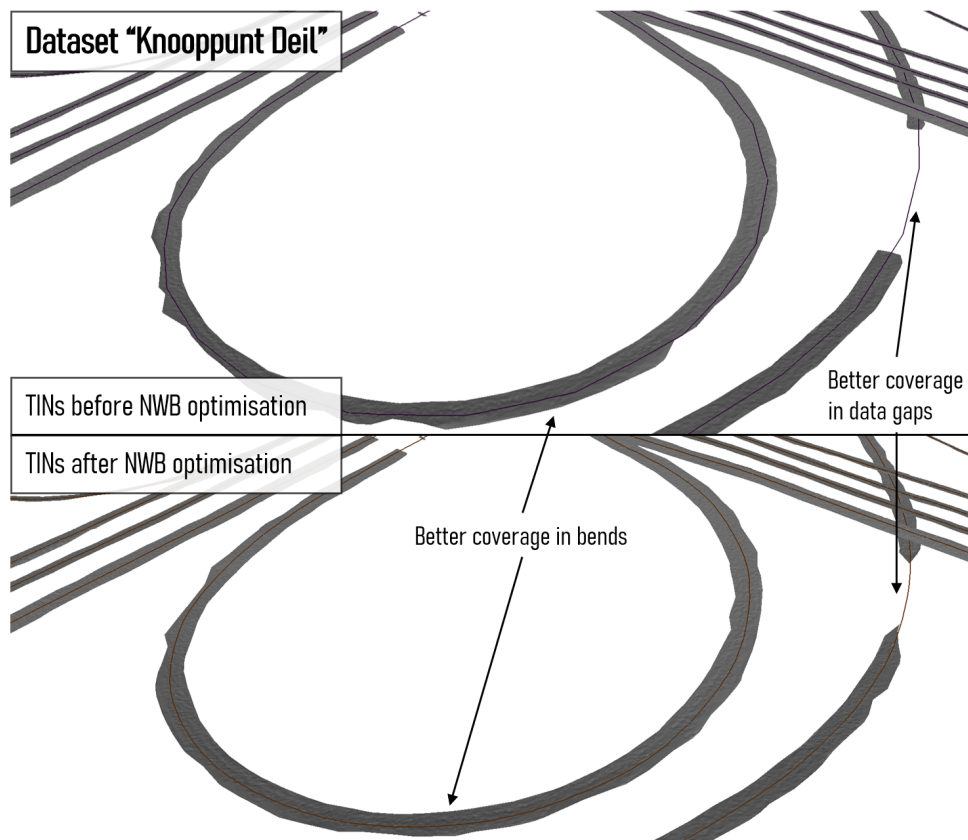


Figure A.3: This visualisation compares the TINs generated using the original NWB centrelines (above) with the ones derived from the refined centrelines (below).

The latter improvement also benefits the generation of the final 3D-NWB geometries, since less elevations will need to be interpolated linearly. The former improvements (away from occluded areas) only have this effect where NWB’s 2D referencing was so bad, that the preliminary edge approximation algorithm needed to skip enough cross-sections for the centreline to become located outside of the area delineated by the preliminary edges. This is extremely rare, hence we may safely conclude that the 3D-NWB elevations improve primarily in and directly around occluded lengths of roads.

A.1.4 On improving NWB’s 2D georeferencing dynamically

As the discussion and figures presented in this section indicate, improving NWB’s stock georeferencing is certainly desirable, and NDW’s recent efforts to realise this are already very promising. However, there are still many centrelines in NWB which have not been refined yet, and even in the case of motorways, the refinement is only partial (because DTB is incomplete).

My pipeline produces two main types of data: road surface TIN models and 3D-NWB geometry. Both of these appear to benefit significantly from improving the quality of the 2D georeferencing of the centrelines. However, some of these improvements may be possible to achieve internally, without relying on refinements carried out on NWB. In other words, the georeferencing of NWB could be improved dynamically at various points in my pipeline.

Refinement during edge approximation

In the TIN construction step, the TINs are seeded via a seed line derived from the preliminary or optimised edges. Since the road edges are generated in a way that attempts to counteract the effects of NWB’s

coarse georeferencing, the seed line is often a more accurate representation of the road's centreline than NWB is, itself. The same type of geometry could be easily derived already during the edge approximation step and then used as surrogate centrelines. It may be advisable to simplify or smooth the line somewhat, so that small-scale issues with the preliminary edges are not reflected in it. Before continuing, it would be necessary to perform edge approximation once again, but this time starting from the surrogate centreline. Without this additional step, the TIN construction stage would still make use of the *original* preliminary edges, and not the ones that were improved based on the surrogate centrelines.

Refinement during TIN construction

Alternatively, one may instead attempt to derive the skeleton of the generated TINs rather than that of the polygon formed by the preliminary or optimised edges. The edges of the road surface would first need to be located inside the generated TINs. One could employ the same tactics that I utilised to export and visualise the models in this project, i.e. to remove large triangles and sliver triangles. The triangle edges that define the road edge could either be identified procedurally as part of the triangle removal step, or an α -shape generation program could be used on the vertices of the accepted triangles.

To improve the TINs based on the derived surrogate centrelines, the preliminary edges would then need to be re-generated and the TINs would need to also be built from scratch again, based on the new edges. This would increase runtimes by a significant margin, hence performing centreline refinement as part of or as an extension of the edge approximation step is my recommendation.

Effects on 3D-NWB

The above refinements would primarily target the improvement of the generated TINs via improving the centrelines. The surrogate centrelines would certainly not be accurate enough to be used in place of the original NWB geometries when producing the output 3D-NWB geometries. Hence, the output centrelines would still be in the same horizontal locations as the original ones. However, since the TINs would be more accurate, the elevation interpolation step would need to resort to linear interpolation less frequently. The improved TINs, themselves, would be the other main reason why one may wish to add such routines to the pipeline.

I judge such methods not to be reliable enough to serve as a means to refine stock NWB 2D georeferencing. Approaches that involve pre-existing RWS and third-party datasets (or surveying new data) are almost certainly better suited to this task, such as the approaches of the ongoing projects of NDW.

A.2 Reproducibility self-assessment

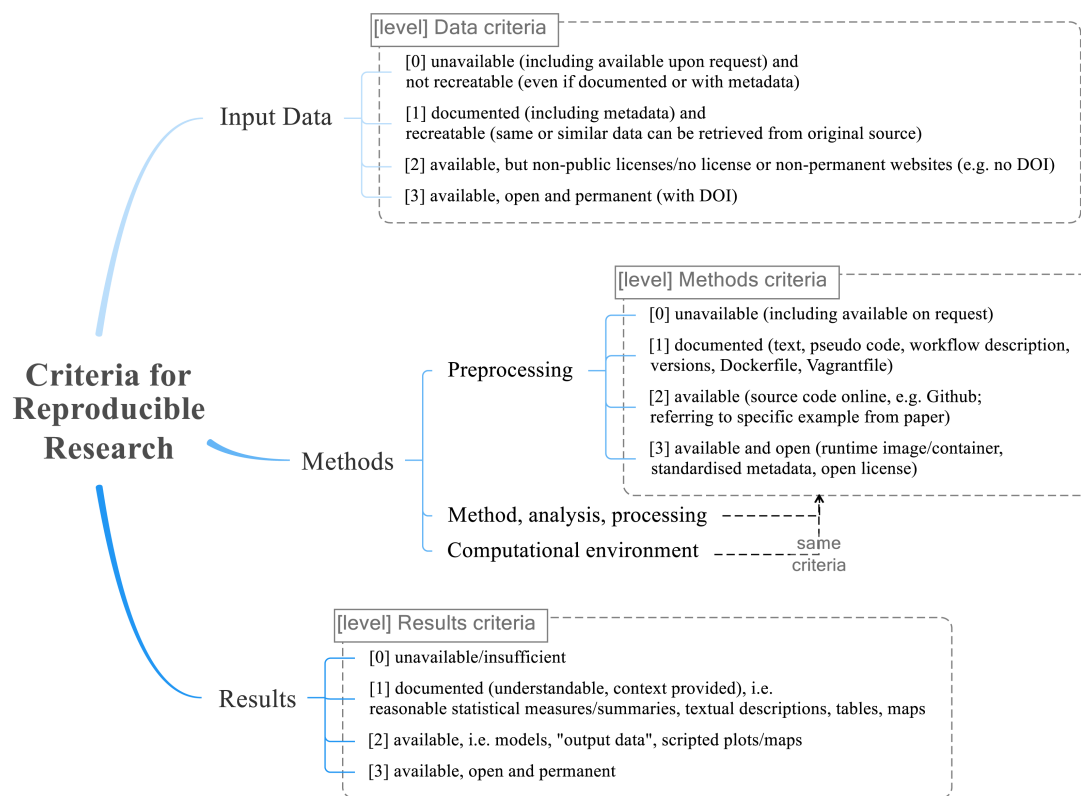


Figure A.4: Reproducibility criteria to be assessed.

Reproducibility self-assessment grades on the scale introduced in Figure A.4:

1. Input data - **Grade = 2**
2. Pre-processing - **Grade = 1**
3. Methods - **Grade = 2**
4. Computational environment - **Grade = 2**
5. Results - **Grade = 2**

A.3 Self-reflection

It is both my personal belief and my faculty's standpoint that all parts of university research should be made public in a manner that allows all results to be reproduced, that are necessary to reach the research's conclusions. To exercise this notion in practice, I made 3 crucial logistical choices in consultation with my supervisors.

Firstly, all datasets used in my research are open data, accessible and reusable for both academic and commercial purposes. Secondly, my methods are not only well-documented, but the proof-of-concept implementation of my system design is available as an open-source Python application. Lastly, no tools were employed in the execution of the present research that require a commercial license. The only exception from this rule is FME, which I used to produce many of the visualisations shown here in the report. An academic license for FME can be obtained for free, although its use is not strictly necessary in terms of reproducing my results. There are other, equally suitable programs available that one can use to visualise my results.

To make it particularly easy for potential reusers to make use of my results, I maintain repositories hosting the source code of the present report, and that of the implementation. In addition, a package of example input datasets and output files (with various intermediate results included) are accessible via a link in the code repository. These are the same files on which most of the results described in the present report are based on. Reasonable efforts will be made to keep both the source repositories and the package of input/output files online at all times.

The only parts of my research whose reproducibility is somewhat less straightforward are the manual pre-processing and the commercial comparison steps. While the relevant steps have been described in-depth in this report, project files (e.g. for QGIS) and relevant source code are not available. These parts of the project can also be reproduced via basic knowledge of GIS tools and operations, and by following the steps outlined in this report. I decreased the pre-processing grade in the above list from 2 to 1 to reflect this limitation. Overall, the methods of the research still comply with the definition of grade 2, apart from the comparison with the commercial results.

References

- Aguilar, F., Agüera, F., M.A., A., and Carvajal, F. (2005). Effects of terrain morphology, sampling density, and interpolation methods on grid dem accuracy. *Photogrammetric Engineering and Remote Sensing*, 71:805–816.
- Aguilar, F., Mills, J., Delgado, J., M.A., A., Negreiros, J., and Pérez, J. (2010). Modelling vertical error in lidar-derived digital elevation models. *ISPRS Journal of Photogrammetry and Remote Sensing*, 65:103–110.
- Bater, C. and Coops, N. (2009). Evaluating error associated with lidar-derived dem interpolation. *Computers and Geosciences*, 35:289–300.
- Bell, M. and Lida, Y. (1997). *Transportation network analysis*.
- Bennett, J. (1997). The application of geographic spatial analysis in modeling traffic noise propagation away from a freeway. *Journal of The Acoustical Society of America*, 102.
- Boyko, A. and Funkhouser, T. (2011). Extracting roads from dense point clouds in large scale urban environment. *ISPRS Journal of Photogrammetry and Remote Sensing*, 66.
- Cai, H. and Rasdorf, W. (2008). Modeling road centerlines and predicting lengths in 3-d using lidar point cloud and planimetric road centerline data. *Computer-Aided Civil and Infrastructural Engineering*, 23:157–173.
- Caltagirone, L., Scheidegger, S., Svensson, L., and Wahde, M. (2017). Fast lidar-based road detection using fully convolutional neural networks. pages 1019–1024.
- Chow, E. and Hodgson, M. (2009). Effects of lidar post-spacing and dem resolution to mean slope estimation. *International Journal of Geographical Information Science*, 23:1277–1295.
- Clode, S., Kootsookos, P., and Rottensteiner, F. (2004). The automatic extraction of roads from lidar data. *International Archives of Photogrammetry, Remote Sensing and Spatial Information Sciences*, 35.
- Clode, S., Rottensteiner, F., Kootsookos, P., and Zelniker, E. (2007). Detection and vectorization of roads from lidar data. *Photogrammetric Engineering and Remote Sensing*, 73:517–535.
- Durán Fernández, R. and Santos, G. (2014). A gis model of the national road network in mexico. *Research in Transportation Economics*, 46.
- Ekpenyong, F., Brimicombe, A., Palmer-Brown, D., Li, Y., and Lee, S. (2007). Automated updating of road network databases: road segment grouping using snap-drift neural network. *Proceedings of Advances in Computing and Technology*, pages 160–167.
- Fan, L., Smethurst, J., P.M., A., and Powrie, W. (2014). Propagation of vertical and horizontal source data errors into a tin with linear interpolation. *International Journal of Geographical Information Science*, 28:1378–1400.
- Fouque, C. and Bonnifait, P. (2008). Tightly coupled gis data in gnss fix computation with integrity test. *Journal of Intelligent Information and Database Systems*, 2:167–186.
- Gross, H. and Thoennessen, U. (2006). Extraction of lines from laser point clouds. *Fraunhofer FOM*, 36.
- Guarnaccia, C. and Quartieri, J. (2012). Analysis of road traffic noise propagation. *International Journal of Mathematical Models and Methods in Applied Sciences*, 6:926–933.
- Guo, Q., Li, W., Yu, H., and Alvarez, O. (2010). Effects of topographic variability and lidar sampling density on several dem interpolation methods. *Photogrammetric Engineering and Remote Sensing*, 76.
- Göpfert, J., Rottensteiner, F., and Heipke, C. (2011). Using snakes for the registration of topographic road database objects to als features. *ISPRS Journal of Photogrammetry and Remote Sensing*, 66:858–871.
- Hatger, C. and Brenner, C. (2003). Extraction of road geometry parameters from laser scanning and existing databases. *International Archives of Photogrammetry, Remote Sensing and Spatial Information Sciences*, 34:225–230.
- Hodgson, M. and Bresnahan, P. (2004). Accuracy of airborne lidar-derived elevation: Empirical assessment and error budget. *Photogrammetric Engineering and Remote Sensing*, 70:331–339.
- Hu, X., Tao, C., and Hu, Y. (2004). Automatic road extraction from dense urban area by integrated processing of high resolution imagery and lidar data. volume 35.
- Hu, Y. (2003). *Automated extraction of digital terrain models, roads and buildings using airborne lidar data*. PhD thesis, University of Calgary.

REFERENCES

- Ishiyama, T., Tateishi, K., and Arai, T. (1991). An analysis of traffic noise propagation around main roads in Tokyo. *Noise Control Engineering Journal*, 36.
- Kadaster (Accessed 07/05/2021). *BGT Homepage*. <https://www.kadaster.nl/zakelijk/registraties/basisregistraties/bgt>.
- Kass, M., Witkin, A., and Terzopoulos, D. (1988). Snakes: active contour models. *International Journal of Computer Vision*, 1:321–331.
- Kraus, K., Karel, W., Briese, C., and Mandlbürger, G. (2006). Local accuracy measures for digital terrain models. *The Photogrammetric Record*, 21:342–354.
- Lin, Y., Wang, C., Cheng, J., Chen, B., Jia, F., Chen, Z., and Li, J. (2015). Line segment extraction for large scale unorganized point clouds. *ISPRS Journal of Photogrammetry and Remote Sensing*, 102.
- NDW (Accessed 07/05/2021). *Hoogte in NWB*. <https://nationaalwegenbestand.nl/nieuws/hoogte-nwb>.
- NDW (Accessed 09/12/2020). *NWB is Geometrisch Gecorrigeerd*. <https://nationaalwegenbestand.nl/nieuws/nwb-geometrisch-gecorrigeerd>.
- Oude Elberink, S. (2010). *Acquisition of 3D topography: automated 3D road and building reconstruction using airborne laser scanner data and topographic maps*. PhD thesis, University of Twente.
- Oude Elberink, S. and Vosselman, G. (2006). Adding the third dimension to a topographic database using airborne laser scanner data. *International Archives of Photogrammetry, Remote Sensing and Spatial Information Sciences*, 36.
- Oude Elberink, S. and Vosselman, G. (2009). 3d information extraction from laser point clouds covering complex road junctions. *Photogrammetric Record*, 24:23–36.
- Oude Elberink, S. and Vosselman, G. (2012). Quality analysis of 3d road reconstruction. *International Archives of Photogrammetry, Remote Sensing and Spatial Information Sciences*, 36.
- PDOK (Accessed 07/05/2021). *Luchtfoto Homepage*. <https://www.pdok.nl/introductie/-/article/luchtfoto-pdok>.
- PDOK (Accessed 09/12/2020). *AHN3 Downloads*. <https://downloads.pdok.nl/ahn3-downloadpage/>.
- Peng, J., Parnell, J., and Kessissoglou, N. (2020). Spatially differentiated profiles for road traffic noise pollution across a state road network. *Applied Acoustics*, 172.
- Peng, M.-H. and Shih, P. T.-Y. (2006). Error assessment in two lidar-derived tin datasets. *Photogrammetric Engineering and Remote Sensing*, 72:933–947.
- Raber, G., Jensen, J., Hodgson, M., Tullis, J., Davis, B., and Berglund, J. (2007). Impact of lidar nominal post-spacing on dem accuracy and flood zone delineation. *Photogrammetric Engineering and Remote Sensing*, 73:793–804.
- Rijkswaterstaat (2020b). *Handboek DTB*.
- Rijkswaterstaat (2020c). *Handleiding Nationaal Wegenbestand (NWB-Wegen)*.
- Rijkswaterstaat (2020d). *Productspecificaties Digitaal Topografisch Bestand*.
- Rijkswaterstaat (Accessed 09/12/2020a). *AHN Kwaliteitbeschrijving*. <https://www.ahn.nl/kwaliteitsbeschrijving/>.
- Shi, W., Li, Q., and Zhu, C. (2005). Estimating the propagation error of dem from higher order interpolation algorithms. *International Journal of Remote Sensing*, 26:3069–3084.
- Smith, S., Holland, D., and Longley, P. (2005). Quantifying interpolation errors in urban airborne laser scanning models. *Geographical Analysis*, 37:200 – 224.
- Su, J. and Bork, E. (2006). Influence of vegetation, slope, and lidar sampling angle on dem accuracy. *Photogrammetric Engineering and Remote Sensing*, 72:1265–1274.
- Taylor, G., Blewitt, G., Steup, D., Corbett, S., and Car, A. (2001). Road reduction filtering for gps-gis navigation. *Transactions in GIS*, 5:193–207.
- Thomson, R. and Richardson, D. (1995). A graph theory approach to road network generalisation. *Int. Cartographic Conference*, pages 1871–1880.
- Vosselman, G. and Liang, Z. (2009). Detection of curbstones in airborne laser scanning data. *Remote Sensing and Spatial Information Sciences*, 38.
- Wang, J., Lawson, G., and Shen, Y. (2014). Automatic high-fidelity 3d road network modeling based on 2d gis data. *Advances in Engineering Software*, 76:86–98.

- Yang, B., Fang, L., and Li, J. (2013). Semi-automated extraction and delineation of 3d roads of street scene from mobile laser scanning point clouds. *ISPRS Journal of Photogrammetry and Remote Sensing*, 79:80–93.
- Yue, Y., Yeh, A., and Li, Q. (2008). Road network model for vehicle navigation using traffic direction approach. pages 613–629.
- Zhang, H. (2011). *Uncovering road network structure through complex network analysis*. PhD thesis, Hong Kong Polytechnic University.
- Zhang, W. (2010). Lidar-based road and road-edge detection. pages 845 – 848.
- Zhu, L. and Hyyppä, J. (2014). Fully-automated power line extraction from airborne laser scanning point clouds in forest areas. *Remote Sensing*, 6(11):11267–11282.
- Zhu, Q. and Li, Y. (2007). Review of road network models. pages 471–476.
- Zhu, Q. and Li, Y. (2008). Hierarchical lane-oriented 3d road-network model. *International Journal of Geographical Information Science*, 22:479–505.
- Zhu, Q. and Mordohai, P. (2009). A minimum cover approach for extracting the road network from airborne lidar data.

Colophon

This document was typeset using L^AT_EX, using the KOMA-Script class scrbook. The main font is Palatino.

